DEVELOPMENT OF 3D LATTICE MODELS FOR PREDICTING NONLINEAR TIMBER JOINT BEHAVIOUR

A thesis submitted in partial fulfilment of
the requirements of Edinburgh Napier University
for the degree of Doctor of Philosophy
in the Faculty of Engineering, Computing & Creative Industries

August 2009

By
Thomas Reichert
School of Engineering and the Built Environment

Acknowledgements

I would like to thank foremost my supervisor Dan Ridley-Ellis for the support and encouragement during the progress of this dissertation; his guidance, knowledge and diligence is most appreciated.

Furthermore, I would like to thank my second supervisor Ian Pyrah for the input and time that he has spent and Johnson Zhang for his ideas and thoughts in the field of finite elements.

I would like to extend further thanks to the technicians and personnel in the workshops: Alan Barber, Willie Laing, Stefan Lehneke and Andrew Lyon. Their help and advice solved a lot of problems and made the experimental side of the project achievable.

Final thanks are directed to Julia and my family for their patience and support.

Abstract

This work presents the development of a three-dimensional lattice material model for wood and its application to timber joints including the potential strengthening benefit of second order effects. A lattice of discrete elements was used to capture the heterogeneity and fracture behaviour and the model results compared to tested Sitka spruce (*Picea sitchensis*) specimens. Despite the general applicability of lattice models to timber, they are computationally demanding, due to the nonlinear solution and large number of degrees of freedom required. Ways to reduce the computational costs are investigated.

Timber joints fail due to plastic deformation of the steel fastener(s), embedment, or brittle fracture of the timber. Lattice models, contrary to other modelling approaches such as continuum finite elements, have the advantage to take into account brittle fracture, crack development and material heterogeneity by assigning certain strength and stiffness properties to individual elements. Furthermore, plastic hardening is considered to simulate timber embedment.

The lattice is an arrangement of longitudinal, lateral and diagonal link elements with a tri-linear load-displacement relation. The lattice is used in areas with high stress gradients and normal continuum elements are used elsewhere. Heterogeneity was accounted for by creating an artificial growth ring structure and density profile upon which the mean strength and stiffness properties were adjusted.

Solution algorithms, such as Newton-Raphson, encounter problems with discrete elements for which 'snap-back' in the global load-displacement curves would occur. Thus, a specialised solution algorithm, developed by Jirasek and Bazant, was adopted to create a bespoke FE code in MATLAB that can handle the jagged behaviour of the load displacement response, and extended to account for plastic deformation.

The model's input parameters were calibrated by determining the elastic stiffness

from literature values and adjusting the strength, post-yield and heterogeneity parameters of lattice elements to match the load-displacement from laboratory tests under various loading conditions.

Although problems with the modified solution algorithm were encountered, results of the model show the potential of lattice models to be used as a tool to predict load-displacement curves and fracture patterns of timber specimens.

Contents

List of Figures

List of Tables

Nomenclature

Greek Letters

α	angle between Y-axis and vector from lattice centre to pith	[°]
Δr_n	ring width of ring n	[mm]
Δr_{centre}	ring width of central ring	[N]
$\Delta r_{diff,n}$	difference of ring width from previous one	[mm]
$\Delta_{i,l,ref}$	reference displacement of link l in load step i	[mm,rad]
$\{\Delta\}$	displacement vector	[-]
$\{\Delta_i\}$	displacement vector in load step i	[mm,rad]
$\{\Delta_{ref}\}$	reference displacement vector	[mm,rad]
ϵ	strain	[-]
$\epsilon_{C,f,l}$	strain at compression failure load of link l	[-]
$\epsilon_{C,P,l}$	strain at compression peak load of link l	[-]
$\epsilon_{cr,l}$	critical strain of link l	[-]
$\epsilon_{i,l}$	strain of link l in load step i	[-]
ϵ_l	strain of link l	[-]
$\epsilon_{T,f,l}$	strain at tensile failure load of link l	[-]
$\epsilon_{T,P,l}$	strain at tensile peak load of link l	[-]
η, ξ, ζ	parametric coordinates	[-]
$d\epsilon_{i,l}$	strain-increment of link l in load step i	[-]
$\gamma_{T,j}$, $\gamma_{C,j}$	parameters defining tensile/comp. softening curve (direction j)	[-]
λ_i	load factor in load step i	[-]
λ_i^+	positive load factor in load step i	[-]
λ_i^-	negative load factor in load step i	[-]
$\lambda_{C,j}$	influence of density variation on the comp. strength (linktype j)	[-]
$\lambda_{i,l}$	load factor of link l in load step i	[-]
$\lambda_{K,j}$	influence of density variation on the stiffness (linktype j)	[-]
$\lambda_{T,j}$	influence of density variation on the tensile strength (linktype j)	[-]
μ	mean value	[-]
ν_{xy}	Poisson ratio (load applied in X and displacement in Y)	[-]

Π	potential energy	[-]
φ	probability density	[-]
$\overline{\rho}(r)$	normalised density at radial distance r	[-]
$\overline{\rho}_{diff,n}$	difference between max. normalised density and min. (ring n)	[-]
$\overline{\rho}_{exp,n}$	exp. parameter in approx., normalised density function (ring n)	[-]
$\overline{\rho}_{l}$	density represented by link l	[-]
$\overline{\rho}_{min,n}$	min. parameter in approx., normalised density function (ring n)	[-]
σ	standard deviation	[-]
σ	stress	[N/mm^2]
σ_{ij}	2$^{\text{nd}}$ order stress tensor	[N/mm^2]
w	Gauss weights	[-]

Latin Letters

A	cross-sectional area	[mm^2]
A_j	representative cross-sectional area of link type j	[mm]
$[B]$	global strain-displacement matrix	[-]
$[B^{el}]$	element strain-displacement matrix	[-]
$\{B^{el}\}$	element strain-displacement vector	[-]
$c_{v,j}$	coefficient of variation (direction j)	[-]
c_v	coefficient of variation	[-]
$[\hat{D}_i]$	stiffness matrix of all changed links in load step i	[-]
$[D_i]$	stiffness matrix of all links in load step i	[-]
dx	infinitesimal displacement in x	[mm]
dx, dy, dz ...	lattice spacing in X, Y and Z	[mm]
E_x	elastic modulus in X	[N/mm^2]
$\{F\}$	load vector	[N,Nmm]
$\{F_{ref}\}$	reference load vector	[N,Nmm]
F_l	force acting in one spring l	[N]
F_y	yield condition	[-]
G	energy release rate	[Nmm/mm^2]
G_c	critical energy release rate	[Nmm/mm^2]
G_{xy}	shear modulus in XY-plane	[N/mm^2]
i, j, k, m	arbitrary variables	[-]
$[K]$	global stiffness matrix	[-]
$[K_i^j]$	global stiffness in load step i iteration j	[-]
$[K^{el}]$	element stiffness matrix	[-]
$\overline{K}_{\textcircled{1},j}$	mean initial stiffness parameter in direction j	[N/mm]

$\overline{K}_{\textcircled{1}}$	mean initial stiffness of spring	[N/mm]
K	stress intensity factor	[Nm$^{-3/2}$]
K_c	fracture toughness	[Nm$^{-3/2}$]
$K_{\textcircled{1},l}$	actual initial stiffness parameter of link l	[N/mm]
l	element length	[mm]
l	link number	[-]
$l_{y,j}$	representative cross-sectional area of link type j	[mm]
$l_{z,j}$	representative cross-sectional area of link type j	[mm]
len_l	element length if link l	[mm]
$\{N^{el}\}$	element shape function	[-]
$P_l(x_c, y_c, z_c)$.	vector from pith to centre coordinates (x_c, y_c, z_c) of link l	[mm]
$[\hat{R}]$	special matrix in MIF routine	[-]
$\overline{r}_{shift}$	relative position of specimen in central growth ring	[-]
r	radial distance from pith	[mm]
r'_n	radial distance from pith to interpolated ring n	[mm]
r_n	radial distance from pith to ring n	[mm]
r_{pith}	distance from lattice centre to pith	[mm]
r_{shift}	parameter defining position of specimen in central growth ring	[mm]
$\overline{S}_{T,j}$, $\overline{S}_{C,j}$	mean tensile/compressive strength parameter in direction j	[N]
$\overline{S}_T$, $\overline{S}_C$	mean tensile/compressive strength	
$\{\hat{s}\}$	vector with inelastic forces and moments	[N,Nmm]
$S_{T,l}$, $S_{C,l}$	actual tensile/compressive strength parameter of link l	[N]
U	elastic energy	[-]
u	displacement	[mm,rad]
U^{el}	elastic energy stored in one element	[-]
U_P	potential energy of applied forces	[-]

Acronyms

AMD	**A**proximate **M**inimum **D**egree
CM	**C**uthill **M**cKee
DoF	**D**egrees **o**f **F**reedom
DM	**D**amage **M**echanical Model
DMoE	**D**ynamic **M**odulus **o**f **E**lasticity
DVW	**D**ensified **V**eneer **W**ood
EYM	**E**uropean **Y**ield **M**odel
FE	**F**inite **E**lement
FM	**F**racture **M**echanics
LDP	**L**oad **D**isplacement **P**lot
LEFM	**L**inear **E**lastic **F**racture **M**echanics
LSL	**L**aminated **S**trand **L**umber
MFA	**M**icro **F**ibril **A**ngle
MIF	**M**ethod of **I**nelastic **F**orces
MIFM	**M**ethod of **I**nelastic **F**orces and **M**oments
MoE	**M**odulus **o**f **E**lasticity
MoR	**M**odulus **o**f **R**upture
NLFM	**N**on**L**inear **F**racture **M**echanics
OSB	**O**riented **S**trand **B**oard

PY	**P**ost **Y**ield
RCM	**R**everse **C**uthill **M**cKee
SSC	**S**tep **S**ize **C**ontrol

1 Introduction

1.1 General

Joints often represent the weakest link in timber structures. Various modelling approaches have been suggested to predict the load displacement and failure behaviour of an entire joint which is made of various components. The main challenge in these models is the application of an accurate material model for timber. In the most general case of a timber joint, a complex 3D stress state, fracture mechanical aspects and plastic deformation, need to be addressed.

This research aims to develop a 3D material model that takes into account the plastic hardening and quasi-brittle behaviour of timber. Wood, as a natural material, makes great demands on the modelling technique. Anisotropy, material heterogeneity on several length scales, and apparent plastic deformation need to be considered and complicate any analysis technique. In this research, lattice models shall be used to meet these requirements. These consist of single bar elements that can reflect distinct material features on a small scale.

A special solution algorithm, more suitable for lattice structures, by Jirasek & Bazant (1995) was extended to account for plastic hardening behaviour. A 3D lattice arrangement was devised in order to model timber. These lattices are able to predict nonlinear material and fracture behaviour while the heterogeneous character of the material can be easily implemented. With the incorporation of other element types such as solid, contact and beam elements, the lattice can be used in a 3D joint model. These new elements required another extension to the methods described in Jirasek & Bazant (1995) in order to incorporate geometric nonlinearity.

Commonly, models for timber joints address only specific arrangements. For example, either ductile joint behaviour is assumed: timber is allowed to deform plastically and no fracture process is considered. This is the assumption made in

the widespread European Yield Model (EYM). The potential failure modes for a single shear dowel-type joint are shown in Fig. 1.1. On the other hand simpler models with simple stress states are used when brittle failure is considered and fracture mechanical models are used.

The model described in this thesis shall be used for both joint behaviours. Although only mode c) in a single shear joint (embedment failure in both timber members, Fig. 1.1) is presented here, the model itself could be extended to account for plastic fastener deformation relatively easily.

Generally, the work presented here can be divided into four main parts. Firstly, a simple 2D finite element FE model is used to predict geometric nonlinear joint behaviour for single shear bolted joints. A novel solution technique and other optimisations are used in order to minimise the computational effort of the numerical model, chapter 4. Secondly, a material model is developed in the framework of lattice structures, chapter 5. Thirdly, the model is calibrated and validated by tested specimens under simple stress states. As a final step, the model is used in an attempt to predict the load-displacement and failure behaviour of a bolted single shear timber joint. For this, the principle idea of geometric nonlinear beam elements that represent bolt deformation in the simpler 2D model is reused, chapter 6.

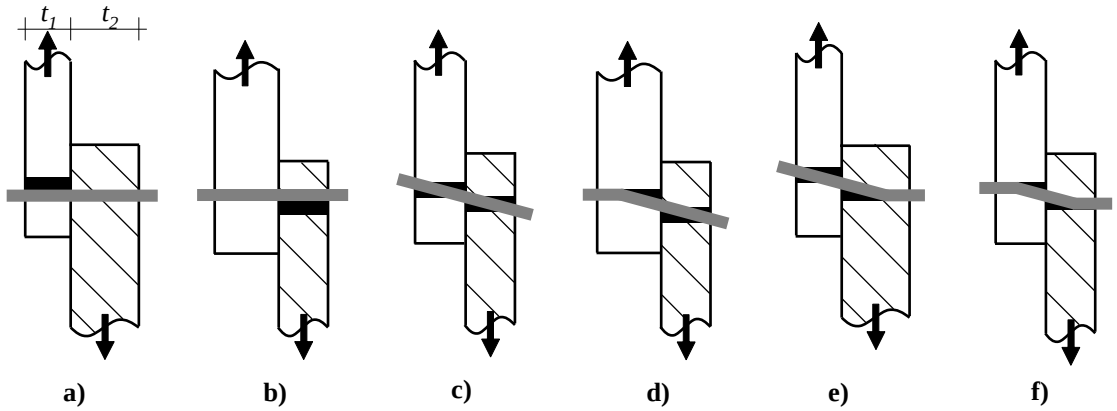

Figure 1.1: *Failure modes of single shear timber joints according to the European Yield Model (BS EN 1995-1-1, 2004).*

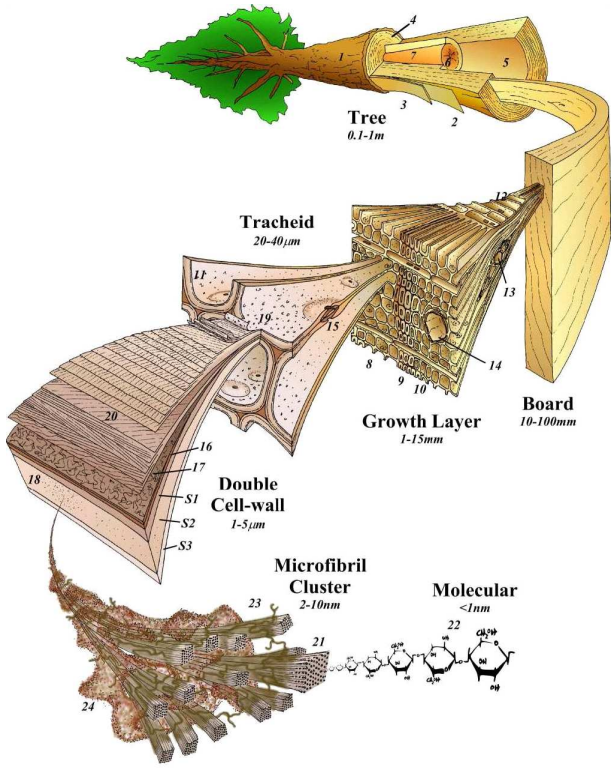

Figure 1.2: *Various scales of wood morphology, for key see reference, courtesy of Harrington (2002) (original in colour).*

1.2 Wood Modelling

The modelling of fibrous materials such as wood involves a vast number of complexities. The very nature of the material makes it hard to develop appropriate material models. Plastic deformation and fracture governing failure results from inherent flaws in the material on several different size scales. Due to its naturally grown structure anisotropy and morphology of wood (such as the growth ring structure, knots, grain deviation and other variable defects in the material) have to be considered in a model to predict realistically yield and fracture behaviour.

Fig. 1.2 presents graphically the different length scales that are involved in describing timber behaviour. Wood has varying strength and stiffness properties over all these different scales. The inherent differences range between species, trees within a species and even within trees down to the growth rings and beyond. This complicates the development of a material model for timber.

Numerical methods, such as the continuum finite element method, have been used

to take the orthotropic and nonlinear, plastic behaviour into account. Failure analysis can be applied to these models but is limited to the averaging effect inherent in continuum models. The material is viewed as a continuous stress state and, therefore, high peak stresses, that occur in material flaws, can not accurately be accounted for.

On the other hand, fracture mechanics accounts for high peak stresses at crack tips that result from either already existing inherent flaws of the material or intentional notches. The methods developed around fracture mechanics FM are useful tools to predict failure loads and crack development in brittle material. However, despite the fact that nonlinear effects such as plastic deformation in the vicinity of a crack tip can be taken into account, the technique stands and falls with appropriately measured fracture parameters and a realistic fracture mechanical model.

Other, harder to predict, effects in failure analysis, such as material heterogeneity, crack bridging and crack paths hitting inclusions, can best be described with lattice models. Distinct elements represent material features on a certain length scale. Material heterogeneity can easily be implemented by assigning varying material properties to individual lattice elements.

However, the practicality of numerical models greatly depends on the required processing speed and memory capacity. Often, analytical solutions applied to more simple models reach a sufficient solution while numerical models, applied to a more complex geometry, simply become too expensive in terms of computation time. Especially, lattice models require a high number of Degrees of Freedom (DoFs) to represent the detailed morphological features. In case of a model that accounts for a complex 3D stress state, the required computation time quickly reaches the limits imposed by standard computers.

1.3 Lattice Model

Morphological lattice models to simulate failure in heterogeneous quasi-brittle material can be used and solved with various techniques. The simplest technique, that is commonly used in lattice fracture models, is based on the sequential removal of broken elements due to exceeded strength properties. Then, with the application

of a new displacement step, the softer system (due to several removed springs) is recalculated and a new equilibrium found. The method will be described in more detail in the Literature Review, subsection 3.3.4.

While this technique is simple to apply and bulk softening of the structure can be predicted, plastic deformation and softening behaviour of individual links (cohesive crack relation) are not incorporated. This can only be accomplished by the use of an iterative incremental method. For this, traditional iterative techniques such as the Newton-Raphson algorithms (with specialised load or displacement control) are required to solve for the nonlinear solution. The problem with such techniques is that mechanical response such as 'snap-back', where a decrement in load and displacement is required, can not be handled very well. Points of instability in the load displacement curve (global stiffness matrix is singular due to negative values as a result of the link's softening branch) represent another problem for numerical techniques. This complicates a solution algorithm for lattice models that accounts for plasticity.

A solution to these issues can be found in Jirasek & Bazant (1995) who developed an efficient specialised solution algorithm called the 'Step-Size-Control Algorithm' (SSC). In essence, the technique treats each change of stiffness in individual links as single linear steps. The overall load displacement curve of a lattice system consists of load-steps in which only one single element changes its stiffness. Thus, no additional iterations are necessary and 'snap-back' is accounted for. This might seem, at first, to be more complex than traditional methods, but the algorithm should perform, according to Jirasek & Bazant, more robustly and more efficiently on large systems.

Furthermore, a technique called the 'Method of Inelastic Forces' (MIF) has been used by Jirasek & Bazant that treats stiffness changes of individual lattice elements with additional external forces. An 'inelastic force' is calculated that represents the force which is required to be applied to the system in order to simulate the system with the changed stiffness due to the broken or changed link element. With this, it is unnecessary to resolve the global stiffness matrix when springs are experiencing stiffness change. The initial solution can be used with these new external forces applied. The calculation of these forces is still time consuming, but the time to solve a global stiffness matrix of a large lattice system is much greater. Furthermore, the inelastic force needs only to be applied to the changed links whose number in most

lattice models is rather small. Hence this method shows its usefulness, especially for large systems for which a large global stiffness matrix would need to be solved otherwise (with a relatively small number of changed link elements).

1.4 Application to Timber Joints

As an example of the applicability of the developed lattice model, a timber joint shall be used.

Joints, the connection of two or more timber members, come in various forms. There are a vast number of different arrangements of joints with mechanical fasteners. The list includes connections with dowel-type fasteners such as glued-in bolts, bolts with washers, head and nut, metal dowels, nails or similar joints with shear plates, punched metal plates, toothed-plates. The focus of this research is on dowel-type joints in particular bolted joints.

Joints represent a distinct obstacle for the force flow in the overall structure. Load is transmitted through a bottle neck of one ore more fasteners which consist of, in most cases, much stiffer and more ductile steel. Furthermore, the hole drilled for the fastener leads to stress concentration and thus drives cracking. Usually, joints mark the weakest link in the mechanical response of the whole timber structure. Consequently, joints receive large attention in timber research.

Joints loaded perpendicular, as well as parallel to the grain, lead to tensile stresses in the timber member. In case of a joint loaded in the perpendicular to the grain direction tensile forces develop in the radial and tangential direction simply due to the loading direction of the fastener. For the parallel case radial and tangential tensile stresses develop as a result of the fastener acting like a wedge that tries to split open the timber member. Additionally, shear stresses develop as parts of the timber member in front of the fastener gets displaced. The actual contribution of both effects on joint failure, depend on the friction between fastener and timber contact.

To prevent brittle failure, and thus a sudden loss of structural resistance, minimum edge and end distances for joints are required as outlined in BS EN 1995-1-1 (2004).

But even with these limit values adhered, fracture might still occur as shown by Schmid et al. (2002) and Daudeville et al. (1999). In order to create a joint that exhibits a more ductile behaviour, engineers use slender fasteners where one or more plastic hinges can form, and thus the greater part of deformation takes place in the metal fastener.

The aim of this research is to investigate the possible use of lattice models for timber joints. Furthermore, the geometric nonlinear effects, that result from a deformed and/or rotated fastener, shall be included. In such cases axial forces and a rotational constraint develop from the fixation of head, nut and washer (described in more detail in the following subsection 1.4.1). Additionally, the length of timber embedment alongside the fastener changes due to these effects.

Future research might involve a larger parameter study with these lattice models. Joint parameters such as end and edge distances, fastener diameter and different wood parameters can be varied to investigate the different failure mechanisms and loads. Secondly, the model can be used in various applications to investigate the simultaneous plastic and brittle timber behaviour. These can range from single systems such as notched beams or torsion beams to further combined systems such as multiple joints with different timber and bolt arrangements.

Ultimately, the goal of these models is to represent an alternative to continuum and fracture mechanical models for predicting timber behaviour. After their validity has been demonstrated, they can reduce costly experimental investigations of timber structures. Lattice models are able to deliver a larger spectrum of possible tests based on varying wood morphology. Therefore, lattice models are a type of Monte Carlo method where after several model runs, certain fractile values of e.g. strength, stiffness, maximum deformation etc. can be evaluated.

1.4.1 Neglected Effects

In the European code for timber design (BS EN 1995-1-1, 2004) the ultimate strength of a timber joint is calculated according to the European Yield Model developed by Johansen (1949). Conservatively, geometric nonlinear effects used to be neglected. These include the tensioning of a fastener (called 'rope effect') due to the end-fixity and the rotational constrain provided by washer, head and nut or

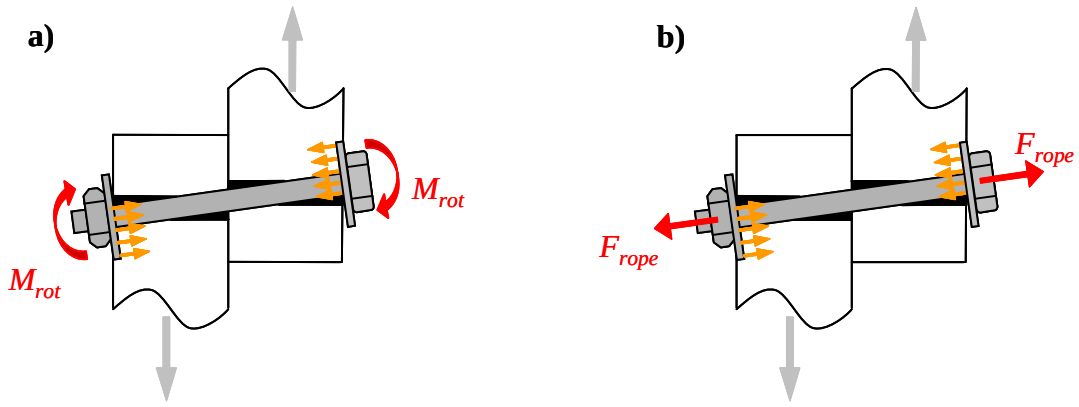

Figure 1.3: *Geometric nonlinear effects in a single shear bolted joint, a) rotational constraint due to washer and b) axial tension acting on fastener (rope effect).*

nail head (Fig. 1.3).

This occurs while the timber members displace and thus the fastener or parts of it start to rotate in a single or multiple shear joint. The washers or the nail head are pulled into the side member and therefore increase the joint's resistance. These strengthening effects are a function of: the displacement of the timber members, different joint parameters such as timber thickness, fastener diameter, withdrawal strength (e.g. nailed connection) and embedment strength underneath the washer (e.g. bolted connections).

BS EN 1995-1-1 (2004) incorporates these strengthening effects with a term added to the original Johansen's equation. This term is based on the withdrawal strength of a fastener and thus accounts only for the rope effect at the limit state. Other effects, such as the rotational constraint provided by a washer or nail head, are still neglected. The term was derived analytically and is not really founded on an extensively researched mechanical basis. Furthermore, the rotational constraint facilitates the development of a plastic hinge in the fastener and thus leads to a shift of failure mode from brittle to more ductile.

1.5 Problem Outline

The resulting stress state around the fastener of a single shear joint can not be represented assuming 'in plane' stress or strain. Lateral strain and stress vary

over the depth of the joint due to the inclined embedment of the rotated fastener shank. Thus, the appropriate solution is a full three dimensional model. This adds significantly to the model's complexity and the computational demand. Lattice models may be used to capture the quasi-brittle fracture process and to account for the morphology of wood.

In most previous research papers, these types of models mainly consisted solely of perfectly brittle elements, i.e. no ductility of the single elements or plastic behaviour was taken into account. In this case a simple solution algorithm could be used which is described in more detail in the Literature Review, chapter 3.

To account for plasticity, as observed in timber under compression, elements can be defined with a tri-linear load-displacement curve: an initial stiffness, a softening branch under tension and a reduced stiffness under compression. However, these models require a general incremental solution method such as the Newton Raphson algorithm with certain load or displacement control techniques (e.g. the arc length method). They have, to the author's knowledge not been attempted yet for timber. In this project the SSC algorithm has been used and extended to work with a tri-linear load displacement definition for link elements.

1.6 Scope and Limitations

After the lattice model has been calibrated against test data, it is possible to predict plastic and brittle material behaviour for arbitrary 3D stress states. It would have been difficult to implement such a lattice model into an already existing commercial FE package. Therefore, a bespoke FE software to generate and calculate such a lattice has been written in *MATLAB* (The MathWorks, Inc., 2007). The thesis focusses mainly on the development of this software, *LAT3D*, with its implemented solution algorithm and the different element types that are required in the final joint model.

The program is capable of simulating 2D and 3D lattice/solid models. Both are used in the calibration routine. While the program is structured so that it can solve several problems and rearrange the geometry of the models freely it has specifically elements such as 3D beam and contact elements implemented to solve the problem

of a single shear bolted timber joint.

Problems arose when larger lattice models have been calculated with the proposed program *LAT3D*. A high number of links that switch to the plastic state lead to a slowing down of the solution algorithm. Furthermore in certain stress states the solution algorithm collapsed and lead to an erroneous load step. The encountered problems are described in the discussion chapter 7.

2 Methodology

2.1 General

This chapter introduces the general methodology of the project. The objective of this research is to predict nonlinear timber joint behaviour by the use of FE models. The research can be divided into three distinct major parts: firstly a preliminary 2D model that investigates the material and geometric nonlinear behaviour of a single shear joint using a beam on elastic-plastic foundation model, secondly a 3D lattice material model for timber that predicts the brittle nonlinear material behaviour and thirdly the combination of both a 3D model of a single shear timber joint with a lattice that represents nonlinear timber embedment combined with 3D beam elements taking into account geometric nonlinear deformation of the fastener.

The 2D model is a quick approach to investigate the geometric nonlinear behaviour for a fastener in elastic-perfectly plastic embedment. It is akin to other 2D models such as Sawata & Yasumura (2003) and Nishiyama & Ando (2003) as described later in the Literature Review. The commercial FE package ANSYS was used for this model.

The 3D lattice is a further approach to model 3D material behaviour. Individual elements that represent material behaviour in certain directions are allowed to change their stiffness until entire removal, thus enabling it to model fracture development inside the material. Heterogeneity and wood morphology can be taken into account by adjusting the parameters which define the load-displacement curve of individual lattice elements (links).

For the combination of both approaches, the lattice material model is connected to beam elements which represent a fastener. This can be done via special contact links in a geometric nonlinear analysis.

This chapter introduces the chosen approach and the concept of the two models.

2.2 Model Concept: 2D Beam-Foundation Model

The 2D approach is a first attempt in this project to create a model for a single shear joint based on the 'beam on elastic-(plastic) foundation' principle. It takes into account nonlinear effects such as perfect plastic timber embedment and geometric nonlinearity. The development of this model along with results is published in Reichert & Ridley-Ellis (2006). The approach was chosen in order to overcome some problems with the prediction of joint behaviour. Johansen's failure modes, as employed in the Eurocode 5 for timber structures BS EN 1995-1-1 (2004), can only predict a limit state with the assumption of a perfectly plastic material. Certain aspects are neglected, such as the geometric nonlinear effects, and no influence of failure modes on the joint stiffness can be obtained from the model. Johansen's Yield Model and its derivation is explained in more detail in the Literature Review (subsection 3.4.1).

Rather than only calculating the limit state of the timber joint, the 2D model employs a nonlinear FE solution. Although the model can not be used in a simple way, and does not represent a substitution to the widely used EYM, it gives insight into the different geometric nonlinear effects of a bolted timber joint and can be used to investigate these separately. Therefore, it can be used to adjust certain parameters in the EYM to better incorporate geometric nonlinear effects (subsection 3.4.2 and chapter 4).

2.3 Model Concept: 3D Lattice

The significant larger portion of the project was dedicated to develop a material model for timber. In order to accomplish this a bespoke FE code has been written that enables the user to define model parameters and instruct the program to create a variety of different geometries. For the following chapters the name *LAT3D* is used to refer to this program.

This numerical approach was chosen due to the complex 3D stress state that occurs

in a deformed timber joint.

The aim was to create a material model that is capable of predicting nonlinear failure phenomena and accurate load-displacement responses of timber structures. According to recent developments in timber research, lattice models produce reasonable results and can be used instead of continuum material models. The main advantage is that instead of averaging stresses in a continuum model, forces and the resulting failure are calculated at individual elements which can represent material features on the meso scale. Additionally, variability can be incorporated by assigning different properties to these elements.

The 3D lattice in this investigation consists of different nonlinear springs that model timber behaviour. The springs are able to represent the heterogeneous character of timber by assigned (to single elements) mean stiffness and strength values along with their coefficients of variation. The morphological structure on the scale of growth rings is implemented by adjusting these mean values according to the position of the elements in a randomly created ring structure. Density profiles are used to map certain strength and stiffness variability on the lattice.

In a final step, both models (beam-foundation and lattice) are combined. Geometric nonlinear beam elements representing a fastener are implemented in the lattice model by means of contact links. These elements exhibit a penalty stiffness when contact between the predicted bolt line and lattice surface nodes is made and are close to zero when there is no contact.

Consecutive update of the nodal displacements along with stiffness update of the beam elements in each load step accounts for geometric nonlinearity.

3 Literature Review

3.1 General

This chapter gives an overview on the relevant aspects of wood morphology and its influence on modelling approaches, further it shows possible material models for timber and looks into more detail on previous joint models.

Wood as a building material has a long tradition. Despite its common use, ranging from residential buildings in from of stud walls, flooring systems and pertinently roofs to wide spanning structures such as bridges, sports halls, domes etc., the matter of accurately predicting the mechanical response of timber still attracts large research interest.

Based on the fact that wood in its raw from is a naturally grown material, it is evident that this very useful material has certain advantages and disadvantages when used as a load carrying member in other structural systems.

Foremost on the list of advantages of using wood are the ecological and economical aspects. Producing a structure made of timber requires much less energy when compared to concrete and steel. Due to the positive CO_2 balance, wood has the potential to mitigate the effects of global warming, since the tree in its time of growth stores a substantial amount of atmospheric carbon e.g. (Canadian Wood Council, 2008). It is further a sustainable building material since it can be reproduced on a large scale and is accessible in most parts of the world.

From a mechanical aspect, a significant advantage for timber, compared to other common construction materials, is the high ratio of load carrying capacity over self-weight, for stresses parallel to the grain. As well as house construction, this enables wood to be used in wide spanning structures. Besides this, timber structures have a beneficial effect on the dynamic response due to the relative high

damping ratio, which is due, in part, to friction and impact damping.

Wood is also a material that is very workable without having to use heavy machinery as it is the case e.g. for steel and concrete. On the other hand, it is not so easily joined. Despite much research development in gluing and even 'welding' timber, most modern timber joints consist of metal fasteners. Bolts, nails, staples and special connector types are commonly used since they can be easily manufactured. Furthermore, these types of fasteners facilitate the assembling of a joint. On the contrary, glueing timber requires a conditioned environment and often long curing times. Further, traditional carpentry joints are complicated and expensive to form.

On the side of disadvantages, wood's sensitivity to temperature and moisture which have further an influence on its mechanical properties must be mentioned (Smith et al., 2003, p.33). Research by Rammer & Winistorfer (2001) shows that moisture content influences the dowel-bearing strength. This has been confirmed by Harada et al. (2005) while testing full timber joints. It is clear that humidity has to be considered as an influencing factor when timber structures are designed. However, in most studies this parameter is neglected by keeping the moisture content of test samples at a fixed value.

Other influences that are damaging the material are weathering effects such as Ultraviolet light, rain as well as insects and fungi. Treatment of timber when used in critical environments is therefore required.

Due to wood's natural growth pattern, it is a heterogeneous material with distinct axis-dependent material properties. The relative low tensile strength of wood in the radial and tangential direction, in comparison to its longitudinal strength, represents a major weak point. This is not as crucial for flexural members as it is for joints and notches, where stress concentration leads to high tensile stresses and therefore cracks can easily propagate.

In conclusion, wood needs special attention when structures are being designed. It has its drawbacks and challenges. But most problems can be overcome when the material is used with caution and structures are designed by timber experienced engineers. Joints, being often the weakest point in the entire structure, usually govern the size of structural members. Therefore special consideration must be taken in this regard.

3.2 Wood Anatomy

In order to have a clear understanding of bulk timber behaviour, a closer look on the micro structural anatomy is necessary. This section gives a brief overview of wood characteristics that influence its mechanical behaviour.

Wood is an inhomogeneous material. It is a fibre based composite consisting of cells that are roughly $3-5$ mm in length for softwoods (Smith et al., 2003, p.15). These tube-like, often hexagonal shaped cells are added in the tree's lifetime every year as a new layer in the cambium. This outer layer of the tree along with the sapwood are the only 'living' part of the trunk and transport water and food. The width of the new formed annual growth ring can range widely depending on the species and as well within one species.

The main influence of variation in this layer is the environment in which the tree is grown (Park & Spiecker, 2005). This is most evident when looked at trees in very different climates. In temperate regions especially for softwoods a pattern of dense (latewood) and less dense (earlywood) wood can be found as a result of changing summer-winter seasons. The two parts vary according to the amount and time of growth that occurred. This is consequently less distinct for tropical trees, where the climate is relatively constant throughout the year.

The density variation in softwoods (conifers) is a result of the growth of thin walled earlywood cells and thicker latewood cells. The cells, called tracheids, are responsible for the transport of water and food for growth. The tree creates thin cells for good 'conductivity' in spring time, while in summertime the growing of supporting cells is more important and thus denser cells are created. Winter again, is a time when growth stops completely (Thibaut et al., 2001). For temperate softwoods, a steep increase in density can be seen towards the latewood region and a sharp change from latewood to earlywood corresponding to winter.

On the contrary to softwoods, hardwoods (broadleaves) have special cells to transport water. These are, depending on the species, more prominent in the earlywood area, and are called vessels. However, this research concentrates on the

modelling of softwoods.

3.2.1 Microstructural Influences

While the tracheids make 90-95% of the volume, softwoods consist of a few other cell types that fulfil various tasks. Among them are ray tracheids and ray parenchyma for transportation of water radially. Some researchers link these radially aligned cells to the different behaviour of radial and tangentially stressed timber. Additionally, resin canals exist which are tubular spaces for transporting resin. These, have no significant influence on the mechanical behaviour, (Smith et al., 2003, p.15).

Each tracheid cell consists of a wall which in turn has several layers. The most influential on mechanical properties is the S_2 middle layer with around 30-150 lamellae (Smith et al., 2003, p.13). The orientation of microfibrils, of which the wall is made, characterises this layer. Consequently, much research in micro structure of wood has been conducted to measure the angle of these fibrils (MFA)and relate these to the meso- and macro-scale structural behaviour of wood (Fig. 3.1). Furthermore, by selecting trees by their microfibril structure potentially better performing timber can be bred for.

Numerous micromechanical models can be found in the scientific literature. However, research by Ping & Huawu (2004), shows that even on the small scale of a single cell, microfibrils require a complex model taking into account the anisotropy of cell walls, as a result of the different lamellae, to accurately predict the mechanical behaviour of cells.

3.2.2 Anisotropic Behaviour

Wood's most important characteristic, that has a major impact on timber design, is its anisotropy. Due to the alignment of the long tubular cells, especially in softwoods, in roughly circular rings around the pith, the material exhibits different mechanical responses in the three main axes (Fig. 3.3). This can be described as cylindrical orthotropy. (L) depicts the longitudinal direction in height, (R) is the radial axis perpendicular to the tree's central axis and (T) depicts the direction tangential to the growth rings.

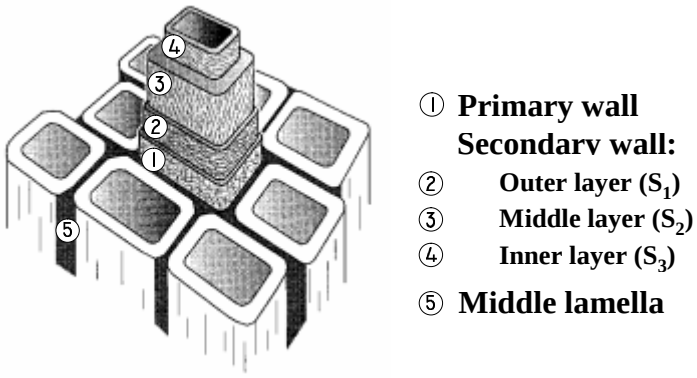

Figure 3.1: *Single wood cell and its components, courtesy of Holmberg et al. (1998).*

In hardwoods, on the other hand, one has to differentiate between ring-porous wood (vessels are orientated in a radial alignment) and diffuse-porous wood (pores are evenly distributed over the ring). The latter, therefore exhibits less transversely anisotropic behaviour. A good example for ring-porous and diffuse-porous timber are white ash and yellow birch (Smith et al., 2003, p.16). Different micro structure between soft and hardwoods can be seen in Fig. 3.2.

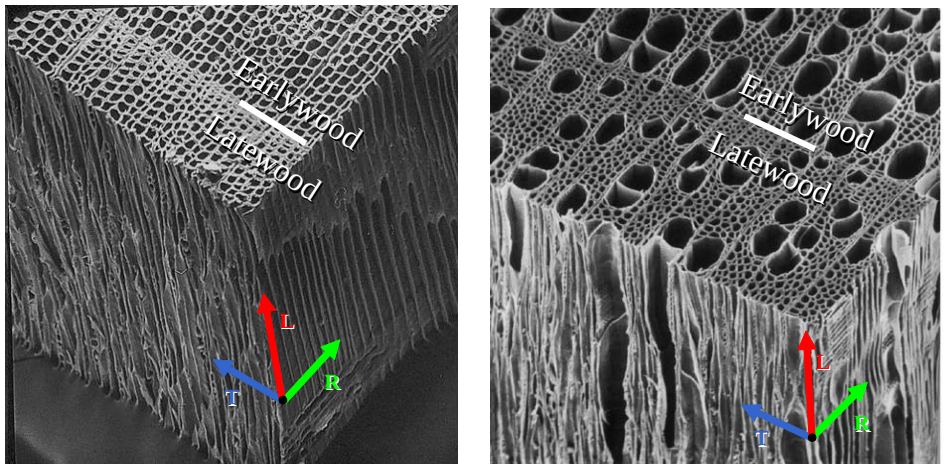

(a) **(b)**

Figure 3.2: *Cell structure, a) softwood and b) hardwood, courtesy of Thibaut et al. (2001).*

Sitka Spruce (*Picea sitchensis*)is the most important commercial species in the UK accounting for some 47% (9.0 million green tonnes) of the round wood harvested (Forestry Commission, 2008). It has been used throughout the experimental part of this research.

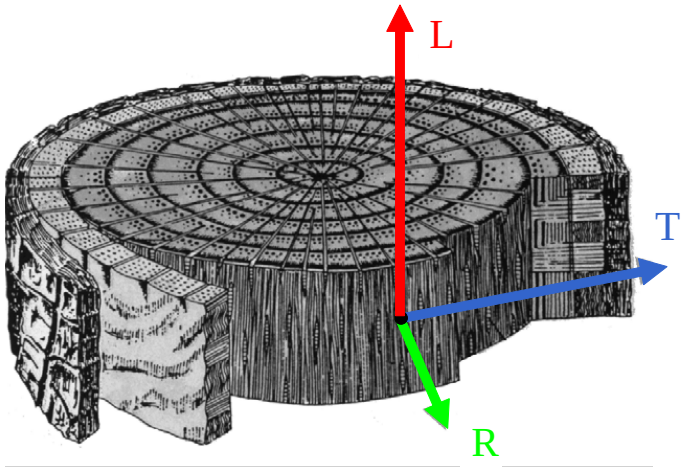

Figure 3.3: *Anisotropy of wood, courtesy of Thibaut et al. (2001).*

From the engineering perspective, timber stressed parallel to the grain (longitudinal direction) provides most interest. This is, first, the strongest axis and second, the direction it is most commonly stressed as in e.g. beams and columns. This leads to the often used machine grading system for timber in which sawn timber is loaded in three point bending and the elastic modulus (MoE) is determined and modulus of rupture (MoR) inferred (MoE and MoR are defined in BS EN 408 (1995)).

The relative weak axes perpendicular to the grain represents the weakest link in timber design. Tensile stresses in these directions lead to delamination and cracking of single cells, as will be discussed in section 3.3.

For practical applications (e.g. in a continuum model for timber) it is often assumed that the specimen is cut far away from the pith and therefore the radial alignment can be neglected. The cylindrical orthotropy becomes normal orthotropy. This will be explained further in section 3.3.

3.2.3 Macrostructural Influences

Other influences on timber properties is spiral grain which results from the cell growth not being perfectly aligned in the longitudinal direction of the tree. Further, the general grain deviation (slope of grain) of cut logs is also affected by the cut not being properly aligned to the axis of the tree either. A deviation of 10° can have a

decrease in MoR of about 40% (USDA, 1999). This has also a significant influence on the elastic stiffness, as shown by Gong (1990) presented in Smith et al. (2003). Cracks usually follow this grain angle. The 3D lattice model in this dissertation assumes perfectly aligned cells.

The natural spiral grain is measured away from perturbations such as knots and defects which influence the grain growth. Knots, therefore introduce certain eccentricities to the force flow and causes stresses to concentrate. Thus, they generally have a negative effect on strength properties. Size of the knots is an important parameter to characterise the potential effect and contribute to the observed size effect of timber. For example, Thibaut et al. (2001) state that by the presence of knots above 3 mm diameter the bending strength of boards is reduced by a factor of 2 (this should depend as well on the dimensions of the tested board). Most research studies on material models for timber (as does this) try to eliminate these influences by testing only clear wood specimens or try to ensure that knots are not in the vicinity of the observed mechanical timber behaviour.

An investigation of the effect of knots in beam specimens can be found in Nardin et al. (2000). They devised a fictitious crack model (explained in subsection 3.3.2) to predict load-displacement curves of timber beams. Nardin uses nonlinear springs that exhibit a negative stiffness to model softening fracture behaviour. These springs are calibrated against measured values obtained from material tests performed on wood that was taken from the vicinity of knots. Good agreement was found among tested beam specimens and FE model predictions.

3.2.4 Growth Ring Structure

For this research, local density variation on the level of growth rings is used in the FE lattice model to account for strength and stiffness variation. The influence of these density variations shall be explained in more detail here.

For bulk material behaviour the literature shows a certain relation of density with MoR and MoE (e.g. Smith et al., 2003, p. 29). This is less the case for shear moduli which does not correlate to the MoE as shown by Khokhar et al. (2008).

Many experimentally derived strength properties such as the compressive

strength perpendicular to the grain, dowel bearing strength etc. in Eurocode 5 (BS EN 1995-1-1, 2004) are based on the density of timber. Although density is, per se, a poor indicator of stiffness and strength, the approach to use density as the main driving factor of variation was also chosen in this research due to the straightforwardness of measuring this property.

Despite this assumed correlation of bulk density, bulk stiffness and strength properties this does not account for the variation in one test specimen. This is mainly, as described above, due to certain micro- and meso- scale structural features such as variation in knots, defects, latewood and earlywood and varying cell structure, including the MFA.

Lin et al. (2007) studied the effects of different ring characteristics such as ring width, ring density and the proportions of earlywood and latewood on compressive strength and the dynamic modulus of elasticity (DMoE). They showed that there is a strong correlation among ring width, ring density and compressive strength. However, the proportions of earlywood and latewood need to be considered as well. Additionally, an overall strong positive relation among DMoE and strength can be observed.

While strength and stiffness properties perpendicular to the grain are largely affected by the density, this is less the case for longitudinal elasticity which depends strongly on the microfibril angle, (Smith et al., 2003, p.45).

Although, density is only one factor that determines strength and stiffness properties of wood there is a clear basis to relate these properties. It is attempted in this research to correlate the variation observed in density with the variation of strength and stiffness parameters of lattice link elements in the FE model. This is at least a valid approach to account for the observed variation among specimens.

Thibaut et al. (2001) states as a rough estimate, a general factor of 2-4 for strength and stiffness difference between latewood and earlywood. Fournier et al. (2007) in their 2D lattice model use roughly similar factors (strength ratio EW/LW: 1.53 in L and 3.33 in R stiffness ratio: 2.24 in L and R and shear) based on the density difference. No stiffness difference in shear is assumed.

3.3 Material Models for Wood

Timber is an inelastic material, hence structural models face two main challenges:

First there is the 'plastic' deformation capability of wood under compression. At the small scale of wood cells, the walls crush and buckle locally, Fig. 3.4. In case of dowel-type timber joints, wood in the vicinity of the fastener is deformed plastically (depending on the specimen dimensions) in the parallel and perpendicular to the grain direction. Important to note is the difference of fibre buckling and cell wall crushing which leads to significantly different behaviour in the lateral and longitudinal direction. This has been modelled sufficiently with elastic-plastic continuum FE models, which will be discussed in the first part of this section.

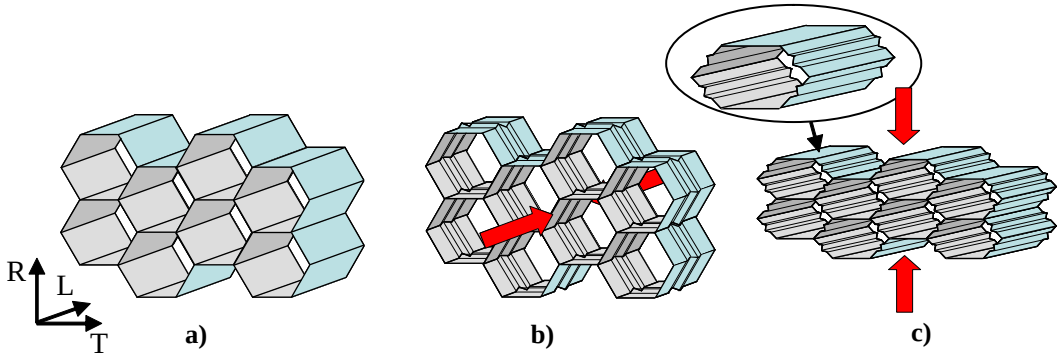

Figure 3.4: *Schematic of failure in group of cells, b) compressive failure in the RT-plane and c) in the LT-plane (original in colour).*

Secondly, wood exhibits quasi brittle behaviour in tension. This occurs, on the micro scale, as either a separation of cell walls perpendicular to the crack surface, a peeling off of cell walls in the crack plane or a separation of individual cells in the longitudinal direction and peeling as shown in Fig. 3.5.

These cracks can occur rapidly and lead to brittle failure. However, foremost fibre branching, cracks hitting an inclusion and partly plastic deformation at the crack tip lead to a decrease in fracture energy, and thus creating nonlinear fracture phenomena. Several linear and nonlinear fracture mechanical approaches have been applied to wood and shall be discussed in the second part of this section.

An electron microscope image taken of a tested Sitka spruce (*Picea sitchensis*) specimen with a tensile failure in the longitudinal direction can be seen in Fig. 3.6.

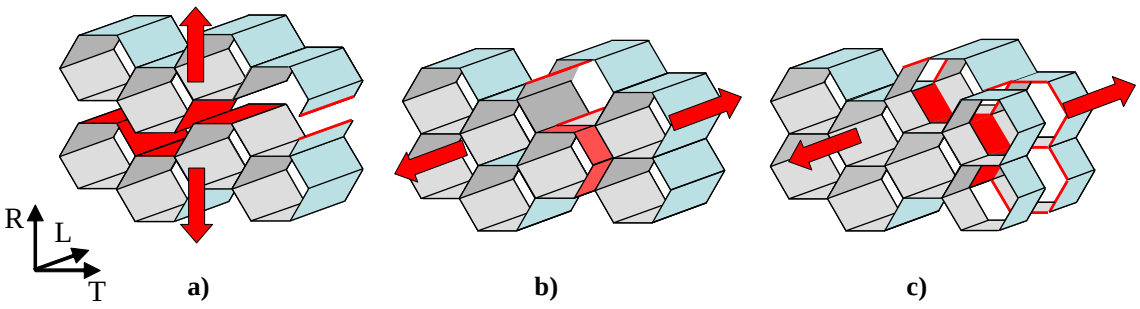

Figure 3.5: *Schematic of failure in group of cells, a) tensile fracture running in the LR plane partly through cells, b) shear fracture in the LR plane and c) tensile failure in L combined with shear in the LR plane (original in colour).*

A recent literature overview on different finite element material models for wood can be found in Mackerle (2005). Research can be subdivided into several categories. It is attempted here to split this large field into elastic and plastic continuum models that use the FE method, fracture mechanical approaches (partly using analytical and numerical FE techniques), fictitious crack and lattice models. The following subsections give first descriptions of the general concepts of modelling techniques and then present recent examples.

3.3.1 Continuum Models

Elastic Continuum Model

In continuum mechanics, the relationship between stresses σ_{ij} and strains ϵ_{kl} can be mathematically described for an anisotropic material with the 4^{th} order stiffness tensor C_{ijkl} as

$$\sigma_{ij} = C_{ijkl}\epsilon_{kl} \tag{3.1}$$

The inverse of C_{ijkl} is the more commonly used compliance tensor S_{ijkl}.

Due to symmetry only 21 are independent parameters. With the assumption of shear stresses not causing any normal strains the matrix can be reduced again to

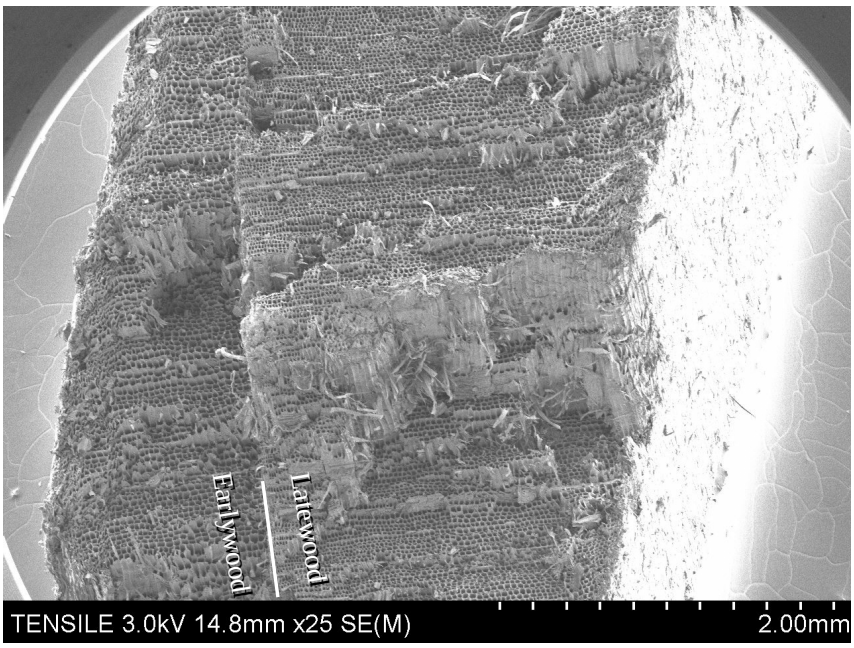

(a)

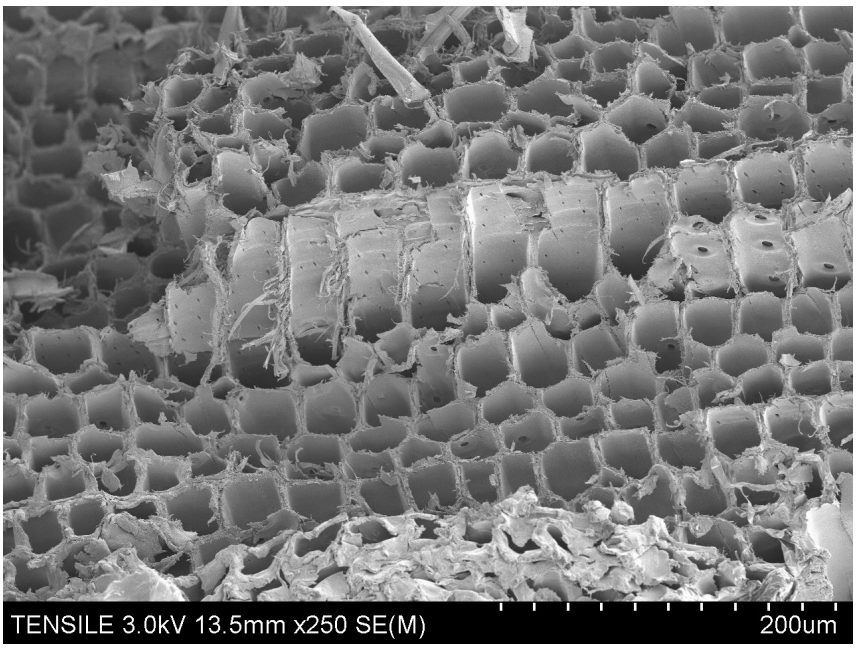

(b)

Figure 3.6: *Tensile failure of tested Sitka spruce (Picea sitchensis) specimen, the boundary between early and latewood is clearly visible in the fracture path, (above). Magnified section, (below), shows tensile along with shear failure.*

only 9 independent parameters. This can be formulated in 'Voigt' notation[1] as

$$\begin{pmatrix} \epsilon_{xx} \\ \epsilon_{yy} \\ \epsilon_{zz} \\ \gamma_{yz} \\ \gamma_{zx} \\ \gamma_{yx} \end{pmatrix} = \begin{bmatrix} s_{11} & s_{12} & s_{13} & 0 & 0 & 0 \\ s_{21} & s_{22} & s_{23} & 0 & 0 & 0 \\ s_{31} & s_{32} & s_{33} & 0 & 0 & 0 \\ 0 & 0 & 0 & s_{44} & 0 & 0 \\ 0 & 0 & 0 & 0 & s_{55} & 0 \\ 0 & 0 & 0 & 0 & 0 & s_{66} \end{bmatrix} \begin{pmatrix} \sigma_{xx} \\ \sigma_{yy} \\ \sigma_{zz} \\ \tau_{yz} \\ \tau_{zx} \\ \tau_{yx} \end{pmatrix}. \tag{3.2}$$

For this study the longitudinal direction is assigned to index X, the radial to index Y and tangential to index Z.

In case of 3D orthotropy, the 9 independent parameters become

$$\begin{array}{lll} s_{11} = \frac{1}{E_{xx}} & s_{22} = \frac{1}{E_{yy}} & s_{33} = \frac{1}{E_{zz}} \\ s_{44} = \frac{1}{G_{yz}} & s_{55} = \frac{1}{G_{zx}} & s_{66} = \frac{1}{G_{yx}} \\ s_{12} = -\frac{\nu_{xy}}{E_{xx}} & s_{13} = -\frac{\nu_{xz}}{E_{xx}} & s_{23} = -\frac{\nu_{yz}}{E_{yy}}, \end{array} \tag{3.3}$$

where ν_{yx} stands for the Poisson coefficient in case of load applied in the Y-direction and displacement in the X-direction. Due to symmetry the 3 Poisson coefficients are

$$\nu_{yx} = E_{yy}\frac{\nu_{xy}}{E_{xx}} \quad \nu_{zx} = E_{zz}\frac{\nu_{xz}}{E_{xx}} \quad \nu_{zy} = E_{zz}\frac{\nu_{yz}}{E_{yy}}. \tag{3.4}$$

When growth rings are neglected, this orthotropic character of timber reduces to cross-anisotropy (also called transverse isotropy). This will be exploited in the here described lattice model *LAT3D* (chapter 5). It is assumed that the general anisotropy of timber is an effect that results from the included stiffness and strength variation at the growth ring level. Therefore, on the lattice mapped structural variation is meant to reflect the orthotropic mechanical behaviour.

With this assumption of transverse isotropy, the elasticity matrix reduces again to 5 independent parameters (E_{xx}, $E_{zz} = E_{yy}$, $G_{zx} = G_{yx}$, $\nu_{xz} = \nu_{xy}$ and ν_{yz} or G_{yz})

$$\begin{array}{lll} s_{11} = \frac{1}{E_{xx}} & s_{22} = \frac{1}{E_{yy}} & s_{33} = \frac{1}{E_{yy}} \\ s_{44} = \frac{1}{G_{yz}} & s_{55} = \frac{1}{G_{zx}} & s_{66} = \frac{1}{G_{yx}} \\ s_{12} = -\frac{\nu_{xy}}{E_{xx}} & s_{13} = -\frac{\nu_{xy}}{E_{xx}} & s_{23} = -\frac{\nu_{yz}}{E_{yy}}. \end{array} \tag{3.5}$$

[1] 'Voigt' notation reduces the 2nd order stress and strain tensors and 4th order stiffness tensor to two vectors and one matrix.

Either, ν_{yz} or G_{yz} is an independent parameter. They are related with

$$\nu_{yz} = \frac{E_{yy}}{2G_{yz}} - 1. \tag{3.6}$$

Besides traditional mechanical tests such as static tension and compression tests, mechanical properties can be determined with more unusual test procedures. A thesis on the determination of elastic constants of timber can be found in Grimsel (1999). This author uses a modal analysis of flexural specimens to obtain the complete elasticity matrix. Furthermore, he investigated the rheological behaviour of wood and compared an FE analysis for drying timber boards with experiments.

Plastic Continuum Model

Plastic continuum models for more commonly used engineering material as e.g. steel have been researched since the 1950s. Steel's micro structural components can experience a substantial amount of reworking, hence it exhibits large plastic capacity where energy is dissipated. To account for this potential in mechanical models, one can assume elastic-perfectly plastic material behaviour.

A definition has to be formulated that distinguishes between the elastic and plastic part of the strain state. This is called a flow condition. Commonly a yield stress is used that defines the stress and strain at which for further strain increments only plastic work is done and no further elastic strain occurs.

In 3D plasticity the latter definition becomes a surface in the three dimensional principal stress state. A simple and commonly used form is the Von Mises yield criterion: in case of an isotropic material the yield surface is a infinite cylinder with its axis inclined at equal angles to the principal axes. This implies that for an hydrostatic stress state ($\sigma_{xx} = \sigma_{yy} = \sigma_{zz}$) no yielding occurs. Research by Bridgeman (1952) confirmed that this is applicable to metals.

The therefore used Von Mises stress criterion can be calculated as follows

$$F_y^2 = \frac{1}{2}\left[(\sigma_{xx} - \sigma_{yy})^2 + (\sigma_{yy} - \sigma_{zz})^2 + (\sigma_{xx} - \sigma_{zz})^2\right] + 3\left(\sigma_{xy}^2 + \sigma_{xz}^2 + \sigma_{yz}^2\right). \tag{3.7}$$

Stresses inside this cylinder are elastic. With the restriction of no elastic strains are permitted outside this surface elastic stresses only develop at the maximum on

the yield surface. Plastic strains are allowed to develop perpendicular to this surface.

An incremental solution algorithm needs to be used. Since the amount of plastic strain in one incremental step is initially unknown, a solution is first sought with the assumption of no plastic straining and then iterations are performed to determine the plastic strain increment as a vector perpendicular to the yield surface. While respecting that the flow condition is met ($F_y = 0$) this vector needs consecutively updating and thus with a new iteration moves closer to the actual stress state at the specific increment.

Additionally to the assumption of elastic-perfectly plastic material behaviour a hardening rule can be assigned, which defines the proportional inflation of the yield surface. Thus, it is possible to mimic a non perfectly plastic material as e.g. timber.

These constitutive equations for plasticity in isotropic materials can be extended to account for anisotropy. Instead of a regular yield surface the yield condition is formulated according to Shih & Lee (1978) (as presented in Smith et al. (2003)) as

$$F_y = (\sigma_{ij}, \alpha_{ij}, A_{ijkl}, k) = 0. \tag{3.8}$$

where σ_{ij} are the 2^{nd} order stress tensor, A_{ijkl} is the 4^{th} order strength tensor that defines the shape and α_{ij} the origin of the yield surface. k represents the reference yield surface.

When hardening for anisotropic material is considered, it is distinguished between proportional and non-proportional hardening. This describes the development of the yield surface in the specific material axis.

If strength degradation is to be considered, the yield surface shrinks according to a softening instead of a hardening rule. This has been used in material model as e.g. in Grosse & Rautenstrauch (2004).

Strength Criteria

Strength criteria can be used to determine the failure location and load in continuum models. The reader is referred to the general formulation in Tsai & Wu (1971). There are numerous versions of this criteria in simplified form. However as stated

in (Smith et al., 2003, p.53), strength criteria can merely indicate the location of failure, rather than absolute failure loads. Strength criteria would not be applicable to areas with high stress gradients, since in continuum models stresses are averaged. Further, variability of strength properties across growth rings are not accounted for.

Different strength criteria for anisotropic material can be found in Cazacu & Cristescu (1999), Cazacu et al. (1999), Arramon et al. (2000), Aicher & Kloeck (2001) and others. An extensive bibliography on proposed failure criteria for composite material can be found in Paris (2001).

Examples of Continuum Models

An example for the application of a simplified continuum FE model for timber can be found in Tabiei & Wu (2000). In this model, the authors apply a simple rule of changing the elastic modulus E_{ij} in the resulting stiffness matrix. An effective elasticity matrix is calculated for the nonlinear case that keeps the matrix symmetric. Tabiei & Wu used power functions, fitted to test data, that simulate the stiffness change. No 3D yield stress had to be formulated. The stiffness change results from simply updating the various $E-$moduli in an incremental manner. Although for this model the 3D stress state is not calculated iteratively, as described before, for simple stress situations the model delivers good predictions. The authors accounted as well for the effect of strain rate.

Zhu et al. (2005) modelled OSB with a simple nonlinear constituive material model that takes into account proportional strain hardening under compression. Piecewise linear stress-strain curves that resembled a parabolic curve after the initial yield stress and the ultimate stress serve as an input to the material model. Very good agreement was found among model and tests. Failure was detected when plastic compressive strain reached a certain value. A linear stress-strain relation in tension is assumed and failure determined when the Tsai-Hill criterion is met. However, strain softening was not included in the model.

A more complex 2D orthotropic constitutive plasticity model has been presented by Mackenzie-Helnwein et al. (2003). The authors extend the common single Tsai-Wu strength criteria, which represents an ellipsoid in the 2D principale stress space

Tsai & Wu (1971) to four surfaces. They undertook a comprehensive experimental study with bi-axial loaded specimens for which strain measurements could be taken via a 3D Electronic Speckle Pattern Interferometer. Failure could be correctly determined and the post failure behaviour based on the four different surfaces could be predicted well.

Schmidt & Kaliske (2006) based on the previous model extend the idea to three dimensions. The model includes 7 yield surfaces of which at most 4 can be active. Since no experimental tri-axial loading data was available for this research the model was compared and verified with previous material models.

3.3.2 Fracture Mechanics (FM)

The main drawback for traditional continuum mechanics is that stresses are calculated in an averaging sense over the domain of a continuous medium. This may be applicable to problems where the material, under ordinary loading conditions, exhibits large plastic deformation. However, the assumption of continuous stresses breaks down at points were stress singularities can occur (e.g. cracks). Wood due to its weak cellular bonding strength and its natural inherent flaws exhibits stress concentration with little plastic deformation under tension and thus brittle failure in form of fracture can occur.

This field of study, named Fracture mechanics (FM) started in the early 20th century and has been developed to incorporate a variation of different nonlinear fracture phenomena since(NLFM). An example is steel, where the ability to deform plastically in the vicinity of a crack reduces again the stresses at the ideal singularity and thus decreases the susceptibility to fracture.

Details on several linear and nonlinear FM techniques can be found in standard literature e.g. Anderson (1991) or for timber Smith et al. (2003), from who part of the following subsection is taken. In the following a brief introduction to FM and its application to timber will be given.

A more general overview on different concepts to simulate fracture behaviour can be found in Smith et al. (2007). The authors look at differences in continuum, fracture mechanical and lattice approaches.

Linear Elastic Fracture Mechanics (LEFM)

In cracks high peak stresses occur at the crack tip and are dependent on the shape of the opening. Inglis (1913) developed first an equation determining the peak stress occurring in the crack vicinity of an elliptical shaped hole. Under uniaxial tension for an ideal material the vertical stress is determined by

$$\sigma_y = \sigma \left[1 + 2\sqrt{\frac{a}{\rho}}\right], \tag{3.9}$$

where σ is the acting tensile stress far away of the hole, a is the half of the wide diameter of the ellipse and ρ is the radius of the 'crack tip'.

While this describes stress concentrations at the vicinity of a hole, no condition is formulated which allows for cracks to form or further develop. Griffith (1921) instead formulates the balance of energy of a cracked system. The total energy can be described as

$$\Pi = U + U_p + W = U - F + W, \tag{3.10}$$

where U is the stored strain energy, U_p is the potential energy of the load system, F is the external work of the applied load and W the surface energy associated with crack formation.

According to Griffith the overall energy of the system must be reduced or unchanged for a crack to propagate. Thus,

$$\frac{d\Pi}{dA} = \frac{d}{dA}(U - F + W) = 0 \text{ or} \frac{d}{dA}(F - U) = \frac{dW}{dA} \tag{3.11}$$

By using Inglis' solution for an elliptical hole with a width of zero in the minor axis, the strain energy can be calculated as

$$U = \frac{\pi\sigma^2 a^2 b}{E}, \tag{3.12}$$

where again σ is the applied stress in a uniaxial tension field, a is the crack length, b is the plate's thickness and E is the Young's modulus. Furthermore, it can be shown that the external work done by the applied load is twice the internal strain

energy U.

$$F = 2U. \tag{3.13}$$

And finally, the surface energy W is

$$W = 4ab\gamma, \tag{3.14}$$

for which γ is the surface energy required to form a new surface and thus a material constant. $4ab$ stems from the area of 2 surfaces of length $2a$ and width b.

Substituting (3.12), (3.13) and (3.14) into (3.11) and solve for stress, results in the fracture strength σ_f

$$\sigma_f = \sqrt{\frac{2E\gamma}{\pi a}} \tag{3.15}$$

This strength value agreed well with measurements taken from glass specimens by Griffith. However, for other more usable construction materials, which are not as brittle as glass, the formula needs some modification.

The left hand side of equation (3.11) is generally referred to as the strain energy release rate G. While the right hand side is the material's resistance to crack growth.

$$G = \frac{d}{dA}(F - U) \tag{3.16}$$

Instead of W being calculated with the material's surface energy it can be formulated as itself a material constant G_c with a unit of energy per area (e.g. $\mathrm{J/m^2}$).

$$G_c = \frac{dW}{dA} \tag{3.17}$$

It can be stated that a crack progresses when $G = G_c$.

In many cases this material constant is actually itself dependent on the fracture length a and is then referred to as the parameter R.

By deriving the energy strain rate G of a crack development for a certain system and comparing it to the material's crack resistance G_c, the critical load for crack propagation can be predicted. For instance the strain energy increment of a system (Fig. 3.7) can be described in case of displacement control with energy before and

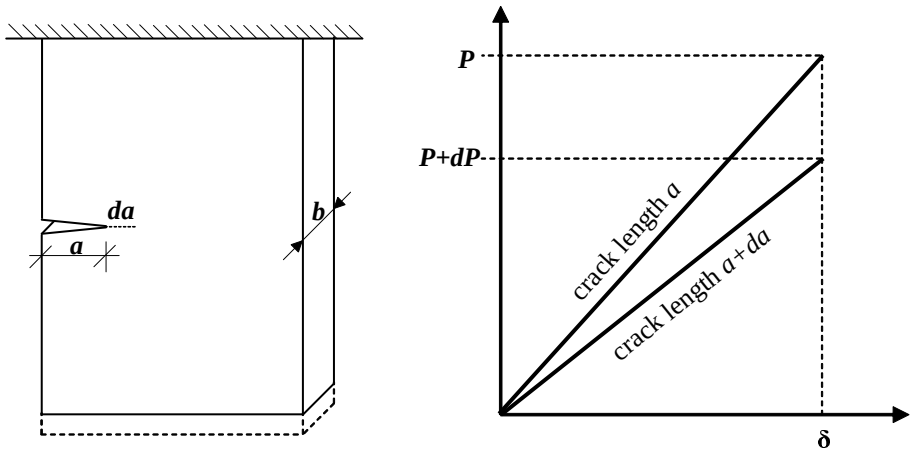

Figure 3.7: *Crack growth under displacement control.*

after crack growth as follows,

$$U_1 = \frac{1}{2}\delta P \text{ and } U_2 = \frac{1}{2}\delta(P + dP) \tag{3.18}$$

Thus,

$$dU = U_2 - U_1 = \frac{1}{2}\delta(P + dP) - \frac{1}{2}\delta P = \frac{1}{2}\delta dP \tag{3.19}$$

When substituted into (3.16) results to

$$G = \frac{1}{b}\left[\frac{dF}{da} - \frac{dU}{da}\right] = \frac{1}{b}\left[\delta\frac{dP}{da} - \frac{1}{2}\delta\frac{dP}{da}\right] = \frac{1}{2b}\delta\frac{dP}{da}. \tag{3.20}$$

This equation can be expressed with the compliance of the system C being the reciprocal of the slope of the load-displacement curve. $C = \delta/P$

$$G = \frac{1}{2b}P^2\frac{dC}{da}. \tag{3.21}$$

An example shall be given for the application of the former derivation (Smith et al., 2003, p.74): a cantilever beam that has been used for predicting strength of timber joints will be described, Fig. 3.8. According to common beam theory the deflection of a cantilever beam can be expressed as

$$\Delta = \frac{PL^3}{3EI}, \tag{3.22}$$

where E refers to the Young's modulus, I to the moment of inertia, P to the applied load and L to the beam length.

For a double cantilever beam the crack opening is twice that of a single one ($\delta = 2\Delta$). When length L is replaced with crack length a and for I the proper moment of inertia is calculated, the former can be rewritten as

$$\delta = \frac{8Pa^3}{Ebh^3}, \tag{3.23}$$

Thus, the compliance is

$$C = \frac{8a^3}{Ebh^3}, \tag{3.24}$$

Further inserting (3.25) into (3.21) results in

$$G = \frac{12P^2a^2}{Eb^2h^3}, \tag{3.25}$$

This can be extended further to account for anisotropic materials.

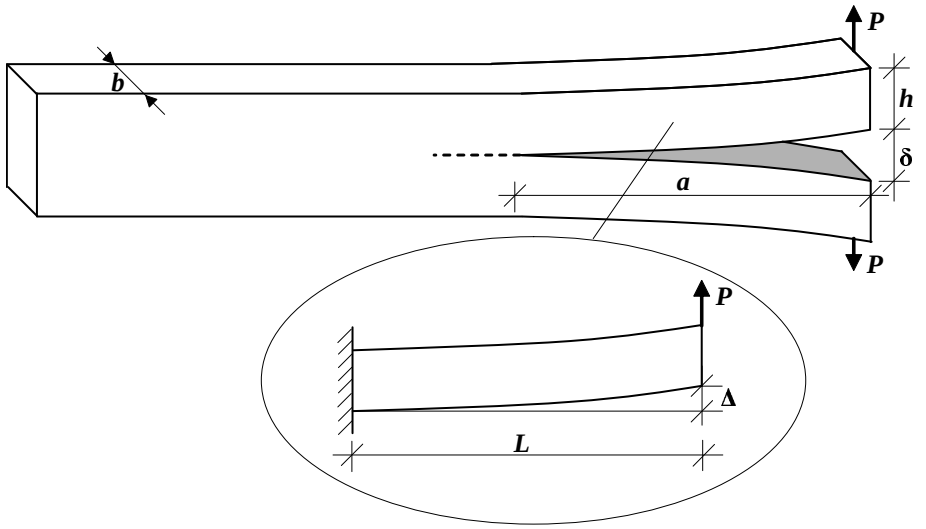

Figure 3.8: *Double cantilever beam specimen.*

Since it is often not feasible to formulate the energy balance of the uncracked and later cracked system, another approach can be applied by using the stress intensity factor K.

This second concept in fracture mechanics enables to formulate the actual stress in the vicinity of a crack. By choosing an appropriate stress function with a singularity at the tip. One has to differentiate for three basic modes of fracture, Fig. 3.9. For each, a different stress function with a geometry and load dependent parameter K

is formulated. K is a parameter that defines the strength of the stress singularity, it is either taken analytically derived (e.g. taken from literature) or can be calculated from results of a FE package that is able to exhibit similar stress functions, e.g. with special 'quarter-node' elements or appropriate meshing to capture the stress concentration.

A crack is said to propagate when $K \geq K_c$, while K_c can be seen as a measured material constant.

For a mixed mode cracking, certain failure criteria are used. The most common is the Wu criterion (Wu, 1967) for a mixed shear and crack opening failure can be calculated as

$$\frac{K_I}{K_{I,C}} + \left(\frac{K_{II}}{K_{II,C}}\right)^2 = 1 \tag{3.26}$$

Jernkvist (2000) developed a mixed mode fracture criteria based only on fracture toughness $K_{I,C}$. Due to the observation that cracks initially aligned across the fibres almost always develop along the fibre direction, the author extended the fracture criterion to relate the fracture toughness $K_{I,C}$ and $K_{II,c}$ for cracks oriented across fibres as well to mode I fracture toughness.

Despite the method's usefulness for homogeneous material such as steel and glass. the application to timber is rather limited because of different micro-structural phenomena that occur in timber due to the heterogeneity of the material. These phenomena prevent formation of a clear crack tip that is assumed by the stress intensity factor method.

An examples of the application of LEFM can be found in Snow et al. (2004). The authors determined energy release rates G and stress intensity factors K for fracture for mode I and mode II specimens made of LSL. The respective properties were taken from the literature for pine. Joint tests of pin loaded timber members (loaded perpendicular to the grain) were then compared to a numerical analysis for different crack lengths. A J-integral approach was used to determine the stress intensity factors for different crack lengths from the FE models. A Wu failure criteria was used to assess the failure load. While the failure was reasonably well predicted for solid wood, this was not the case for LSL. As the authors suggest this is due to the actual failure mechanism of the LSL joint since cracking developed from the extreme fibre at the tension side of the LSL beam.

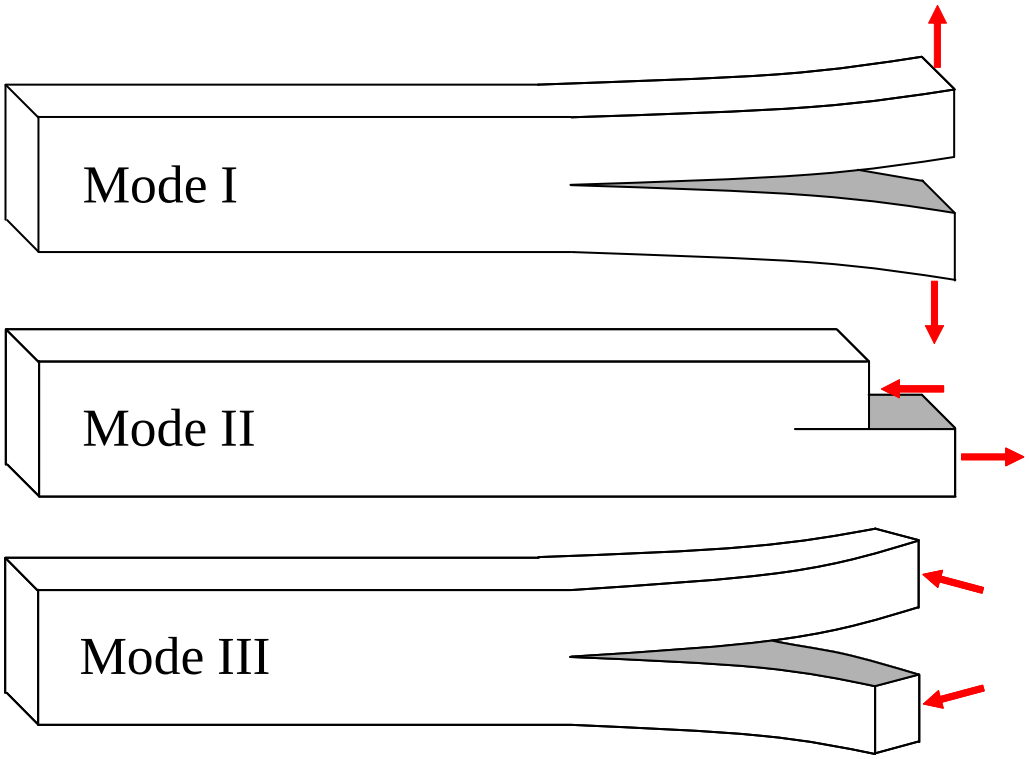

Figure 3.9: *Schematic of the three fracture modes: tension, in-plane shear and out-of-plane shear.*

Nonlinear Fracture Mechanics (NLFM)

As mentioned in Vasic et al. (2005) linear elastic fracture mechanics has its limitations and, especially for wood, nonlinear techniques to investigate post peak stress situations should be applied. The authors give an overview of different fracture mechanical approaches for the application to wood.

The validity of LEFM rests on the assumption that a plastic zone that develops in any any material to a certain degree is relative small in comparison to the stress field that is influenced by the stress singularity,Anderson (1991).

3.3.3 Fictitious Crack Model and Cohesive Zone

A way to account for this plastic zone is the introduction of closing stresses at the crack tip which close the ideally existing crack. This has been done by Dugdale (1960) for steel, where the yield stress of the material σ_{YS} is applied and thus the

length of this process zone can be calculated, Fig. 3.10.

In a similar way for concrete, Hillerborg et al. (1976) assume that the maximum tensile stress (tensile strength) of the material is being transferred at the crack tip. This stress decreases according to a defined curve (bi-linear, continuous etc.) to zero along the so called cohesive zone at the front of the crack, Fig. 3.11.

In case of the fictitious crack model nonlinear springs at the crack surface can be used for the transfer the closing stresses. Usually the cracked surface has to be known in advance and elements adjacent to the crack surface are linked together with spring elements. The obvious advantage is that nonlinear fracture phenomena can be incorporated into the spring's load-displacement curve.

Examples can be found in Vasic & Smith (2000), Nardin et al. (2000).

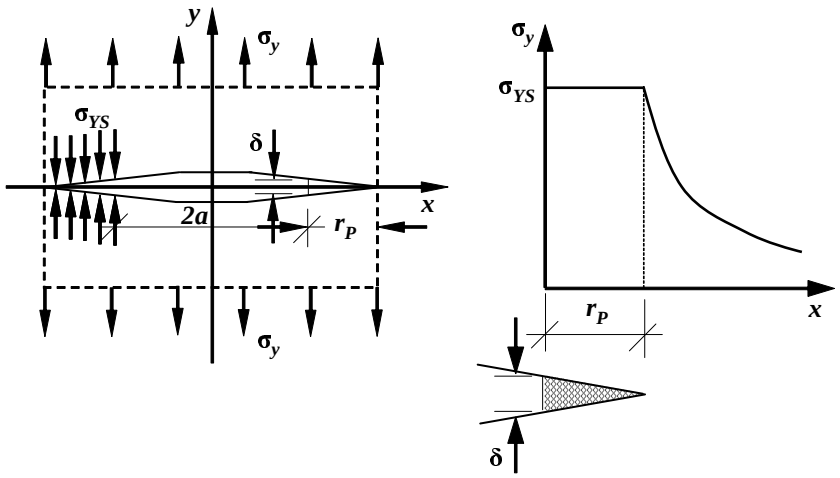

Figure 3.10: *Dugdale's model (after Saouma (1997)).*

A continuum damage mechanical model (DM) was used in Daudeville (1999) for a mode I failure test, where joint elements are used to model the decohesion between parts of the structure. The joint elements followed a constitutive behaviour in mode I. A special FE routine was required to pass an instability point that might occur during the nonlinear load-displacement response of the model. Fracture energy release rate G could be determined and compared to the previous model.

Holmberg et al. (1998) devised a 2D plastic continuum model based on a

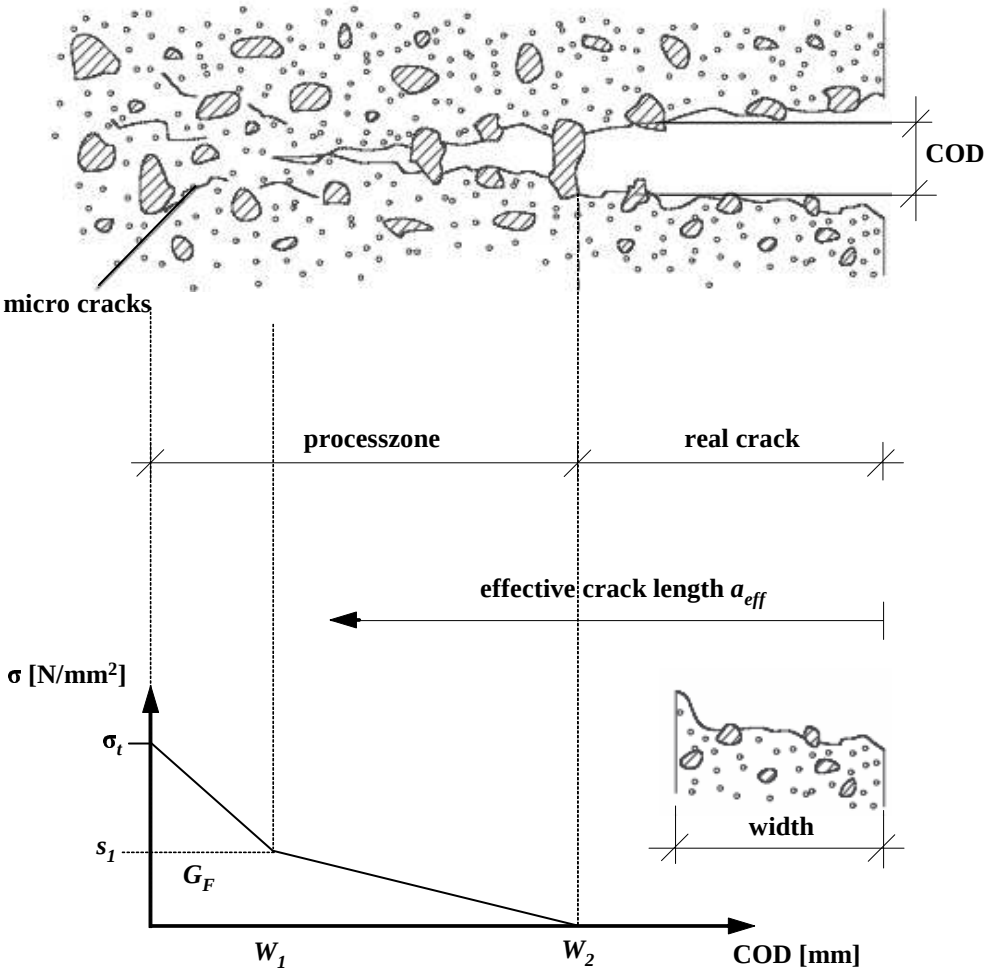

Figure 3.11: *Hillerborg's model.*

constitutive isotropic material model for foam including a strain hardening rule. To account for different mechanical behaviour in the wood morphology, the authors used 5 different material definitions and thus elements for early wood and one for late wood. Fracture was captured by the use of a fictitious crack model. This was achieved with special crack elements in between each solid elements which exhibit a nonlinear stress-displacement curve and acted in tension and shear. The relation was assumed to be a bi-linear softening curve that was obtained from experimental measurements. Numerical instability was avoided since no 'snap back' was encountered with the used softening crack elements. The model was used to simulate shear failure (shear box) of small specimens orientated in the the radial and the tangential direction. Excellent agreement was found among the predicted and observed failure patterns. While the overall stiffness was slightly overestimated an accurate prediction of, at least, the shape of the load-displacement curve and absolute strength could be obtained.

As a further technique, the material point method (MPM) can be used to incorporate material heterogeneity. The reader is referred to Nairn (2007a) and Nairn (2007b) as an example for a 2D transverse fracture model.

3.3.4 Lattice Models

Lattice models on the contrary to continuum models consist of distinct elements that represent the material at a certain length scale. They are a natural choice for material modelling since structured and random heterogeneity can be incorporated easily by statistical variation of element stiffness and strength characteristics. The lattice elements itself can thus represent actual morphological features of the material.

Similar to fictitious crack models, where in most cases, the crack has to be defined first and modelled with nonlinear springs, lattice models take the idea one step further and use a mesh with discrete elements for every part of the structure.

There are different cell arrangements possible for lattice models. Either the lattice structure consists of a regular or an irregular mesh depending on the way material variability is incorporated. The models can consist in the simplest form of lateral and longitudinal bar elements or beam elements connected via diagonals.

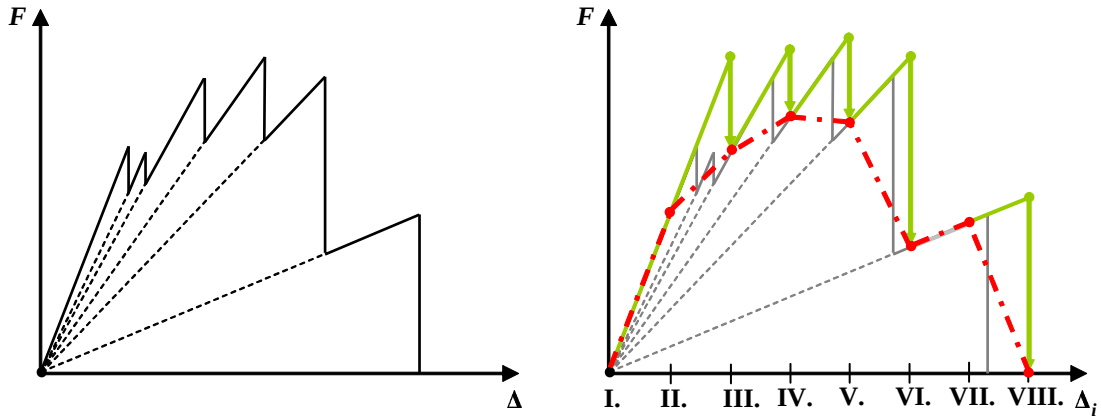

Figure 3.12: *Ideal load-displacement response of an elastic perfectly brittle lattice structure (left) and applied solution method, Algorithm 1, with resulting* LDP (red line) and number of load steps.

Additionally to the diagonal elements, angular springs can be used to model shear behaviour.

Neither is the pre knowledge of the location of the occurrence of a crack required nor the actual microstructural failure mechanism. However, lattice models, due to their sheer size, require a larger amount of computational time and memory space.

Solution Strategies for Discrete Lattice Models (Non-Incremental)

There are several ways to simulate discrete lattice models. One can distinguish primarily on whether discrete stiffness reduction of elements is used and on the way this is implemented in the solution algorithm. The *Elastic Perfectly Brittle* approach as described in this subsection represents the most simple solution, for which the element's stiffness is set to zero after the maximum strength of this element is reached. The ideal result of this type of analysis is a 'saw-tooth' like load-displacement curve as seen in Fig. 3.12 (left) and the possible solution outcome by the below described algorithm (right).

To the author's knowledge there is no commonly accepted name that describes this specific method and will be therefore referred to as simply *Elastic Perfectly Brittle Lattice* method. It only works for systems where stiffness change occurs due to elements that are deactivated and thus removed from the system. Most lattice models are solved with this method. Examples can be found in Davids et al.

(2003), Fournier et al. (2007) and Sedighi-Gilani & Navi (2007) etc. The principal formulation of this algorithm can be described as seen in Algorithm 1.

Algorithm 1 *Elastic Perfectly Brittle Lattice* Method (displacement control).

Require: global stiffness K_1^1
Require: u_i displacements for each step i (particular degree of freedom)
load step $i = 0$
repeat
  $i = i + 1$
  iterative Step $j = 0$
  repeat
    $j = j + 1$
    solve: $[K_i^j]\{\Delta_i\} = \lambda^j\{F_{ref}\}$ for iteration j in load step i
    displacement control: obtain $\overline{u_i}$ from $\{\Delta_i\}$ and calculate $\lambda^j = \overline{u_i}/u_i$
    for all l **do**
      calculate: resulting load F^l in link element l
      if $F^l > S^l$ **then**
        remove local $[k^l]$ from global $[K_i^j] \Rightarrow [K_i^{j+1}]$
      end if
    end for
  until no further link is broken ($F^l > S^l$)
  $\{F_i\} = \lambda^j\{F_{ref}\}$
until either $[K]$ becomes singular or $\{F_i\} = 0$

A single step i of the algorithm can be represented graphically as seen in Fig. 3.13: for each load step the structure is solved for a certain displacement u_i. If elements l are exceeding their maximum strength $F^l > S^l$ they 'break' (are removed) and the new updated stiffness matrix is calculated $[K_i^{j+1}]$. The latter two steps are repeated until no further link breaks and an admissible solution is found. Finally the next displacement step u_{i+1} is applied and the whole process starts again with the next larger displacement. This is done until the system becomes singular or the load reaches zero $\{F_i\} = 0$.

Obviously, a significant number of steps are required to accurately present sudden (vertical) drops in the load-displacement plot (LDP).

Most crucial about this algorithm is it is a non-incremental method. Hence, it is assumed that although stiffness changes occur, the tangent stiffness gradient is always placed in the graph's origin at zero load and displacement. Thus, the method only works assuming there is no ductile behaviour present where plastic

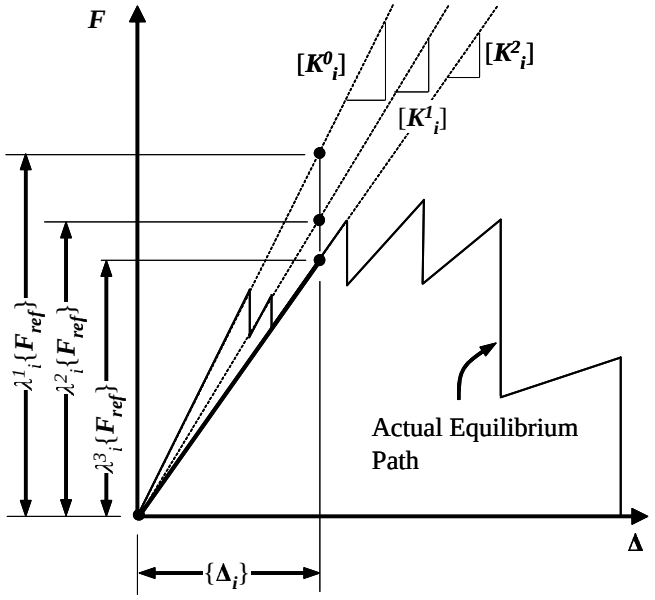

Figure 3.13: *'Elastic Perfectly Brittle Lattice' method.*

strain accumulates. For that reason it is not very useful when modelling wood in joints where a great part of energy is dissipated by deforming timber plastically in the parallel to the grain direction. Neither would this method be useful to model contact nonlinearity nor to account for microductility of broken links under tension.

Bazant & Cedolin (1979) object that this type of method is mesh dependent and will not yield the correct energy consumption upon mesh refinement. A softening branch has to be included to simulate the dissipation of energy on the element level. Including a softening branch will still result in a model response that depends on the mesh-size but the strain softening can be adjusted to fit experimental data or measured energy release rates (Jirasek & Bazant, 1995).

Another type of non-incremental analysis is mentioned in Rots & Invernizzi (2004). Although these authors use 2D continuum elements, they employ a special solution technique which would be as well applicable to lattice models with, for example, bar elements. The principal idea is that instead of bar elements, entire continuum elements can experience strain softening. The principle tensile stresses are calculated for each element. Those for which the principle stresses reach their strength will experience a sequential reduction in stiffness and strength. The main advantage is that no incremental-iterative solution technique (such as Newton-Raphson with arc-length, displacement control etc.) is required and a

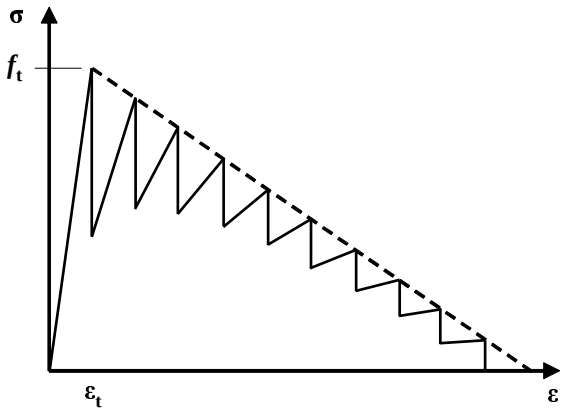

Figure 3.14: *Example of a softening stress-strain diagram with the saw-tooth approximation, softening is divided into 10 steps with positive stiffness.*

negative stiffness which might lead to convergence problems is absent. However, as with lattice models, mesh refinement is a major issue, therefore the softening curve of an element needs adjustment to the element's size. The algorithm can be described as follows (Algorithm 2).

Algorithm 2 *Sequential Reduction* Method.

Require: global stiffness K_0
Require: unit load F_{ref}
load step $i = 0$
repeat
  solve: $[K_i]\{\Delta_{i,ref}\} = \lambda_i\{F_{ref}\}$ in load step i
  extract the element l for which one of the principle stresses is closest to its maximum strength f_t
  calculate λ_i so that element l reaches its maximum load
  reduce local stiffness K^l and strength f_t of critical element l for all principle directions according to a saw-tooth tensile softening stress strain curve as seen in Fig. 3.14
  update stress and strain status of each element
  calculate global displacement and load response
  $F_i = \lambda_i F_{ref}$
  $\Delta_i = \lambda_i \Delta_{i,ref}$
  $i = i + 1$
until either $[K]$ becomes singular or $\{F_i\} = 0$

This method can also be applied to discrete lattice models. Despite the robust way to determine nonlinear fracture, the method is computationally quite expensive since the number of computational steps amounts to the number of broken elements multiplied with the number of the divisions in the stress-strain saw-tooth diagram.

Most important, plastic behaviour for the elements can not be incorporated due to its non-incremental nature.

Examples of Lattice Models

Early lattice models have been used for predicting fracture behaviour of concrete. The main difference to timber is the assumed local isotropy of the single lattice cells. Recent examples can be found in Lilliu & van Mier (2000), Lilliu & van Mier (2003) and Prado & van Mier (2003). All authors employ in their 2D and 3D lattice models the simple *Elastic Perfectly Brittle Lattice* method. An ordered triangular arrangement of beam elements was used. The heterogeneity of the material is simulated with different assigned properties for aggregate, matrix and the interface bond between them. Thus, it is possible to investigate different aggregate distributions on fracture energy and load-displacement curves.

Berton & Bolander (2006) devised a 3D irregular lattice model for concrete based on a Voronoi discretisation of the material domain. Although, auxiliary nodes can be strategically introduced to create material features such as inclusions etc. in later models, only a homogeneous material was considered. A cohesive crack model is assumed with a tri-linear stress-displacement relation (tension softening) for the individual links. One type of links simulates the stress perpendicular to the facets from the Voronoi tessellation and two link types simulate the two shear stresses acting on that plane. The nonlinear solution is found by breaking only one individual link at one computational cycle and degrading the element's stiffness with a damage parameter. This is analogous to the before described crack band model or 'Sequential Reduction' method. Negative stiffness of individual links is therefore avoided.

Another application of a lattice model for concrete can be found in Cusatis et al. (2006), where for the material nonlinearity a constitutive law is enforced. Thus, ordinary nonlinear solution algorithms such as the Newton Raphson with line search or arc-length control can be used.

Lattice models can be easily used to study the size effect in structures. Once a lattice is calibrated, different sized lattices can be computed and compared to experimental specimens. Investigations with lattice models for concrete beams

exhibiting a size effect compared to size effect laws from literature can be found in Ince et al. (2003), Bazant & Yavari (2005) and Jirasek & Bazant (1995). The latter paper describes, as mentioned in the introductory chapter 1, a special solution algorithm called SSC along with a more efficient method to recalculate the global tangential stiffness matrix (MIF). This will be discussed in detail in section 5.6

Timber, in contrast to concrete is a transverse isotropic material at its meso structure. Strength and stiffness properties are linked to the main material axes and thus complicate the model's behaviour. Examples for 2D lattice models for timber at the meso scale can be found in Landis et al. (2002), Landis et al. (2003), Davids et al. (2003), Parrod (2002), Parrod et al. (2002), Vasic (2000) and Fournier et al. (2007). These authors use simple perfectly brittle lattice elements and therefore can use the computational inexpensive *Elastic Perfectly Brittle Lattice* method as a solution algorithm.

Elastic properties (Young's, shear- moduli and Poisson coefficients) are assigned to the elements via an optimisation technique that compares model results of standard loading situations with elastic values obtained from the literature. Interesting to note is the way shear and Poisson effects are incorporated into the lattice. The diagonals of the lattice cell are used to serve for both shear transference and lateral strain. The contributing stiffness that results from these elements is determined by a adjustable 'effective' angle. Thus, it is possible, according to these authors, to better fit the elastic properties.

However, with this assumption, the lattice becomes size dependent in terms of the elastic behaviour. In addition, a pure shear situation cannot be represented accurately. Forces that act in the lateral lattice elements would be present, this is discussed in more detail in subsection 6.3.1. The above named authors assume that these imperfections of the lattice have no significant effect on the model's bulk behaviour. The element's strength properties are found by iteratively comparing experimental tests with model results. This is as shown in the papers in the case of tension radial to the grain in good agreement with the experiments.

The perfectly brittle timber lattice model is taken a step further by Fournier et al. (2007), who incorporated morphological features such as growth rings. The authors distinguish between certain latewood and earlywood elements and assign different strength properties. Elastic properties are left undistinguished. Unrealistic

fracture prediction for certain load cases could be overcome with this incorporated structured strength variation of elements. Very good agreement between lattice model and experimental results could be found. However, the study only looked at the shear and tensile behaviour of timber. The assumption of in plane stresses and thus the use of a 2D lattice model reduced the computational demand significantly.

Sedighi-Gilani & Navi (2007) developed a 3D lattice model for timber on the cellular level for perpendicular to the grain mode I fracture. Two types of box-beam elements were used to represent single cells. Large elements (40 μm x 40 μm) for early wood cells and smaller ones (40 μm x 20 μm) for late wood cells. A thickness of 2 and 6 μm was assumed respectively. The lattice represented only a small volume of the entire cleavage sample. The remaining was modelled using orthotropic linear solid elastic elements. Shear and lateral resistance between the cells was transferred via diagonal and lateral springs. All elastic parameters of the lattice elements were calibrated against values from the literature in an iterative manner similar to Landis et al. (2002). Strength criteria were only adjusted for lateral and diagonal springs by comparison between fracture mode I tests conducted by Vasic (2000) and a trial and error method to obtain best fit. No plastic deformation capability for links under compression is included. The authors used the FE package ABAQUS with sequential removal of failed elements, thus in principle they also use the *Elastic Perfectly Brittle Lattice* method. Very good agreement was found among observed and predicted fracture path. It was possible to capture the fibre branching mechanism well with the assumption of box-beam elements. Furthermore, it could be demonstrated how small micro cracks develop into larger cracks on the meso scale.

3.4 Joint Modelling

Now having presented various modelling techniques for a timber material model, these can be applied in the framework of a complete timber joint model.

Research on timber joints compasses numerous issues. An attempt to summarise the wide field of joint models can be best achieved by structuring the individual aspects of the models:

Joint types dowel-type (nails, bolts staples etc.), split rings, shear plates

Model type empirical, analytical, numerical

Model technique continuum models, fracture mechanical model, morphological lattice models, material and geometric nonlinearity

Loading monotonic, dynamic, load history, strain-rate effects

Joint arrangement single or multiple fastener, single or multiple shear

Environmental influences fire, moisture, fatigue (and other time dependent effects)

A mathematical model to describe joint behaviour is always limited in some respect. Commonly a number of individual aspects are considered. This research tries to look at the geometric nonlinear effects in single shear joints under consideration of nonlinear material and fracture behaviour. Important properties of a joint to investigate are the initial stiffness, ultimate load and overall ductility and failure mode.

Starting with the earliest attempt to quantify the load bearing capacity of timber joints with the European Yield Model (EYM) this section will present more detailed joint models on the basis of the before discussed modelling techniques such as continuum models, fracture mechanical and lattice models.

3.4.1 European Yield Model

Because the use of the European Yield Model to calculate timber joint strength is so widespread it will be described here in more detail. It was developed by Johansen (1949) and has entered several design codes since (USA, Canada, Europe and Australia). Named after the Danish researcher the model is also known as Johansen's Yield Model. Its ease of use and applicability to several joint arrangements, such as multiple shear joints consisting of timber/timber or timber/steel plate members, increased its popularity. The basic principle, underlying the model, is the assumed perfectly plastic behaviour for both materials timber and steel. The model predicts the strength of a joint based on the equilibrium of moments and forces acting on the fastener at a specific state of the joint, namely the yield point.

For a single shear joint with a dowel-type fastener, assuming different embedment strengths for the members, six different failure modes can occur. These are depicted

in Fig. 3.15. The first three images show failure modes resulting from a rigid fastener: a) and b) represent timber embedment in one of the two timber members, c) represents embedment failure in both timber members. The last three images show a slender dowel which exhibits one (mode d) and e)) or two plastic hinges developing (mode f)).

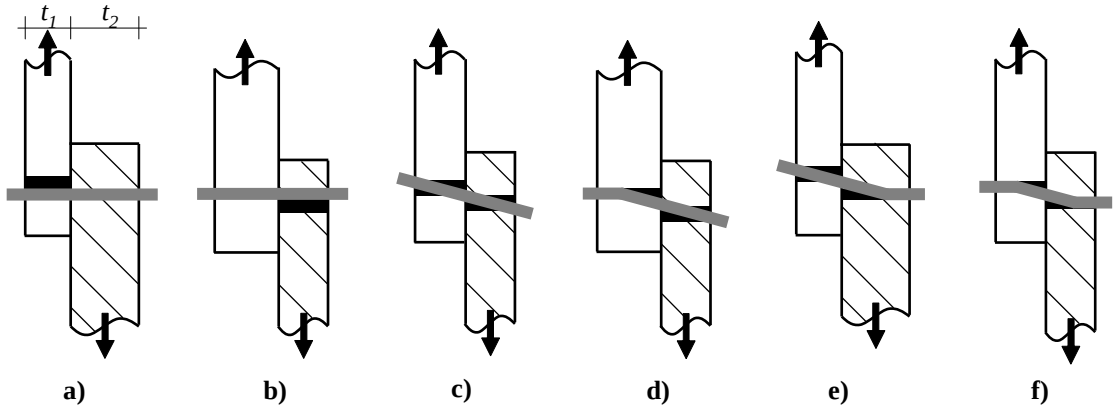

Figure 3.15: *Failure modes according to the European Yield Model (BS EN 1995-1-1, 2004).*

Johansen assumes timber and steel behave with perfect plasticity. Hence the deformed timber acts as a uniform load on the fastener. The equilibrium of forces and moments, acting at the joint's shear plane on the fastener, is formulated for the different failure modes and solved for the characteristic joint capacity $F_{v,Rk}$ individually. This can be seen in Fig. 3.16 for mode c). To determine which failure mode applies for a specific joint arrangement, the minimum value of all calculated strength values from the 6 modes is taken.

Despite the usefulness of the model, the major assumption is that the timber shows large plastic deformation. This is only true when minimum edge and end distances are adhered to and thus a ductile behaviour can be expected, which is clearly not the case for some joint arrangements. Further, the true failure mode is a combination of the individual limit states described by Johansen, since neither steel nor timber does behave as perfectly plastic. Although reliable yield and ultimate load values can be calculated the model does not allow to obtain a load state related to a specific joint deformation. Neither ductility nor joint stiffness can be quantitatively determined.

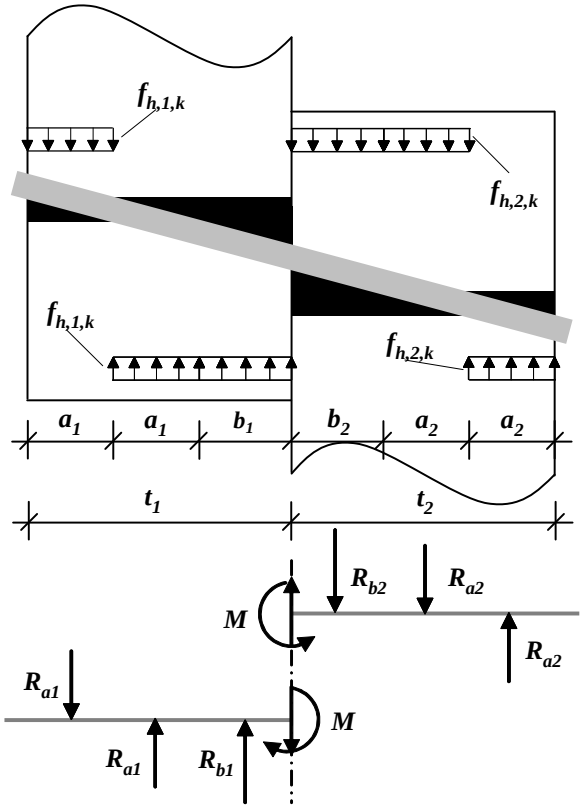

$$F_{v,Rk} = f_{h,1,k} b_1 d = f_{h,2,k} b_2 d \quad (1)$$

$$M = R_{a1}\left(b_1 + a_1 + \frac{1}{2}a_1\right) - R_{a1}\left(b_1 + \frac{1}{2}a_1\right)$$

$$\ldots \quad - R_{b1}\frac{1}{2}b_1 = f_{h,1,l} d \left(a_1^{\,2} - \frac{b_1^{\,2}}{2}\right)$$

with $\sum M=0$

$$M = f_{h,1,l} d \left(a_1^{\,2} - \frac{b_1^{\,2}}{2}\right) = f_{h,2,l} d \left(\frac{b_2^{\,2}}{2} - a_2^{\,2}\right) \quad (2)$$

with $\sum F_v=0$

$$b_1 = \frac{f_{h,2,k}}{f_{h,1,k}} b_2 = \beta b_2 \quad (3)$$

$$a_1 = \frac{t_1 - b_1}{2} = \frac{t_1 - \beta b_2}{2} \quad (4)$$

$$a_2 = \frac{t_2 - b_2}{2} \quad (5)$$

1. substituting (5),(4) and (3) into (2)
2. solving for b_2
3. solving (1) to obtain $F_{v,Rk}$

Figure 3.16: *Example of the derivation of* EYM mode c).

The yield strength of a timber joint as set out in Eurocode 5 (BS EN 1995-1-1, 2004) is calculated as follows,

$$F_{v,Rk} = \min \begin{cases} f_{h,1,k} t_1 d & (a) \\ f_{h,2,k} t_2 d & (b) \\ \frac{f_{h,1,k} t_1 d}{1+\beta} \left[\sqrt{\beta + 2\beta^2 \left[1 + \frac{t_2}{t_1} + \left(\frac{t_2}{t_1} \right)^2 \right] + \beta^3 \left(1 + \frac{t_2}{t_1} \right)^2} \right. & \\ \qquad \left. -\beta \left(1 + \frac{t_2}{t_1} \right) \right] + \frac{F_{ax,Rk}}{4} & (c) \\ \mathbf{1.05} \frac{f_{h,1,k} t_1 d}{2+\beta} \left[\sqrt{2\beta(1+\beta) + \frac{4\beta(2+\beta) M_{y,Rk}}{f_{h,1,k} d\, t_1^2}} - \beta \right] + \frac{\mathbf{F_{ax,Rk}}}{\mathbf{4}} & (d) \\ \mathbf{1.05} \frac{f_{h,1,k} t_2 d}{2+\beta} \left[\sqrt{2\beta(1+\beta^2) + \frac{4\beta(1+2\beta) M_{y,Rk}}{f_{h,1,k} d\, t_2^2}} - \beta \right] + \frac{\mathbf{F_{ax,Rk}}}{\mathbf{4}} & (e) \\ \mathbf{1.15} \sqrt{\frac{2\beta}{1+\beta}} \sqrt{2 M_{y,Rk} f_{h,t,k} d} + \frac{\mathbf{F_{ax,Rk}}}{\mathbf{4}} & (f) \end{cases} \tag{3.27}$$

with

$$\beta = \frac{f_{h,2,k}}{f_{h,1,k}} \tag{3.28}$$

where

		Unit
β	ratio between the embedment strength of the members	-
d	fastener diameter	mm
$f_{h,i,k}$	characteristic embedment strength of timber member i	N/mm^2
$F_{ax,Rk}$	characteristic axial withdrawal capacity of the fastener	N
$F_{v,Rk}$	characteristic load-carrying capacity per shear plane per fastener	N
$M_{y,Rk}$	characteristic fastener yield moment	Nmm
t_i	timber thickness or penetration depth of timber member i	mm

The additions to the original derived equations from Johansen are the account of geometric nonlinear effects in mode d), e) and f) with the factors of 1.05 and 1.15 respectively for all dowel type fasteners. In addition to that the term $+\frac{F_{ax,Rk}}{4}$ (modes c), d), e) and f)), described in more detail in the subsequent section, was added to account further for geometric nonlinear effects that result from the head fixity of nailed joints and from the washers in bolted joints.

Blass & Kraemer (2001) describe that, in most joint arrangements, the plastic hinge does not form completely. Consequently, he adjusted the fastener's moment

resistance that is used in the EYM to account for this non perfectly plasticised hinge.

In similar fashion to Johansen, Aune & Patton-Mallory (1986b) derived the same equations of the EYM with the principle of virtual work. In a subsequent step, instead of plastic emebedment they included a fourth-root curve to describe the fastener foundation. With this, they calculated decreased yield loads that result from the nonuniform load distribution along the fastener shank of about 6%. With this assumption it should be possible to predict full load-displacement curves. However, bolt bending is not included. Experimental verification of the EYM can be found in Aune & Patton-Mallory (1986a).

In numerous subsequent research papers, the EYM has been proven to be valid with the assumption of no brittle failure occurring in a timber joint and no end fixity is involved. Examples can be found e.g. in Wilkinson (1993).

3.4.2 Geometric Nonlinear Effects

Ramskill (2002) states that little research has been undertaken into geometric nonlinear effects in timber joints. Experimental studies by Heine (2001) and Anderson (2001) revealed a change of failure mode from EYM mode (c) to mode (f) due to the rotational constrain that results from outer steel plates (steel-timber-steel joint). Similar effects should also occur for bolted joints with large washers.

Despite the possible strengthening influence of geometric nonlinear effects as reported for experimental bolted timber joint tests (Heine (2001), Anderson (2001), Luschnitz (1997)) or for wood plastic composites Balma (1999), the 'rope effect' and rotational constraint resulting from the fastener's ends were commonly neglected in joint models and in EYM implementations in the codes.

As mentioned in the previous section two types of geometric nonlinear effects are accounted for. The strengthening effect due to

- an inclined part of the fastener in mode d), e) and f), (applicable to any dowel type fastener)
- the end fixity that results from the head (in case of a nailed joint) and nut and washer (in case of a bolted joint)

The first strengthening effect is accounted for by an additional factor (1.05 and 1.15 in (BS EN 1995-1-1, 2004)) and the second is accounted for by an added term which includes the axial withdrawal strength of the fastener ($\frac{F_{ax,Rk}}{4}$).

History of the EYM as implemented in BS EN 1995-1-1 (2004) in the UK

The BS 5268:Part 2 (1991) version used empirically derived values for joint resistance therefore a distinction was made between the higher strength of bolted connection when compared to dowelled joints. This code was replaced by BS 5268-2 (1996) which adopted the EYM modified to the permissible stress approach used in the British standards. In this version only mode e) d) and f) obtained a factor (=1.1) that accounts for the strengthening effect as a result from an inclined part of the dowel type fastener.

However, when the draft of the Eurocode DD ENV 1995-1-1 (1994) was introduced, the additional strengthening effect that results from the end fixity was not incorporated as it was reasoned that the effect might be lost in service due to timber shrinkage. Furthermore, the enhancing factors in mode d) and e) were discarded.

This meant that for British designs where bolted connection were more commonly applied, the advantage for these connector types could not be used when designed according to the Eurocode. For this reason a new factor K_{2b} has been introduced to BS 5268-2 (2002) (a code based on permissible stresses) which accounts for end fixity in mode c) and increased the joint's capacity by 33% for bolted joints.

The committee in charge of the Eurocode adopted the idea of the strengthening effects due to end fixity and added the term $\frac{F_{ax,Rk}}{4}$ in BS EN 1995-1-1 (2004) for mode c), d), e) and f). This additional value is limited again to a certain percentage of the Johansen part, e.g. 25% in case of a bolted joint. Despite this improvement of the otherwise more conservative original model, the additional term is only an empircally determined value and does not consider explicitly the rotational constraint that also contributes greatly to the additonal joint's capacity (subsection 1.4.1). Also it is not entirely clear whether splitting could in practice, limit this strength improvement for some joint designs, even when edge distances are within the prescribed limits.

Modelling attempts to take into account the effect of end fixity and the effect of a partly inclined fastener can be found in Nishiyama & Ando (2003) and Kamachi & Ando (2006). With the model it is possible to study the effects separately in more detail, based on a sound mechanical approach. They used nailed joints for which, being slender fasteners, the 'rope effect' has a major influence on the joint's strength and secondary stiffness. This is explained in more detail in the subsequent subsection.

3.4.3 Beam on Elastic(-Plastic) Foundation

A fastener under lateral load embedded in wood can be seen as representing a beam on an elastic foundation. While the EYM assumes that, at the point of failure, the reaction force along the fastener is uniformly distributed, it is impossible to relate any other loading state of the joint to a certain displacement. On the other hand when an elastic foundation is assumed as in a 'Winkler' foundation only the elastic range can be predicted. Foschi (1974) uses a non-elastic foundation model of the following form

$$F = (F_0 + K_2 x) \cdot \left(1 - e^{\frac{-K_1 \cdot x}{F_0}}\right), \tag{3.29}$$

where

		Unit
F	reaction force of foundation	N
K_1	initial stiffness	N/mm
K_2	slope of the asymptote	N/mm
F_0	y-intercept	N
x	displacement	N

The relevant parameters can be obtained from common embedment tests as outlined, for example in BS EN 383 (2007). Other researchers used this foundation model to predict single joint behaviour. A finite element analysis can be used to solve for the unknown displacements of the deformed fastener.

Erki (1991) first used a geometric nonlinear 2D finite element model with an elastic-plastic foundation model. A plastically deformable fastener was considered. She further included the effect of end-rotation with a linear rotational spring and

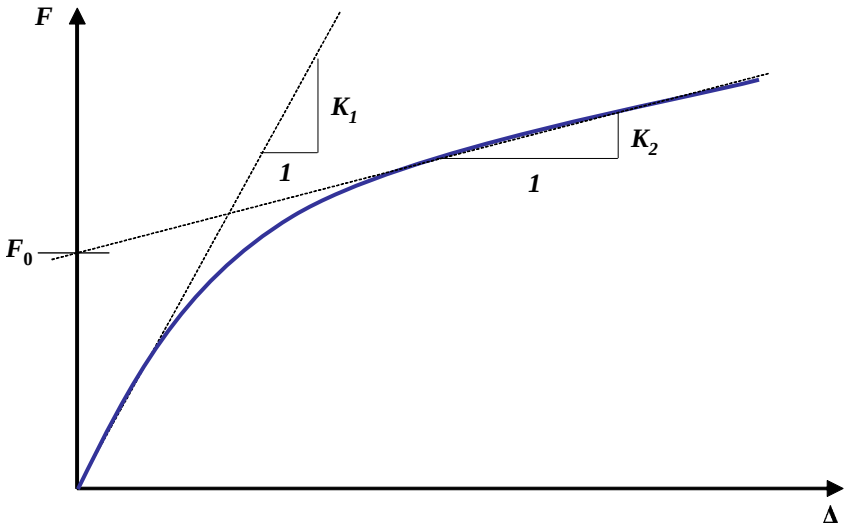

Figure 3.17: *Foundation model (Foschi, 1974)*

the withdrawal resistance of the fastener shank with friction forces as fractions of the embedment. The foundation model was calibrated with test data from embedment tests and good agreement has been found between these numerical results and tested bolted, riveted and nailed joints. However, for larger fastener ends, such as large washers the rotational constraint might be different from the assumed linear spring.

Similar research was conducted (geometric linear case) for timber joints loaded perpendicular and parallel to the grain by Sawata & Yasumura (2003). In the case of nails, where the rope effect plays a more prominent role, Nishiyama & Ando (2003) performed a geometric nonlinear analyses on similar basis.

In more recent research, Kamachi & Ando (2006) used the Weighted Residual Method on double shear bolted joints to obtain a polynomial function that describes the full deflection curve of a fastener. For timber embedment a beam on elastic foundation was assumed. The initial stiffness of a bolted timber joint until yield can thus be calculated. Yield loads were then determined on the basis of the principle of virtual work and the moments that can be determined from the displacement curve. It is assumed that a secondary stiffness results only from the rope effect in which the washer pushes against the side members. Rotational constraint was neglected. Further the authors didn't consider the case of joints loaded perpendicular to the grain for which, due to nonlinear timber emebedment, an additional secondary stiffness would result. However in case of parallel loaded joints in double shear and

in most failure modes the load-deflection curve could sufficiently be predicted.

3.4.4 Continuum Models

Although the assumption of a beam on an elastic-plastic foundation is a close enough prediction of the fastener embedment for predicting load-slip curves, it does not say anything about the real timber behaviour in the vicinity of a fastener. Furthermore, only an additional fracture or failure criteria that is in most cases based on a stress analysis, provides information on the point of failure. Friction between the fastener and the timber is another neglected factor in the foundation model.

Timber around the contact area of a fastener experiences a rather complex stress state even for a relative simple joint arrangement, as e.g. a pin loaded plate (Fig. 3.18). When more complicated situations are considered, e.g. non-uniform stress distribution along the fastener shank as it would occur for EYM mode (c-f), a finite element continuum model is the most versatile method. In the following some examples shall be presented.

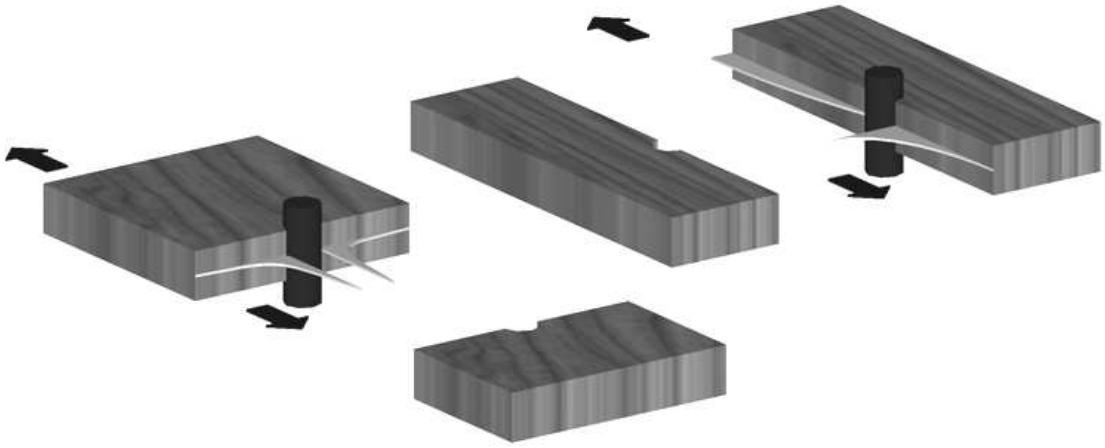

Figure 3.18: *Stress distribution along the X-axis and Y-axis of a pin loaded plate, courtesy of Heine (2001).*

Chen et al. (2003) presents a simple linear elastic 2D joint model. Joint elements are used to model the interaction between dowel and timber with a friction angle $\phi = 18°$. Using a simple failure criterion based on the tensile stress and strength perpendicular to the grain and the shear stress and strength it was possible to

calculate failure loads. The authors compared several numerical analysis for different end distances and simulated plane timber and fibreglass reinforced joints. A good overall agreement in terms of the failure load was found among tests and numerical results.

Patton-Mallory et al. (1998) tested and modelled a pin loaded timber member (in tension) with different end distances and fastener slenderness. They chose from different available material models for the timber and the steel pin (LEI linear elastic isotropic, LEO linear elastic orthotropic, EPP elastic perfectly plastic (pin) and trilinear wood). However, for the trilinear wood model a simplified nonlinear material model was implemented. The nonlinear solution is found by an Euler type method with successive small incremental steps. The authors ran the model for several different material models and stress-strain curves. As expected the closest fit to test data was obtained with the EPP model for the steel pin and a specific trilinear stress-strain model for timber. For slender pins the plastic deformation had a great influence on the joint behaviour. The analysis was stopped at a displacement of 0.03in (0.762mm) to keep it within the small deformation theory. At this point, depending on whether the plastic steel deformation took place, brittle or ductile failure could accurately be predicted.

Considering that the previous model does not obey the laws of constitutive modelling in continuum media, Kharouf et al. (2003) used a Hill yield criterion for biaxial compression including non-proportional hardening. With strain gauges monitoring the strain close to the fastener contact area good agreement between strain measurements and strain predictions has been found.

Alam & Ansell (2003) used a Hill yield criterion (subsection 3.3.1) in a 2D joint model of a multiple timber-steel-timber joint with shot-fired nails. They accurately predicted plastic hinges forming in the fasteners at the steel plate and plastic longitudinal strain in the timber. Furthermore, the results agreed with previous research that the maximum plastic strain occurred farthest away from the loaded edge. With a fitted logarithm curve on the calculated load-displacement points, the model agreed reasonably well with tested specimens up to 3.5mm displacement, at which point some specimens failed.

Moses & Prion (2003, 2004) used a Hill plastic model with work hardening and an associative flow rule. For failure prediction the authors use a probabilistic strength

criterion based on the Weibull distribution. With this it is possible to take into account the size effect that occurs specifically for timber due to the inherent flaws.

Grosse & Rautenstrauch (2004) used a plastic model for timber which is capable of strength degradation in order to simulate the softening effect of timber under tension. The authors modelled different connection types for timber-concrete-composite constructions.

The previous material model (in this case without strength degradation) for timber was verified with a special photogrammetric measuring procedure to obtain the deformations and thus strains on the surface of the tested specimens (Franke et al., 2008).

3.4.5 Brittle Failure

Timber joints can fail in brittle manner for several reasons. In the case of single joints loaded parallel to the grain, insufficient edge- and end-distances can lead to sudden failure. But even if those distances are adhered for multiple fastener connection, the interaction of several fasteners leads to uneven load distribution and therefore to high perpendicular to the grain stresses. A major factor is the fastener spacing since lateral stresses accumulate for several fasteners (Jorissen, 1998). Joints loaded perpendicular to the grain exhibit brittle behaviour depending on the location of the fastener(s) within the depth of the wood member.

For timber joints loaded perpendicular to the grain brittle failure is more evident, due to the fact that perpendicular to the grain tensile stresses are directly induced by the fastener(s). To account for this, the design shear force induced by the fasteners is limited according to BS EN 1995-1-1 (2004). This theoretical formula is based on an energetic fracture mechanical approach by van der Put (1990). A further semi-empirical equation for lateral loaded joints based on tests and the Weibull's failure theory can be found in the German design standard DIN 1052:2004-08 (2004) developed by Ehlbeck et al. (1989). The idea has been extended to also include normal forces acting in the loaded beam and an existing initial crack by Jensen (2005d).

Reshke et al. (2000) analytically derived a model based on an effective area which

experiences the tensile and shear stresses as a result of loading perpendicular to the grain. This fracture plane is assumed to occur at the line of fasteners furthest from the loaded edge. These authors formulate an equation that takes therefore into account the location of the fasteners relative to the joint dimension. This equation can be used to extend the Eurocode 5 (BS EN 1995-1-1, 2004).

In order to minimise splitting in timber joints, practical mechanical solutions have as well been investigated. Blass et al. (2000) suggests nail plates to reinforce the timber tensile strength perpendicular and parallel to the grain. Guan & Rodd (2000) try to minimise splitting with local reinforcement of Densified Veneer Wood (DVW) and plywood respectively, that exhibits higher resistance to tensile stresses, attached to the sides of the timber joint member. Schmid (2002) uses lateral-to-grain self-tapping screws to reinforce the splitting strength for multiple timber joints.

3.4.6 Multiple Fastener Joints

According to elastic theory, a multiple fastener joint carries less load than the respective sum of the capacity of its participating single fasteners. The effect is due to an uneven load distribution among the fasteners and is called 'row-effect' or 'group action effect'. It is however, depending on the ductility of the used fasteners more or less pronounced. For example for slender nails failing in EYM failure mode (f) one can assume that no effect takes place (Blass, 1994).

For more rigid fasteners, such as bolts, one has to account for the uneven load distribution. An extensive literature review on the topic of multiple bolted joints can be found in Moss (1997).

An elastic model describing this effect in the parallel to the grain direction was first devised independently by Cramer (1968) and Lantos (1969). Later Wilkinson (1986) extended the model to include fabrication tolerances and a nonlinear load-slip curve for individual fasteners.

Based on research by Jorissen (1998) the concept of an effective number of fasteners in one row has been introduced to BS EN 1995-1-1 (2004) in the following form:

$$F_{v,ef,RK} = n_{ef} F_{v,RK} \tag{3.30}$$

with

		Unit
$F_{v,Rk}$	characteristic load-carrying capacity of each fastener parallel to the grain	N
$F_{v,ef,Rk}$	characteristic load-carrying capacity of one row of fasteners parallel to the grain	N
n_{ef}	effective number of fasteners in line parallel to the grain	-

The effective number of fasteners for bolts, loaded parallel to the grain, can be calculated according to

$$n_{ef} = \min \begin{cases} n \\ n^{0.9} \sqrt[4]{\frac{a_1}{13d}} \end{cases} \tag{3.31}$$

where

		Unit
a_1	spacing between bolts in the grain direction	mm
d	fastener diameter	mm
n	number of bolts in the row	-

Jorissen (1998) uses Lantos's linear relation among several fasteners to model the interaction in a multiple joint. He included random load-slip curves for the individual fasteners based on Foschi's foundation equation (3.29). The curves were capped at the individual fastener's strength which is determined with the EYM plus an additional limit strength based on fracture mechanical considerations. Shear stresses and stresses perpendicular to the grain can then be calculated for the individual fastener at a presumed failure path along the length of a joint. This was calculated according to the beam on an elastic foundation principle which is described in more detail in subsection 3.4.7 for a model by Schmid et al. (2002). Uniform stresses over the timber thickness was assumed. The stresses can then be added and the stress accumulation plotted. Since these accumulated stresses can not exceed the maximum stresses in a single fastener without failing, the load per fastener needs to be reduced. This was achieved with a computer program which redistributed the load per fastener iteratively. Good agreement was found among the 950 multiple joint specimens and this model in terms of the ultimate load. However, the load-displacement prediction was relative poor (Heine, 2001).

3.4.7 Fracture Mechanics (FM)

A brief overview on the application of fracture mechanics to timber joints can be found in Kharouf et al. (1999). Although LEFM can predict failure loads due to cracks developing in timber, nonlinear phenomena such as the development of a plastic zone at the crack tip can only be considered with more sophisticated nonlinear fracture mechanics (NLFM) that takes into account crack closing stresses in a cohesive zone where the crack is forming.

Subsection 3.3.2 gave already an overview on different FM techniques. Here, several applications of FM to timber joints shall be presented.

Daudeville et al. (1999) and Daudeville & Yasumura (1996) describe a linear elastic fracture model for a timber joint consisting of a pin loaded parallel and perpendicular to the grain. The authors used the crack closure technique with the calculation of several 2D orthotropic finite element models for different crack lengths. The mesh was refined at the modelled crack tip. With a given critical energy release rate for mode I and mode II the applied load can be determined. The maximum load for several crack lengths gives then the calculated load carrying capacity. The above named authors found very good agreement among calculated loads and experimentally determined load carrying capacities for different bolt diameters. By comparison to the EYM the research shows that for the adhered edge distance of $3d$ for the joints loaded perpendicular to the grain, the EYM predictions are higher than the experimental results, and thus questions the validity of the EYM. In case of joints loaded parallel to the grain, this was less the case but the EYM still is slightly overestimating the load carrying capacity. In conclusion, linear elastic fracture mechanics can be used as a tool to extend the EYM to take into account brittle failure.

Similarly to Jorissen (1998), Schmid et al. (2002); Schmid (2002) represent a multiple bolted joint under parallel to the grain loading with two beams on an elastic foundation as seen in Fig. 3.19. The fastener acts on the single beam with the elastic foundation K (bottom part if the figure) with vertical force V an moment M. The displacement of this beam can be analytically solved with the program *Mathematica* (as it is done by Schmid). Due to the low length-width ratio, shear deformation is taken into account. Schmid assumes similarly to Jorissen $M = \frac{F/2}{h/2}$ and $V = \frac{F}{7}$. Unlike Jorissen, Schmid et al. consider crack growth and

therefore different fracture loads for the respective crack lengths. Further, he assumes equal load distribution and linear loading of the fasteners on the timber member while, according to Jorissen, the unequal loading is exactly the reason for crack initiation. From the deformation and applied force F, the energy release rate G can be calculated for different geometry (half beam width h, crack length x_1 and end distance x_0) and material properties (E,I,G and A). From the model and the experimental tests stable crack growth was observed until a crack length of about $3d$. The model can be extended to multiple fasteners although equal load distribution was assumed.

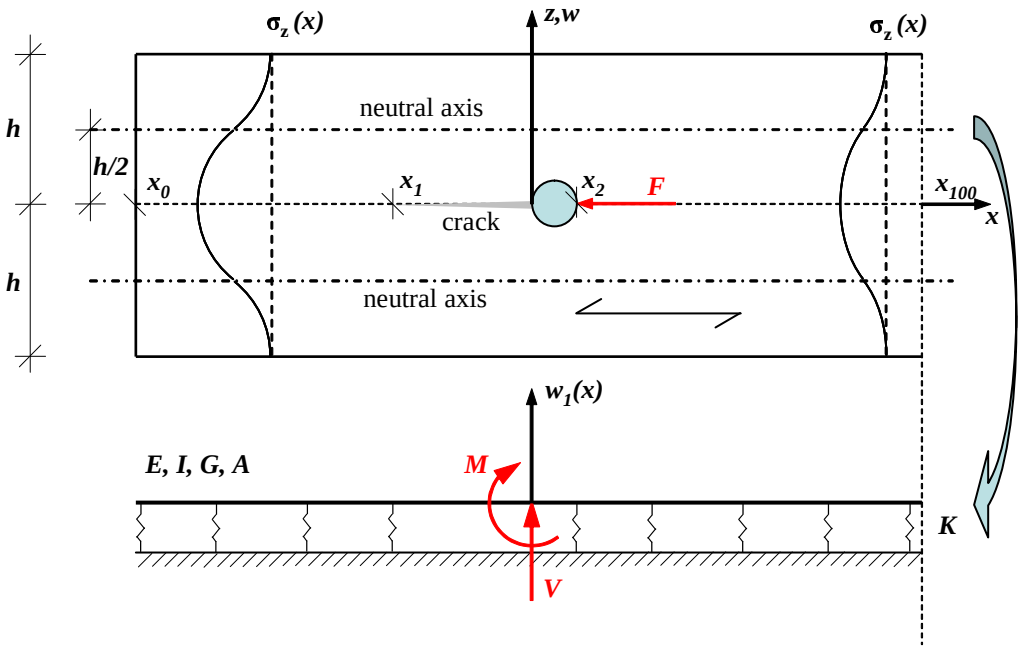

Figure 3.19: *Model of a cracked joint as a beam on elastic foundation (original in colour).*

A similar model with the assumption of the pin loaded timber member representing an elastic beam for joints loaded perpendicular to the grain can be found in Jensen (2005b) and Jensen (2005c). This has been applied to a moment resisting joint as well (Jensen, 2005a).

Ballerini & Rizzi (2005) conducted a numerical parametric study of beams loaded perpendicular to the grain. The numerical models consisted of a set of different connection arrangements (1 row of 2 fasteners and 2 rows of 1 fastener, different location of fasteners) with individual cracks that form at each fastener in the row of fasteners furthest away from the loaded edge. Stress intensity factors from the

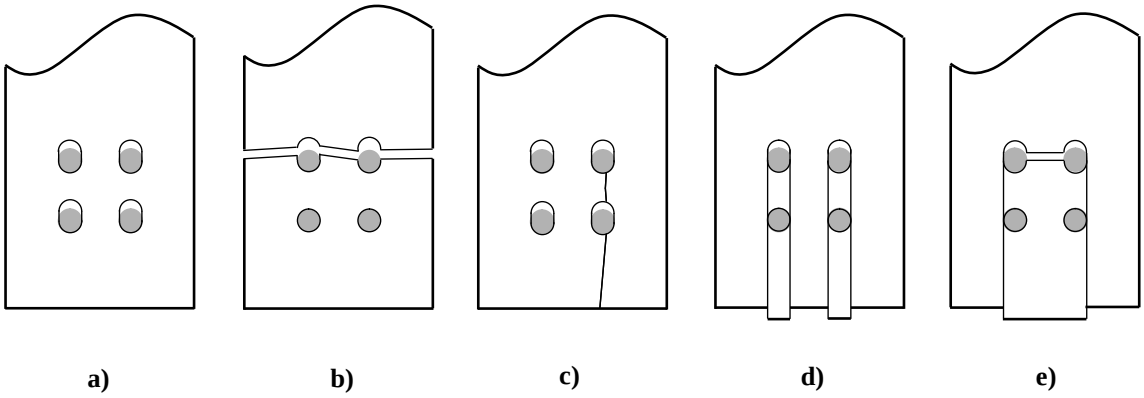

Figure 3.20: *Different failure modes for multiple timber joints, according to Mohammad & Quenneville (1999) (Failure net tension added).*

LEFM analysis were determined with two FE packages (ANSYS and ABAQUS). The Wu failure criteria was applied and thus fracture loads for several geometries and crack lengths determined. Additionally, the author presents a semi empirical formula which in contrast to the one in BS EN 1995-1-1 (2004) considers the influence of the connection geometry (e.g. connection height, number of rows etc.) as laboratory tests strongly suggest. In a case study the numerical analysis was applied to a connection with 4 rows of 3 dowels (diameter 16 mm) which represents a more realistic joint arrangement. While the agreement among numerical analysis and tests was generally not as good as the semi-empirical formula in the parametric study, a general good agreement was found in the case study.

Other types of failure for multiple joints need to be considered as well. Many researchers describe possible brittle and ductile failure mechanism. The different failure modes according to Mohammad & Quenneville (1999) can be seen in Fig. 3.20 and can be summarised as:

(a) **Embedment**, fasteners compress the surrounding timber without cracking.

(b) **Net tension**, tensile failure across the whole width of a timber member.

(c) **Cleavage**, Mode I failure.

(d) **Row tear-out**, several crack planes with Mode II failure.

(e) **Block shear**, also known as plug shear, for which a whole block of timber is shearing off the timber member.

Block shear failure can be typically seen in shear-plate and toothed-plate joints. In multiple bolted joints all of the above named failures can occur and need to be

considered. Since for fracture mechanical approaches generally a mesh is created to investigate a certain crack with the presumed stress concentration it is hard for these models to take into account all possible crack formations.

Lattice models on the contrary have the potential to predict any type of cracking with no restriction of crack initiation, path or number of cracks and are therefore an ideal choice for multiple joint models. Mixed mode fracture often governs crack growth which has to be considered as well in joint models, lattice models are very suitable since they can easily account for different fracture modes and their combination based on the simulation of morphological features with discrete elements.

3.4.8 Lattice Models

Snow (2006) used a 2D lattice to predict timber joint behaviour with a lattice model for parallel and perpendicular to the grain loading. The pin loaded joints were made of Eastern white pine (*Pinus strobus*), LVL (Laminated Veneer Lumber), PSL (Parallel Strand Lumber) and LSL (Laminated Strand Lumber). These were compared for their different failure loads and fracture patterns. The lattice model was used only for a comparison of joint tests made of LVL and pine. Snow used link elements with perfectly brittle behaviour under tension and a tri-linear plastic load-displacement curve for lateral and longitudinal links under compression. The calibration of elastic parameters was accomplished by directly transferring the E moduli to the respective link element's stiffness. Strength properties were determined by simulating simple stress states and iteratively adjusting the link's strength parameters.

Although, relative good agreement of absolute failure loads among model and experiment can be observed this is less the case for the overall joint stiffness. Furthermore, it is not entirely clear how the solution algorithm used for the lattice model works. The predicted load-displacement curves of a joint which exhibits sudden brittle failure differ from the more ductile behaviour of the respective experimental tests. It is therefore questionable if the lattice spring's capability of plastic deformation is correctly taken into account.

A pseudo lattice model for a pin loaded joint is described in Racher & Bocquet

(2005) and Bleron et al. (2001). The authors use 2D bar elements in lateral and longitudinal direction with plastic behaviour under compression and perfectly brittle behaviour for tension perpendicular to the grain. Diagonal elements are not used, therefore no lateral strain effect can be simulated. However, shear was modelled using special joint elements in the lateral direction which exhibit perfectly plastic response after yielding. The pseudo lattice is used only in the close area around the fastener, the remaining timber was modelled by elastic orthotropic elements. The model was created with the FE software package CAST3M and used an ordinary solution algorithm. No 'snap-back' was encountered as the joint model did not fail in brittle manner. Failure was determined by a maximum strain which was set for the individual elements. Therefore, the nonlinear load-displacement curve for the entire joint could be predicted for a small deformation. However, entirely brittle behaviour of joints could not.

In Bocquet (1997), the author extends the idea to a 3D multiple joint model made of several layers of the before described lattices. Bolts are modelled with beam elements and the end rotation is taken into account with nonlinear springs.

3.4.9 Empirical Joint Models and Further Experimental Studies

Numerous experimental studies on timber joints can be found in the literature and shall be presented here in a short list for the sake of completeness. The experimental results were partly analysed to obtain empirically derived design equations: among others are Hassan & Mohamedien (1997), Porteous & Kermani (2005), Anderson (2001), Dodson (2003), Ramskill (2002), Mischler et al. (2000), Mohammad & Quenneville (2001) and Quenneville & Mohammad (2000).

One recent development in empirical models is the application of neural networks which make use of a large database of tested dowelled joint specimens. This model is described in Cointe & Rouger (2004). Almost 1400 joint arrangements were listed in a database with different parameters such as wood density, angle of loading, dowel diameter, number of rows and columns etc. Relatively good agreement of the model with predictions by the EYM was found. The model itself is rather complicated and can not be used directly as an engineering tool, thus by a multiple regression 20 terms have been extracted with which the prediction of ultimate loads was still reasonably accurate. However, it is questionable if an extrapolation can

be drawn to joints that do not confirm to joint arrangements that are already in the database.

4 Beam-Foundation Model

4.1 General

A 2D model was created in order to simulate the behaviour of a bolt in a single shear joint. It consists of a modelled fastener, washers, head, nut and timber embedment. Geometric nonlinear effects are accounted for which occur in this joint arrangement when larger displacements are reached. Load-displacement plots of individual model elements (timber displacement, axial force in fastener, fastener rotation) can be obtained and were compared to tested joints.

The FE package *ANSYS* (SAS IP, Inc., 2007) was used. This package enables the model to be run in a 'batch' mode. For this purpose a text file is created that contains all necessary information on nodes, element properties, applied loading and constraints. This file can be transferred to *ANSYS* which runs the FE analysis. Several text files can be created with different input parameters (fastener diameter, timber thickness, washer size, embedment properties etc.) that define the joint arrangement.

The development of this model along with results is published in Reichert & Ridley-Ellis (2006). A brief version of this paper is presented here.

4.2 Model Concept

In the 2D model beam elements are used to represent bolt bending and axial tension. Nonlinear springs that are linked via contact elements to these beams represent timber embedment. Vertical springs represent embedment along the bolt shank, while horizontal ones represent embedment underneath the washer. They are adjusted to respective experimental embedment tests. A similar study

for a geometric linear case can be found in Sawata & Yasumura (2003) and for a geometric nonlinear analysis in Nishiyama & Ando (2003).

The model consists of three main parts: a) nonlinear beam elements that represent one steel bolt and b) a number of nonlinear springs that represent timber embedment in the longitudinal and perpendicular to the grain direction. These two parts are linked together with contact elements. Further, c) washers, head and nut of the bolt were modelled as a flexibly connected rigid beam that also is able to come into contact with the embedment springs.

A schematic representation of the model can be seen in Fig. 4.1.

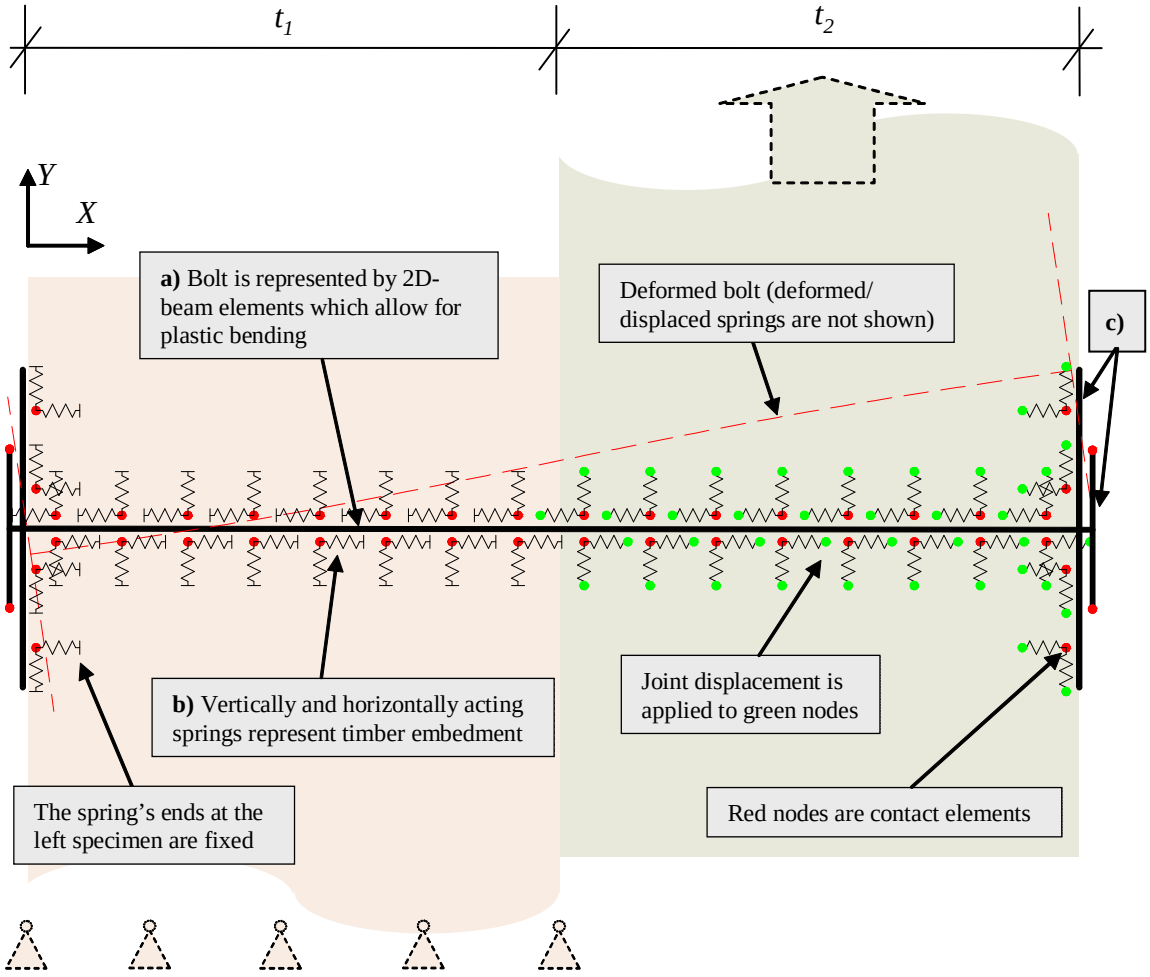

Figure 4.1: *Schematic of the 2D joint model (original in colour).*

In experimental tests, the load-displacement of the abutting timber members was

measured with displacement transducers (5 mm LVDTs) along with the rotation of the bolt. Further, it was tried to measure the developing tensile force inside the bolt that results from the end fixity of the head, nut and washers. This was achieved by inserting a strain gauge (BTM Bolt Strain Gauge) in the centre of the bolt. A test was run to investigate the influence of the bending strain acting on the strain gauge compared to the overall tensile strain and found to be negligible. The strain gauge was calibrated with a tensile test of the bolt. The nonlinear springs representing timber embedment were calibrated against embedment tests with bolts and washers respectively. The Sitka spruce timber (grade C16), that was used in the experiments, was provided by James Callander & Son Ltd., Falkirk. Before testing, the battens were left in a controlled environment chamber set to a constant temperature of 21 °C and 65% humidity until they attained constant weight.

The experiment set-up is shown in Fig. 4.2. LVDT displacement transducers were used to measure the displacement between the two timber members. Further LVDTs were fixed vertically to obtain measurements of the bolts rotational movement, as can be seen in the figure. The symmetric single shear joint consisted of two timber members with a thickness of 50 mm and 120 mm in width. The edge distance of the bolt was $> 7d$ =130 mm, to ensure that the joint would not fail in a brittle manner. The loading rate of this quasi static test was chosen to reach the maximum displacement after 5-10 min.

An overall good agreement was found among experimental tests compared to the model's prediction in terms of load-displacement of the timber members, rotation of the bolt as well as the tensile force in the bolt, Fig. 4.3 and 4.4.

The difference in predicted ultimate loads by the EYM for the draft of DD ENV 1995-1-1 (1994) and BS EN 1995-1-1 (2004) is the neglected strengthening effect for mode c), horizontal, dashed lines in Fig. 4.3. The difference of the FE predicted values to the EYM might be even more pronounced when a non symmetric joint arrangement is used.

Tests with slender fasteners with an expected ductile failure mode f) have not been conducted, as it would be not possible to measure the axial force in such a small bolt with the above described method. However, the model is fully capable of predicting the formation of a plastic hinge for these slender fasteners. The model has been merely used to investigate the possibility to use certain FE elements

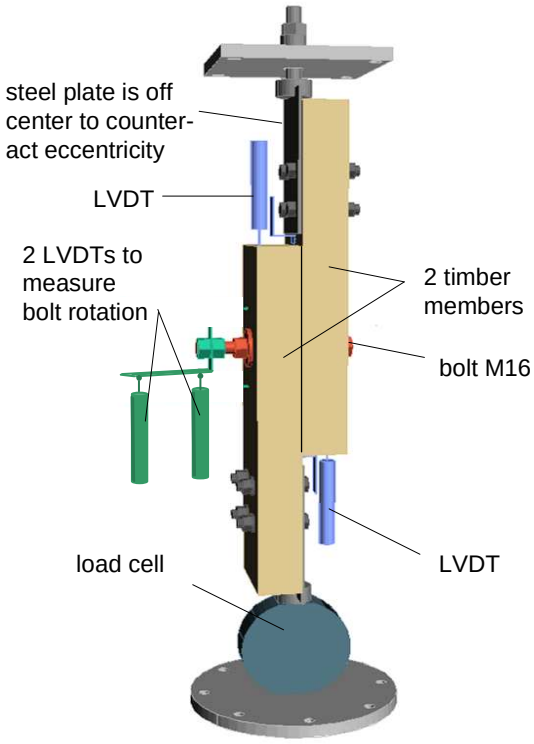

Figure 4.2: *Schematic of the laboratory test set-up for the joint tests (original in colour).*

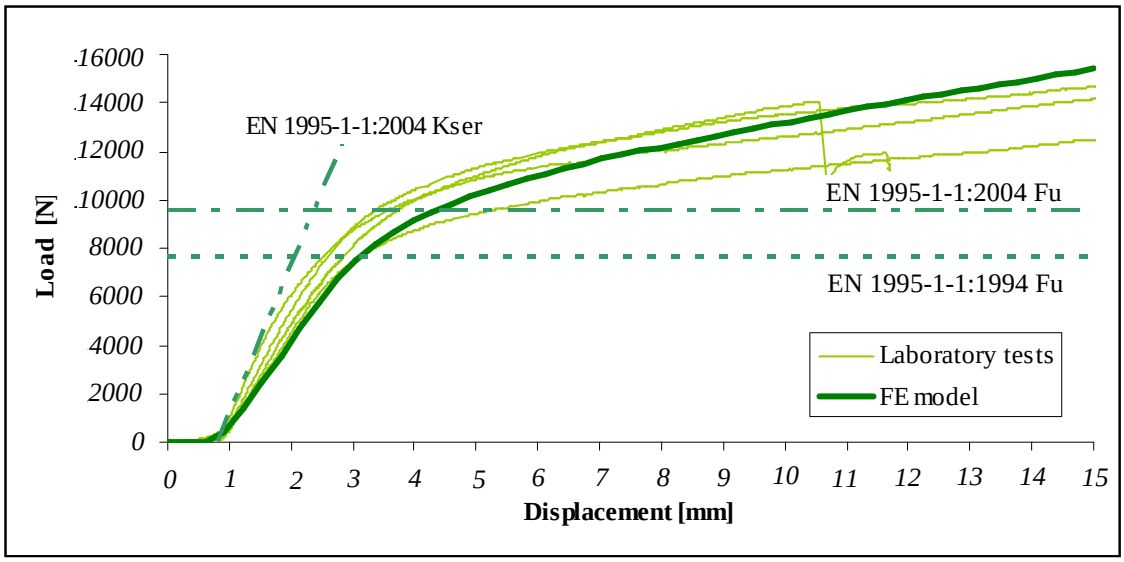

Figure 4.3: *Load-displacement plots of the 2D joint model compared to an experimental test series with M16 bolts and Sitka spruce timber members (original in colour).*

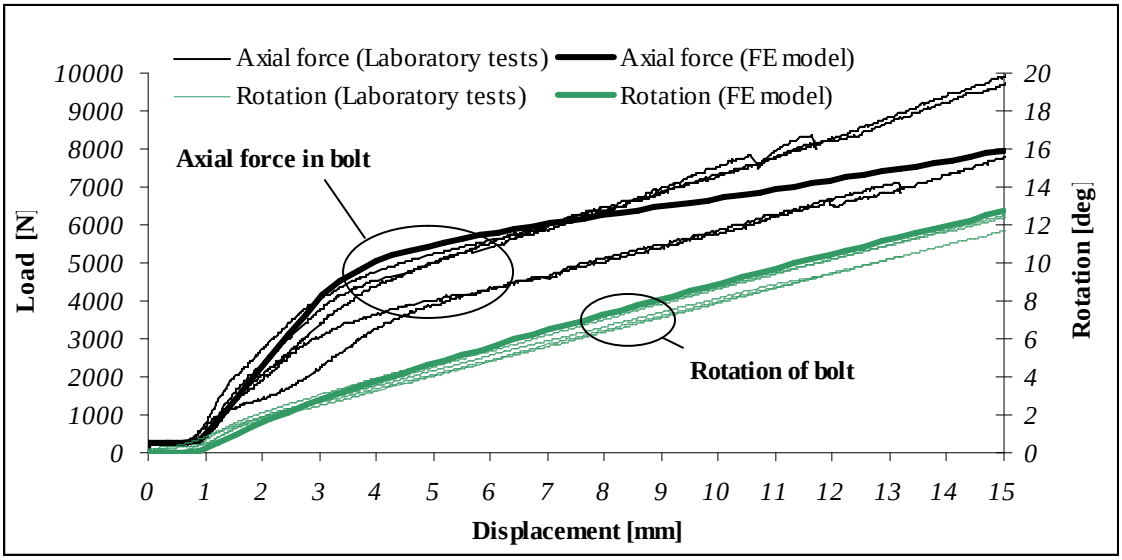

Figure 4.4: *Load-displacements of 2D joint model compared to experimental test series, axial tension (black), bolt rotation (green) (original in colour).*

for a geometric nonlinear joint model. And furthermore, to obtain an idea of the reliability of the predicted load displacement plots, the axial force developing inside the bolt and the rotation of the bolt.

5 Lattice Model LAT3D

5.1 General

Lattice models derive from the concept of discrete element models. The principal idea is that one dimensional spring elements can reflect the behaviour of a material rather than continuum elements. By deactivation or change of the element's stiffness, it is possible to model fracture processes and plastic deformation. Furthermore the material's morphology can be incorporated. Thus, individual elements can simulate the actual behaviour of material on the small scale of features such as growth rings.

This chapter starts with an introduction to the FE method and the derivation of element types used (section 5.2). The *MATLAB* environment (section 5.3), with which the program to calculate the lattice model was developed, is presented briefly. Furthermore, the chapter addresses issues such as the composition of the lattice structure (section 5.4) and how the implementation of the wood structure into the model is accomplished and what assumptions were made in this regard (section 5.5).

It describes in greater detail the development and functions of the FE program *LAT3D* that is used to create and compute 3D lattice models. Insight will be given on the nonlinear solution algorithm and various optimisations that were adopted to speed up the computation process (section 5.6). Namely, this is an adaptation of a method proposed by Jirasek & Bazant (1995), the Step-Size-Control (SSC) algorithm and the Method of Inelastic Forces (MIF). The MIF is extended to account for inelastic moments, which is necessary for the accounted geometric nonlinearity of beam elements that were used in a full 3D joint model. Additionally the SSC was extended to accommodate ductile behaviour for lateral and longitudinal links, to simulate plastic hardening of real wood under compression (section 5.7).

The link between the lattice and beams that were used to represent the fastener

in the full 3D joint model is managed by the use of special contact elements for which the geometry is continuously updated. The same applies for the fastener beam elements to account for their geometric nonlinearity. These elements will be discussed in section 5.8 and 5.9.

The chapter finishes with details on the functionality of the program LAT3D and presents a short example (section 5.10 and 5.11).

5.2 Finite Element Method

This section introduces the finite element method and derives the local stiffness matrices of elements that are used in the program *LAT3D*.

The FE method is a numerical approximation technique to simulate physical (or non-physical) behaviour by obtaining the solution of partial differential equations. In the case of structural mechanics, the known field variables act on a structure (domain) are either forces or prescribed displacements. The task is to solve for the unknown field variables, namely the displacements (and therefore strains and stresses) inside the structure. Despite its common use in static structural engineering, the technique is also applied to many other fields ranging from fluid, soil mechanics to dynamics, electromagnetism etc. or a combination of them.

The principal idea is that partial differential equations are solved approximately for smaller elements for which a solution is known. By connecting the equations via nodal values for several elements the problem for a whole domain can be obtained.

As an example, a differential equation for a one dimensional flexural member along the X-axis with bending about axis (Z) has the form of $M_z{=}EI_z\frac{d^2v}{dx^2}$. It describes the relation between the moment M about the z-axis and displacement v in the y-axis. The solution is known and can be approximated with a second order polynomial function also called Hermitian shape function.

By the *direct stiffness* method these functions can directly be translated into a local stiffness matrix that relates local displacements with forces acting on the element. For more complex elements or problems where the underlying physical meaning

such as forces and displacements can not be directly translated into matrix form, more general methods such as the weighted residual method (Galerkin) or the minimum potential energy are used.

5.2.1 Variational Form: Minimum Potential Energy Principle

The total potential energy of a system (Fig. 5.1) can be described as

$$\Pi = U + U_p \tag{5.1}$$

where U stands for the elastic energy stored in the deformed body and U_p for the potential energy of the applied forces.

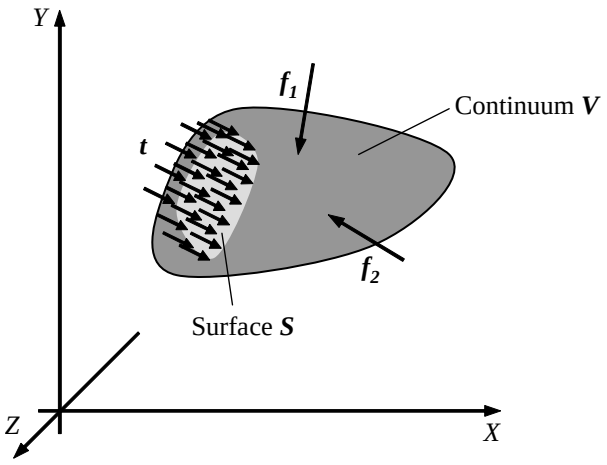

Figure 5.1: *Schematic of a three dimensional body V, with body forces f and surface traction t.*

The total strain energy U of a continuum is defined as

$$U = \frac{1}{2}\int_V \epsilon^T \sigma \; dV \tag{5.2}$$

By using the constitutive relationships between stress and strain matrix $[C]$ and the strain-displacement vector $\{B\}$ one can rewrite the former equation as

$$U = \frac{1}{2}\int_V \{\delta(x,y,z)\}^T \{B\}^T [C] \{B\} \{\delta(x,y,z)\} dV \tag{5.3}$$

The applied external nodal forces and surface tractions can be written as

$$U_p = \int_S \{\delta(x,y,z)\}^T t(x,y,z) dS + \sum_{i=1}^{n_f} \left(d_i^T f_i\right) \tag{5.4}$$

where

- $\delta(x,y,z)$ is the exact displacement function (displacement vector at position x,y,z)
- $t(x,y,z)$ is the vector of surface traction (i.e. applied stress)
- f_i is the i-th nodal force vector
- d_i is the i-th nodal displacement
- n_f is the number of applied nodal forces

The principle of minimum potential energy can be stated as follows:

> Out of all geometric possible displacement functions $\delta(x,y,z)$ the one which minimises the total potential energy, Π, is the displacement solution that will satisfy equilibrium, and will be the actual displacement due to the applied forces.

This can be formulated mathematically,

$$\frac{\partial \Pi}{\partial \delta} = \frac{\partial (U + U_p)}{\partial \delta} = 0 \tag{5.5}$$

The domain can be discretised into smaller elements, ensuring continuity of displacement, that the total potential energy of the system is the sum of the individual energies of each element.

$$\Pi = \sum_{el=1}^{n_{el}} \Pi^{el} \tag{5.6}$$

The exact displacement function $\delta^{el}(x,y,z)$ for an individual element is approximated via a shape function in between nodal displacements.

$$\delta^{el}(x,y,z) \approx N(x,y,z)\Delta^{el} \tag{5.7}$$

Substituting this definition of the displacement function and inserting (5.3) and (5.4) into (5.1) results in

$$\Pi^{el} = \frac{1}{2}\int_{V^{el}} \Delta^{el\ T} N(x,y,z)^T [B^{el}]^T [C][B^{el}] N(x,y,z)\Delta^{el} dV^{el} ... \\ - \int_{S^{el}} \Delta^{el\ T} N(x,y,z)^T t(x,y,z) dS^{el} - \Delta^{el\ T} f^{el} \tag{5.8}$$

where V^{el} represents the element's volume and S^{el} the element's surface where tractions are applied.

By minimising the total potential energy for one element according to (5.5) the above equation results in

$$\frac{\partial \Pi^{el}}{\partial \Delta^{el}} = \int_{V^{el}} N(x,y,z)^T [B^{el}]^T [C][B^{el}] N(x,y,z)\Delta^{el} dV^{el} ... \\ - \int_{S^{el}} N(x,y,z)^T t(x,y,z) dS^{el} - f^{el} = 0 \tag{5.9}$$

Since Δ^{el} is not a function of the position (x, y, z) it can be taken outside the integral. The remaining term is called the element stiffness matrix.

$$[K^{el}] = \int_{V^{el}} N(x,y,z)^T [B^{el}]^T [C][B^{el}] N(x,y,z) dV^{el} \tag{5.10}$$

Depending on the definition of the strain-displacement matrix $[B^{el}]$, $N(x, y, z)$ vanishes from the above definition of the local stiffness matrix. Thus,

$$[K^{el}] = \int_{V^{el}} [B^{el}]^T [C][B^{el}] dV^{el} \tag{5.11}$$

After the local element stiffness matrices are created and (if necessary) the DoFs are rotated to match the global ones, they can be assembled to the global stiffness matrix $[K]$. Acting forces and boundary conditions of the structure are applied to a force vector $\{F\}$. In the general case for a linear solution, a set of simultaneous algebraic equations of the form

$$[K]\{\Delta\} = \{F\} \tag{5.12}$$

need to be solved.

Since strain energies can not be negative, and due to the nature of the matrix

Table 5.1: *Different element types used in* LAT3D.

element type	nodes	DoFs	dimensions	application
bar	2	6	3D	lattice
beam	2	10	2D	fastener
hexahedral	8	24	3D	remaining solid structure

multiplication, single element stiffness matrices are symmetrical and positive definite. Consequently, the global stiffness matrix $[K]$ is also symmetrical and positive definite. The solution of linear equations in *LAT3D* is described in more detail in subsection 5.2.3.

5.2.2 Derivation of FE Elements

This subsection will present in brief the derivation of the stiffness matrix of the finite element types which are used in *LAT3D*. Namely, these are,

Bar Element

The lattice structure is composed of single bar elements. The linear displacement u^{el} along the element's length x can be described with the two shape functions N_1^{el} and N_2^{el} as a linear interpolation between the two nodal displacements u_1^{el} and u_2^{el}.

$$u^{el}(x) = N_1^{el}u_1^{el} + N_2^{el}u_2^{el} = \left\{ \begin{array}{cc} N_1^{el} & N_2^{el} \end{array} \right\} \left\{ \begin{array}{c} u_1^{el} \\ u_2^{el} \end{array} \right\} = \{N\}\{u\}^{el}. \tag{5.13}$$

These linear isoparametric shape functions can be written as

$$N_1^{el} = 1 - \tfrac{x}{l} = 1 - \xi \quad N_2^{el} = \tfrac{x}{l} = \xi. \tag{5.14}$$

The graphical representation of these shape functions can be seen in Fig. 5.2.
The axial strain over the element is calculated by

$$\epsilon = \frac{du^{el}}{dx} = (u^{el})' = \left\{ \begin{array}{cc} \frac{dN_1^{el}}{dx} & \frac{dN_2^{el}}{dx} \end{array} \right\} \left\{ \begin{array}{c} u_1^{el} \\ u_2^{el} \end{array} \right\} = \frac{1}{l} \left\{ \begin{array}{cc} -1 & 1 \end{array} \right\} \left\{ \begin{array}{c} u_1^{el} \\ u_2^{el} \end{array} \right\} = \{B^{el}\}\{u\}^{el}. \tag{5.15}$$

where

$$\{B^{el}\} = \frac{1}{l} \left\{ \begin{array}{cc} -1 & 1 \end{array} \right\}. \tag{5.16}$$

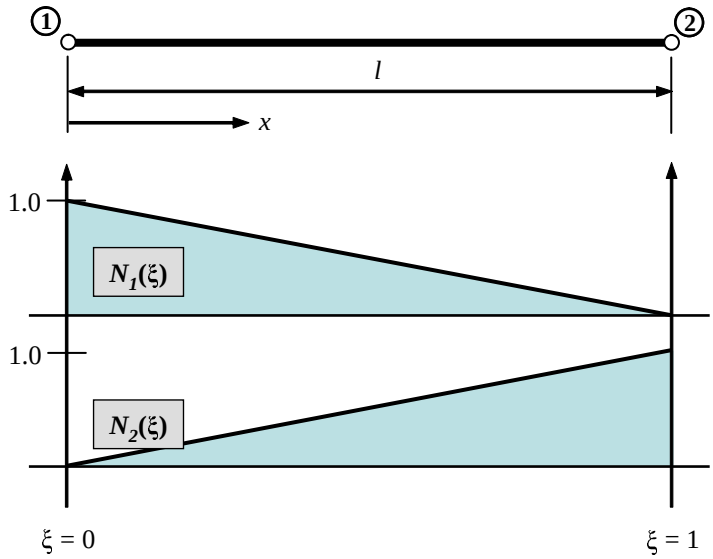

Figure 5.2: *Shape functions and schematic of 1D bar element.*

Now the stiffness matrix can be obtained via the variational principle described above. This leads to the element's internal strain energy U^{el}

$$U^{el} = \frac{1}{2}\int_{x_1}^{x_2} \epsilon EA\epsilon dx = \frac{1}{2}\int_0^1 \epsilon EA\epsilon l d\xi, \tag{5.17}$$

with strain ϵ expanded with the strain-displacement matrix $[B]$ as $\epsilon = [B^{el}]u^{el}$ it follows that

$$U^{el} = \frac{1}{2}\int_0^1 \left\{ \begin{array}{cc} u_1^{el} & u_2^{el} \end{array} \right\} \frac{1}{l} \left\{ \begin{array}{c} -1 \\ 1 \end{array} \right\} EA \frac{1}{l} \left\{ \begin{array}{cc} -1 & 1 \end{array} \right\} \left\{ \begin{array}{c} u_1^{el} \\ u_2^{el} \end{array} \right\} l d\xi. \tag{5.18}$$

When the nodal displacements are moved out of the integral the equation can be solved, thus

$$U^{el} = \frac{1}{2} \left\{ \begin{array}{cc} u_1^{el} & u_2^{el} \end{array} \right\} \int_0^1 \frac{EA}{l^2} \left[\begin{array}{cc} 1 & -1 \\ -1 & 1 \end{array} \right] l d\xi \left\{ \begin{array}{c} u_1^{el} \\ u_2^{el} \end{array} \right\} \tag{5.19}$$

in which

$$[K^{el}] = \int_0^1 EA\{B^{el}\}^T\{B^{el}\} l d\xi = \int_0^1 \frac{EA}{l^2} \left[\begin{array}{cc} 1 & -1 \\ -1 & 1 \end{array} \right] l d\xi. \tag{5.20}$$

After the local element is assembled it might need to be rotated to the global coordinates with a rotation matrix. The parameters EA are combined to the

stiffness value K.

Beam Element

Unlike the bar element, the 2D beam element uses *Hermetian cubic* shape functions to ensure C^1 continuity of the displacement function (i.e. first derivatives are equal). With this requirement, it is ensured that displacement $v(x)$ and slope $\theta(x)$ of the beam is continuous. They can be written with respect to ξ as

$$\begin{array}{ll} N^{el}_{v,1} = \frac{1}{4}(1-\xi)^2(2+\xi) & N^{el}_{v,2} = \frac{1}{4}(1+\xi)^2(2-\xi) \\ N^{el}_{\theta,1} = \frac{1}{8}l(1-\xi)^2(1+\xi) & N^{el}_{\theta,2} = -\frac{1}{8}l(1+\xi)^2(1-\xi). \end{array} \tag{5.21}$$

The four shape functions are plotted in Fig. 5.3.

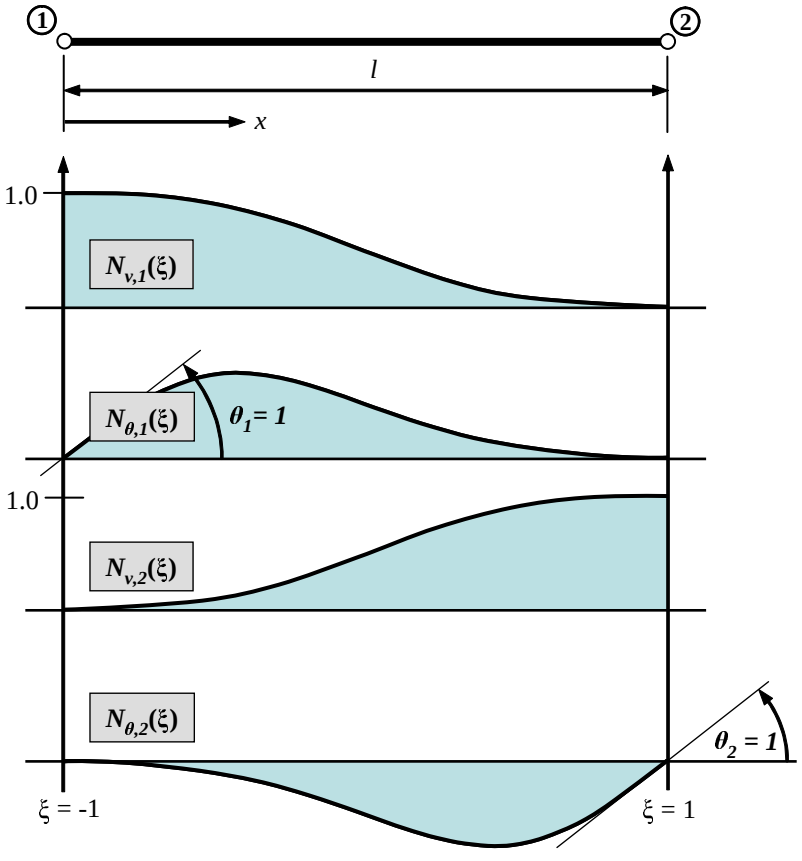

Figure 5.3: *Shape function of a 2D beam element (only flexural behaviour is considered). ξ varies from -1 at node ① ($x = 0$) to 1 at node ② ($x = l$).*

The curvature can be described as the second derivative with respect to ξ (with $\xi = \frac{2x}{l} - 1$ and $\frac{dx}{d\xi} = \frac{1}{2}l$)

$$\kappa = \frac{d^2v(x)}{dx^2} = \frac{4}{l^2}\frac{d^2v\xi}{d\xi^2} = \frac{4}{l^2}\frac{\{dN^{el}\}}{d\xi^2}\{u\} = \{B^{el}\}\{u\} = \{N^{el''}\}\{u\}. \tag{5.22}$$

The beam element is depicted in Fig. 5.4.

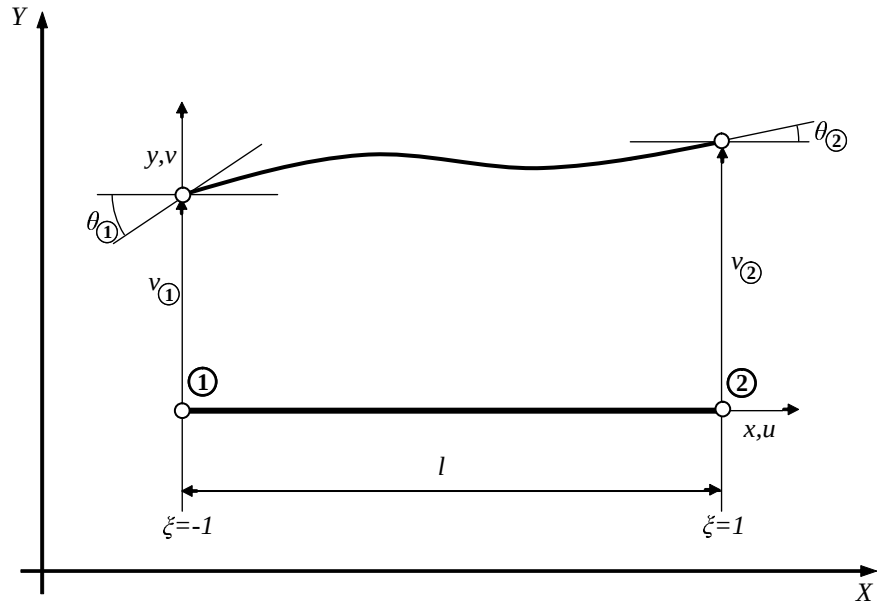

Figure 5.4: *Two node linear Bernoulli-Euler element, 2D.*

With $\{B^{el}\}$ being the second derivative of the shape function $\{N^{el''}\}$:

$$\{B^{el}_{(\xi)}\} = \left\{ \; 6\frac{\xi}{l^2} \quad \frac{3\xi-1}{l} \quad -6\frac{\xi}{l^2} \quad \frac{3\xi+1}{l} \; \right\}. \tag{5.23}$$

Thus follows the stiffness matrix for the beam element (with included stiffness properties: Young's modulus E and moment of inertia I) as

$$[K^{el}] = \int_0^l EI\{B^{el}_{(\xi)}\}^T\{B^{el}_{(\xi)}\}dx = \int_{-1}^{+1} EI\{B^{el}_{(\xi)}\}^T\{B^{el}_{(\xi)}\}d\frac{1}{2}l\xi, \tag{5.24}$$

along with the previously described stiffness matrix for bar elements.

Assuming the beam element can transmit axial forces as well and further that they are independent of the flexural behaviour (no stress stiffening), the definition of $\{B^{el}\}$ can be superimposed with the strain-displacement matrix for the axial direction. Thus, the two shape functions and consequently the resulting stiffness matrix for bar elements from the previous derivation is added.

This element is then extended to a 3D beam with flexure about the Z and Y axis. Torsion about the X axis is neglected. Thus, the element consists of 5 DoFs for each node respectively. Torsional rigidity plays only a minor role since, as long as the joint deformation remains moderate, no eccentric loads (that would result in

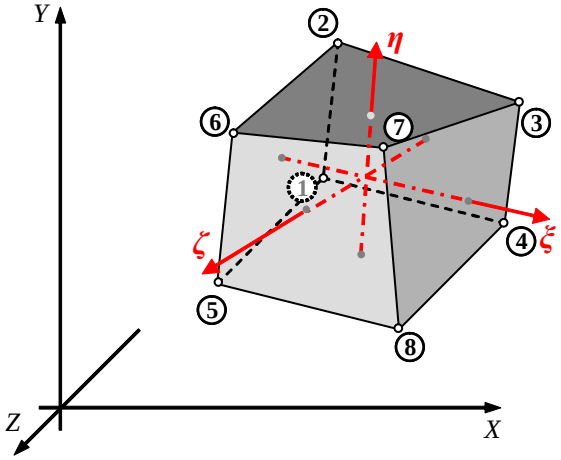

Figure 5.5: *Schematic of 8-node hexahedral element.*

torsion) will be applied to the bolt. This is true when friction can be neglected.

Hexahedral Element

Hexahedral solid elements are used for the remaining area of the timber model which experience no plastic deformation and therefore remain elastic. Fig. 5.5 shows the schematic of the 8-node element in its isoparametric form.

The linear shape functions with respect to the nodal definitions can be written as follows

$$\begin{aligned} N_1^{el} &= \tfrac{1}{8}(1-\xi)(1-\eta)(1-\zeta) \quad N_2^{el} = \tfrac{1}{8}(1-\xi)(1+\eta)(1-\zeta) \\ N_3^{el} &= \tfrac{1}{8}(1-\xi)(1+\eta)(1+\zeta) \quad N_4^{el} = \tfrac{1}{8}(1-\xi)(1-\eta)(1+\zeta) \\ N_5^{el} &= \tfrac{1}{8}(1+\xi)(1-\eta)(1-\zeta) \quad N_6^{el} = \tfrac{1}{8}(1+\xi)(1+\eta)(1-\zeta) \\ N_7^{el} &= \tfrac{1}{8}(1+\xi)(1+\eta)(1+\zeta) \quad N_8^{el} = \tfrac{1}{8}(1+\xi)(1-\eta)(1+\zeta). \end{aligned} \tag{5.25}$$

To create the strain-displacement matrix $[B]$, the partial derivatives need to be formulated in respect to the global coordinates, which looks in matrix form as follows

$$\begin{bmatrix} \frac{\partial N_i^{el}}{\partial x} \\ \frac{\partial N_i^{el}}{\partial y} \\ \frac{\partial N_i^{el}}{\partial z} \end{bmatrix} = \begin{bmatrix} \frac{\partial \xi}{\partial x} & \frac{\partial \eta}{\partial x} & \frac{\partial \zeta}{\partial x} \\ \frac{\partial \xi}{\partial y} & \frac{\partial \eta}{\partial y} & \frac{\partial \zeta}{\partial y} \\ \frac{\partial \xi}{\partial z} & \frac{\partial \eta}{\partial z} & \frac{\partial \zeta}{\partial z} \end{bmatrix} \begin{bmatrix} \frac{\partial N_i^{el}}{\partial \xi} \\ \frac{\partial N_i^{el}}{\partial \eta} \\ \frac{\partial N_i^{el}}{\partial \zeta} \end{bmatrix}. \tag{5.26}$$

The 3x3 matrix is the inverse *Jacobian matrix* of (x, y, z) with respect to (ξ, η, ζ).

The isoparametric definition of the element geometry is given by

$$x = x_i N_i^{el} \quad y = y_i N_i^{el} \quad z = z_i N_i^{el}, \tag{5.27}$$

where i loops through all 8 nodes with the coordinates (x_i, y_i, z_i).

The Jacobian can now be computed with respect to the above geometry definition as

$$J = \begin{bmatrix} x_i \frac{\partial N_i^{el}}{\partial \xi} & y_i \frac{\partial N_i^{el}}{\partial \xi} & z_i \frac{\partial N_i^{el}}{\partial \xi} \\ x_i \frac{\partial N_i^{el}}{\partial \eta} & y_i \frac{\partial N_i^{el}}{\partial \eta} & z_i \frac{\partial N_i^{el}}{\partial \eta} \\ x_i \frac{\partial N_i^{el}}{\partial \zeta} & y_i \frac{\partial N_i^{el}}{\partial \zeta} & z_i \frac{\partial N_i^{el}}{\partial \zeta} \end{bmatrix} \tag{5.28}$$

Stress-strain matrix $[B^{el}]$ can be written with the derivatives with respect to each global dimension as:

$$[B^{el}] = \begin{bmatrix} \frac{\partial}{\partial x} & 0 & 0 \\ 0 & \frac{\partial}{\partial y} & 0 \\ 0 & 0 & \frac{\partial}{\partial z} \\ \frac{\partial}{\partial x} & \frac{\partial}{\partial y} & 0 \\ 0 & \frac{\partial}{\partial y} & 0 \\ 0 & 0 & \frac{\partial}{\partial z} \end{bmatrix} \begin{bmatrix} q & 0 & 0 \\ 0 & q & 0 \\ 0 & 0 & q \end{bmatrix} = \begin{bmatrix} q_x & 0 & 0 \\ 0 & q_y & 0 \\ 0 & 0 & q_z \\ q_y & q_z & 0 \\ 0 & q_z & q_y \\ q_z & 0 & q_x \end{bmatrix}, \tag{5.29}$$

where

$$\begin{aligned} \{q\} &= \left\{ N_1^{el} \ \cdots \ N_n^{el} \right\} \\ \{q_x\} &= \left\{ \frac{\partial N_1^{el}}{\partial x} \ \cdots \ \frac{\partial N_n^{el}}{\partial x} \right\} \\ \{q_y\} &= \left\{ \frac{\partial N_1^{el}}{\partial y} \ \cdots \ \frac{\partial N_n^{el}}{\partial y} \right\} \\ \{q_z\} &= \left\{ \frac{\partial N_1^{el}}{\partial z} \ \cdots \ \frac{\partial N_n^{el}}{\partial z} \right\} \end{aligned} \tag{5.30}$$

with these it is possible to calculate matrix $[B^{el}]$ for a given isoparametric coordinate. To obtain the element stiffness matrix $[K^{el}]$ a numerical Gauss integration needs to be performed.

Stiffness matrix $[K^{el}]$ can be written in general form as

$$[K^{el}] = \int_{V^{el}} [B^{el}]^T [E] [B^{el}] dV^{el}. \tag{5.31}$$

The above integration can be replaced by the numerical Gauss integration, that

$$[K^{el}] = \sum_{i=1}^{p_1}\sum_{j=1}^{p_2}\sum_{k=1}^{p_3} w_i w_j w_k [B_{ijk}^{el}]^T [E][B_{ijk}^{el}] J_{ijk}, \tag{5.32}$$

where p_1, p_2 and p_3 are the number of Gauss points with weights w and

$$[B_{ijk}^{el}] = [B^{el}(\xi_i, \eta_j, \zeta_k)] \quad J_{ijk} = detJ(\xi_i, \eta_j, \zeta_k). \tag{5.33}$$

5.2.3 Solving Linear Equations

In an ordinary FE solution for every load step the global stiffness matrix needs to be solved, which is simply the solving of a system of linear equations. This task can be divided into two different techniques: iterative and direct elimination. The fundamental difference is that iterative methods, such as the Gauss-Seidel, Jacobi and Conjugate Gradient Method result a solution vector close to the true solution with a prespecified error tolerance while the direct methods, such as Gauss and Cholesky, deliver a true result (in the mathematical sense). The main advantage of iterative techniques over direct methods is the reduced number of operations. Iterative techniques gain advantage over the latter when solving matrices with a high number of DoFs. As far as this research, a direct method was adopted and will be discussed in further detail in the following paragraph.

The simplest direct way would be to create the inverse of a stiffness matrix to solve for the unknown displacements. While this may be used for small size problems and has been used in lattice models such as Parrod (2002) it is clearly not useful for larger systems as the creation of this inverse matrix results into a fully occupied matrix. Thus, computation time and storage space of the decomposed matrix would increase dramatically.

Gauss Elimination

A quicker way of solving a system of linear equations can be performed with the Gauss elimination. The principal idea is to obtain the upper triangular matrix. Given the linear system of equations in matrix form $[A]\{x\} = \{b\}$ and applying

forward elimination, the following system

$$[A]\{x\} = \{b\} = \begin{bmatrix} 3 & 2 & 1 \\ 6 & 6 & 3 \\ 9 & 10 & 6 \end{bmatrix} \{x\} = \}b\} \tag{5.34}$$

results in

$$\begin{bmatrix} 3 & 2 & 1 \\ 0 & 2 & 1 \\ 0 & 0 & 1 \end{bmatrix} \{x\} = \{b\}\,. \tag{5.35}$$

Using backward substitution, thus working from the bottom up, the solution vector $\{x\}$ can be obtained.

LU and Cholesky Decomposition

With the Gauss elimination, the matrix $[A]$ can be decomposed into an upper and lower triangular matrix that $[A] = [L][U]$. The upper matrix is the same as the triangular matrix that was obtained as a result of the previous Gauss elimination (5.35). The lower one can be created by the factors that were used in the forward elimination. Thus, the previous example will look as follows:

$$[L][U] = \begin{bmatrix} 1 & 0 & 0 \\ 2 & 1 & 0 \\ 3 & 2 & 1 \end{bmatrix} \begin{bmatrix} 3 & 2 & 1 \\ 0 & 2 & 1 \\ 0 & 0 & 1 \end{bmatrix} \tag{5.36}$$

The decomposition process reduces to much smaller computational effort when the positive definite character of a common global stiffness matrix is considered. The process is then called Cholesky decomposition. Basically a given positive definite matrix, can be separated into the lower triangular part $[L]$ and its transposed form $[L]^T$.

$$[A] = [L][L]^T \tag{5.37}$$

To solve the set of linear equations $[A]\{x\} = \{b\}$ the system becomes:

$$[A]\{x\} = [L][L]^T\{x\} = \{b\} \Leftrightarrow \begin{cases} [L]\{y\} = \{b\} & (2), \\ [L]^T\{x\} = \{y\} & (1). \end{cases} \tag{5.38}$$

thus after the Cholesky decomposition, one only needs a quick forward substitution (1) to obtain $\{y\}$ and a final backward substitution (2) delivers the desired unknown vector $\{x\}$.

This makes it unnecessary to resolve the whole stiffness matrix $[A]$ again for a different load vector $\{b\}$. Only a forward and backward substitution is needed.

This is crucial for the MIF algorithm in *LAT3D*: instead of changing the whole global stiffness matrix only the force vector is adjusted to accommodate stiffness change of elements in a material nonlinear analysis of a lattice system (subsection 5.6.4).

The specific *MATLAB* function that operates on a sparse matrix is called 'ldlsparse'. The function delivers a complete Cholesky decomposition. Full details of the program code can be found in Gilbert et al. (1994).

5.2.4 Optimal Node Ordering

The order of stiffness relations among nodes in the global stiffness matrix has a great influence on the speed of solving the matrix. Several different algorithms can be found in the literature to reorder the matrix and save computation time. Examples are:

- Cuthill McKee (CM)
- Reverse Cuthill McKee (RCM)
- Approximate Minimum Degree (AMD)

Reverse Cuthill-McKee (RCM) vs. Cuthill-McKee (CM)

The CM algorithm along with its reversed form by Cuthill & McKee (1969) provides a simple scheme for reordering nodes. A brief comparison of the two schemes on a test network can be found in (Jennings & McKeown, 1992, p. 144). The results are presented in Table 5.2 and show the superiority of the RCM over the CM scheme in terms of storage and number of computational steps for the decomposition.

Approximate Minimum Degree (AMD)

In the program *LAT3D* the later developed approximate minimum degree ordering by Amestoy et al. (1996) is actually used, which works better for the Cholseky

Table 5.2: *Comparison of CM vs RCM (Jennings & McKeown, 1992).*

		hand numbering	CM	RCM
ring network	Storage requirements	56	61	55
	No. of multiplications for decomp.	102	124	98
triangulated network	Storage requirements	49	122	101
	No. of multiplications for decomp.	192	385	256

decomposition. A comparison of this ordering scheme vs. the RCM applied to a practical lattice problem is described below.

Comparison

Fig. 5.6 shows a comparison of the two different nodal ordering schemes. a) shows the original matrix created from the cleavage model (subsection 6.5.1). It consists of lattice and solid elements with nearly 10,000 DoFs. Besides the influence on the speed of the Cholesky decomposition, the nodal ordering has an effect on the efficiency of the forward and backward substitution. Eventually, the latter is more crucial for *LAT3D*, since the matrix is decomposed in most cases once (or only a few times) during the solution process. The measured times taken can be found in Table 5.3.

Table 5.3: *Comparison of different nodal orderings (on a test computer).*

nodal ordering	**Cholesky decomp.** time elapsed [s]	**forward/backward subst.** time elapsed [s]
none	151.49	4.15
RCM	20.82	3.10
AMD	26.12	0.84

The RCM algorithm produces a matrix with a narrow bandwidth which fills in almost completely during the Cholesky factorization. The Minimum degree ordering produces a structure with large loose blocks of zeros. Thus, the latter ordering requires less time and storage for the factorization.

The graphical representation of the differently ordered matrices from the solid-lattice model can be seen in Fig. 5.6. Since solid elements are connected to the lattice

only after the lattice elements are already defined (continuous node numbering), non-zero elements show up very far from from the diagonal, Fig. 5.6 a). This results after the Cholesky factorisation into a large number of non-zero elements, thus requires more computation time and storage.

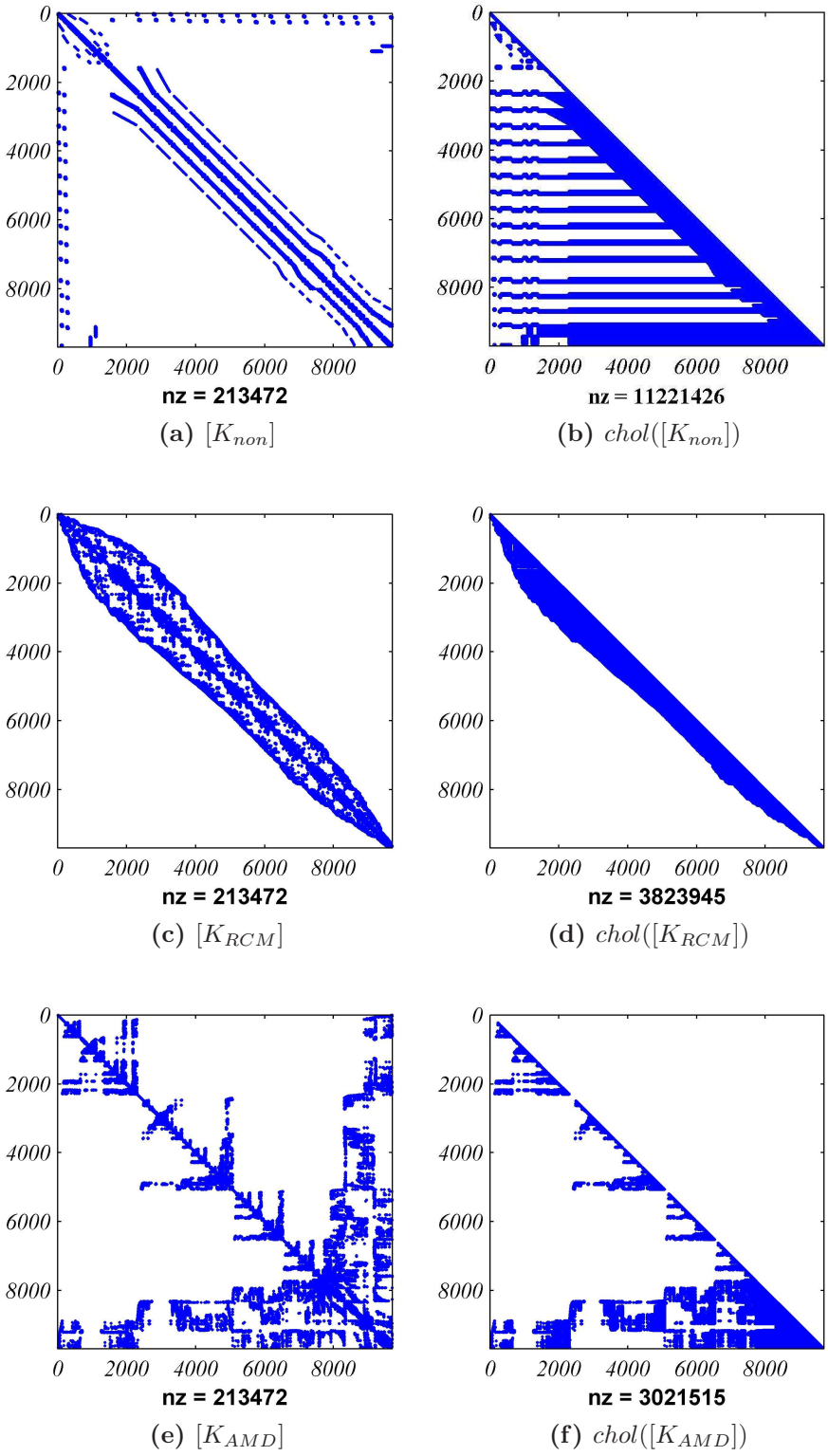

(a) $[K_{non}]$ **(b)** $chol([K_{non}])$

(c) $[K_{RCM}]$ **(d)** $chol([K_{RCM}])$

(e) $[K_{AMD}]$ **(f)** $chol([K_{AMD}])$

Figure 5.6: *Effect of different nodal ordering (non, RCM and AMD), differently ordered stiffness matrices of a sample model with 10,000* DoFs (left) and the corresponding Cholesky factorisation (right), number of non-zero (nz) elements is plotted.

5.2.5 Nonlinear Solution Algorithms

To obtain a more complete structural response of a system, nonlinearities have to be accounted for. The main origins of nonlinear behaviour in structural analyses are:

1. **Material Nonlinearity**
   Material changing its stiffness due to plasticity, cracking etc. (e.g. steel that deforms plastically after yielding)

2. **Geometric Nonlinearity**
   Structural parts that transmit stresses depending on their deformed state (e.g. rope which is being pulled taut)

3. **Contact Nonlinearity**
   Parts of an elastic structure come into contact with other (un)deformable parts and therefore transmit additional stresses (e.g. rubber tire in contact with the ground)

In an FE analysis, bulk nonlinear behaviour results from stiffness change of individual elements. Commonly the global stiffness matrix has to be repeatedly solved several times. Consequently the computational demand increases dramatically. Therefore, additional judgement on side of the engineer is required to choose if and what type(s) of nonlinear behaviour is to be accounted for and which solution algorithm is most appropriate.

In the following, a list of different approaches to solve nonlinear FE problems is presented.

Non-incremental Methods

Non-incremental methods such as the *Elastic Perfectly Brittle Lattice* method and the *Sequential Reduction* method were already discussed in the literature review and the reader is referred to subsection 3.3.4.

Incremental Methods

For the task to track a nonlinear solution path, two different incremental techniques can be distinguished: iterative and single-step.

In a typical nonlinear FE analysis the solution path is taken in small steps for which the resulting stiffness change is relatively small. Additionally, for iterative methods, iterations are performed at every load step to converge to a point that is relatively close to the true solution, i.e. with a negligible small imbalance of outer and inner forces.

Since a large part of this project has been dedicated to developing a quick and efficient solution algorithm, an overview of techniques shall be given. The following list consists of various methods described in more detail in McGuire et al. (2000, chap 12). In any incremental nonlinear solution algorithm a series of single load steps is applied while the global stiffness matrix is recalculated at each step. Mathematically this can be described as

$$\{P\} = \sum_{i=1}^{n} \{dP_i\} \tag{5.39}$$

with n as the number of load steps. Subsequently the displacement response is

$$\{\Delta\} = \sum_{i=1}^{n} \{d\Delta_i\} \tag{5.40}$$

The various methods are distinguished by the different linear analyses in between load steps, in other words if and how iterations are used.

Non-iterative: Euler and Runge-Kutta Method

As the simplest and most efficient algorithm, the non-iterative Euler method can be employed. The algorithm is depicted in Fig. 5.7 for one load step. For each load step i the global stiffness matrix $[K_i]$ is reassembled with the local stiffness matrices $[K^{el}]$ using the deformed geometry and corresponding element forces at the displacement $\{\Delta_i\}$. However depending strictly on the size of the load steps the obtained solution path will quickly diverge from the true solution, since errors accumulate per step.

The method can be further optimised by composing the global tangent stiffness matrix $[K_i]$ out of two or more tangential stiffness which are determined at certain sampling points. The number of points m determines the order of the method. A higher order will result in a better approximation of the true solution. E.g for a

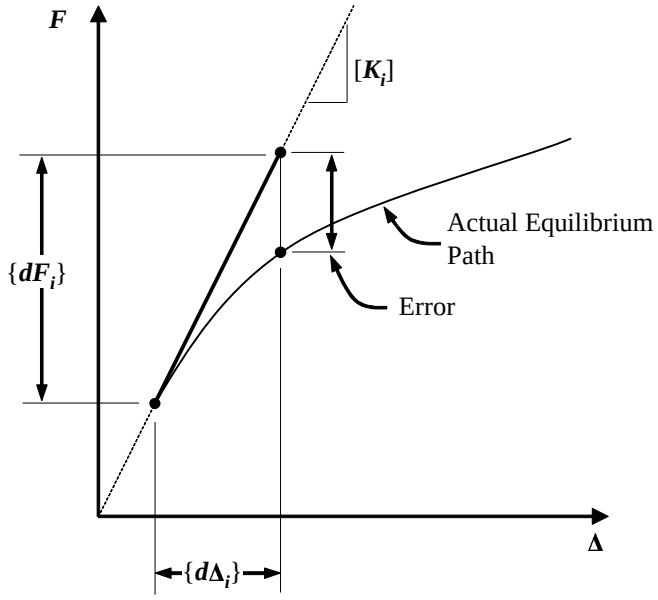

Figure 5.7: *Euler method.*

second order method, the tangential stiffness for the current load step i is taken as

$$[K_i] = \alpha_1[K_1] + \alpha_2[K_2] \tag{5.41}$$

where $[K_1]$ is the stiffness corresponding to the deformation and element forces at $\{\Delta_{i-1}\}$ and $[K_2]$ corresponds to the element forces at $\{\Delta_2\} = \{\Delta_{i-1}\} + \{d\Delta_\mu\}$. The two α values are used as different weights for the two different tangential stiffness.

Further, $\{d\Delta_\mu\}$ is obtained with an intermediate analysis step:

$$[K_1]\{d\Delta_\mu\} = \mu\{dF_i\} \text{ with } 0 < \mu \leq 1 \tag{5.42}$$

There are various forms of this method. The most well known is the Midpoint-Runge-Kutta version with $m = 2$, $\alpha_1 = 0$, $\alpha_2 = 1$ and $\mu = 0.5$. The process is depicted in Fig. 5.8.

Iterative: Newton Raphson

The Runge-Kutta, and especially the Euler method, greatly depend on the number of load steps that are taken. However, as mentioned before, depending on the

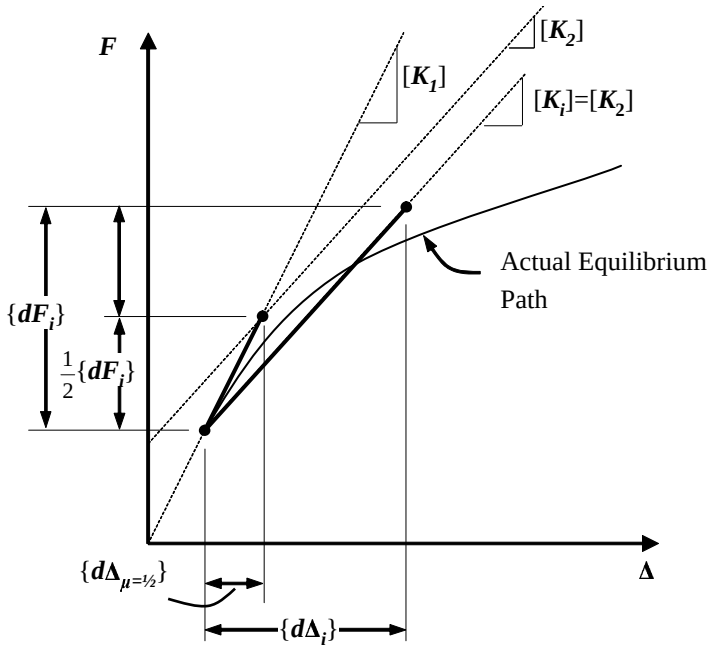

Figure 5.8: *Midpoint-Runge-Kutta method.*

complexity of the exact solution, the load-displacement curve obtained with the Euler method might quickly diverge. Errors accumulate after each load step, thus the internal forces do not balance the outer applied forces. Even with several sampling points the error will accumulate without means to control the imbalance.

Thus, the method can be further improved by taking iterative steps in between load steps. This is done with the Newton-Raphson algorithm. Each load step consists of several iterations as seen in Fig. 5.9.

The method can be modified in order to reduce the computational costs by reusing the tangential stiffness matrix in one load step. The method then becomes the 'Modified Newton-Raphson' algorithm.

For complex load-displacement behaviour special load step control methods such as the arc-length can be used. This is especially necessary for lattice models when dealing with 'snap-back', as mentioned in Gonzalez & Llorca (2007) and Jirasek & Bazant (1995).

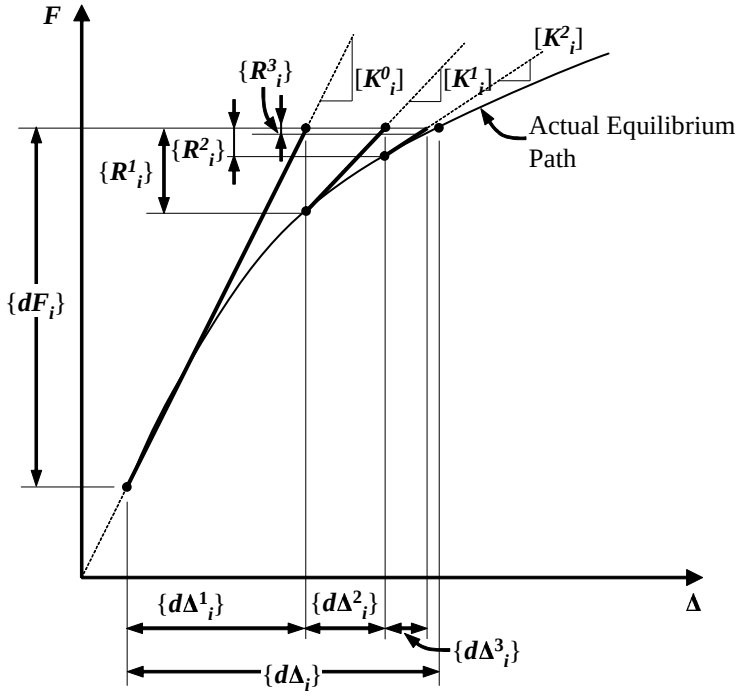

Figure 5.9: *Newton-Raphson method.*

5.3 The MATLAB Environment

The software package *MATLAB* (The MathWorks, Inc., 2007) was chosen as a development environment for writing the *LAT3D* program. *Technical Computing with MATLAB* provides a very user-friendly programming and debugging interface, along with a number of built-in functions for performing tasks such as matrix computations, statistical analysis, function optimisation, plotting graphics and file handling.

New functions (commonly separate *MATLAB* files) can be written, each with input and output parameters of various types. Thus, a complete program consists of several files as 'sub'-functions that can be further used in future projects. In the following, a short listing shall exemplify the function of the very concise *MATLAB* code. Among others, the principal variable type that is used within *MATLAB* is the n-dimensional matrix, which can be manipulated with very short commands.

5.3.1 Matrix Operations in MATLAB

The function *'Chessboard2D.m'* shown in Lst. 5.1 creates a square matrix of given size n with ones and zeros arranged in a checked pattern. The function is needed in *LAT3D* for generating a lattice with a nodal pattern of this particular shape (section 5.4).

After several lines of remarks, *MATLAB* creates a vector $\{C\}$ containing a series from 1 to n (Line 8). After calculating the remainder of $\{C\}$ *mod* 2 one obtains a vector with alternating ones and zeros (Line 9). The vector is then multiplied with a row of ones of the same size in order to extent $\{C\}$ to a matrix of n $\{C\}$s (Line 10). The matrix $[C]$ is added to its transposed form $[C]^T$ (Line 11). And finally the redundant '$2s$' need to be eliminated by element wise multiplying the negative of 'mask'-matrix $[C_2]$. Finally,

$$\begin{bmatrix} 1 & 0 & 1 & 0 & \cdots \\ 0 & 1 & 0 & 1 & \\ 1 & 0 & 1 & 0 & \\ 0 & 1 & 0 & 1 & \\ \vdots & & & & \ddots \end{bmatrix} \tag{5.43}$$

is the resulting matrix $[C]$.

Listing 5.1: *Source Code 'Chessboard2D.m'.*

```
function C = Chessboard2D(size)
%PURPOSE:
%   creates chessboard-like patterned matrix
%INPUT:
%   size... size of square output matrix C
%OUTPUT:
%   C...    chessboard matrix with ones and zeros
C = (1:size);
C = mod(C,2);
C = ones(size,1)*C;
C = C+¬C';
C_2 = (C==2);
C = ¬C_2.*C;
end
```

The actual code which is implemented in *LAT3D* is somewhat more complicated, as the resulting matrix has three dimensions and 'filling' rows and columns of zeros in between the original matrix.

5.3.2 Simplex Algorithm

In subsequent sections of this chapter the Nelder-Mead method, also known as downhill simplex method, an effective nonlinear optimisation algorithm, was used to determine parameters by minimising a target function. The algorithm was developed by Nelder & Mead (1965). It is an already in-built function within the *MATLAB* programming language. Since it was used during this project several times, it shall be explained in more detail here.

For a problem with n-parameters, a $(n+1)$-simplex[1] is created. Each node of this simplex represents a solution on the target function at assumed parameters. Thus $(n+1)$ sets of n parameters have to be guessed at the beginning. In *MATLAB* only one starting point is assumed while the function then estimates the remaining start nodes automatically.

[1] generalised triangle in n dimensions: e.g. triangle (2-simplex), tetrahedron (3-simplex) and pentachoron (4-simplex)

In this study the algorithm has been used for determining the optimal (possible) elastic stiffness parameters K_j of the lattice cell elements that suit the bulk elastic parameters of Sitka spruce best (subsection 6.3). It further contributed to create a standard density profile for this timber species from density measurements (subsection 5.5.2). It also could be used to automate the calibration of strength parameters of the lattice as done in similar research (Vasic, 2000).

5.4 Lattice Parameters

This section shall explain in more detail the workings of the lattice cells and the parameters which need to be defined.

The 3D lattice model used in this project consists of six different link types: three links acting in the longitudinal X, lateral Y and Z direction and three diagonals acting in shear in the planes YX, ZX and YZ (Fig. 5.10). Each of these has different sets of parameters that define a tri-linear load-displacement relation. The required values are the initial mean stiffness $\overline{K}_{①,j}$, mean strength parameters in tension $\overline{S}_{T,j}$ and in compression $\overline{S}_{C,j}$. Additionally, post yield (PY) parameters are needed such as, $\gamma_{T,j}$ and $\gamma_{C,j}$, which define the gradient of the tensile and compressive softening branch.

By default the values for all tensile parameters and for shear links also in compression are close to 1 ($\gamma_{T,j} > 1$, $\gamma_{C,j} > 1$ for $j = XY, YZ, XZ$), thus no microductility is considered, i.e. perfect microbrittle behaviour. The compression PY parameter $\gamma_{C,j}$ is set for the longitudinal $j = X$ and lateral $j = Y = Z$ links to a specific positive value ($0 < \gamma_{C,j} \leq < 1$), which is adjusted further in the calibration process (result chapter 6).

While any distribution function can be applied to the randomisation of the lattice properties, for the program *LAT3D* a normal distribution for stiffness parameters and a log-normal distribution for strength parameters was used. Normal distributions are also used in previous lattice models as described in Landis et al. (2002) and Davids et al. (2003). Additionally, the log-normal distribution for strength properties was chosen in order to circumvent the problem of negative strength values which would occur otherwise.

Fig. 5.11 displays the parameter definitions. The mean strength and stiffness values for an individual link are later adjusted according to the wood morphology that is mapped onto the lattice. This is described in more detail in the following section.

The spacing of the lattice grid was chosen based on the existing heterogeneity at the level of the growth ring structure. Variation in properties is later mapped onto the lattice of the cell size of 2x1x1 mm (dx x dy x dz). This size results from a balance between acceptable computational effort for larger lattices and represented detail of

the growth ring structure. The mean ring width measured from test specimens has been 5.47 mm, with a COV of 24.8%. Specimens with ring width less than 2 mm were discarded. This ensures that one growth ring encompasses at least two lattice cells.

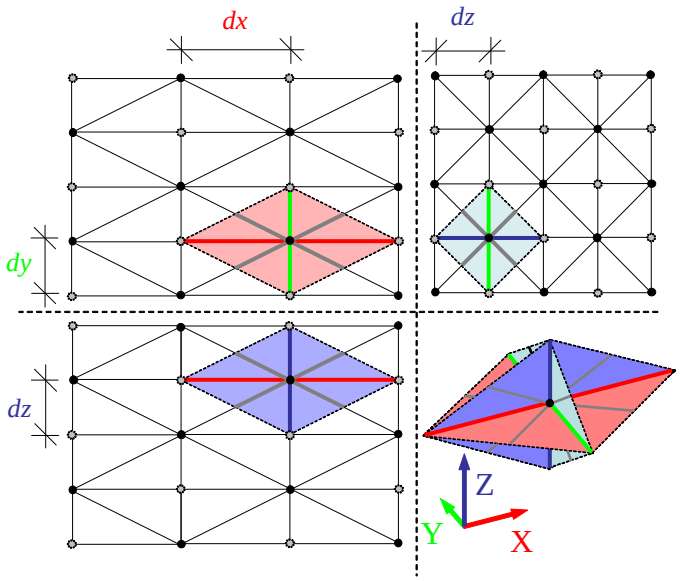

Figure 5.10: *Cell structure viewed in the three material planes (left), one unit cell consisting of 'half'-links (right). Note: grey nodes are shown for presentation purpose of the grid, they are not real nodes with DoFs (original in colour).*

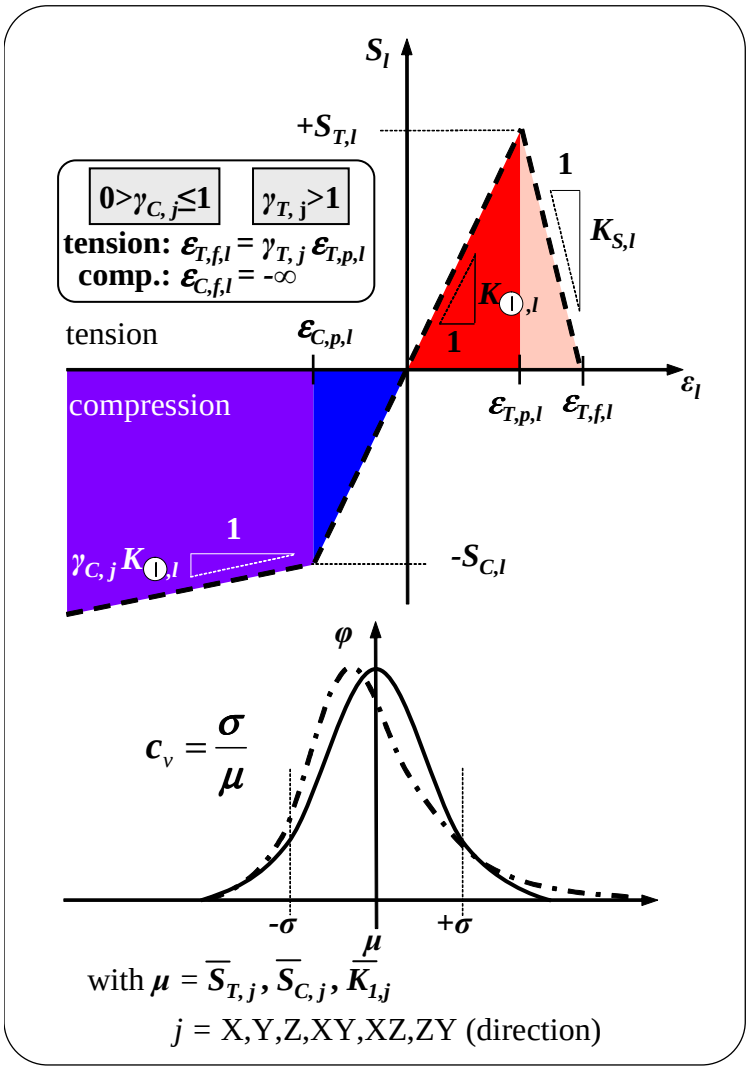

Figure 5.11: *Parameters defining the load-displacement relation of link l with: initial link stiffness $K_{①,l}$, strength parameters in tension $S_{T,l}$ and compression $S_{C,l}$ and softening branch defined by $\gamma_{C,j}$ and $\gamma_{T,j}$ for a link type j in compression and tension respectively (above). In the bottom figure a normal distribution (solid) and respectively log-normal (dashed) distribution is assigned to the link parameters. For different link type j mean values $\overline{K}_{①,j}$, $\overline{S}_{T,j}$ and $\overline{S}_{C,j}$ and their coefficients of variation $c_{v,j}$ need to be defined (original in colour).*

5.5 Incorporated Wood Structure

Details of the wood's morphology was already discussed in the literature review in chapter 3. The focus of this section is on how the wood morphology is implemented into the lattice concept.

It was the aim of this research to account for some of the strength and stiffness variation. Since density is the major driving factor of this variation besides several other properties, density profiles were obtained and characterised. By recreating random profiles based on the obtained characteristics these can then be mapped onto the lattice elements. This included changing the mean stiffness values and strength values according to the position of the respective link in an artificially created growth ring structure.

With the mapped variation realistic fracture paths can be predicted. These paths are obviously directed by variation of properties within the growth rings as it can be observed in tested samples where fracture tends to follow weaker areas.

For simplicity, and as an initial estimate, a one-to-one correlation between the variation in density and the stiffness and strength properties is assumed. However, this can further be refined by adjusting a factor in the model input file.

5.5.1 Structure Profiling

As a first step, the meso scale structure of the mechanically tested samples needs to be characterised. For this purpose scans were taken of the cross-sectional surface of the test specimens to obtain the growth ring structure (Fig. 5.12). This was done for both sides (front and back) with an ordinary flatbed scanner. A program written in *MATLAB* ('GrowthRingDetection.m') served as an interface for the user to draw three-point circles onto the visible rings in the scans. By averaging the centre of these circles, each side separately, the assumed pith position was obtained. The actual averaging process was weighted, where marked 3-point circles with a larger angle of arc were given greater weights than small angles. Thus, a closer approximation (several circles assuming one centre) of the existing growth rings was obtained. The first and last ring (leaping outside of the sample's cross-section) that are later required when recreating the full profile filling the box entirely, are

simply extensions of the previous ring, i.e rings with the same ring width as the previously last one are added at both ends.

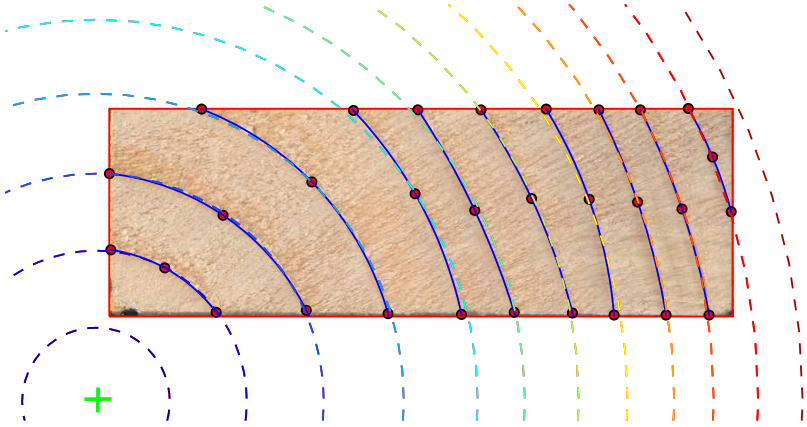

Figure 5.12: *Scans of the cross-section of tested specimens were taken and three-point circles were drawn by the user (blue lines with red markers). After the averaged centre of the rings was determined (green cross) growth ring circles were redrawn (coloured lines) (original in colour).*

From these rings, and the assumed pith position, several parameters can be calculated, which then identify the characteristics of a certain ring structure, Fig. 5.13. First, there is the length of the pith vector starting at the centre of the sample's cross-section to the pith position r_{pith} and the angle between this vector and the Z coordinate axis. Second, the radius r_n to each ring n can be obtained. Further, the ring widths can be calculated by $\Delta r_n = r_n - r_{n-1}$ and the difference in width of a ring to its previous one $\Delta r_{diff,n} = \Delta r_n - \Delta r_{n-1}$. There are two parameters which put the position of the ring structure into relation to the centre of the sample's cross-section. These are Δr_{centre} which is the width of the central ring and $\overline{r}_{shift}$ which is the normalised position of the sample's centre in relation to the central growth ring. The latter is calculated by

$$\overline{r}_{shift} = \frac{r_{shift}}{\Delta r_{centre}}. \tag{5.44}$$

The last parameter r_{var} defines the difference in radius of the front side growth ring to the corresponding ring on the back side of the sample. The parameter is calculated for each ring and averaged per sample. This accounts for the variation in rings seen from different sides of the specimen (the saw cut is never perfectly aligned with the growth rings).

After having determined the parameters for all tested samples of **one** test series (tension, compression, shear and cleavage tests), the average and coefficient of variation is then calculated. They can serve now as an input for recreating a ring structure for one model series and are inputted via the model input file in the section *$WOODSTRUCT*.

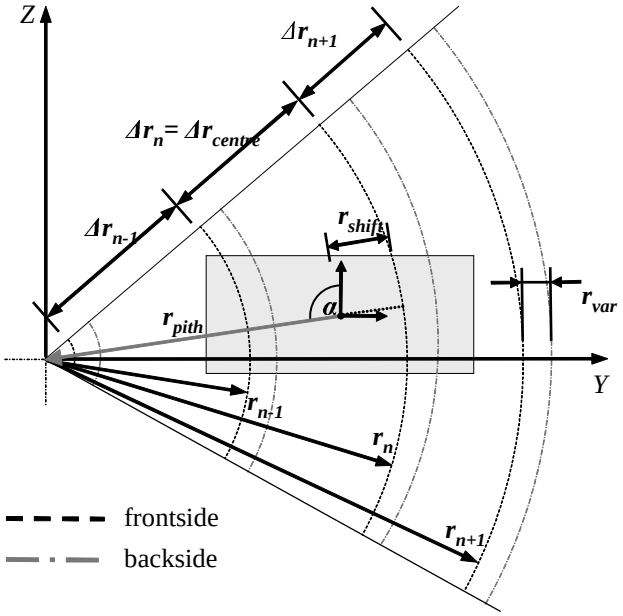

Figure 5.13: *Schematic of the identified growth ring structure, with several parameters.*

5.5.2 Density Profiling

As a collaborative work between Glasgow University and Napier University, density profiles were sampled. Although, samples were taken from a different progeny than the later mechanically tested specimens, the profile is assumed to be representative for the species Sitka spruce (*Picea sitchensis*). First, samples were cut from this species grown at Kershope, Northumbria, UK. They were felled when 36 years old. Radial density profiles have been measured at a resolution of 50 microns in the longitudinal direction on 2 mm thick samples with an Itrax density scanner (Cox Analytical Systems, Sweden) at 0% R.H.. The system was calibrated with a stepped cellulose propionate wedge. All the experimental measurements were published in McLean (2007). These obtained density profiles were then normailised over the average density of the sample to reflect only the variation. The resulting graph of one sample can be seen in Fig. 5.14.

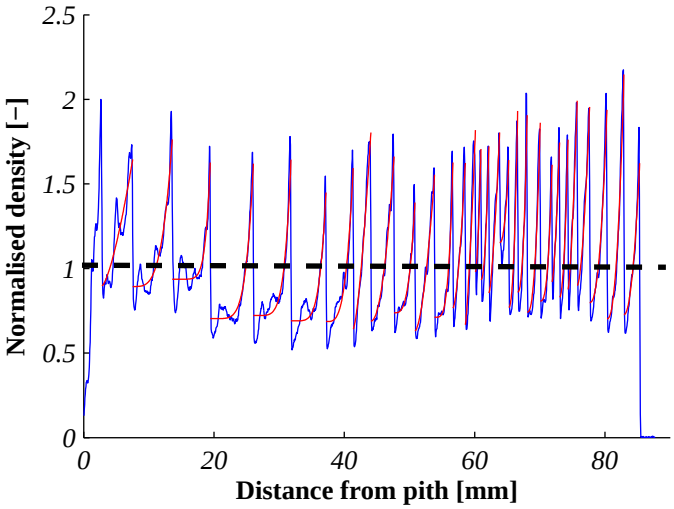

Figure 5.14: *Normalised density profile of a Sitka spruce sample, ranging from pith to bark (blue line). Fitted curves (red line) (original in colour).*

The transition from late to earlywood can clearly be seen as a sharp drop in density. This pattern repeats and additionally a tendency of decreasing ring widths can be observed towards the bark. To characterise the curve in between the peaks a power function was fitted. Thus, the overall function for several rings n can be described by

$$\overline{\rho}(r) = \overline{\rho}_{diff,n} \left(\frac{r - r_n}{r_{n+1} - r_n} \right)^{\overline{\rho}_{exp,n}+1} + \overline{\rho}_{min,n} \quad \text{for} \quad r_n < r \leq r_{n+1}, \tag{5.45}$$

where $\overline{\rho}$ stands for the normalised density at radius r. r_n is the radius at the peak of growth ring n. $\overline{\rho}_{diff,n}$, $\overline{\rho}_{min,n}$ and $\overline{\rho}_{exp,n}$ are parameters defining the power function in height, offset and curvature.

A target function of the sum of squared errors between power function and dataset was established and minimised for several samples with the simplex algorithm, described in subsection 5.3.2. After this curve fitting, the average values and the coefficients of variation of the three parameters can be calculated.

It should be noted, that only growth ring sizes that matched the ring widths in samples that were used in mechanical tests later were taken into account. Thus, since samples for the mechanical tests were sorted for ring widths not less than 2mm, growth rings in the profile smaller than this were discarded as well.

5.5.3 Mapping Density Variation

So far, two parameter types were determined: a) a standardised density profile with its mean parameters and c_vs per growth ring and b) the ring parameters taken from the scans and averaged for each test series (tension, compression, cleavage and shear tests) along with their c_vs. These parameters serve now as an input to recreate a ring structure that is reflecting the original ones from the test samples and a density profile that shall be representative for Sitka spruce.

The idea is to change the mean strength $\overline{S}_{T,l}$, $\overline{S}_{C,l}$ and stiffness $\overline{K}_{0,l}$ values for each individual link l of the newly created lattice model according to its position in this artificially generated ring profile. Note: a general variation with a $c_{v,j}$ of 0.2 for $j = X..YZ$ is already set without the structured heterogeneity that is applied here.

As seen in Fig. 5.16, rings are generated consisting of a pith and concentric circles r'_n in relation to the YZ-plane of the model (grey box representing a cross-section of the lattice). Further, the density profile can be pictured as a three-dimensional graph with peaks at high densities that form concentric rings. Each link represents a certain cross-sectional area cut into this topography. This 'cut-out' can be calculated with a double integral over the density function within the area A_j and limits $l_{y,j}$ and $l_{z,j}$ according to Table 5.4 for link type j. The density variation for link l with vector $P_l(y_c, z_c)$ from the origin can be calculated as follows

$$\overline{\rho}_l(x_c, y_c, z_c) = \frac{1}{A_j} \int_{y_c - \frac{1}{2} l_{y,j}}^{y_c + \frac{1}{2} l_{y,j}} \int_{z_c - \frac{1}{2} l_{z,j}}^{z_c + \frac{1}{2} l_{z,j}} \overline{\rho}(x_c, y, z) dz dy. \tag{5.46}$$

Note, that the profile calculated below this area has to be divided by the same area to solely obtain the variation in density.

The actual density function $\overline{\rho}(x, y, z)$ varies along the X axis since the different radii r_{var} between front and back side need to be considered. However, the density function is actually calculated at a specific point x_c along the X axis. This is done by creating radii $r'_n(x)$ at position x_c as an interpolation between radii $r_{n,back}$ at the back side and $r_{n,front}$ at the front side, Fig. 5.15. The variation from front to back is merely a constant shift in radius from front to back side. The back side radii are simply calculated with the randomly created parameter r_{var}

$$r_{n,back} = r_{n,front} + r_{var} \tag{5.47}$$

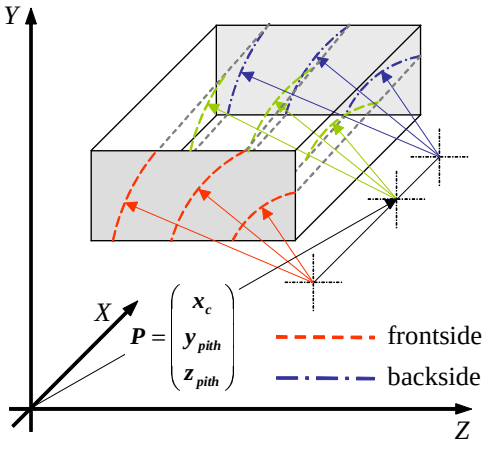

Figure 5.15: *Interpolation of radii (green) in between front (red) and back (blue) side growth rings (original in colour).*

The density function $\overline{\rho}(x_c, y, z)$ is expressed as depending on (x_c, y, z), while the original function depends on $r'(x_c)$. However, the function can be easily transformed via Pythagoras's theorem:

$$\overline{\rho}(x_c, y, z) = \overline{\rho}\left(r'(x_c)\right) = \overline{\rho}\left(\sqrt[2]{y^2 + z^2}, (x_c)\right). \tag{5.48}$$

Since the density function is discontinuous over the growth rings r'_n and r'_{n+1}, the in-built *MATLAB* function 'quad.m' was used for the integration process. It is based on the Simpson's Rule for numerical integration and can cope with any discontinuity. A description of this function can be found in Gander & Gautschi (2000).

Table 5.4: *Cross-sectional area represented by link types.*

link type j	**limit values** $l_{y,j}$	**limit values** $l_{z,j}$	**area** A_j
X (longitudinal)	$\pm\frac{1}{2}dz$	$\pm\frac{1}{2}dy$	$dydz$
Y (lateral)	$\pm\frac{1}{2}dz$	$\pm dy$	$2dydz$
Z (lateral)	$\pm dz$	$\pm\frac{1}{2}dy$	$2dydz$
XY (diagonal)	$\pm\frac{1}{2}dz$	$\pm\frac{1}{2}dy$	$dydz$
XZ (diagonal)	$\pm\frac{1}{2}dz$	$\pm\frac{1}{2}dy$	$dydz$
YZ (diagonal)	$\pm\frac{1}{2}dz$	$\pm\frac{1}{2}dy$	$dydz$

Fig. 5.16 shows this whole process for a lateral link l of type $j = Y$.

After $\overline{\rho}_l(x_c, y_c, z_c)$ is determined, which shall serve as a measure of strength and stiffness variation of link l. The mean strength and stiffness value for this specific

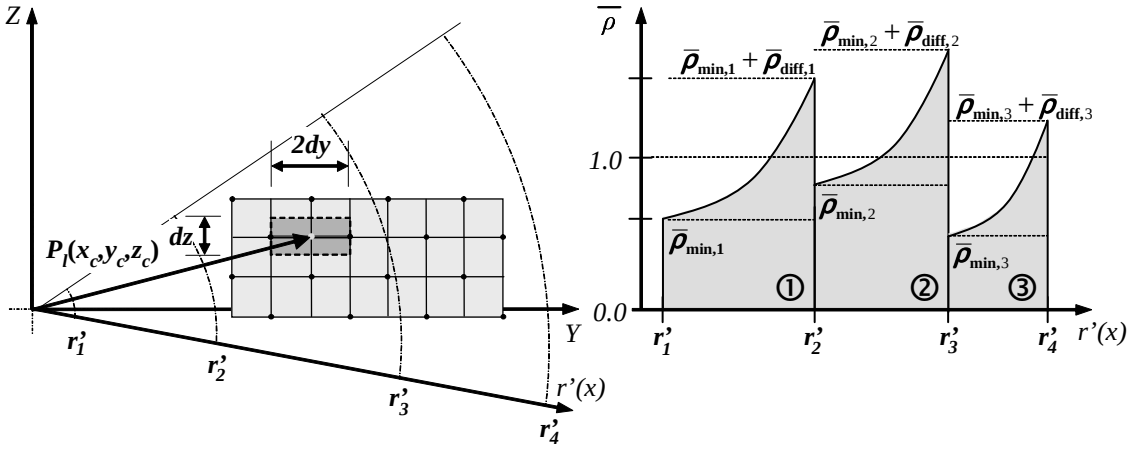

Figure 5.16: *Ring structure with lattice (left) and density profile to be mapped (right).*

link l can be adjusted according to

$$\begin{aligned} \overline{S}_{T,j,l} &= [(\overline{\rho}_l - 1)\lambda_{T,j} + 1]\overline{S}_{T,j} \\ \overline{S}_{C,j,l} &= [(\overline{\rho}_l - 1)\lambda_{C,j} + 1]\overline{S}_{C,j} \\ \overline{K}_{j,l} &= [(\overline{\rho}_l - 1)\lambda_{K,j} + 1]\overline{K}_j. \end{aligned} \tag{5.49}$$

The λ_j values are parameters, set in the model input file, for further fine tuning the influence of density variation in the artificial growth ring structure. E.g. set to zero, no stiffness and strength variation is introduced to the lattice links. Their default value is set to 1, thus the former equations simplify to

$$\begin{aligned} \overline{S}_{T,j,l} &= \overline{\rho}_l \overline{S}_{T,j} \\ \overline{S}_{C,j,l} &= \overline{\rho}_l \overline{S}_{C,j} \\ \overline{K}_{j,l} &= \overline{\rho}_l \overline{K}_j. \end{aligned} \tag{5.50}$$

After *LAT3D* went through all link elements l in a lattice and thus as well all different link types ($j = X, Y, Z, XY, XZ, YZ$), the result looks as seen in Fig. 5.17. The colour of the lines represents the relative tensile strength value $S_{T,j,l}/\overline{S}_{T,j}$ for each link l and link type j. Note, that the figure would look exactly the same if compressive strength or stiffness values were considered, provided that λ_j=1 (default). Only the outer surface of this lattice is shown.

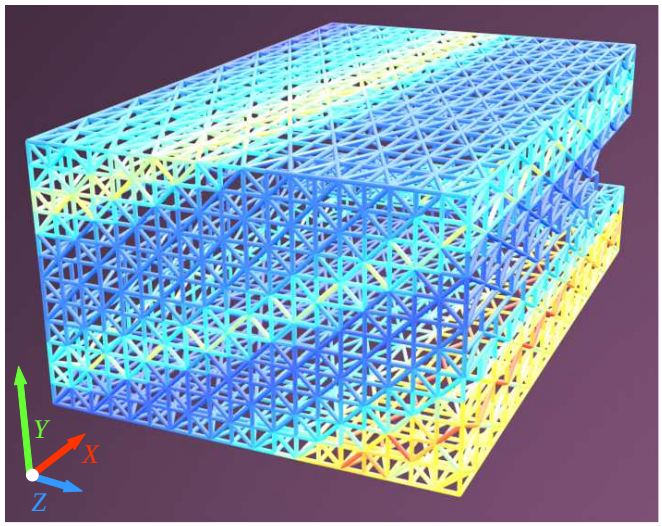

Figure 5.17: *Structured lattice, showing variation in tensile strength (with morphology mapped onto lattice and* $c_{v,j} = 0.2$ *for* $j = X..YZ$*, blue shows lower and red higher strength values, original in colour).*

5.6 FE Implementation in LAT3D

As mentioned in the Literature Review (section 3.3.4) no traditional algorithm (Newton-Raphson, ArcLength-Method etc.) can handle the jagged nature of the nonlinear solution path very well for lattice models. A new method was found in (Jirasek & Bazant, 1995). Rather than iterating towards an admissible solution, the Step-Size-Control (SSC) method treats the overall load-displacement curve as the sum of single linear steps. In each step only one link changes its stiffness. Thus, it is possible to overcome the problems that result from the 'snap-back' phenomena and, additionally, plastic deformation can be accounted for. A drawback of the method is that for large lattice systems the number of load steps amounts to at least the number of broken/changed links. However, no additional iterations are needed. In contrast iterative methods such as Newton-Raphson can require an indefinite number of iterations and might, in certain circumstances, not come to an admissible solution at all.

Furthermore, using the Method of Inelastic Forces (MIF), these load steps require significantly less time to compute. In the following subsections the two methods will be explained in more detail. However, when plastic hardening links are considered, the SSC algorithm has its problems due to the large number of elements that switch to the plastic state.

5.6.1 Original Step-Size-Control (SSC) Algorithm

As described previously, the 3D lattice that is used in this thesis (program *LAT3D*) consists of single link elements that transfer tensile and compressive loads. The stress-strain or respectively load-displacement relation of these links consist of a tri-linear curve. The basic principle, underlying the SSC algorithm, states that loads are applied to the lattice structure in a manner that only one link changes its stiffness in one load step. Thus, after each step i the load factor $\lambda_{i,l}$ is calculated for every link l that is required to bring the respective link into another 'stiffness state' and thus change the respective stiffness. The smallest value is chosen, and the respective link changes its stiffness.

In short this is described by,

$$[K_i]\{\Delta_i\} = \lambda_i\{F_{ref}\}, \tag{5.51}$$

where λ_i is chosen to be $\lambda_{i,l}$ of link l for which the stiffness is changing. This factor is calculated with the previous strain, the critical strain value $\epsilon_{cr,l}$ described in Table 5.5 and the strain increment $d\epsilon_{i,l}$ for link l. (Equation 5.53)

$$\lambda_{i,l} = \frac{\epsilon_{cr,l} - \epsilon_{i-1,l}}{d\epsilon_{i,l}} \tag{5.52}$$

The strain increment of link l in step i can be calculated as

$$\begin{pmatrix} d\epsilon_{i,l} \\ 0 \\ 0 \end{pmatrix} = \frac{1}{len_l} \left[[R_l] \begin{pmatrix} \Delta_{i,l,II,x,ref} \\ \Delta_{i,l,II,y,ref} \\ \Delta_{i,l,II,z,ref} \end{pmatrix} - [R_l] \begin{pmatrix} \Delta_{i,l,I,x,ref} \\ \Delta_{i,l,I,y,ref} \\ \Delta_{i,l,I,z,ref} \end{pmatrix} \right], \tag{5.53}$$

with the obtained nodal reference displacements $\Delta_{i,l,ref}$ for link l, with two nodes I and II and the element rotation matrix $[R_l]$. The reference displacement is the displacement Δ_i calculated for $\lambda_i = 1$.

The possible stiffness states for a microductile brittle link (bi-linear load-displacement curve) are: ① for the initial stiffness, ② for softening, ④ for broken and ⑤ for reloading after 'damage'. The respective load-displacement relation can be seen in Fig. 5.18.

As a first attempt, one can simply choose in each load step i the minimum positive $\lambda_{i,l}$ for link l as the load factor λ_i which brings one of the links into the next status state. However, due to the negative stiffness for the softening branch in the load-displacement curve, a negative load step might be required. This is determined based on whether the strain (while the link is in the softening branch, status ②) in one load step is or is not consistent with the assumed status. If it is not, the respective links have to be switched to unloading (state ③) and thus the link's stiffness changes as well. Since in this case, the change is only known *after* the load step, an 'iteration of status' must be done. Therefore, an extra temporary status is assigned (status ⑤). This is done when the strain increment $d\epsilon_{i,l}$ for link l is not consistent with the assumed status in the softening branch (positive in case of softening, and negative in the case of reloading).

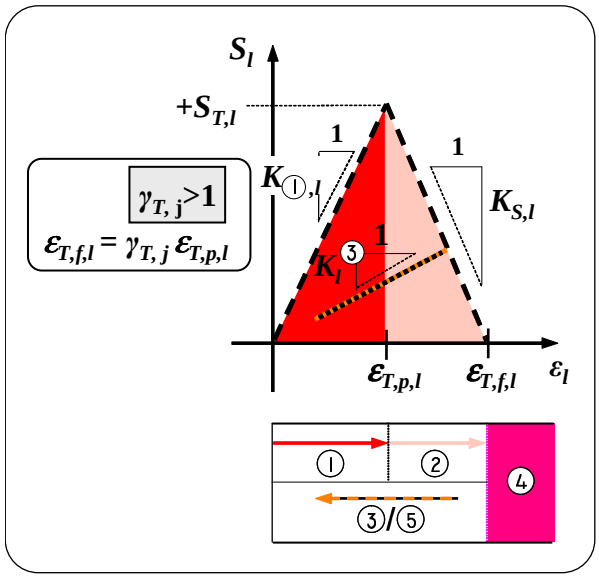

Figure 5.18: *Definition of different link states of link l as described in the original SSC algorithm (original in colour).*

For this temporary status ⑤ a new stiffness needs to be calculated with the current strain (Fig. 5.19, dotted lines). However, it could be the case that with the newly calculated stiffness in the next iteration still some links are not consistent with their assumed strain increment, thus this step has to be repeated until all links are consistent. This in turn would require trying all possible combinations of unloading and softening links, and thus would be very inefficient.

A better solution can be found if one checks the number of consistent and inconsistent links and base the decision of a positive or negative load step on whichever number is higher. Thus, the iteration is only taken once. After this step all links with status ⑤ are transferred to ③ and a new load step $i = i+1$ starts.

The original SSC algorithm is summarised in Algorithm 3.

The original example from Jirasek & Bazant (1995) with the detailed calculations can be found in the Appendix A.1.1 and a modified version with more brittle links in A.1.3.

Furthermore, it could be the case that during the algorithm several links require the identical load factor to be transferred into the next status (e.g. $\lambda^+_{1,i} = \lambda^+_{2,i}$ for links 1 and 2). This needs to be considered in a way that therefore several links are

allowed to change in one step.

Algorithm 3 Step-Size-Control (SSC).

for load step i

repeat
  determine reference displacement $\Delta_{i,ref}$ with MIF
  determine strain increment $d\epsilon_{i,l}$ for all links l:
  calculate load factor $\lambda_{i,l}$ with critical strain $\epsilon_{cr,l}$ for all links l:
  if only positive $\lambda_{i,l}$ **then**
    $\lambda_i = min(\lambda_{i,l})$
    $l_i = l$ for which $\lambda_{i,l} = \lambda_i$
  else
    $\lambda_i^+ = min(\lambda_{i,l} > 0)$
    $\lambda_i^- = max(\lambda_{i,l} < 0)$
    mask links with status (2) and (5)
    $n_{consistent} = \sum d\epsilon_{i,l=(2)} > 0 + \sum d\epsilon_{i,l=(5)} < 0$
    $n_{inconsistent} = \sum d\epsilon_{i,l=(2)} < 0 + \sum d\epsilon_{i,l=(5)} > 0$
    if $n_{consistent} > n_{inconsistent}$ **then**
      $\lambda_i = \lambda_i^+$
      $l_i = l$ for which $\lambda_{i,l} = \lambda_i^+$
      change all links $n_{inconsistent}$, (2) to (5) and (5) to (2)
    else
      $\lambda_i = \lambda_i^-$
      $l_i = l$ for which $\lambda_{i,l} = \lambda_i^-$
      change all $n_{consistent}$, (2) to (5) and (5) to (2)
    end if
    recalculate K_l for links $l =$(5)
  end if
until second iteration or no iteration is required
change status and K_l for link $l = l_i$
$\{F_i\} = \{F_{i-1}\} + \lambda_i\{F_{ref}\}$
$\{\Delta_i\} = \{\Delta_{i-1}\} + \lambda_i\{\Delta_{i,ref}\}$
$\epsilon_{i,l} = \epsilon_{i-1,l} + \lambda_i d\epsilon_{i,l}$ all links l

5.6.2 Extension of the SSC Algorithm

The original SSC algorithm, as described in Jirasek & Bazant (1995), treats only links with a bi-linear load-displacement curve (no stiffness change in compression). This is extended in *LAT3D* to accommodate a softening branch in compression as well. Therefore, new link states are added to the existing method for the respective stiffness changes. These are simply the negative version of the already described states (namely $-$①, $-$②, $-$③ and $-$⑤) and are simply the mirrored version of their positive counterparts (only for a negative strain). Furthermore, an additional load factor calculated from an 'alternative' critical strain has to be considered for links with status $\pm$①. This is due to the fact that these links can change to both states: ② and -② depending on the strain increment and sign of the chosen load factor. Table 5.5) lists these alternative critical strains for the respective link states. An example of the workings of this extended SSC algorithm can be found in the Appendix A.1.2

The algorithm is further extended to take into account a plastic response for links under compression with the new states $-$⑫, $-$⑬ and $-$⑮ as seen in Fig. 5.19. Likewise to their brittle counterparts ($-$②, $-$③ and $-$⑤) the status is changed for links whose status is inconsistent to the strain increment in case of a positive load step and for links that are consistent in case of a negative load step. An additional iteration is also required when the link switches to state -⑮ similar to the other states $\pm$⑤ in the previous version. The only difference is that these plastically compressed links are not considered in the decision whether to take a positive or negative load step This is due to the fact that the stiffness after the change remains positive and thus a negative load step is not required. The defined load-displacement curve with the different link states for the extended version of the SSC is depicted in Fig. 5.19. An example can be found in the Appendix A.1.4 and in combination with also brittle links in A.1.5.

Furthermore, in case of status $\pm$⑤, $\pm$③, $-$⑮ and $-$⑬, alternative critical strains are used for situations where unloading links move from tension to compression and vice versa in one single step. This is depicted for link l in Fig. 5.22. The critical strain values and the subsequent status change is listed in the lower part of Table 5.5. A compressed link l switches from softening -② to unloading ($-$⑤ and subsequently $-$③). The alternative critical strain for a link status change in case of a positive strain increment is $\epsilon_{T,p,l}$. In such case the strength parameter

of the opposite compression or tension side needs to be reduced in order for the possible loading state to remain inside the defined load-displacement curve. This can be seen in Fig. 5.22 on the tensile side for $S_{T,l}$ to $S'_{T,l}$. Along with this change, the softening stiffness $K_{S,l}$ needs to be adjusted to $K'_{S,l}$. This behaviour only occurs for more complex lattice structures with e.g. diagonals and is therefore not demonstrated in the Appendix.

Another change made to the original SSC algorithm is the different critical strain value for links with status $\pm$(5) and $-$(15). In the original version, in these cases, the critical strain value was the current strain ϵ_l. Thus, the link changes from e.g. (5) first automatically to (3) with a load factor of 0 ($min\lambda_i = 0$ was allowed). This led to a problem that the algorithm got stuck when compressed links with plastic hardening were considered. Therefore, a load factor of 0 was discarded as a possible factor and the link's strain therefore changes in every load step. With this change the critical values for the before mentioned link states ($\pm$(5) and $-$(15)) has been changed to $\epsilon_{C,f}$ and $\epsilon_{T,f}$ respectively. This should have no effect on the functionality of the algorithm since status $\pm$(5) and $-$(15) only occur with a previous state $\pm$(2) and $-$(12) respectively. The load factor for these links then will only be chosen when they would switch back to this state due to the inconsistent or consistent strain increment in the iteration step.

The following list is a summary of all different link states for the extended SSC algorithm:

- Tension (brittle, $\gamma_{T,j} < 0$)
  - (1) initial stiffness
  - (2) softening
  - (3) reloading after previous damage
  - (5) extra status for *iteration of status*
  - (4) broken status

Additionally, in case of softening for a link under compression, the respective negative states are labelled:

- Compression (brittle, $\gamma_{C,j} > 1$)
  - $-$(1) initial stiffness (compression)

  - ② softening
  - ③ reloading after previous damage
  - ⑤ extra status for *iteration of status*

Furthermore, links that exhibit plasticity, i.e. have a positive stiffness after the yield point, obtain the respective negative labels (offset by 10):

- Compression (plasticity, $0 > \gamma_{C,j} \leq 1$)
  - ⑫ softening
  - ⑬ reloading after plasticity
  - ⑮ extra status for *iteration of status*

These link states are depicted along with the load-displacement relation in Fig. 5.19 for lateral and diagonal links.

A flow chart of the extended algorithm can be found in Fig. 5.20 along with the detailed decision tree for the case of links that are not consistent with their assumed status in Fig. 5.21. The whole process is explained in an example in the Appendix A.1.

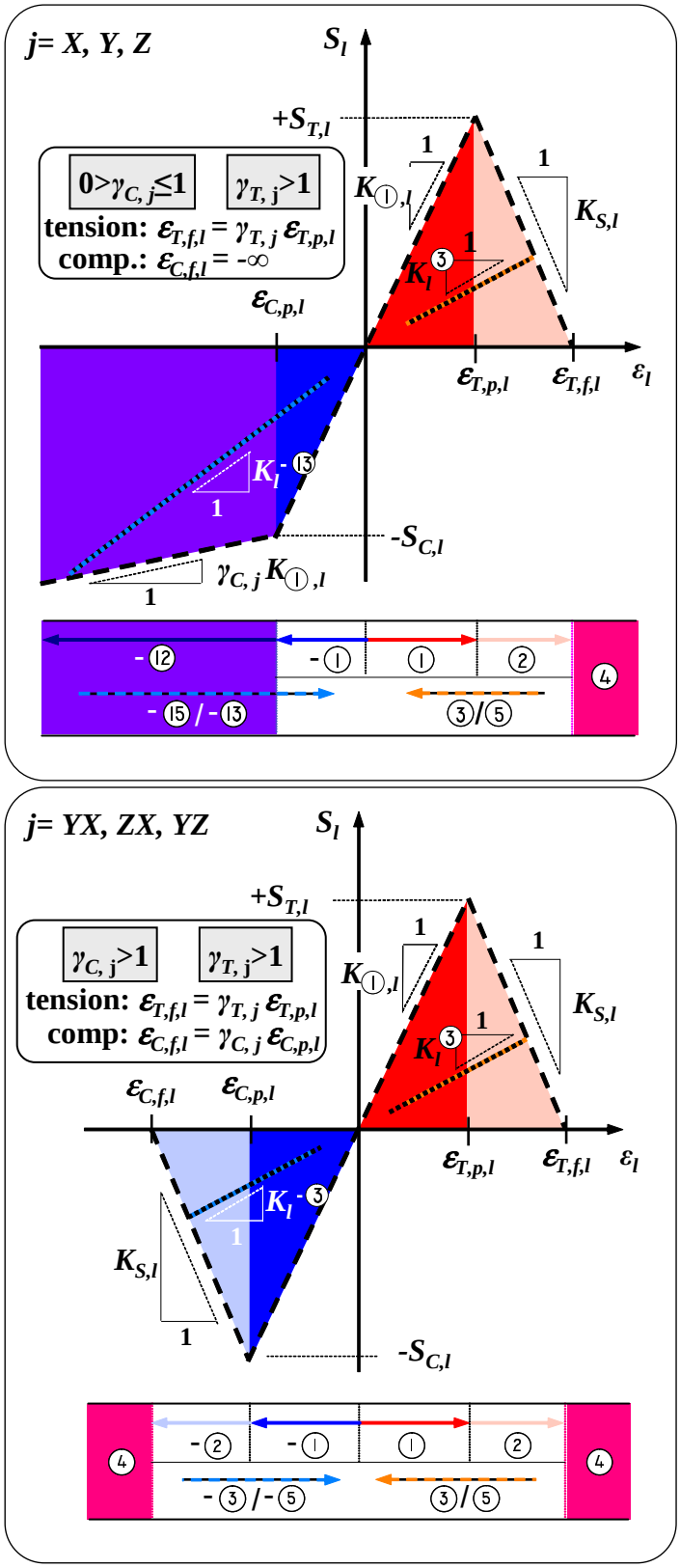

Figure 5.19: *Definition of different link states of link l for lateral links (above, $j = X, Y, Z$) and diagonal links (below, $j = YX, XZ, YZ$) (original in colour).*

Table 5.5: *Critical strain to calculate the required load factor for a respective status of link l and the following next status, that the link is changed to.*

link status	**critical strain**	**status change to**
tension (brittle, $\gamma_{T,j} < 0$)		
①	$\epsilon_{T,p,l}$	②
②	$\epsilon_{T,f,l}$	④
③	$\epsilon_{T,max,l}$	②
⑤	$\epsilon_{T,f,l}$	automatically ③
compression (brittle, $\gamma_{C,j} < 0$)		
−①	$\epsilon_{C,p,l}$	−②
−②	$\epsilon_{C,f,l}$	④
−③	$\epsilon_{C,max,l}$	−②
−⑤	$\epsilon_{C,f,l}$	automatically −③
compression (plasticity, $\gamma_{C,j} > 0$)		
−①	$\epsilon_{C,p,l}$	−⑫
−⑫	$\epsilon_{C,f,l} =\approx \infty$	n.a.
−⑬	$\epsilon_{C,max,l}$	−⑫
−⑮	$\epsilon_{C,max,l}$	automatically −⑬

link status	**alternative critical strain**	**alternative status change**
①	$\epsilon_{C,p,l}$	−②
③	$\epsilon_{C,max,l}$	−②
⑤	$\epsilon_{C,max,l}$	automatically −③
−①	$\epsilon_{T,p,l}$	②
−③	$\epsilon_{T,max,l}$	②
−⑤	$\epsilon_{T,max,l}$	automatically ③
−⑬	$\epsilon_{T,max,l}$	-⑫
−⑮	$\epsilon_{T,max,l}$	automatically ⑬

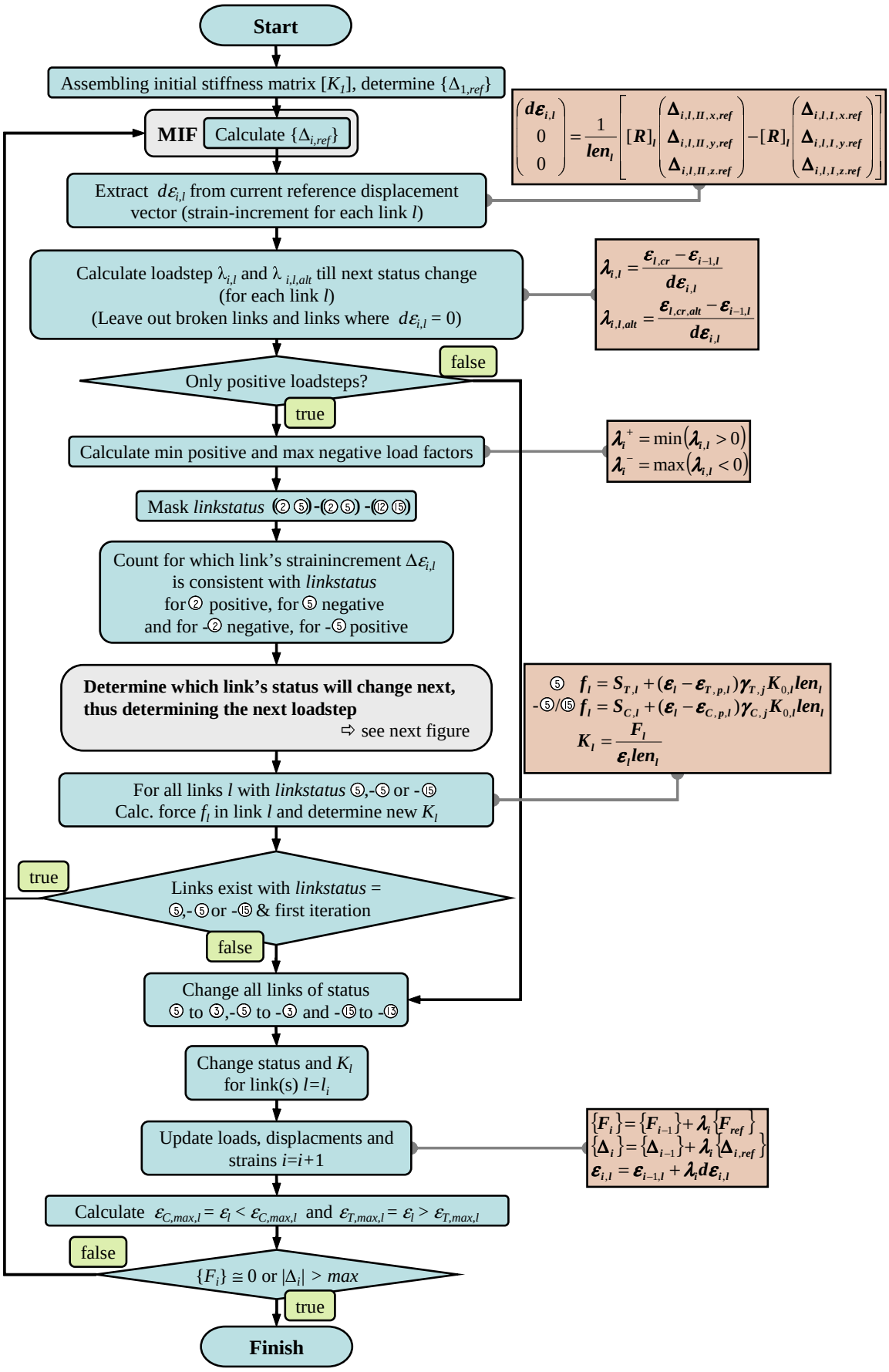

Figure 5.20: *Flow-chart of the extended SSC method as implemented in LAT3D.*

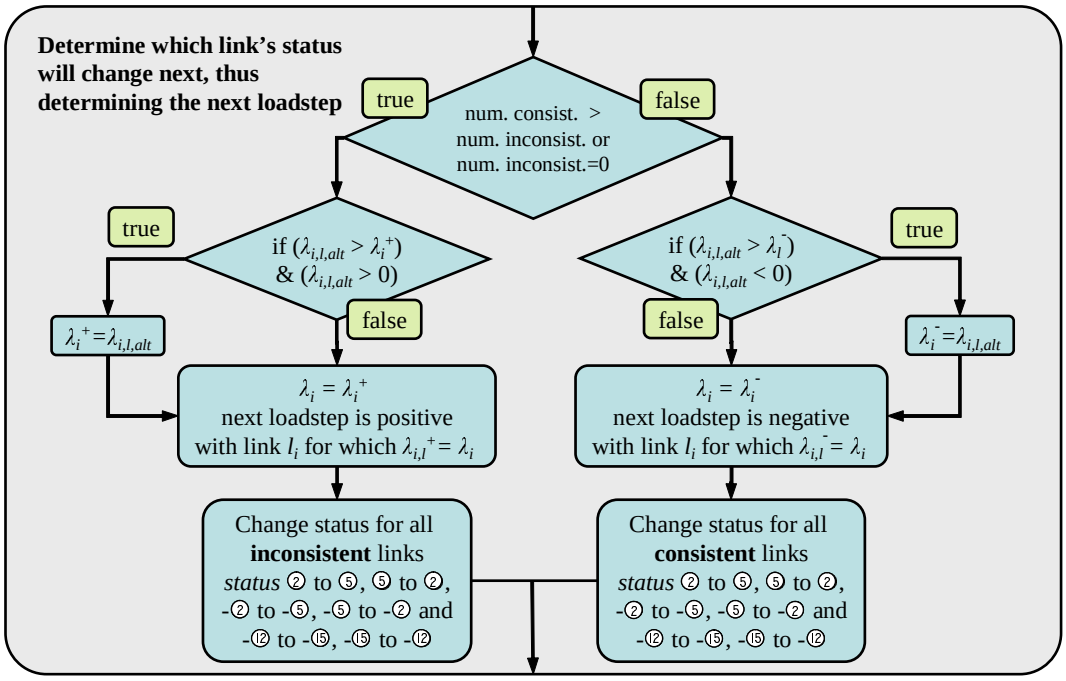

Figure 5.21: *Flow-chart of the extended SSC method, determination of next link change and respective load factor.*

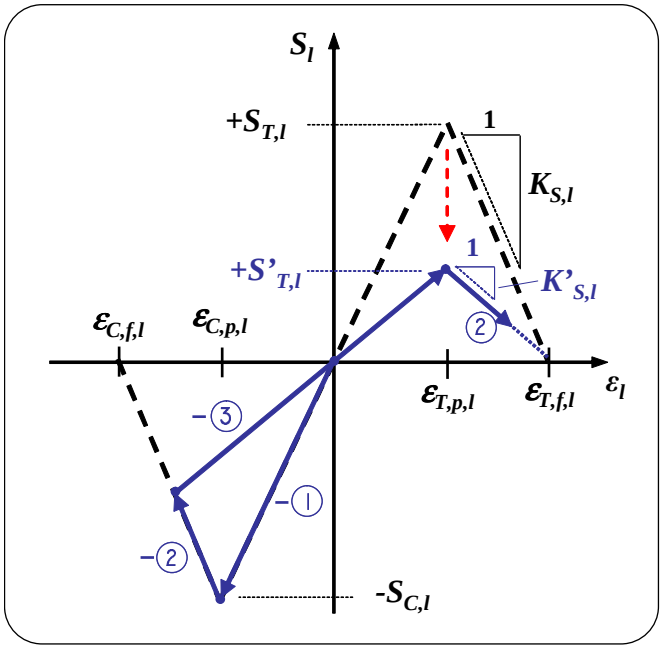

Figure 5.22: *Extension of the SSC algorithm: compressed link goes from unloading in compression −③ to softening in tension ②, alternative critical strain and load factor has to be used. (original in colour).*

5.6.3 Problems with the Extended SSC Algorithm

For models where a large number of links are transferred to the plastic state $-(12)$ the computational advantage due to the SSC algorithm minimises. Each time one brittle link breaks and the strain increment for compressive links changes its direction an additional load step needs to be taken.

During the solution algorithm after one link breaks and obtains a softening stiffness, links in the plastic state under compression $-(12)$ are likely to switch back to reloading and thus a new stiffness needs to be determined (status $-(15)$ and consequently after the iteration $-(13)$). Since this includes a lot of links to switch back in a relatively small load range this would lead to a great number of small load steps. This can be prevented by installing a load threshold in which links can change their status.

The SSC algorithm is therefore altered in a way to allow several links (l_i) to change if they are in a similar load range $\lambda_i - \lambda_{i,l} < \lambda_{Thresh}$. Still, since the minimum $\lambda_i = \lambda_i^+$ or maximum $\lambda_i = \lambda_i^-$ respectively is taken, an error accumulates in the calculation of the global force vector F_i. This error, depending on the threshold load value, is argued to be minor in comparison to the speed gain in the computation process, (Fig. 5.23).

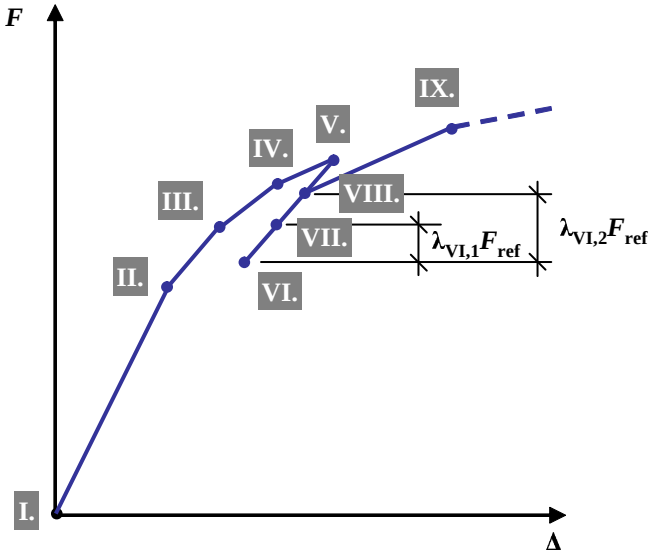

Figure 5.23: *Proposed solution to the problem with the SSC algorithm when plastic hardening links are considered. Example shows exaggerated the LDP of a lattice structure with two plastic links. Load step i=VI is combined with the next step if the difference of the load factors for link $l = 1$ and $l = 2$ are smaller than λ_{Thresh}. Hence, step i=VII. is skipped.*

5.6.4 Method of Inelastic Forces (MIF)

Instead of decomposing the tangent stiffness matrix $[K_i]$ again each load step, which would be a common procedure in an nonlinear solution algorithm, a more efficient method was devised by Jirasek & Bazant (1995). Basically, a stiffness change, that results from elements changing from one status to another, is taken into account as an additional *inelastic* force added to the global force vector $\{F_{ref}\}$. Only this additional inelastic force needs to be calculated for each link instead of the decomposition of the entire stiffness matrix.

Since this method is modified later in section 5.9 to include *inelastic* moments from geometric nonlinear beams, Jirasek & Bazant's original derivation shall be presented here:

The initial global stiffness matrix of a system with only geometric linear link elements can be written as

$$[K_1] = [B]^T[D_1][B], \tag{5.54}$$

where $[B]$ is the geometric matrix with a number of rows being the number of links and the same number of columns as there are DoFs. $[B]$ derives from the link extension-displacement equation $\{e\} = [B]\{\Delta\}$, with vector $\{e\}$ being the axial extension of each link.

The square matrix $[D_1]$ contains the initial link stiffness $[K_1]$ on the diagonal and has the size of the number of links.

Similar to the equation before, the tangential stiffness matrix for the current load step i can be written as

$$[K_i] = [B]^T[D_i][B], \tag{5.55}$$

with all current stiffness contained in $[D_i]$ instead of the initial ones.

The overall aim of the method is to solve a system of equations as stated in the previous subsection (5.51),

$$[K_i]\{\Delta_i\} = \lambda_i\{F_{ref}\}, \tag{5.56}$$

without assembling the actual tangential stiffness matrix K_i and using the solved initial matrix instead K_1. Thus, by adding and subtracting $[K_1]$, the following

equation

$$([K_1] + [K_i] - [K_1])\{\Delta_i\} = \lambda_i\{F_{ref}\}, \tag{5.57}$$

can be rewritten as

$$[K_1]\{\Delta_i\} = \lambda_i\{F_{ref}\} - ([K_i] - [K_1])\{\Delta_i\} \tag{5.58}$$

and substituting $[K_1]$ and $[K_i]$ to the right hand side with the former definition (5.54) and (5.55) leads to

$$[K_1]\{\Delta_i\} = \lambda_i\{F_{ref}\} - [B]^T([D_i] - [D_1])[B]\{\Delta_i\}. \tag{5.59}$$

It is important to note that $([D_i] - [D_1])$ is a diagonal matrix with nonzeros (on the diagonal) only for links where stiffness changes occurred. Thus, is is possible to write much smaller matrices $[\hat{B}]$ and $[\hat{D}]$ by leaving out all the rows in $[B]$ that correspond to zero columns in $([D_i] - [D_1])$, thus

$$[B]^T([D_{i-1}] - [D_1])[B] = [\hat{B}]^T[\hat{D}][\hat{B}]. \tag{5.60}$$

Equation (5.59) can now be written as

$$[K_1]\{\Delta_i\} = \lambda_i\{F_{ref}\} - ([\hat{B}]^T[\hat{D}][\hat{B}])\{\Delta_i\}. \tag{5.61}$$

Since $\{e\} = [B]\{\Delta_i\}$ is the vector of all axial link extensions in step i, $\{\hat{e}\} = \{\hat{B}\}\{\Delta_i\}$ is the axial extension of only the changed links. Thus, multiplied with the stiffness $[\hat{D}]$, the term

$$\{\hat{s}\} = [\hat{D}][\hat{B}]\{\Delta_i\} \tag{5.62}$$

can be interpreted as being the actual *inelastic* force vector of the changed links.

With (5.62), the previous equation (5.61) can be rewritten as

$$[K_1]\{\Delta_i\} = \lambda_i\{F_{ref}\} - [\hat{B}]^T\{\hat{s}\}. \tag{5.63}$$

Since the reference displacement $\{\Delta_{1,ref}\}$ (for the initial load step $i = 1$ and $\lambda_i = 1$) is calculated by

$$[K_1]\{\Delta_{1,ref}\} = \{F_{ref}\}, \tag{5.64}$$

and it can be stated that,

$$[K_1][\hat{R}] = -[\hat{B}]^T. \tag{5.65}$$

It follows by inserting (5.64) and (5.65) into (5.63) that

$$[K_1]\{\Delta_i\} = [K_1]\lambda_i\{\Delta_{1,ref}\} + [K_1][\hat{R}]\{\hat{s}\}. \tag{5.66}$$

Dividing by $[K_1]$ leads to

$$\{\Delta_i\} = \lambda_i\{\Delta_{1,ref}\} + [\hat{R}]\{\hat{s}\}, \tag{5.67}$$

Now, the fundamental equation of this method can be obtained by substituting (5.67) into (5.62) and after rearranging as

$$([I] - [\hat{D}][\hat{B}][\hat{R}])\{\hat{s}\} = [\hat{D}][\hat{B}]\{\Delta_{1,ref}\}\lambda_i. \tag{5.68}$$

From this equation (5.68) the *inelastic* forces $\{\hat{s}\}$ can be solved. By substitution into (5.67) the displacements $\{\Delta_i\}$ are obtained. Since in this step the actual load factor λ_i is not known it is set preliminary to 1. This factor will be determined only after the SSC algorithm delivers the required factor to change a link from one status to another. Thus, not the actual displacement vector is calculated, but the *reference* displacement $\Delta_{i,ref} = \Delta_i$ with $\lambda_i = 1$ for load step i.

The algorithm can be summarised as:

Algorithm 4 Method of Inelastic Forces (MIF).

Require: initial global stiffness matrix $[K_1]$
Require: $\{\Delta_{1,ref}\}$ obtained by solving (5.64)
for load step i

1: construct matrix $[\hat{B}]$ and solve (5.65) to get $[\hat{R}]$
2: construct the coefficient matrix $([I] - [\hat{D}][\hat{B}][\hat{R}])$ and the right hand side $[\hat{D}][\hat{B}]\{\Delta_{1,ref}\}$ from (5.68) and solve for $\{\hat{s}\}$
3: evaluate $\{\Delta_{i,ref} = \Delta_i\}$ with $\lambda_i = 1$ from (5.67)

Further Use of MIF

One key aspect of the MIF methods is that, although Jirasek & Bazant (1995) assumes that the geometric (strain-displacement) matrix does not change during the nonlinear solution process, it actually can be modified to incorporate geometric nonlinearity of link elements. The vector $\{B\}$ for the respective elements is simply updated with the new geometry, thus the *inelastic* forces also represent new

directions. This will be discussed further in section 5.8 on contact elements, where this important aspect of the MIF will be exploited.

Although, only link (bar) elements are considered with a relative simple strain-displacement relation, stiffness change of beam elements can, as well, be incorporated in the MIF method. The reader is referred to section 5.9 on geometric nonlinear beam elements in *LAT3D*.

Computational Considerations

Every link that changes its stiffness is listed in the rows of the $[\hat{B}]$ matrix. Since the actual vector $\{B\}$ of one link does not change (as long as no geometric nonlinearity for these links is considered), every newly changed link is added to an already existing matrix $[\hat{B}]$ as a new row.

Consequently, matrix $[\hat{R}]$ in equation (5.65) does not change either and only an extra column is added. Thus for one load step the only three computation steps that need to be performed are: a) determining for each newly changed link the additional row in $[\hat{B}]$ (algorithm 4 line 1), b) the additional column in $[\hat{R}]$ (line 2) and c) solving for $\{\hat{s}\}$. Besides these changes, the altered link stiffness is incorporated in the diagonals of the $[D]$ matrix as $(K_{i,l} - K_{\textcircled{1},l})$ for link l.

Note, that if a link has already been changed compared to the initial stiffness, then no new $[\hat{B}]$ row or $[\hat{R}]$ column vector needs to be added and only $[\hat{D}]$ needs to be changed.

As mentioned in Jirasek & Bazant (1995), this method is superior over other methods when large lattice systems are considered. Since, then the resolving of the global stiffness matrix is much more time-consuming than the technique used here.

5.6.5 Further Optimisation of the MIF Algorithm

One might argue that, as more links change their stiffness in the process of the nonlinear solution algorithm, the determination of inelastic force vector $\{\hat{s}\}$ from matrix $[\hat{R}]$ with the added column becomes more and more computationally expensive. However, in the case that this becomes more expensive than to

decompose the global stiffness matrix altogether, the initial stiffness matrix $[K_1]$ can be replaced with the current tangential stiffness matrix $[K_i]$. Thus, the matrix $[\hat{R}]$ is emptied again and the MIF algorithm starts all over. Additionally, for any changed link, $K_{\textcircled{1},l}$ has to be updated to the actual link stiffness $K_{i,l}$.

In *LAT3D* the above described routine was implemented in the following way: Since only broken links in tension (status ④) will not change their stiffness again and are definitely permanent in the nonlinear solution, only these links are eliminated from matrix $[\hat{R}]$. Links that are in a plastic state remain in the matrix. An additional parameter can be set in the model input file which denotes the number of broken links after which the updated (smaller) global stiffness matrix is decomposed again. However, when plastic deformation of links is considered, these links will remain changeable during the entire solution process and can not be removed from the $[\hat{R}]$ matrix. Furthermore, a great number of changed links (compressive status) accumulates in a model that experiences large deformation under compression. This significantly slows down the entire algorithm and will be discussed further in the results chapter for the compression samples (subsection 6.5.3).

5.7 Computational Optimisations Employed in LAT3D

Since 'plastic' lattice models still require a significant time to compute (wide-spread plastic links, large lattices etc.) it was attempted to minimise the computational effort by the use of the following three different approaches:

- Hybrid model
  Using elastic solid elements instead of a lattice, where no plastic or fracture behaviour is expected to occur.
- Cell structure
  The lattice cells are arranged in a particular diagonal checked pattern. This enables the heterogeneity to be reflected on a small scale but with fewer nodes and therefore fewer DoFs are used.
- Extended MIF and SSC algorithm
  The use of the MIFM and SSC algorithm combined as described in the previous section.

5.7.1 Hybrid Model - Solid and Lattice Elements

In order to minimise the number of DoFs, larger solid elements are used in areas of the model where no plastic or brittle behaviour is expected. Thus, 3D linear transversely isotropic elements are needed to be connected to the lattice. These elements are generated in a regular shape. Only rectangular blocks with a certain length, height and width are possible as the preprocessor simply divides the defined blocks in regular elements. This was sufficient for the modelling of the experimental specimens which itself were of rectangular shape. However, the program could be improved with a more general mesh generator if other geometries are to be considered.

The link between solids and a lattice is accomplished with the penalty element method. A constraint equation is formulated that links DoFs of the link's ends at the lattice block's surface with the DoFs of the adjacent solid block. The two different block types along with the connecting process are pictured in Fig. 5.24.

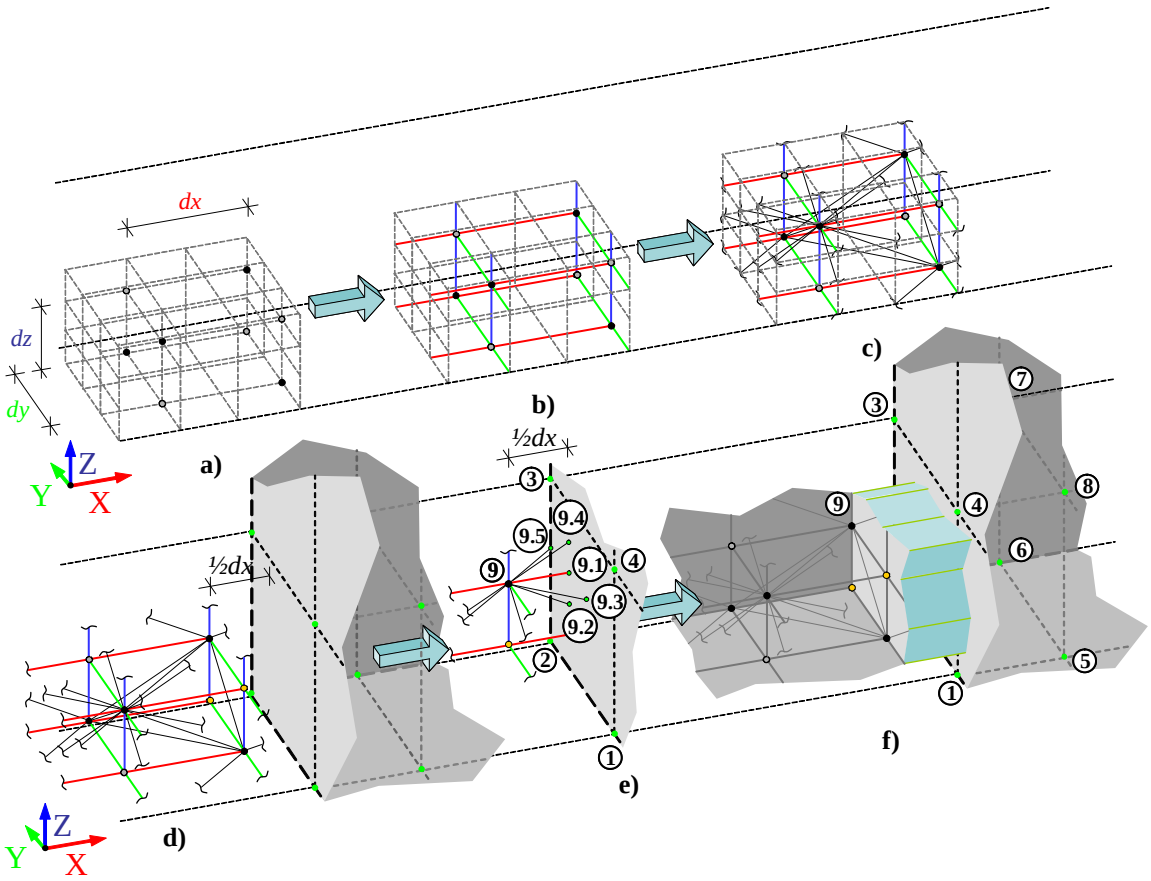

Figure 5.24: *Connection of a lattice block with a solid element block, a) ...grid of a lattice b) ...with longitudinal and lateral links c) ...added diagonal links d) ...with solid elements and added border nodes (yellow) e) fictitious nodes (green) with additional quarter and half links f) elements connecting directly solid nodes and lattice nodes (original in colour).*

The upper part of the figure, a) to c), starts with building up part of the lattice structure (red lines representing links in the longitudinal X direction, green for the Y, blue for links in the Z direction and black for the diagonals). The dotted black lines represent a grid with the spacing of half dx, dy and dz. Lattice nodes (black) are organised in a checked pattern with node gaps (grey dots) on this grid (discussed in the subsequent subsection 5.7.2). These gaps are turned into a functioning node with three DoFs where surfaces of lattice blocks meet (and are connected) with surfaces of solid blocks, Fig. 5.24d(yellow nodes).

Since one link represents larger material surrounding it, the end nodes of the surface of a lattice block need to be shifted away from the solid block surface, as seen in Fig. 5.24d, by half of the spacing in the direction normal to the connecting surfaces. E.g as in this example: $\frac{1}{2}dx$ in the X direction. That equates to a $\frac{1}{4}$ for the longitudinal and lateral link's length, and $\frac{1}{2}$ for the diagonal links. In part e) one can see the additional shortened links which now connect the lattice node (9) with the fictitious nodes (9.1) to (9.5) at the interface between the lattice and solid element zones. These nodes are constrained with the eight solid element nodes ((1) to (8)).

The solid elements are constructed with linear shape functions, subsection 5.2.2. Therefore, link between the solid element nodes and the fictitious node is merely a linear interpolation of the solid element's DoFs. The displacement of, for example node (9.3) can be calculated by the weighted displacement of the solid nodes. This is accomplished by first determining the node's relative position to the solid element's centre, vector $\{n\} = \{n_x, n_y, n_z\}^T$, Fig. 5.25. Since the solid elements are not skewed or distorted no further transformation of this vector is necessary. Thus, the components of this vector can be normalised with respect to the element's size l_x, l_y and l_z and then described as parameters for the shape functions:

$$\xi = n_x/l_x \quad \eta = n_y/l_y \quad \zeta = n_z/l_z \tag{5.69}$$

With these inserted into the element's shape functions N_1 to N_8, (5.25), one obtains the weights for each of the 8 element nodes. These weights can be used to formulate

the constraint equation and become in case of the above shown example:

$$\begin{pmatrix} u_{\textcircled{9.3}} \\ v_{\textcircled{9.3}} \\ w_{\textcircled{9.3}} \end{pmatrix} = N_1 \begin{pmatrix} u_{\textcircled{1}} \\ v_{\textcircled{1}} \\ w_{\textcircled{1}} \end{pmatrix} + N_2 \begin{pmatrix} u_{\textcircled{2}} \\ v_{\textcircled{2}} \\ w_{\textcircled{2}} \end{pmatrix} + N_3 \begin{pmatrix} u_{\textcircled{3}} \\ v_{\textcircled{3}} \\ w_{\textcircled{3}} \end{pmatrix} + \cdots , \tag{5.70}$$

with u, v and w being the displacements in the X, Y and Z direction respectively.

As a final step, the additional purely elastic link element is created with mean stiffness $\overline{K}_j$ and no further strength properties (stiffness is adjusted to the now shorter length). This link connects now node ⑨.③ with node ⑨.

In the actual *LAT3D* program, the nodes (⑨.① to ⑨.⑤) are fictitious nodes with no real DoFs in the global stiffness matrix. The element is formulated directly connecting the lattice ends (node ⑨) with the solid element nodes, incorporating the assigned stiffness $\overline{K}_j$, Fig. 5.24f. This avoids increasing the size of the global stiffness matrix significantly with superfluous DoFs.

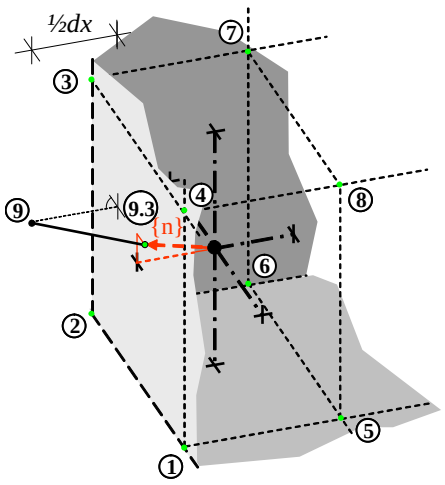

Figure 5.25: *Connection of lattice link with solid element nodes, vector {n} starts in centre of the solid element to the fictitious node ⑨.③ (original in colour).*

5.7.2 Lattice Cell Structure

Similar lattice models to the one described here are mentioned in the literature review, subsection 3.3.4. For example Landis et al. (2002) and Smith et al. (2007) etc. use 2D lattice models for predicting timber behaviour. These lattice models consist of cells with diagonals crossing each other. Thus, a cell of rectangular box shape is created, as seen in Fig. 5.26b (extended to a 3D cell). The structure can

be optimised by alternating the cells in a checked pattern. This lattice (a) has now non-crossing diagonals and thus longer lateral and longitudinal links where gaps in the nodal grid occur (grey nodes). This halves the number of DoFs while the ring structure can still be mapped on a relative small grid.

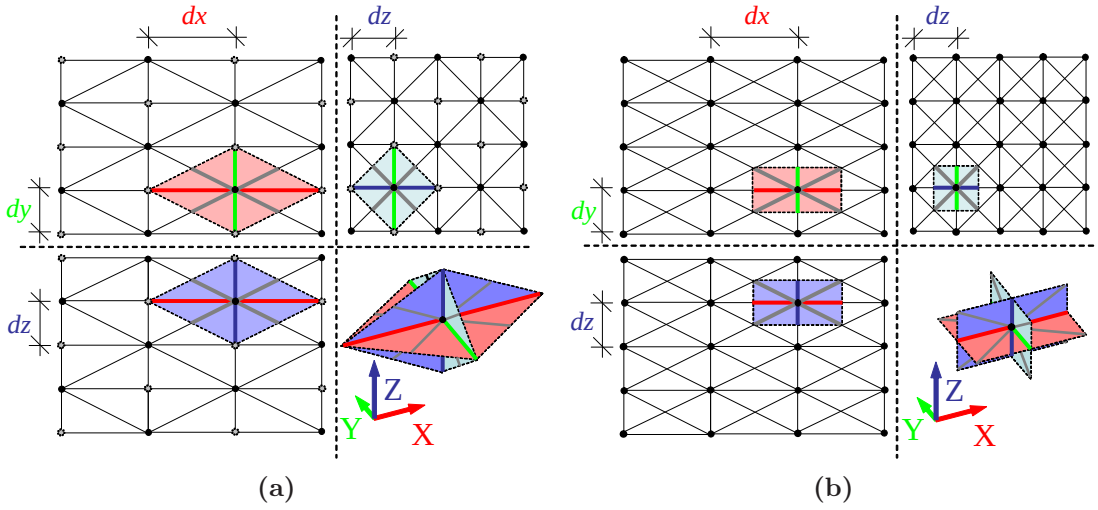

Figure 5.26: *Comparison of two different lattice arrangements: (a) checked pattern and (b) rectangular. In case of the a rectangular lattice (b) the number of nodes and hence* DoFs doubles, when the same spacing is assumed (original in colour).

5.8 Contact Elements

For the timber joint model contact elements are used. These are simply link elements that exhibit a large stiffness when contact is made, and a negligibly small stiffness when a gap exists. The respective load-displacement curve can be seen in Fig. 5.27. Both, the SSC algorithm and the MIF algorithm have to treat these links differently than ordinary lattice links:

- **SSC**
  In the SSC algorithm, for each iterative step that is taken, the geometry of the system and thus vector $\{B^{el}\}$ is updated. Additionally, the contact links obtain different status labels (⑥ to ⑨). In each load step these links are considered to be able to change their stiffness state. Thus, load factors $\lambda_{i,l}$ in load step i are determined for links l and are included in the SSC algorithm. Like the plastic links the stiffness is never negative and therefore the links do not influence the decision whether or not a positive or negative load step is required. After each step, the $\epsilon_{C,p}$ value of the link is adjusted according to the updated geometry and the resulting gap distance.

- MIF
  The MIF is adjusted by changing the $[B]$ and $[D]$ matrix for each contact link that alters its status from open to closed or vice versa. Each link has already a fixed position in the matrices that are used in the MIF, unlike the original method where newly changed links are added.

5.8.1 Generation of Contact Surfaces

The drilled hole in the member of a timber joint is generated by a cylindrical cut in the lattice block. This is accomplished by composing a circular mask at the point when the block data-structure is generated and leaving out all elements which are masked. At the lattice surfaces the fictitious nodes (grey coloured) are activated to enable a more continuous surface. However, this would still be a very 'steplike' contact surface between the bolt elements and the lattice. A smoother contact surface was achieved by subtracting the initial gap between bolthole and bolt surface $r_{s,l}$ for link l in the contact's element definition (Fig. 5.28). Thus, with every update of the geometry, the initial gap is subtracted and contact is established when the bolt elements touch the lattice node at this specific distance.

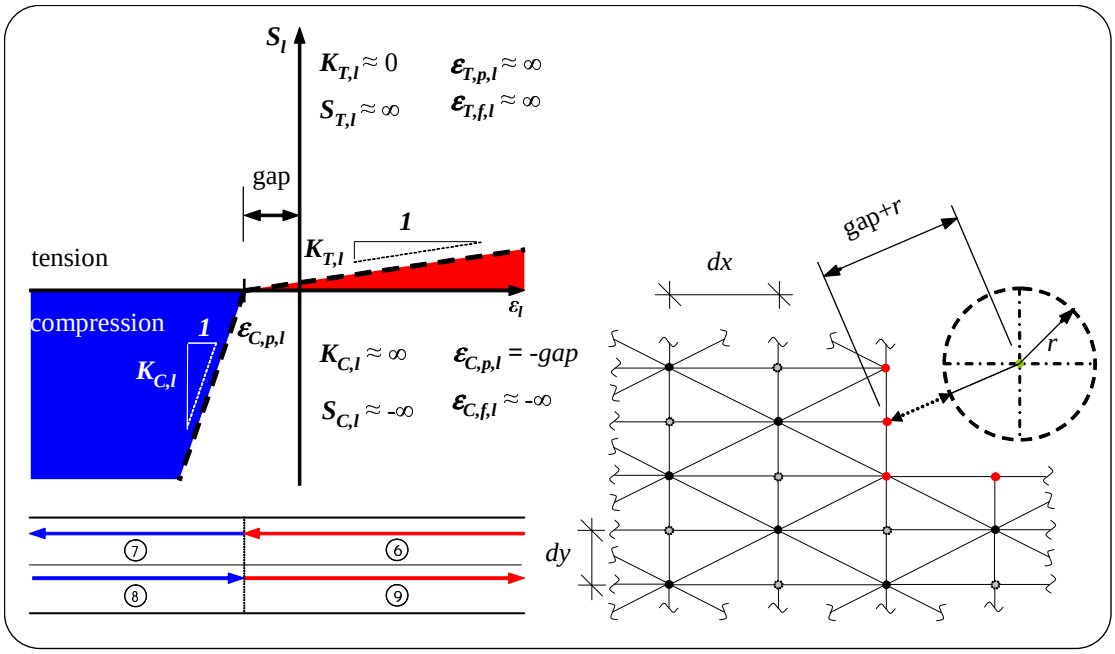

Figure 5.27: *Load-displacement relation of contact elements (original in colour).*

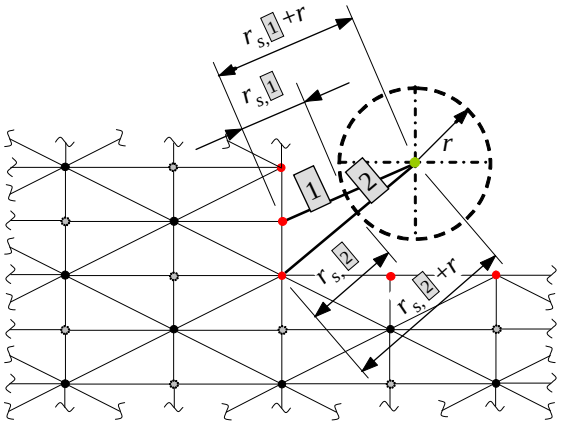

Figure 5.28: *Contact elements* $l =$ 1 *and* 2 *are adjusted to the initially existing gap. The distances* $r_{s,l}$ *from bolt surface to contact-node and bolt radius* r *is stored with the contact element's information. It is subtracted from the node-to-node distance in the calculation of the potential gap later in the* SSC algorithm. Thus, ensuring a smooth contact surface between lattice and beam elements (original in colour).

5.8.2 Geometric Update of Contact Links

After each load step i, all nodal coordinates are updated with the incremental displacement vector $\{d\Delta_i\} = \lambda_i\{\Delta_{i,ref}\}$. Contact nodes are projections on the target surface of other elements such as beam elements (bolt) which itself may change as well. Thus, for each not only the gap distance has to be recalculated but also the orientation of contact elements.

Different types of elements are considered for the two different contact arrangements:

- Lattice-bolt contact
  The lattice node is the actual contact node, while several nodes of the beam elements (bolt) serve as the target 'surface' on which the node is projected and distance is determined.

  $\Rightarrow$ element is depicted in Fig. 5.29a

- Lattice-washer contact
  Unlike the lattice-bolt elements, the contact node is projected onto a washer. This is a circular surface that is defined as an extension from the end node of the beam elements (taking into account the rotational DoFs) with a diameter of $\varnothing_W$.

  $\Rightarrow$ element is depicted in Fig. 5.29b

Lattice-Bolt-Contact Elements

This element type is basically a link between contact nodes of the lattice at the surface and two nodes of the beam on where the contact node can be projected on, perpendicular to the axis of the bolt. Considering the element l reaching from contact node to beam element with vector $C_{B,l}$. The element's displacement vector Δ, e.g. as depicted in Fig. 5.29a (between contact node ④ and bolt nodes ② and ③), can be written as

$$\{\Delta\} = \left\{ \begin{array}{cccccccccc} u_{③} & v_{③} & w_{③} & u_{②} & v_{②} & w_{②} & u_{④} & v_{④} & w_{④} \end{array} \right\}. \tag{5.71}$$

The local geometric vector is

$$\{B^{el,local}\} = \left\{ \begin{array}{cccccccccc} \xi & 0 & 0 & (1-\xi) & 0 & 0 & -1 & 0 & 0 \end{array} \right\}, \tag{5.72}$$

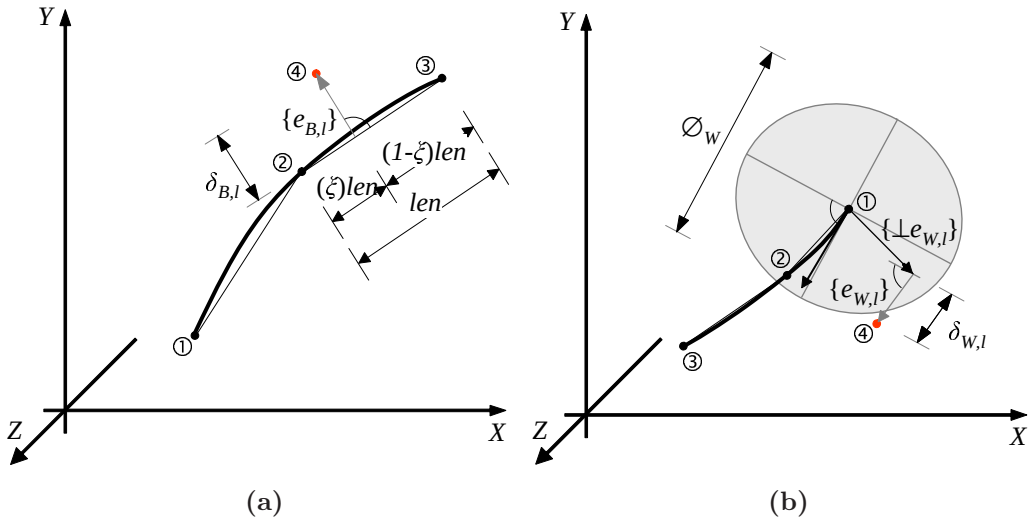

Figure 5.29: *Definition of the gap distance for contact element l: (a) between contact node and beam elements (bolt) delta$_{B,l}$ and (b) between contact node and the washer surface delta$_{W,l}$.*

The global $\{B^{el}\}$ vector can be directly determined with the simplified rotation vector $\{R^{el}\}$

$$\{B^{el}\} = \left\{ \begin{array}{cccc} \xi\{R^{el}\} & (\xi-1)\{R^{el}\} & -\{R^{el}\} \end{array} \right\} \tag{5.73}$$

with

$$\{R^{el}\} = \frac{1}{\delta_{B,l}} \left\{ \begin{array}{ccc} e_{x,l} & e_{y,l} & e_{z,l} \end{array} \right\}. \tag{5.74}$$

Thus the global vector $\{B^{el}\}$ can be written as

$$\{B^{el}\} = \left\{ \begin{array}{ccc} \frac{\xi}{\delta_{B,l}} \left\{ \begin{array}{ccc} e_{x,l} & e_{y,l} & e_{z,l} \end{array} \right\} & \frac{\xi-1}{\delta_{B,l}} \left\{ \begin{array}{ccc} e_{x,l} & e_{y,l} & e_{z,l} \end{array} \right\} & \frac{-1}{\delta_{B,l}} \left\{ \begin{array}{ccc} e_{x,l} & e_{y,l} & e_{z,l} \end{array} \right\} \end{array} \right\}. \tag{5.75}$$

If, during the solution algorithm SSC and the consecutively updating of the geometry, the projection of the contact node moves from one element to another ($\xi < 0$ or $\xi > 1$), the next respective element and its nodes are used. The case that a contact node suddenly moves outside the target surface has not been included. However, this should not occur for the joint model: the two sides where lattice nodes could 'slip over' the ends of the last beam element are a) on one side held by the definition of the washer surface and b) on the other side (where the load is applied) they are pushed inwards away from the edge.

Lattice-Washer-Contact Elements

Similar to the former derivation, an element that models the contact between lattice nodes and the washer, can be formulated. This element is controlled by the bolt end node's displacement and rotation. In the particular example as depicted in Fig. 5.29b with lattice node ④ and bolt end node ①, the displacement vector is

$$\{\Delta\} = \left\{ \begin{array}{cccccccccc} u_{①} & v_{①} & w_{①} & \theta_{x,①} & \theta_{y,①} & \theta_{z,①} & u_{④} & v_{④} & w_{④} \end{array} \right\}. \tag{5.76}$$

Geometric vector

$$\{B^{el,local}\} = \left\{ \begin{array}{ccccccccc} 1 & 0 & 0 & 0 & e_z & -e_y & -1 & 0 & 0 \end{array} \right\} \tag{5.77}$$

can be transferred to the global coordinates

$$\{B^{el}\} = [R^{el}]^T \{B^{el,local}\}. \tag{5.78}$$

The global contact element's rotation matrix is updated with the rotation of the bolt's end node after each load step,

$$[R^{el}] = [R^{①}][R^{el}] \tag{5.79}$$

with

$$[R^{①}] = \left[\begin{array}{ccc} cos(\theta_z) & sin(\theta_z) & 0 \\ -sin(\theta_z) & cos(\theta_z) & 0 \\ 0 & 0 & 1 \end{array} \right] \left[\begin{array}{ccc} 1 & 0 & 0 \\ 0 & cos(\theta_x) & sin(\theta_x) \\ 0 & -sin(\theta_x) & cos(\theta_x) \end{array} \right] \left[\begin{array}{ccc} cos(\theta_y) & 0 & -sin(\theta_y) \\ 0 & 1 & 0 \\ sin(\theta_y) & 0 & cos(\theta_y) \end{array} \right]. \tag{5.80}$$

The angles θ_x, θ_y and θ_z are global rotational DoFs of the bolt's end node ①.

5.8.3 Computational Considerations for MIF

The changes made to the original MIF algorithm will be briefly described here.

It is assumed that the beam elements (bolt) and washer are not in contact in the initial state of the structure. However, a *finite* small stiffness of 10^{-5} is applied to the link between contact node and target surface in order to maintain the non-singularity of the global stiffness matrix. When contact is made the stiffness is set to a 'penalty stiffness' of 10^5.

Writing the equation (5.58) from the original MIF derivation,

$$[K_1]\{\Delta_i\} = \lambda_i\{F_{ref}\} - ([K_i] - [K_1])\{\Delta_i\}, \tag{5.81}$$

for link elements, this can be transferred to

$$[K_1]\{\Delta_i\} = \lambda_i\{F_{ref}\} - \left([B_i]^T[D_i][B_i] - [B_1]^T[D_1][B_1]\right)\{\Delta_i\}. \tag{5.82}$$

Considering now only the contact links similar to the changed links in the original derivation of MIF and since the initial stiffness $[D_1]$ for these is negligible small, the part $-[B_1]^T[D_1][B_1]$ can be discarded,

$$[K_1]\{\Delta_i\} = \lambda_i\{F_{ref}\} - \left([\hat{B}_i]^T[\hat{D}_i][\hat{B}_i]\right)\{\Delta_i\}. \tag{5.83}$$

The rest of the derivation of the *inelastic* forces follows as in the original version of the MIF, equations (5.61) to (5.68). With this new version, contact elements as geometric nonlinear bar elements can be taken into account. Therefore, *LAT3D* can deal with normal material nonlinear link elements (as derived previously in the original MIF algorithm) and with the geometric nonlinear bar elements, derived here, that are used in the contact analysis. In contrast to the material nonlinear bar elements, the contact link elements simply have already a specified place in the $[\hat{B}]$ matrix. In this matrix, individual geometric vectors $\{B^{el}\}$ and their stiffness can change as described above.

An example of the contact elements (geometric nonlinear beam elements in contact with a small lattice structure) can be found in subsection 5.11.4.

With the employed contact definition it is possible to simulate normal contact behaviour without tangential friction. This slip-stick influences the load transferred to the bolt hole surface as demonstrated for example in Racher & Bocquet (2005). However, in the model presented here, this effect was neglected since it would have led to a more complicated element formulation.

5.9 Geometric Nonlinear Beam Elements

In order to model a single shear timber joint, 3D Euler-Bernoulli beam elements were used (derived in subsection 5.2.2). The elements are able to be used in a geometric nonlinear analysis simply by updating the geometry (nodal coordinates) in the solution process. Hence, effects such as stress stiffening or buckling were not considered.

The stiffness change that results from the element's updated geometry has to be accommodated in the MIF algorithm as *inelastic* forces and moments. Thus, to implement these elements into the framework of the nonlinear solution in *LAT3D*, the SSC and the MIF algorithm have to be altered:

- **SSC**
  In the SSC process, for each iterative step that is taken, the geometry of the system is updated, i.e. the displacement vector and the elements rotation angle accumulate.

- MIF
  To circumvent the need of changing the global stiffness matrix at every load step, stiffness change due to geometric nonlinearity was implemented by extending the MIF method to include *inelastic* moments instead of only forces. Thus, a force **and** two moments per node are calculated that represent the stiffness change due to an altered beam element. Additionally, the vector $\{B^{el}\}$ needs to be changed.

The nonlinear beam elements will be derived in this section. A standard Euler-Bernoulli with its assumptions is used. Generally, for the extension of the MIF method the strain-displacement matrix $[B]$ must be allowed to change. The difference of beams to bar elements is that the element vector $\{B^{el}\}$ is a function of the axial position x (or in case of an isoparametric element of the nondimensional parameter ξ). Thus, to derive the element stiffness matrix, the following integration needs to be performed,

$$[K^{el}] = \int_0^l \{B^{el}\}^T [D^{el}] \{B^{el}\} dx = \int_{-1}^1 \{B^{el}\}^T [D^{el}] \{B^{el}\} \frac{1}{2} l d\xi. \tag{5.84}$$

In the original MIF algorithm (subsection 5.6.4), this term (for the global stiffness $[K]$) is split to define the vector of *inelastic* forces after the integration is performed. However, since this is not possible for $\{B^{el}\}$ here, due to the integral, a numerical

Gauss integration is used which enables the term to be separated. This modification of the MIF method shall be described in the following.

5.9.1 Computational Consideration for MIF

The MIF algorithm needs to be changed in a way that it incorporates global stiffness changes that result from an updated geometry, i.e. $[B_i]$ differs from $[B_1]$. Thus, equation (5.58) from subsection 5.6.4,

$$[K_1]\{\Delta_i\} = \lambda_i\{F_{ref}\} - ([K_i] - [K_1])\{\Delta_i\}, \tag{5.85}$$

is modified, according to the general element independent derivation of $[K]$ to

$$[K_1]\{\Delta_i\} = \lambda_i\{F_{ref}\} - \int \left([B_i]^T[D_i][B_i] - [B_1]^T[D_1][B_1]\right) dV\{\Delta_i\}. \tag{5.86}$$

Since, in the case of geometric nonlinear beam elements, $[B_i]$ is not the same as $[B_1]$ (unlike in the original derivation of the MIF algorithm), they are compiled to the modified $[\hat{B}]$ matrix. This, is a collection of rows from both the initial state '1' and from the current state i. Consequently, $[\hat{D}]$ contains separated the negative stiffness value from the state '1' and the positive value from state i in individual rows. Thus, the $[\hat{B}]$ matrix has as many columns as there are DoFs and double as many rows as there are stiffness values. In the case of one 2-node 3D beam element with 2x5 DoFs (no torsion considered) these are 6 rows.

Again both matrices, $[\hat{B}]$ and $[\hat{D}]$ contain only the geometric nonlinear beam elements. In the case of the joint model this is a small number of elements for which the *inelastic* forces and moments need to be determined.

A more complicated solution of the integral is necessary since vector $\{B\}$ for beam elements is dependent on the position along local axis X. One can write generally:

$$[K_1]\{\Delta_i\} = \lambda_i\{F_{ref}\} - \int [\hat{B}]^T[\hat{D}][\hat{B}]dV\{\Delta_i\}. \tag{5.87}$$

According to (5.84) since the strain-displacement matrix $[B^{el}]$ is a function of ξ for

the beam elements, it follows

$$[K_1]\{\Delta_i\} = \lambda_i\{F_{ref}\} - \int_{-1}^{1} [\hat{B}_{(\xi)}]^T[\hat{D}][\hat{B}_{(\xi)}]\frac{1}{2}ld\xi\{\Delta_i\}. \tag{5.88}$$

According to the Gaussian quadrature rule, an integral can be approximated by

$$\int_{-1}^{1} f(\xi)d\xi \approx \sum_{j=1}^{n} w_j f(\xi_j), \tag{5.89}$$

which results into the exact solution when $f(x)$ is a polynomial function. In the case of a first order polynomial (as in vector $\{B^{el}\}$) $n = 2$ with weights $w_j = \{1, 1\}$ at points $\xi_j = \{-\frac{1}{\sqrt{3}}, \frac{1}{\sqrt{3}}\}$.

With this quadrature rule, the above equation can be rewritten as (note, the $[\hat{D}]$ matrix is internally multiplied with $\frac{1}{2}l$)

$$[K_1]\{\Delta_i\} = \lambda_i\{F_{ref}\} - \sum_{j=1}^{2} \left([\hat{B}_{(\xi_j)}]^T[\hat{D}][\hat{B}_{(\xi_j)}]\right)\{\Delta_i\}. \tag{5.90}$$

Hence, the new definition for the inelastic forces **and** moments $\{\hat{s}\}$ with respect to ξ similar to the original MIF (5.62) is,

$$\sum_{j=1}^{2}\{\hat{s}_{(\xi_j)}\} = \sum_{j=1}^{2} \left([\hat{D}][\hat{B}_{(\xi_j)}]\right)\{\Delta_i\}. \tag{5.91}$$

Consequently, the $[R]$ matrix with respect to ξ, set to the two Gauss points, can be determined with

$$[K_1]\sum_{j=1}^{2}[\hat{R}_{(\xi_j)}] = -\sum_{j=1}^{2}[\hat{B}_{(\xi_j)}]^T. \tag{5.92}$$

Thus the displacement can be written as,

$$\{\Delta_i\} = \lambda_i\{\Delta_{1,ref}\} + \sum_{j=1}^{2} \left([\hat{R}_{(\xi_j)}]\{\hat{s}_{(\xi_j)}\}\right). \tag{5.93}$$

Similar to the original MIF, the main equation can be written when (5.93) is

substituted into (5.91) as

$$\left([I] - \sum_{j=1}^{2}\left([\hat{D}][\hat{B}_{(\xi_j)}][\hat{R}_{(\xi_j)}]\right)\right)\sum_{j=1}^{2}\{\hat{s}_{(\xi_j)}\} = \sum_{j=1}^{2}\left([\hat{D}][\hat{B}_{(\xi_j)}]\right)\{\Delta_{1,ref}\}\lambda_i. \quad (5.94)$$

The now used method to determine Δ_i can be described as seen in Algorithm 5:

Algorithm 5 Method of Inelastic Forces and Moments (MIFM).

Require: initial global stiffness matrix K_1
Require: $\{\Delta_{1,ref}\}$ obtained by solving (5.64)
for load step i
1: construct matrix $[\hat{B}_{(\xi_j)}]$ and solve (5.92) to get $\sum_{j=1}^{2}[\hat{R}_{(\xi_j)}]$
2: construct the coefficient matrix $[I] - \sum_{j=1}^{2}\left([\hat{D}][\hat{B}_{(\xi_j)}][\hat{R}_{(\xi_j)}]\right)$ and the right hand side $\sum_{j=1}^{2}\left([\hat{D}][\hat{B}_{(\xi_j)}]\right)\{\Delta_{1,ref}\}$ from (5.94) and solve for $\sum_{j=1}^{2}\{\hat{s}_{(\xi_j)}\}$
3: evaluate $\{\Delta_{i,ref}\} = \{\Delta_i\}$ with $\lambda_i = 1$ from (5.93)

Again, since λ_i is determined in the SSC algorithm, thus is preliminary set to 1 in the MIF and only the reference displacement vector for step i is obtained $\{\Delta_{i,ref}\}$.

The geometry is updated in each step. This is depicted in Fig. 5.30a for the geometric nonlinear beam elements. All displacements and rotations are accumulated, i.e. they are added in each step to the ones from the previous step. However, despite the accumulated nodal rotations $d\theta_{z,①,i}$ and $d\theta_{z,②,i}$, in respect to the element's new stiffness, the element is assumed to be straight again in the following load step. The new rotation angle $\theta_{z,el,i+1}$ is calculated from the local displacements of nodes ① and ② .

The forces are updated in a similar manner as depicted in Fig. 5.30b.

An example of the geometric nonlinear elements can be found in subsection 5.11.3.

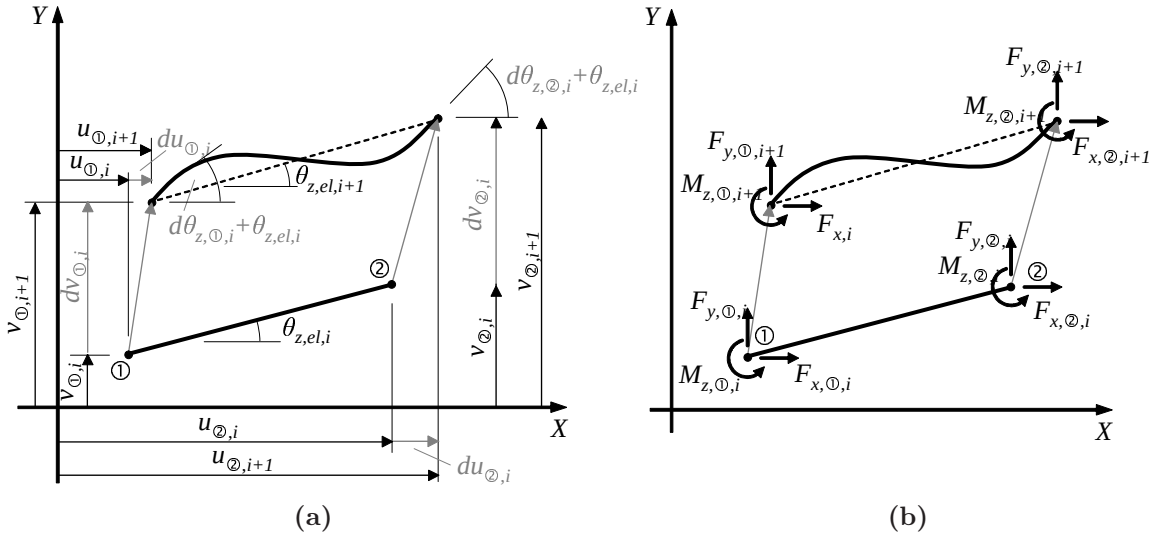

Figure 5.30: *Schematic of the updating process of a geometric nonlinear beam element: updating of (a) displacements and (b) forces.*

5.10 Functionality and Handling of LAT3D

The software *LAT3D* (FE preprocessor, main FE calculation) and *PLOT3D* (post processor) plus several additional functions were programmed in *MATLAB* (The MathWorks, Inc., 2007). The complete source code listings can be found in a CD that is attached to this document. *MATLAB* also allows to create executable files which do not require the actual programming and debugging environment. Thus ordinary PCs could be used to run computations of the models on several machines.

LAT3D as the main part of the program consists of the following major parts:

a) Model input file '.lat'
The model input file represents a user interface in which one can operate on parameters that define the lattice model.

⇒ subsection 5.10.1

b) Preprocessor
The Preprocessor fulfils the following main tasks:

- generating the growth ring structure
- writing node and element information (node position, element's stiffness and strength parameters) into a database
- creating local element stiffness matrices
- composing the global stiffness matrix

⇒ subsection 5.10.2

c) Main routine
A specialised solution algorithm was developed to solve efficiently for a nonlinear solution. It takes into account the material nonlinearity of link elements and the geometric nonlinearity of beam and contact elements (3D model with fastener).

⇒ section 5.6

d) Post processor
The program *PLOT3D* was written to enable the user to view either the load-displacement plots or the deformed lattice with additional stress, strain or fracture information of the lattice.

⇒ subsection 5.10.3

This is depicted as well in Fig. 5.31.

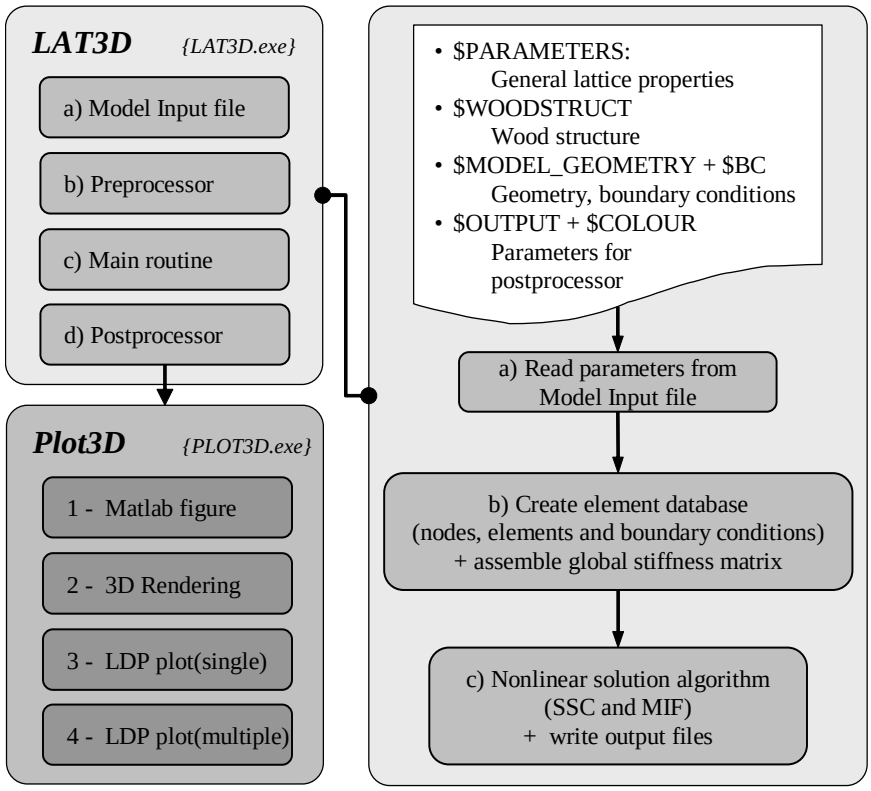

Figure 5.31: *Overview of* LAT3D*'s functionality.*

The basic structure is either a 2D plane or 3D block which can be defined in the model input file. Fig. 5.32 shows this block with its respective surface, edge and corner indices.

5.10.1 Model Input File

The model input file is used as an interface with which the user can specify the lattice models. It serves as a list which sets all relevant parameters that are needed to create

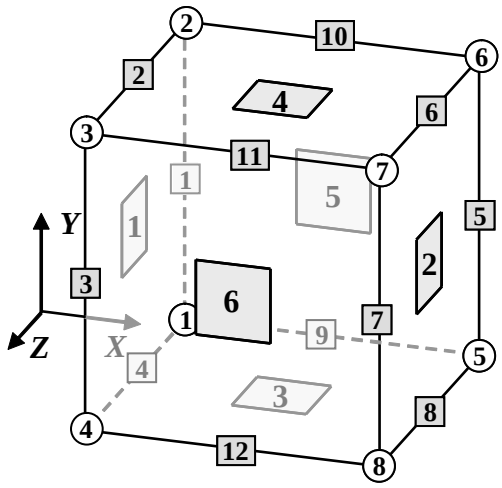

Figure 5.32: *Definition of basic model structure. 3D block with respective indices for surfaces, edges and corners.*

the lattice model and describes the model geometry and boundary conditions. The listing consists of four distinct parts which are marked in the text file with a '$'-sign:

1. *$PARAMETERS*
   - Mean strength, PY and stiffness values plus their coefficient of variation
   - FE control parameters (number of runs, etc.)

   ⇒ further details in section 5.4

2. *$WOODSTRUCT*
   - Parameters defining the standardised density profile
   - Parameters defining the growth ring structure

   ⇒ further details in section 5.5

3. *$MODEL_GEOMETRY* and *$BC*
   - Commands, to create blocks of lattices, solid and beam (bolt) elements
   - Commands, to create notches, holes etc. in lattice blocks
   - Commands, to connect surfaces of lattice blocks with the bolt/washer element
   - Boundary conditions applied to block surfaces, edges and corners

4. *$OUTPUT* and *$COLOUR*

- Parameters controlling the output type, frequency of save steps, plot steps etc.
- Control parameters describing the appearance of the output figures
- Parameters defining the colours for individual element types, symbols etc.

If one parameter is not set, a default value is chosen by the program. To automate the computation for multiple models, several model input files ('.lat') can be started in a type of 'batch' mode. The program *LAT3D* first looks up the text file 'MODEL.txt' in which all model input files are listed that are to be executed. It then starts with the first and completes each consecutively.

A complete list of commands and available parameters can be found in the Appendix A.3 along with the model input files that are used in the result chapter 6.

5.10.2 Preprocessor

The preprocessor first generates randomly an 'artificial' growth ring structure based on parameters set in the section '$WOODSTRUCT' in the model input file. It then creates, according to the commands in '$MODEL_GEOMETRY', the nodes and element structures. The parameters that define the load-displacement curve of an individual link are set by mean values and coefficients of variation outlined in '$PARAMETERS'. Finally it composes the global stiffness matrix by filling in the local stiffness matrices of the individual elements.

5.10.3 Post Processor

The last part of the model input file consists of parameters that define the post processor's functions. Two different types of output files are created and saved while the model is being computed in the main routine:

- Load-Displacement-Plot file '.ldp'
  The load-displacement curve is saved after each load step into the file '<*modelname*>.ldp'.
- Model Output file '.out'
  The model data file consists of all relevant variables to plot later the

resulting deformed geometry, stress state, fractured model etc. (node vector, displacement vector, element stresses, element status etc.). One file contains one particular state of the model at a certain load step. It is saved every x-th load step, while x can be set as a parameter in the model input file. The '.out' file name holds the model input file name, the count number of the saved step and the count number of runs (e.g. 'MODEL(Test.lat) CO-1 SC-1.out').

The user has three options to view results with the program 'PLOT3D.exe':

1. Rendered output
   Several '.obj' files are created. They contain the graphical representation of the lattice model. Every element (links, solids, contact elements and boundary conditions each in separate files) is presented as a geometric shape made of several surfaces. These surfaces with assigned colour and opacity can be viewed with a rendering program. For this project, the program *Bryce3D* (DAZ Production, Inc., 2004) was used, but any other commercial or public domain rendering software would be sufficient. It further can show the broken links as shaded surfaces in the lattice cells. This feature was particularly designed to depict the fracture path in a three dimensional lattice which would be otherwise hard to picture. The '.obj' file name holds: the type of elements that it contains, the model input file name, the count number of runs, the count number of the saved step and an number which is the internal load step at which the output file was saved (e.g. 'BC(Test.lat) CO-1 SC-1 (LS-100).obj'.
   LAT3D ⇒ Model Output file '.out' ⇒ *PLOT3D* ⇒ Object file '.obj' ⇒ Rendering Software ⇒ picture file e.g. '.jpg'
   Further details follow in subsection 5.11.2.

2. *MATLAB* figure window
   The general lattice and solid element lines can also be displayed in a *MATLAB* figure window.
   LAT3D ⇒ Model Output file '.out' ⇒ *PLOT3D* ⇒ *MATLAB* figure '.fig'

3. Load-Displacement plot *'.ldp'*
   The resulting load-displacement curve can be plotted in a *MATLAB* figure.
   LAT3D ⇒ Model LDP file '.ldp' ⇒ *PLOT3D* ⇒ *MATLAB* figure '.fig'

Listing 5.2: *Model input file (output parameters, shortened).*

```
$OUTPUT
SaveSteps = 1000
ShowSurfaceLines = true
ShowAllLines = true
ShowBrokenLines = 1,1,1,1,1,1,1,1,1
ShowNormalForceStrain = 1
Scale = 1
ScaleBCs = 2
ScaleForce = 0.01
CircleDiv = 48
OBJFrameGridSize = 3.0
OutSave = true

PlotCount = 1
PlotStep = 3
PlotType = 1
PlotOBJs = 1,2,3,4,5,6,7

OBJlinewidth = 0.05
OBJlinediv = 6
OBJframe = −20, 40, −20, 40, −20, 40
OBJpath = pwd
OBJfile = 'ObjectFiles\OBJ'
.
.
OUTpath =pwd
OUTfile = 'ModelData\MODEL'
LDPsave = true
LDPpath = pwd
LDPfile = 'LDP\LDP'
$END
```

5.11 Examples and Visualisation

5.11.1 Modification of LDP curve

Since, the laboratory tests deliver a LDP with constantly increasing displacement (i.e. no 'snap-back', due to displacement control), the resulting curves from the model output were modified in order to produce comparable plots.

This process is depicted in Fig. 5.33 where the original output of the model (green dashed line) is modified to show an increasing displacement (red line).

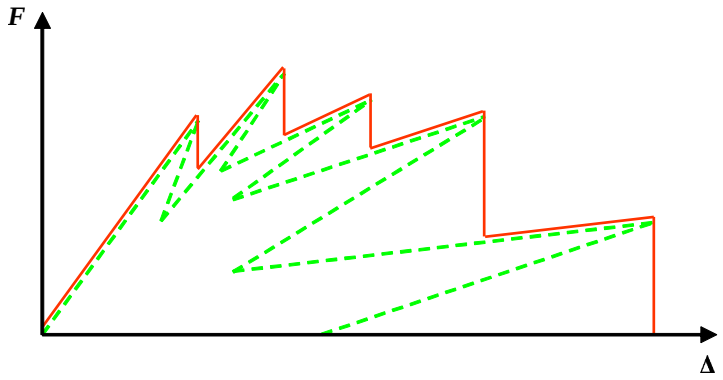

Figure 5.33: *Modification of model LDP output.*

5.11.2 3D Visualisation

The graphical representation of the model output, due to the large number of depicted elements, can be accomplished, as described in subsection 5.10.3, with a 3D render program (e.g. *Bryce3D*). The post processor of *LAT3D* makes use of the Wavefront file format '.obj' (Wavefront Technologies, 1984) which defines triangular or quadrangular surfaces and can be read generally by numerous graphics software.

Raytracing software such as *Bryce3D* (DAZ Production, Inc., 2004) calculates the colour of each pixel in a virtual screen by tracing the imagined 'ray' from the viewer to the various objects. The used file format makes it a quick and easy way to create meaningful graphics.

An example listing can be found in Lst. 5.3. This short 'obj.' file creates a cube with 8 nodes (voxels 'v')and 6 surfaces ('f') and using material '*BLUE*' that is

defined in the material file '*MAT.mtl*'.

Listing 5.3: *Output file for 3D render program '.obj'.*

```
mtllib MAT.mtl
usemtl BLUE
v 0.000000 2.000000 2.000000
v 0.000000 0.000000 2.000000
v 2.000000 0.000000 2.000000
v 2.000000 2.000000 2.000000
v 0.000000 2.000000 0.000000
v 0.000000 0.000000 0.000000
v 2.000000 0.000000 0.000000
v 2.000000 2.000000 0.000000

f 1 2 3 4
f 8 7 6 5
f 4 3 7 8
f 5 1 4 8
f 5 6 2 1
f 2 6 7 3
```

LAT3D creates several '.obj' files for various layers with different element types: boundary conditions 'BC[...].obj', frame of the coordinate system 'BOX[...].obj', solid surface elements 'SOLID[...].obj', lattice elements 'LAT[...].obj', 'LATBROKE[...].obj', 'OBJ[...].obj' and 'VIS[...].obj'. Each '.obj' file requires a definition of the used colours. This information is stored in a separate file ('.mat' file) and included in the actual '.obj' file ('**mtllib** *file*'). For each element the chosen colour is picked with '**usemtl** *colour*' and coordinates are defined ('**v** *x,y,z*'). The surface is defined with '**f** *r1,r2,r3,r4*'.

The fracture pattern is depicted as coloured surfaces on the lattice cells. Pink for broken links under tension/compression (status ④) and purple for links in compression (status -⑫).

The boundary conditions are represented in the form of geometric cones, (for 'fixed' in the direction of the cone's longitudinal axis) and arrows for forces acting in the respective direction. The contact elements are depicted as blue (open) and red (closed) nodes while the target surfaces are a green circular area (washer) or line

(bolt), respectively.

5.11.3 3D Bolt Example

A brief example shall show the validity of the 3D geometric nonlinear beam elements. Fig. 5.34 shows the load-displacement plots of a geometric nonlinear cantilever beam ($\varnothing$=10 mm, E_{Steel}=210 kN/mm^2). The beam is loaded with F =30 kN at a lever arm of l=100 mm and divided into 5 elements. The plot depicts the tip displacement in direction of X (applied loading) and Z (beam axis). For a comparison, the green curve represents the same model solved with the program MASTAN2 v1.0 (presented in McGuire et al. (2000)) which included stress stiffening. This lead to a slight deviation from the calculated *LAT3D* curve. The load is applied in 10 consecutive linear steps (Euler method as described in subsection 5.2.5). The displaced and initial rendered model output can be seen in Fig. 5.35. Each element is represented as a cylinder on a straight line between nodes with top and bottom circles that are rotated to match the respective nodal rotation.

5.11.4 2D Bolt-Lattice-Contact Example

The following example demonstrates the use of geometric nonlinear beam elements getting in contact with a small 2D lattice structure. The beam elements represent a bolt with a certain diameter, which is fixed and free to rotate at one end and has a force applied at the other unconstrained end. All DoFs in the Y direction are fixed for this 2D example. The parameters for the lattice and bolt elements are arbitrarily chosen and don't reflect any true lattice timber behaviour. The example shall only serve to show the functionality of certain element types and the working of the SSC algorithm. The smoothing of the contact surface is switched off (refer to Fig. 5.28).

Fig. 5.36 shows the load-displacement response of the described example. The underlying blue line is the original load-displacement response of the system with the red line being the modified version. Next to the load-displacement plot are model depictions placed for different load steps (I.,II., IV., V., VI. and IX.). For the nonlinear solution the geometry of bolt and contact elements is updated in every

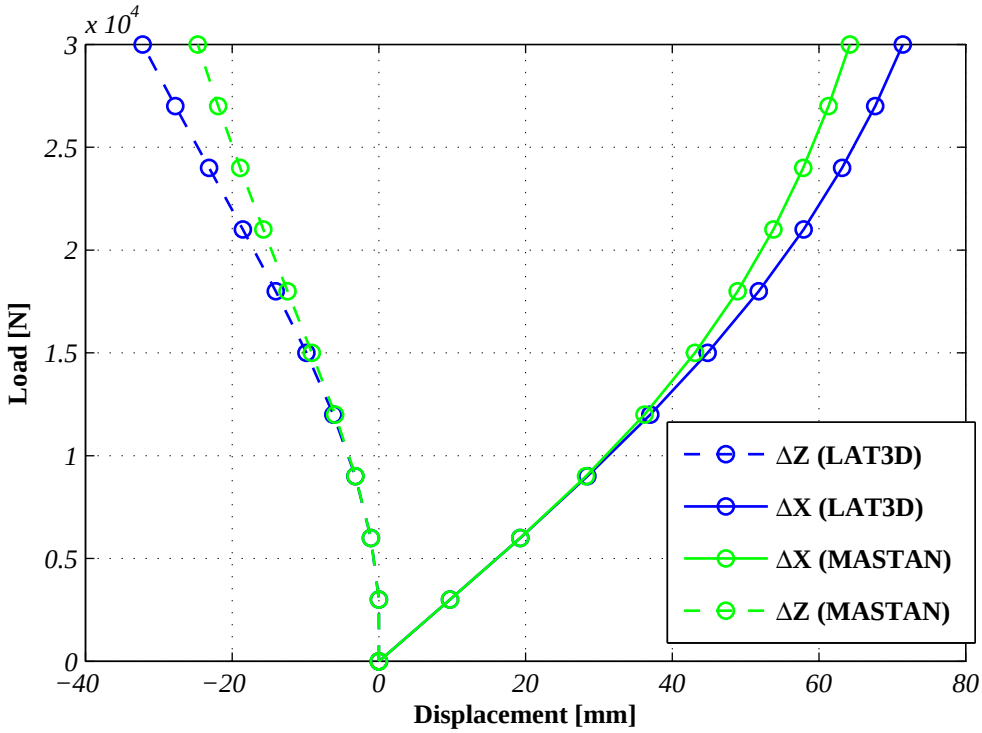

Figure 5.34: *LDP of cantilever example, displacement in X (solid) and Z (dashed) versus applied load, (original in colour).*

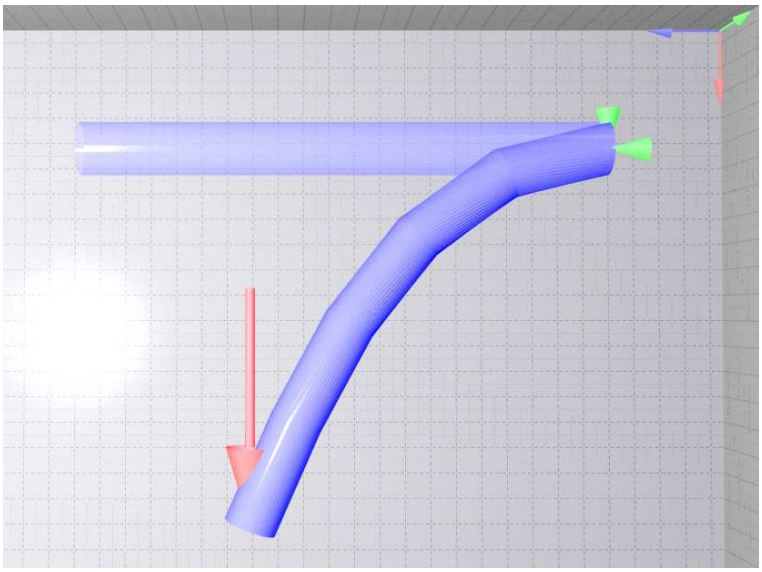

Figure 5.35: *Rendered output plot of cantilever example with geometric nonlinear beam elements.*

load step. One or more intermediate steps (blue dots) can be added in between the normal material nonlinear step (green dots) in which stiffness changes for a link occur. In these intermediate steps the geometry is still updated, thus geometric nonlinearity is accounted for in an 'Euler Method' type fashion (subsection 5.2.5). Instead of applying the calculated load step in the SSC algorithm $\lambda_{i,SSC}$ that is required to bring one link into the next status, an increasing fraction of this factor in an intermediate step j is consecutively applied, λ_i. This is calculated according to

$$\lambda_i = \frac{j}{j_{max}} \lambda_{i,SSC} \tag{5.95}$$

As $\lambda_{i,SSC}$ gets smaller during these intermediate steps, since it is determined again in each intermediate step, factor $\frac{j}{j_{max}}$ gets bigger. Thus, the intermediate steps are placed exactly evenly distributed on the line between on main load step, as can be seen in the load-displacement curve of the example. This is different to the previous described example where no material nonlinearity is considered and the consecutively applied load factor is simply the same ratio.

In the example here, one additional intermediate step is chosen ($j_{max} = 2$). Table 5.6 describes the status changes of the different link elements.

Table 5.6: *Link status changes for 2D bolt-lattice-contact example.*

main load step i	**status change**
I.	initial state
II.	1. contact link closes
III.	1. diagonal link changes to softening
IV.	1. diagonal link changes to broken
V.	2. contact link closes
VI.	3. contact link closes
VII.	1. lateral link changes to softening (compression, $0 > \gamma_C < 1$)
VIII.	2. diagonal link changes to softening
IX.	2. diagonal link changes to broken
X.	2. lateral link changes to softening (compression, $0 > \gamma_C < 1$)
XI.	3. lateral link changes to softening (compression, $0 > \gamma_C < 1$)
XII.	maximum set displacement (0.75mm) is reached

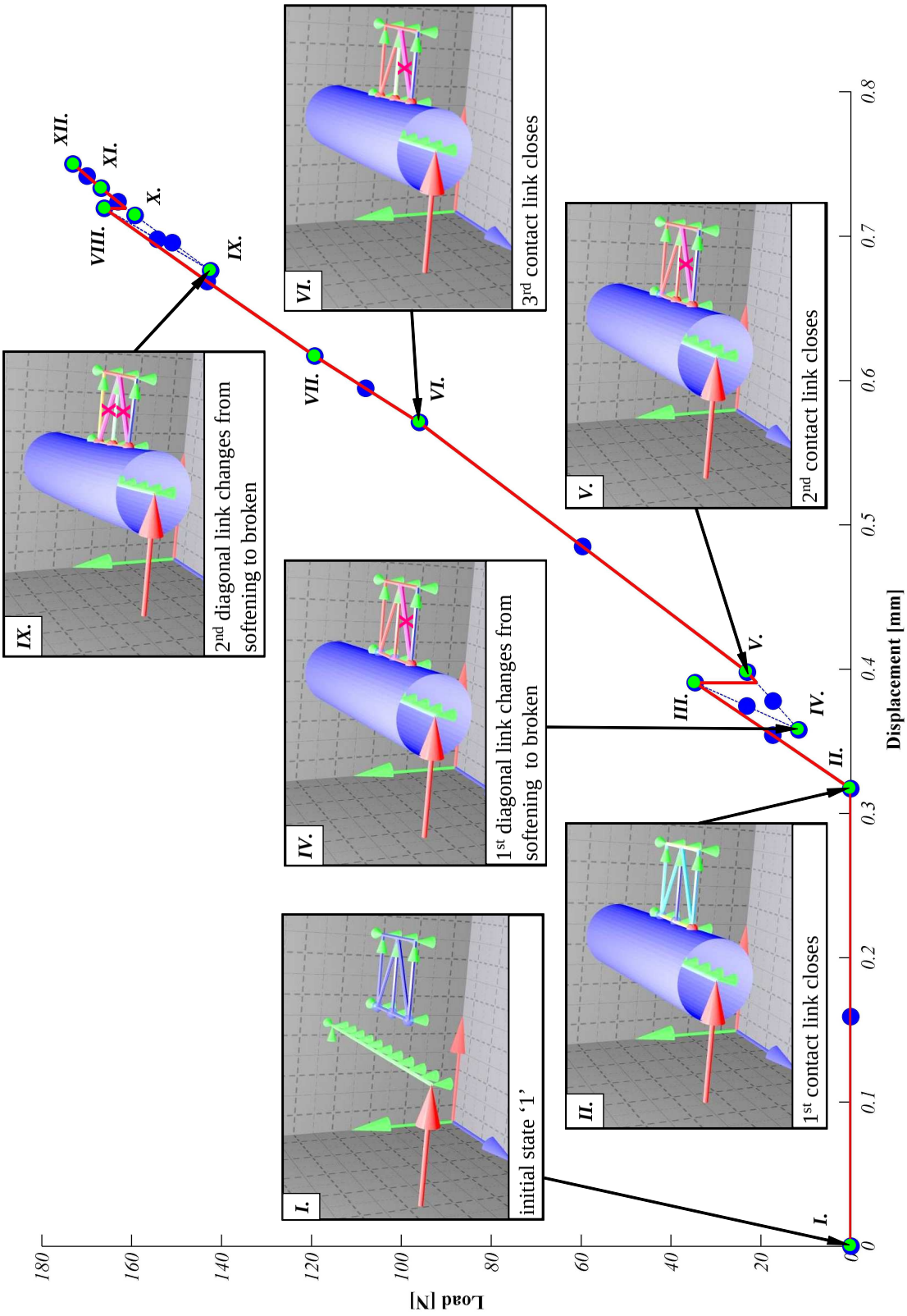

Figure 5.36: *Load-displacement plot from 2D bolt-lattice-contact example, blue dots mark intermediate load steps (original in colour).*

5.12 Summary

In this chapter the various elements that are used in *LAT3D* program along with the specialised FE routines were presented. All relevant parameters that define lattice models were listed and the mapping of structured and unstructured variation of these parameters on the lattice was described. Furthermore, the functionality of the program and its elements was shown with several examples. The following chapter uses the before described program to calibrate the lattice model and presents comparisons to experimental laboratory tests.

6 Results

6.1 General

This chapter introduces a possible calibration routine for the lattice model. Four different types of parameters have to be determined in order for *LAT3D* to create the tri-linear load-displacement relation of the individual link elements:

- elastic parameters
  mean stiffness $\overline{K}_j$ and $c_{v,j}$
- strength and PY parameters
  mean strength $\overline{S}_j$, γ_j and $c_{v,j}$

  for $j = X, Y = Z, YX = ZX, YZ$

and in order to adjust the mean strength and stiffness values of individual links:

- wood morphology parameters (structure)
  mean parameters $mean(\alpha, r_{pith}, \overline{r}_{shift}, \Delta r, r_{var})$ and c_vs
- wood morphology parameters (normalised density)
  mean parameters $mean(\overline{\rho}_{min}, \overline{\rho}_{diff}, \overline{\rho}_{exp})$ and c_vs

For the determination of these input parameters of the 3D lattice models, 6 test series were conducted with small Sitka spruce (*Picea sitchensis*) samples. These are listed with the respective label in Table 6.1 with the additional joint test.

An additional letter in the label, A or F indicates the origin of the timber (Forest Ae and Fingland respectively).

Since the calibration of the lattice strength parameters is an iterative process, only the first results of this approach are presented here. Reichert & Ridley-Ellis (2008) describe the model and the calibration routine in general and present a preliminary

Table 6.1: *Test series with respective labels.*

label	load type	direction of load
T-R/T-*no*	mode I fracture test, tension	radial and tangential
S-RL/TL-*no*	shear	RL and TL plane
T-L-*no*	tensile	longitudinal
C-L-*no*	compression	longitudinal
C-R-*no*	compression	radial
C-T-*no*	compression	tangential
J-M10-*no*	joint test with bolt M10	[-]

result.

However, even after several iterations the model can not be adjusted to a completely arbitrary set of parameters due to the constraints of the lattice cell structure. This limits the match between test results and FE model. A further constraint is the cell size which determines the possible modelled maximum stress concentration at a crack tip.

From each test specimen, parameters that determine the characteristics of the growth ring structure were measured. These influence the variation of the link's strength and stiffness parameters by mapping an artificial growth ring structure and density profile onto the lattice model, as described in section 5.5.

Measurements of moisture and density were in accordance with the oven dry method (BS EN 13183-1, 2002). A complete list of moisture content and density values of all tested samples can be found in the Appendix A.2.

The model input files for each tests series with the parameters used can be found in the Appendix A.4.

6.2 Calibration

The lattice model's parameters are calibrated against test data. This is performed in several steps. Different tests on small clear timber specimens were undertaken to replicate relatively simple stress states. A cleavage test and a simplified shear test were carried out instead of an actual tension perpendicular to the grain test and

a standard shear test, which would have required special fixings for the test machine.

The 6 different test series are: a compression test and tension test parallel to the grain, a compression test and cleavage test perpendicular to the grain and a simplified shear test in the longitudinal direction. For each test series the respective element types ($j = X, Y = Z, YX = ZX, YZ$) can be calibrated.

From the test samples several different parameters were determined, regarding the geometry and boundary conditions, elastic and strength properties and the parameters defining the wood morphology:

- **Geometry and Boundary Conditions**
  Geometric parameters and boundary conditions were in accordance with the experimental tests.

- **Elastic Parameters**
  The longitudinal tensile E-modulus (MoE) was obtained from a tensile test. The remaining elastic properties and Poisson ratios were calculated from ratios for Sitka spruce (*Picea sitchensis*) published by the USDA (1999).

- **Growth Ring Structure Parameters**
  Characteristic parameters that define the growth ring structure of the specimens (such as ring widths, pith position, growth ring shift between back and front side of the specimen) were determined via scanned images of the specimen's cross-section. These parameters serve as an input to recreate an artificial growth ring structure (subsection 5.5.1).

Further parameters were derived indirectly:

- **Density Profile**
  It is assumed that the variation of strength and elastic properties vary according to the density profile of the specimen, thus parameters of a density profile were taken from different Sitka spruce samples. These parameters serve as an input to recreate a density profile for the model (subsection 5.5.2).

- **Strength Parameters**
  Values were determined by means of trial and error of comparing load-displacement plots resulting from the lattice models to the respective experimental test series.

Each parameter consists of a mean value μ and its coefficient of variation c_v. The different kind of input parameters along with the calibration routine are summarised in Fig. 6.1.

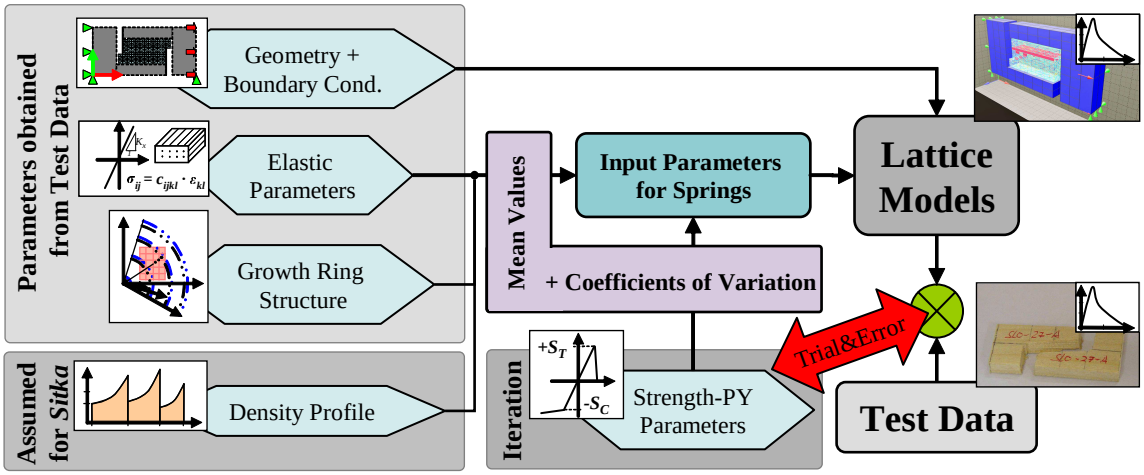

Figure 6.1: *Schematic of the calibration routine.*

In the following sections the determined elastic, strength, PY and wood morphology parameters are presented.

6.3 Elastic Parameters

The aim is to determine elastic parameters of the lattice based on given E-moduli. This can be accomplished by comparing one lattice cell to the equivalent elastic continuum volume. Therefore, the elastic lattice parameters K_j can be directly determined from a given set of elastic moduli and Poisson's ratios. The method can be formulated according to Ostoja-Starzewski (2002) as follows:

The stiffness K_j is determined by equating the strain energy U of a lattice with the strain energy of the equivalent continuum of the same volume as,

$$U_{cell} = U_{continuum}. \tag{6.1}$$

These strain energies can be determined in case of a single lattice cell with 'half'

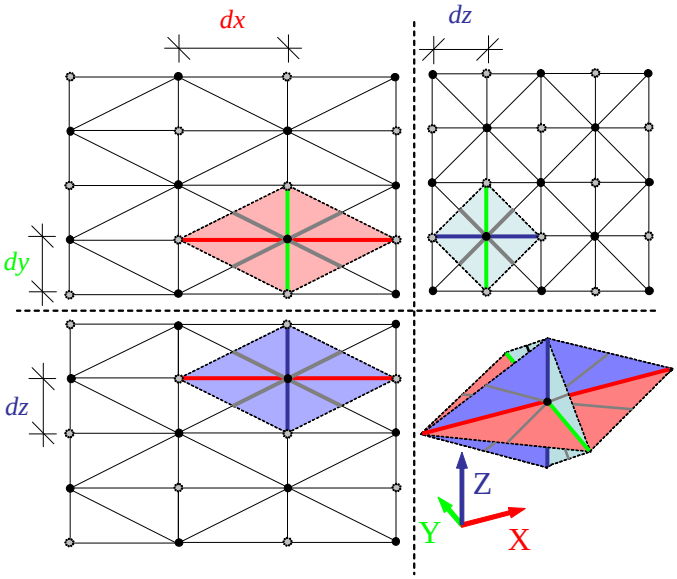

Figure 6.2: *Single lattice cell with 'half' links.*

links as shown in Fig. 6.2.

$$U_{cell} = \frac{1}{2}\sum_{b}^{N_b}(F \cdot u)^{(b)}, \; U_{continuum} = \frac{1}{2}\int_V \sigma\epsilon dV, \tag{6.2}$$

with F being the force and u the displacement of b-th link element, further σ is the stress field and ϵ the respective strain occurring in the reference volume V.

These equations can be further arranged as:

$$U_{cell} = \frac{1}{2}\sum_{b}^{N_b}(Ku \cdot u)^{(b)}, \; U_{continuum} = \frac{1}{2}\epsilon C \epsilon, \tag{6.3}$$

where K is the link's stiffness and C the 4^{th}-order stiffness tensor.

A subsequent step, assuming linear strain fields, involves equating both strain energies ($U_{continuum} = U_{lattice}$) and connecting displacement u with strain ϵ, thus deriving stiffness tensor C.

$$C_{ijkl} = \frac{1}{V}\sum_{b}^{N_b} l^{(b)^2} \cdot K^{(b)} \cdot n_i^{(b)} \cdot n_j^{(b)} \cdot n_k^{(b)} \cdot n_l^{(b)} \quad i,j,k,l = x,y \text{ and } z, \tag{6.4}$$

with length $l^{(b)}$ and unit vector $n^{(b)}$ of link element b. V represents the volume of

the unit cell repeating in space ($V = 2 \cdot dx \cdot dy \cdot dz$). The resulting stiffness tensor of size 3x3x3x3 can be reduced into Voigt notation with C_{ij} of size 6x6. By calculating the inverse of C, the elastic parameters E and Poisson's ratios can be determined.

$$C^{-1} = \begin{pmatrix} \frac{1}{E_{xx}} & -\frac{\nu_{yx}}{E_{yy}} & -\frac{\nu_{zx}}{E_{zz}} & 0 & 0 & 0 \\ -\frac{\nu_{xy}}{E_{xx}} & \frac{1}{E_{yy}} & -\frac{\nu_{zy}}{E_{zz}} & 0 & 0 & 0 \\ -\frac{\nu_{xz}}{E_{xx}} & -\frac{\nu_{yz}}{E_{yy}} & \frac{1}{E_{zz}} & 0 & 0 & 0 \\ 0 & 0 & & \frac{1}{G_{yz}} & 0 & 0 \\ 0 & 0 & & 0 & \frac{1}{G_{zx}} & 0 \\ 0 & 0 & & 0 & 0 & \frac{1}{G_{yx}} \end{pmatrix} \tag{6.5}$$

For the shown lattice cell, both, the effects of transverse strain and shear strain are combined in the diagonals of the respective plane. This restricts the lattice from representing any arbitrary orthotropy. Due to this, a routine was written that optimises the K values to match as closely as possible the elastic properties to a target function. A discussion follows this section on how a different method could be used to adjust the lattice's elastic properties more freely and thus match the given elastic properties better.

The longitudinal modulus of elasticity (E^*) is determined via a tensile test, which is described in more detail in subsection 6.5.4. For expediency the remaining elastic properties (E_j^*) are set according to the ratios for Sitka spruce that were obtained from the Wood Handbook (USDA, 1999).

Table 6.2 shows the ratios of elastic moduli to the longitudinal stiffness E_{xx} and Poisson coefficients obtained from the Wood Handbook. Furthermore, the resulting elastic moduli are listed based on the mean value E_{xx}=9792 N/mm^2 as measured in the tension tests.

Due to symmetry and the assumed transverse elasticity the following elastic parameters are equalised (mean values are taken):

$$E_{yy}^* = E_{zz}^*, \quad E_{zx}^* = E_{yx}^*, \quad \nu_{xz}^* = \nu_{xy}^*, \quad \nu_{zy}^* = \nu_{yz}^* \text{ and } \quad \nu_{zx}^* = \nu_{yx}^*. \tag{6.6}$$

The following table shows the target elastic properties along with the optimised values.

Table 6.2: *Resulting elasticity parameters.*

	ratio	**resulting E moduli** [N/mm^2]
E_{yy}/E_{xx}	0.043	421
E_{zz}/E_{xx}	0.078	764
E_{yx}/E_{xx}	0.061	597
E_{zx}/E_{xx}	0.064	626
E_{yz}/E_{xx}	0.003	29
		[-]
ν_{xz}	0.372	
ν_{xy}	0.467	
ν_{zy}	0.435	
ν_{yz}	0.245	
ν_{yx}	0.04	
ν_{zx}	0.025	

parameter	**target value*** [N/mm^2]	**result** [N/mm^2]
E_{xx}	9792	9608
$E_{yy} = E_{zz}$	592	681
$E_{zx} = E_{yx}$	612	557
E_{yz}	-	325
	[-]	[-]
$\nu_{xz} = \nu_{xy}$	0.42	0.49
$\nu_{zy} = \nu_{yz}$	0.34	0.37
$\nu_{yx} = \nu_{zx}$	-	0.035

The resulting K values are presented in Table 6.3.

The target function can be formulated with the target values (E^*, ν^*, from the Wood Handbook and the measured longitudinal E-modulus) and the determined

Table 6.3: *Resulting stiffness parameters.*

parameter	**result** [N/mm]
$K_{①,1}$	1424
$K_{①,2} = K_{①,3}$	357
$K_{①,4} = K_{①,6}$	1392
$K_{①,8}$	1298

values (E, ν, from the above described method) as,

$$\Phi^2 = \frac{1}{6}\left[\left(\frac{E^*_{xx} - E_{xx}}{E^*_{xx}}\right)^2 + \left(\frac{E^*_{yy} - E_{yy}}{E^*_{yy}}\right)^2 + \left(\frac{E^*_{yx} - E_{yx}}{E^*_{yx}}\right)^2 + ... \right.$$
$$\left. \left(\frac{E^*_{zx} - E_{zx}}{E^*_{zx}}\right)^2 + \left(\frac{\nu^*_{zy} - \nu_{zy}}{\nu^*_{zy}}\right)^2 + \left(\frac{\nu^*_{xz} - \nu_{xz}}{\nu^*_{xz}}\right)^2\right] \tag{6.7}$$

The simplex algorithm, as described in subsection 5.3.2 was used to optimise the target function. The goodness of fit as a result of the optimisation routine was calculated to be $\Phi = 0.0635$.

Note: the determined K_j values are used as the mean stiffness parameters in the lattice model $\overline{K}_j$. When a lattice block ($c_v = 0$) with these parameters is linked with solid elements set to the resulting elastic parameters and Poisson coefficients ($E_{xx}...E_{yz}$ and $\nu_{x,y}...\nu_{y,z}$, Table 6.2, right column) the lattice should behave exactly the same in terms of elastic deformation. This is true, provided that the solid block has an averaging effect on the lattice i.e. the mesh size is not smaller than the unit cell size of the lattice. Still, as soon as there is structured variation applied to the lattice elements (model input file: $WOODSTRUCT, enable=*true*), the blocks will behave slightly differently. This should not have a significant impact on the bulk hybrid structure since only minor stresses are expected to occur in the solid element region.

6.3.1 Alternative: Indirect Approach

Another way to calibrate the elastic properties of the lattice unlike the direct method described in the previous section can be found in Davids et al. (2003). The authors use a 2D lattice similar to the 3D version shown in Fig. 5.26. There,

the elastic parameters are determined indirectly by simulating a lattice of fixed size (6x4 cells) under single loading conditions (compression in X and Y, and shear in XY). A deformation is applied in the elastic range for the three different loading conditions (longitudinal, radial/tangential and shear). The bulk elastic properties are determined for the respective lattice models from the calculated load and deformation. Along with a target function and optimisation routine (simplex algorithm in subsection 5.3.2) similar to the one described in the previous section. The elastic parameters K are then optimised to the best fit.

The main difference of the used lattices here in this thesis to the 2D lattices described in Davids et al.'s paper is the implementation of the diagonal elements. In this paper, the angle under which the elements act between the node of one cell to the neighbouring cell can be adjusted freely and is left as an additional parameter in the optimisation routine. However, while this improves the goodness of fit the whole lattice is now size dependent. With this freely adjusted angle an element has been created whose stiffness contributions in X and Y are not according to the alignment of the connected nodes. Hence, an eccentric force is introduced to the lattice which is taken on by the lateral and longitudinal elements, Fig. 6.3. The result is a system which can't represent, for example, a state of pure shear nor a uniform transverse strain. The lattice system, further, becomes size dependent in the elastic range.

Davids et al. dismiss these differences between a lattice structure and the equivalent system of continuum elements since in their work only lattice elements are used. The bulk elastic behaviour is then predicted correctly for a certain given size in their calibration routine. For the program LAT3D here, where a hybrid form of 3D elastic continuum elements in combination with a lattice are used, it was tried to create comparable element behaviour. Hence, the above described method of equating both strain energies (lattice and continuum) is used, with the resulting inability to represent arbitrary orthotropic elasticity.

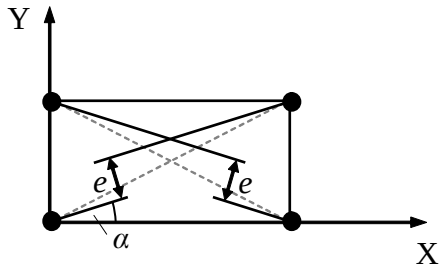

Figure 6.3: *Eccentricity as a result from the stiffness contributions (X and Y) of the diagonals which are not the same ratio as if the diagonals are aligned to their attached nodes.*

6.4 Wood Morphology Parameters

A detailed description on how the wood morphology is characterised and mapped onto the lattice model is explained in section 5.5.

The method to determine the parameters that characterise the ring structure is described in subsection 5.5.1. The resulting mean values and their coefficient of variation are listed in the following tables for each test series, Table 6.4.

It is assumed that all wood morphology parameters are normally distributed except for $\overline{\rho}_{exp}$. For this parameter a log-normal distribution is assumed since a negative value, which might occur for a normal distribution, would result in an unrealistic shape of the density profile.

Table 6.4: *Resulting parameters for the growth ring characterisation.*

test series		α [rad]	r_{pith} [mm]	$\overline{r}_{shift}$ [-]	Δr_{centre} [mm]	**mean** Δr_{diff} [mm]	**mean** r_{var} [mm]
T-R/T	mean	3.865	39.507	0.408	5.884	-0.072	-0.007
	stdev	0.320	8.495	0.293	1.629	0.274	1.917
(20 samples)	cov	0.083	0.215	0.719	0.277	-3.803	-283.0
S-RL/TL)	mean	1.815	33.168	0.609	6.313	-0.031	-0.119
	stdev	0.634	8.166	0.300	1.214	0.156	0.909
(17 samples)	cov	0.349	0.246	0.493	0.192	-5.031	-7.641
C-L	mean	2.885	50.990	0.421	5.170	-0.096	0.204
	stdev	2.047	14.269	0.294	1.265	0.189	1.275
(20 samples)	cov	0.710	0.280	0.699	0.245	-1.975	6.242
C-R	mean	7.788	54.761	0.528	5.247	-0.120	0.319
	stdev	0.370	12.574	0.328	1.081	0.146	0.750
(10 samples)	cov	0.048	0.230	0.621	0.206	-1.224	2.345
C-T	mean	3.131	49.493	0.503	5.125	-0.049	0.229
	stdev	0.444	8.539	0.283	1.183	0.137	0.553
(10 samples)	cov	0.142	0.173	0.562	0.231	-2.796	2.412
J-M10	mean	2.907	48.809	0.540	5.881	-0.138	0.361
	stdev	0.918	15.010	0.301	1.242	0.220	2.672
(10 samples)	cov	0.316	0.308	0.560	0.211	-1.599	7.402

The normalised density profile characterisation was obtained from 7 radial

specimens from pith to bark. After the curve fitting of a power function, as described in subsection 5.5.2, the mean values and their coefficients of variation were determined as shown in Table 6.5.

Table 6.5: *Resulting parameters for the density profile characterisation.*

		$\overline{\rho}_{min}$ [-]	$\overline{\rho}_{diff}$ [-]	$\overline{\rho}_{exp}$ [-]
	mean	0.717	0.982	1.958
(7 samples)	stdev	0.105	0.207	1.985
	cov	0.146	0.211	1.014

6.5 Strength and Post-Yield Parameters

A set of 6 different test series were conducted in order to obtain their load-displacement curves. The failure behaviour was then qualitatively assessed. Equivalent lattice models were constructed and could then be compared to the test results in terms of fracture behaviour and load-displacement.

For the experimental test set-up, small clear specimens were cut from Sitka spruce (*Picea sitchensis*) battens. The timber originated from two sites in the south of Scotland, Forest of Ae (A) and Fingland (F) with an age of 53 and 34 years, respectively. Although an overall difference in MoE and MoR was measured for these two sites both, were equally used in the calibration routine of the lattice model. All specimens were left in an environment controlled laboratory set to a constant temperature of 21 °C and 65% humidity until they attained constant weight.

The testing machine used was a Zwick Roell Z050 with a load cell of 50kN or 1kN, depending on the force range.

All test series were displacement controlled. Further, it was tried to reach the maximum displacement after $5 - 10$ min, therefore different test speeds were chosen. Table 6.6 shows the different speeds and pre loads used.

test series	**test speed** [mm/min]	**pre-load** [N]
T-R	1	2
T-L	0.2	10
S-LR/LT	0.1	10
C-L	1	1000
C-R	1	400
C-T	1	400
J-M10	2	100

Table 6.6: *Test speed and pre-load.*

In the next subsections the following results (laboratory set-up, experimental and model results of the respective test series with preliminary input parameters) will be presented:

- test set-up with fixing
- image of failed specimen
- FE lattice/solid model abstraction with boundary conditions
- model output figure
- load-displacement plots (LDPs) of lattice models compared to laboratory tests

Except for compression tests parallel and perpendicular to the grain, the S_{max} was determined as the maximum load of the LDPs. Initial stiffness was measured with the LDP points at 10 and 40% of S_{max}.

The set input values for the link parameters are listed in Table 6.8. Note: due to symmetry of the diagonals the following mean stiffness and strength parameters are the same: $\overline{K}_{①,4} = \overline{K}_{①,5}$, $\overline{K}_{①,6} = \overline{K}_{①,7}$, $\overline{K}_{①,8} = \overline{K}_{①,9}$, $\overline{S}_{T/C,4} = \overline{S}_{T/C,5}$, $\overline{S}_{T/C,6} = \overline{S}_{T/C,7}$ and $\overline{S}_{T/C,8} = \overline{S}_{T/C,9}$. Furthermore, due to the assumed transverse isotropy $\overline{K}_{①,2} = \overline{K}_{①,3}$, $\overline{K}_{①,4} = \overline{K}_{①,6}$ and $\overline{S}_{T/C,4} = \overline{S}_{T/C,6}$. The same applies to the respective coefficients of variation $c_{v,j}$.

Table 6.7: *Preliminary input parameters for the following lattice models.*

parameter	**value**	**unit**
elastic parameters		
elasticity parameters E_j		⇒ Table 6.2
stiffness parameters $\overline{K}_j$		⇒ Table 6.3
strength and PY parameters		
$\overline{S}_{T,1}$	100	[N]
$\overline{S}_{C,1}$	12	[N]
$\overline{S}_{T,2}$	7	[N]
$\overline{S}_{C,2}$	4	[N]
$\overline{S}_{T,4}$=$\overline{S}_{C,4}$	20	[N]
$\overline{S}_{T,8}$=$\overline{S}_{C,8}$	7	[N]
$\gamma_{T,1}$	1.01	[-]
$\gamma_{C,1}$	0.01	[-]
$\gamma_{T,2}$	1.01	[-]
$\gamma_{C,2}$	0.01	[-]
$\gamma_{T,4}$=$\gamma_{C,4}$	1.01	[-]
$\gamma_{T,8}$=$\gamma_{C,8}$	1.01	[-]
wood morphology		
$c_{v,l}$	0.2	[-]
$\lambda_{T,l}$	2	[-]
$\lambda_{C,l}$	2	[-]
$\lambda_{K,l}$	2	[-]
		for l=1..9
growth ring parameters		⇒ Table 6.4
wood density profile		⇒ Table 6.5

6.5.1 Perp. to the Grain Tension, Fracture Mode I (T-R/T)

The test specimens were small clears with the dimensions: 70x60x20 mm. A notch was cut to a previously drilled hole of 4 mm diameter. The round surface of this hole creates a consistent point of crack initiation among the test specimens. As long as the cleavage model represents this hole comparably in the respective lattice structure, it should be possible to calibrate the strength parameters to the tested specimens.

Two holes with a diameter of 8 mm provided a fixity for the test rig which was mounted onto the Zwick test machine. One displacement transducer was mounted on the notch side which measured the relative movement of both displacing parts of the specimen. Load from a 50 kN load cell along with the measurement from one displacement transducer was recorded. The test was stopped after 5 mm displacement.

Fig. 6.4 shows the schematic of the test set up with the two fixing clamps and one displacement transducer mounted on the side of the specimen, Fig. 6.5 a failed specimen and Fig. 6.6 depicts the respective FE model abstraction with applied forces and constraints. The rendered output figure is shown in Fig. 6.8. LDPs of model output and test were compared in Fig. 6.9.

Relative good agreement was found in terms of maximum load and fracture pattern. The large influence of growth ring structure on the fracture path can be clearly seen. Stiffness predictions did not match the actual LDP so well, this is due to the fact that the perpendicular to the grain E-modulus as obtained from the Wood Handbook did not match the measured stiffness. However, a lower modulus would not be possible in the elastic calibration routine without also changing the longitudinal or shear parameter.

Fig. 6.9 shows a comparison of the load-displacement plot from the tested specimens to the respective plot from the FE model.

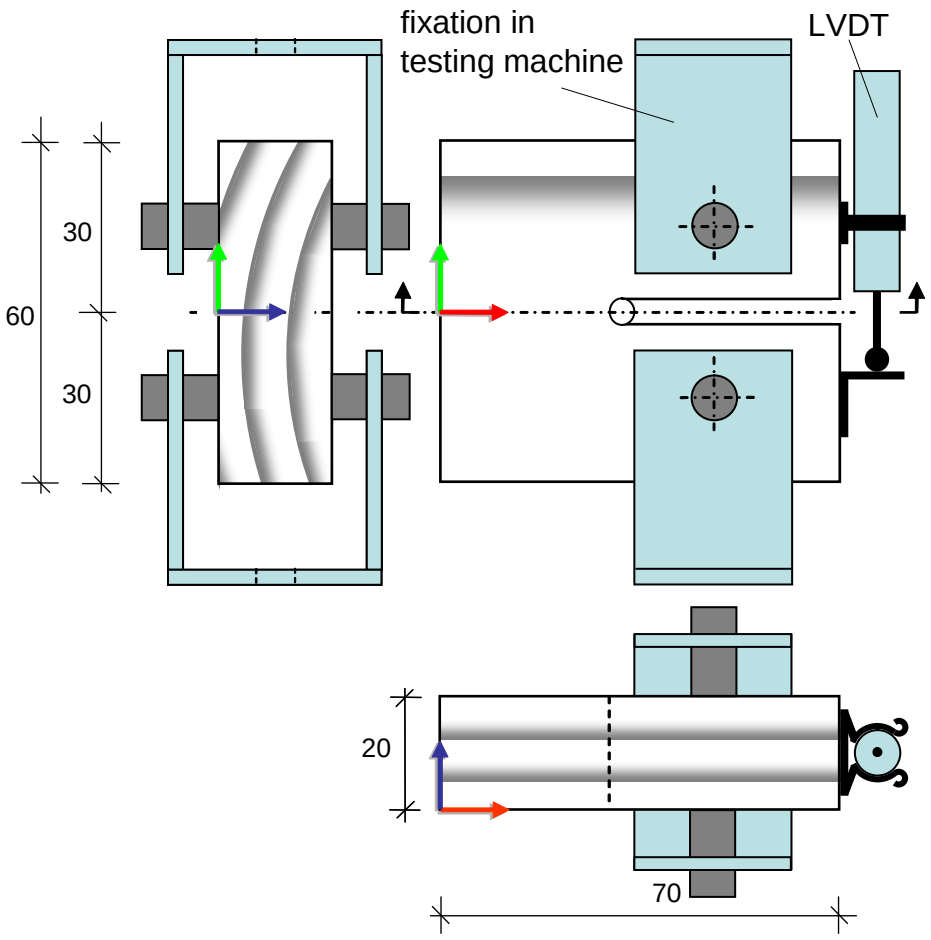

Figure 6.4: *Schematic of cleavage test **T-R/T**, fixation in the test rig and displacement measurement (original in colour).*

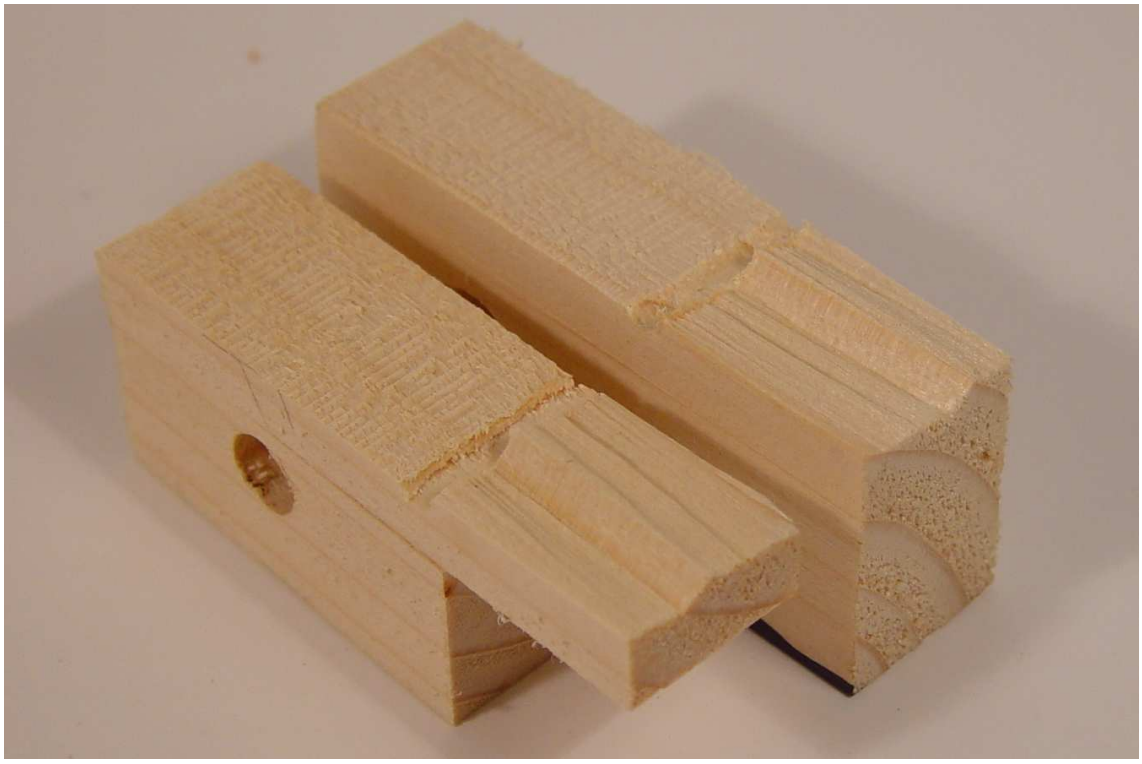

Figure 6.5: *Tested specimen* ***T-R/T*** *(original in colour).*

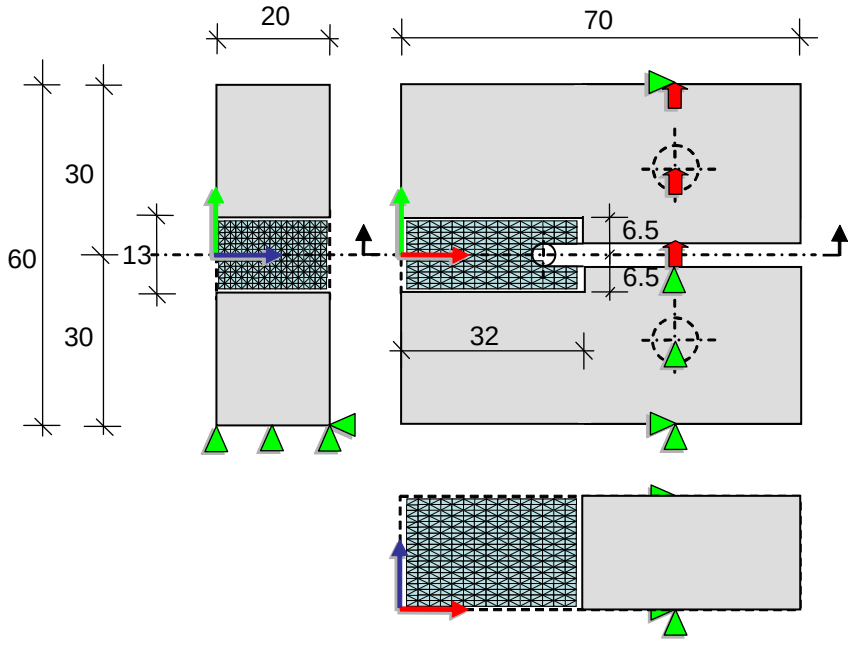

Figure 6.6: *Schematic of cleavage model (original in colour).*

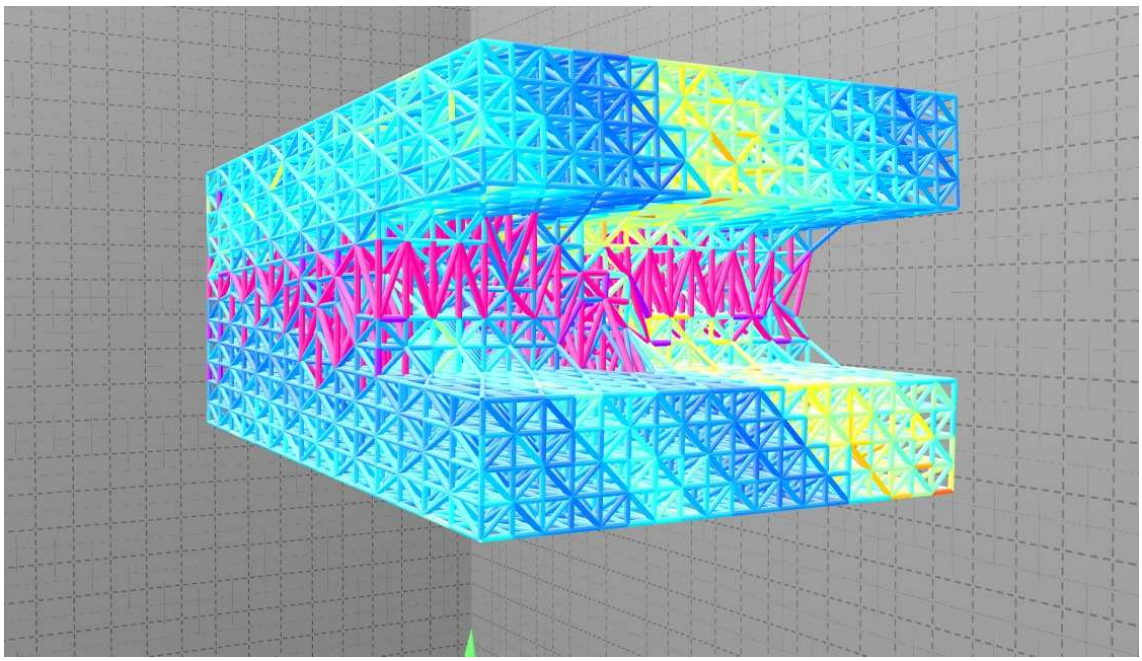

Figure 6.7: ***T-R/T*** *fracture pattern following the growth ring structure (original in colour).*

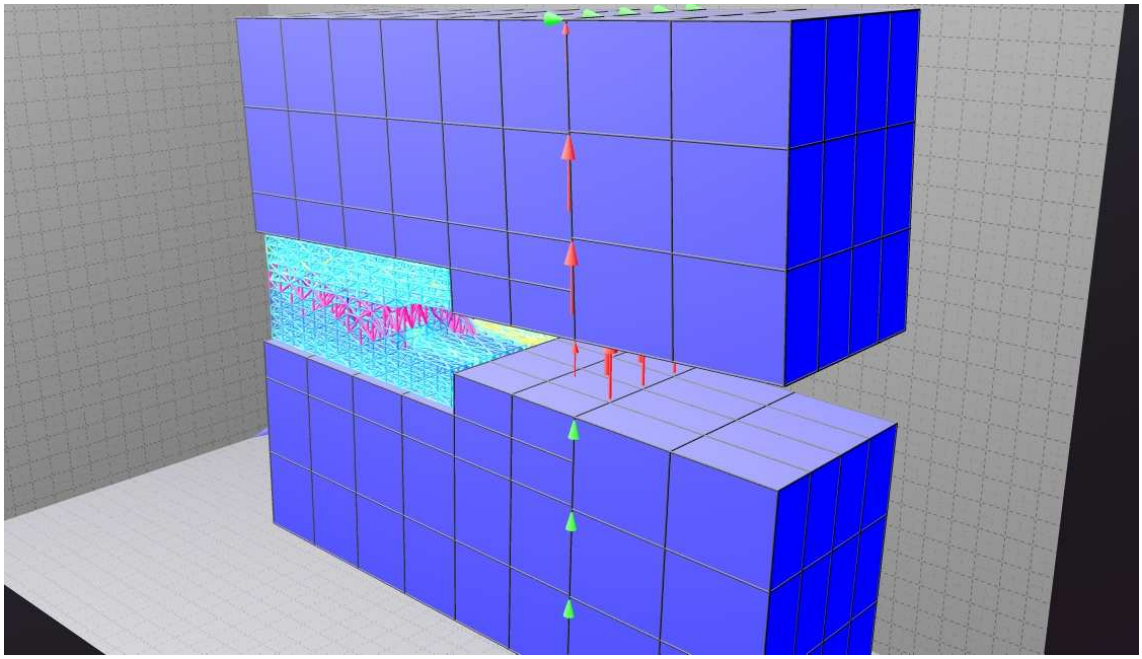

Figure 6.8: *Rendered output of* ***T-R/T*** *series, broken links and strength ratio is depicted on links (original in colour).*

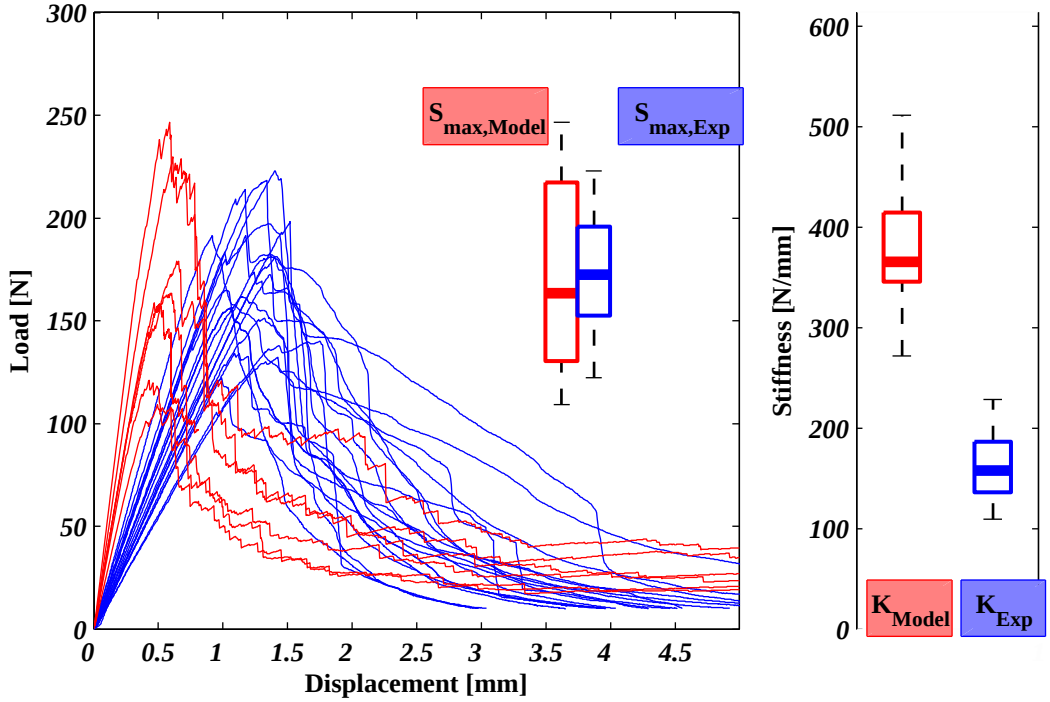

Figure 6.9: *Comparison of load-displacement among test and model for* ***T-R/T*** *series (original in colour).*

6.5.2 Parallel to the Grain Shear (S-RL/TL)

Test specimens measured 140x22x6 mm. Two notches of 12 mm were cut for the initiation of the crack. These specimen dimensions were in accordance with specimens tested in Fournier et al. (2007) with the modification to fit a 2x4 mm grid. The specimen was fixed in the testing machine via a vice-type grip at the right hand and left hand side (Zwick Z050 equipment 2.5 kN). Relative displacement was measured at a distance of 48 mm with an improvised extensometer as seen in Fig. 6.10. Load was measured with a 1 kN load cell. The test was stopped after 1 mm displacement.

Fig. 6.11 shows a failed specimen and Fig. 6.12 depicts the respective FE model abstraction with applied forces and constraints. The rendered output figure is shown in Fig. 6.13. LDPs of model output and test were compared in Fig. 6.14.

Predicted maximum loads were slightly lower than the laboratory measurements. However, a higher parameter for the diagonal lattice elements would conflict with a relative low value for lateral links, which is required in the **T-R/T** and **C-R/T** test series. A straight fracture line observed in the specimens can also be seen in the rendered output figure. As with the **T-R/T** tests, stiffness predictions did not match the actual LDP well.

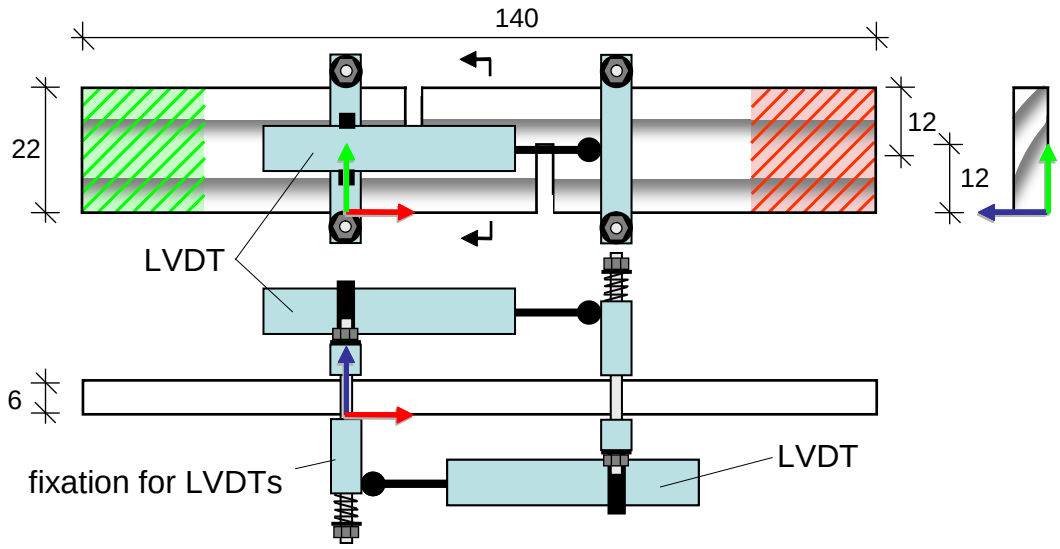

Figure 6.10: *Schematic of shear model **S-RL/TL**, fixation in the test rig and displacement measurement (original in colour).*

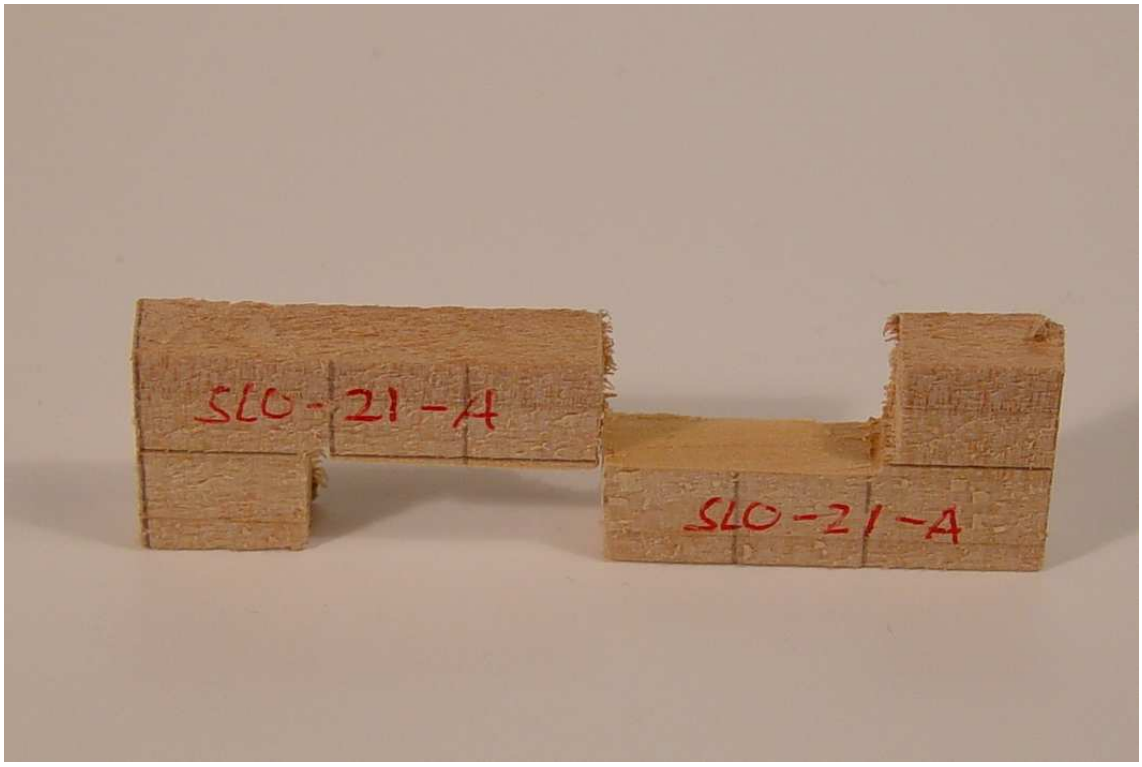

Figure 6.11: *Tested specimen* ***S-RL/TL*** *(original in colour).*

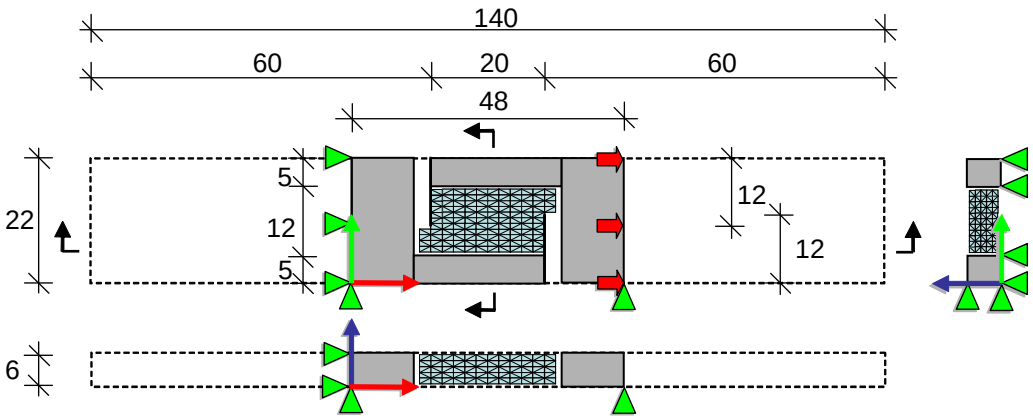

Figure 6.12: *Schematic of shear model (original in colour).*

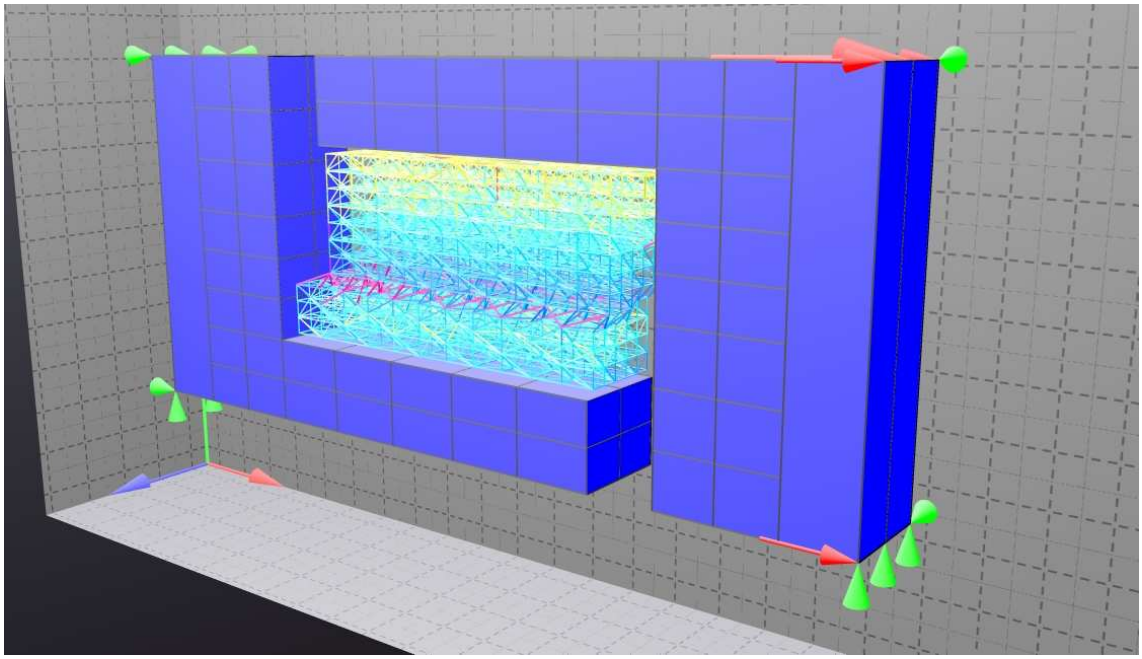

Figure 6.13: *Rendered output of **S-RL/TL** series, broken links and strength ratio is depicted on links (original in colour).*

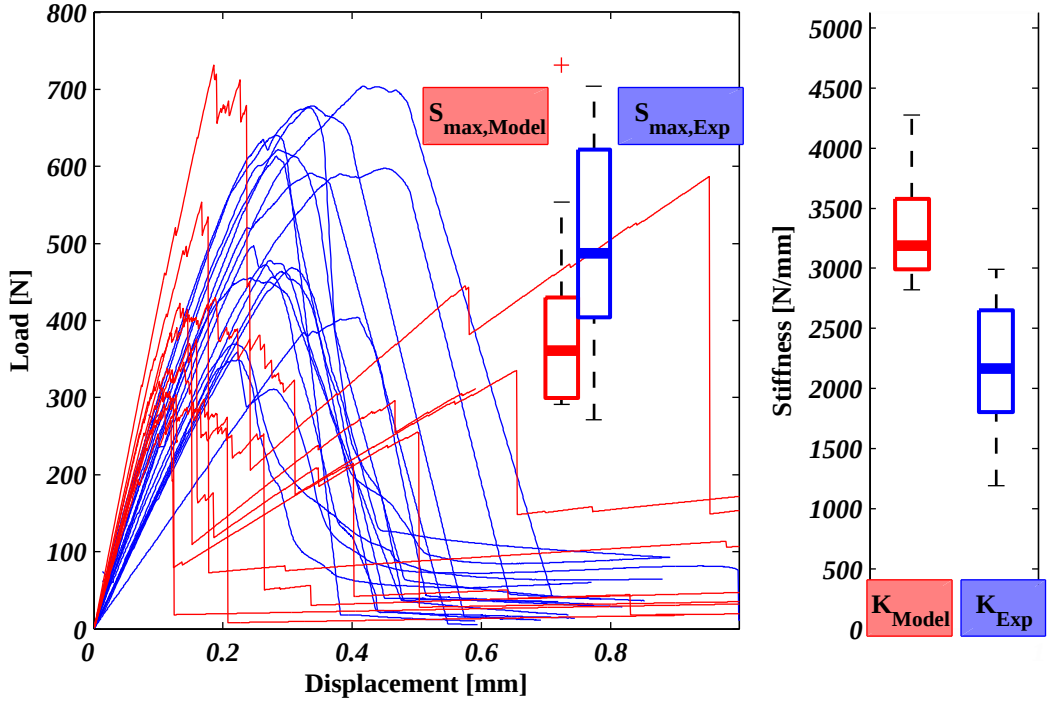

Figure 6.14: *Comparison of load-displacement among test and model for **S-RL/TL** series (original in colour).*

6.5.3 Parallel and Perpendicular to the Grain Compression (C-L, C-R and C-T)

Compression tests parallel and perpendicular to the grain were conducted. While the grain orientation for specimens loaded in the longitudinal direction (**C-L**) did not matter, tests perpendicular to the grain were distinguished between the radial and tangential loading direction. This can also be seen in the different orientation angle α in Table 6.4 for both series (**C-R** and **C-T**).

The dimensions of the specimens was chosen in accordance with BS 373 (1957), 20x20x60 mm for **C-L** and 20x20x20 mm for **C-R** and **C-T** respectively. Load was measured with a 50 kN load cell. The movement of the test machine head was taken as the measured displacement. The test was stopped after 5 mm displacement.

Due to the fact that the SSC algorithm with included plastic hardening links takes a very long time to compute, only half of the compression specimens of the **C-R/T** series and a quarter of the **C-L** series was modelled. Therefore, the obtained load in the LDP was multiplied with a factor of 2 and 4 respectively, in order to make the LDPs of the model and laboratory tests comparable. Note: the actual tested specimen is in fact not equal to the half and quarter model size, due to the mapped growth ring structure. The eventual difference that results from the smaller model size on the output LDPs was neglected in the comparison to test data.

Fig. 6.16 shows the test arrangement. Examples of failed specimens can be seen in Fig. 6.17 and Fig. 6.19. Fig. 6.18 depicts the respective FE model abstraction with applied forces and constraints. The rendered output figures are shown in Fig. 6.20 and Fig. 6.21. LDPs of model output and test were compared in Fig. 6.22, Fig. 6.23 and Fig. 6.24.

Maximum load, initial and secondary stiffness was determined by fitting a certain bi-linear curve to the LDP according to Fig. 6.15. The initial stiffness K, similar to the other test series, was determined at 10 and 40% of S_{max}. Maximum load for series **C-R/T** was measured in the same way as the other test series. S_{max} for series **C-L** is measured at the intersection point of line K_2 with the Y-axis.

While relative good agreement among fracture patterns can be found this was less the case in terms of maximum load. Especially for series **C-T** where a large

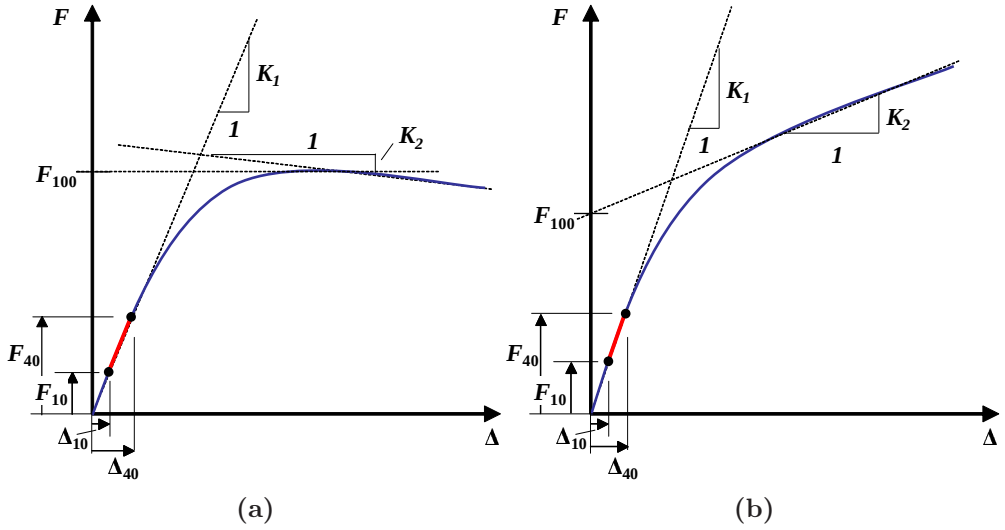

Figure 6.15: *Schematic of the determination of maximum load a) for test series* ***C-L*** *and b) for* ***C-R/T*** *respectively (original in colour).*

variation in ultimate strength is observed in the model this is much less the case in the tested specimens. Although a general higher strength for the tangentially loaded specimens than perpendicular ones is predicted (as seen also in tests), the model fails to predict the more uniform maximum strength in the **C-T** specimens.

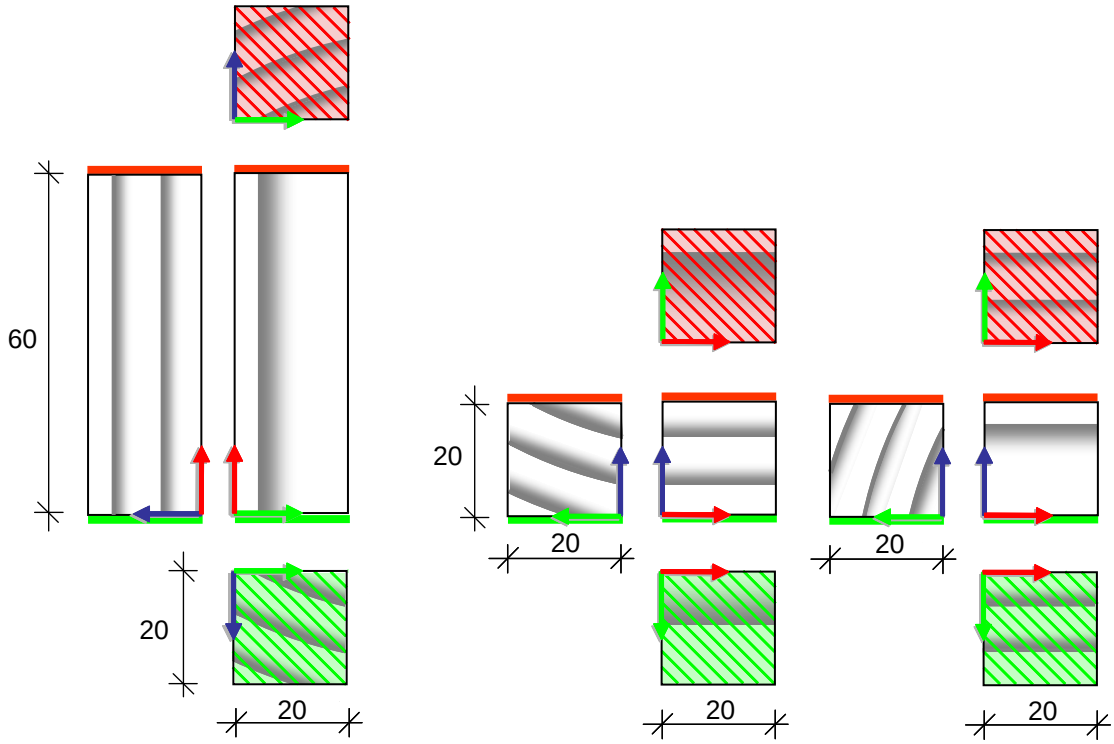

Figure 6.16: *Schematic of compression tests (longitudinal and radial/tangential to the grain) (original in colour).*

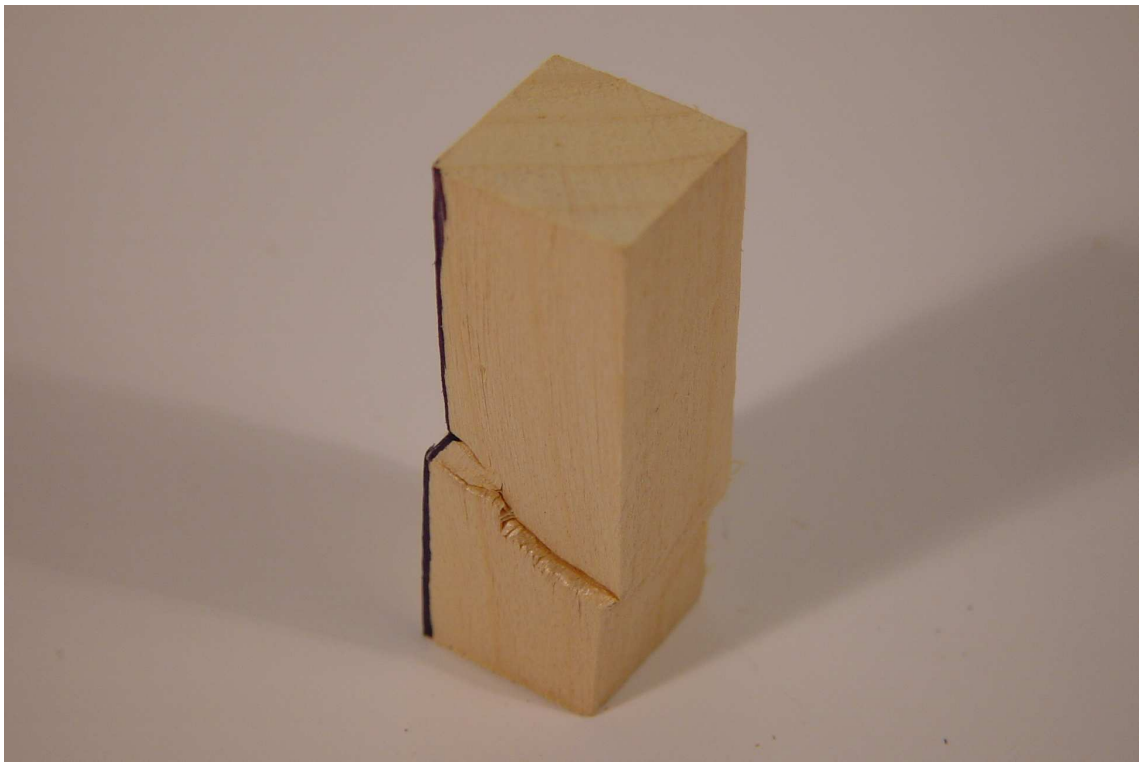

Figure 6.17: *Tested specimen* ***C-L*** *(original in colour).*

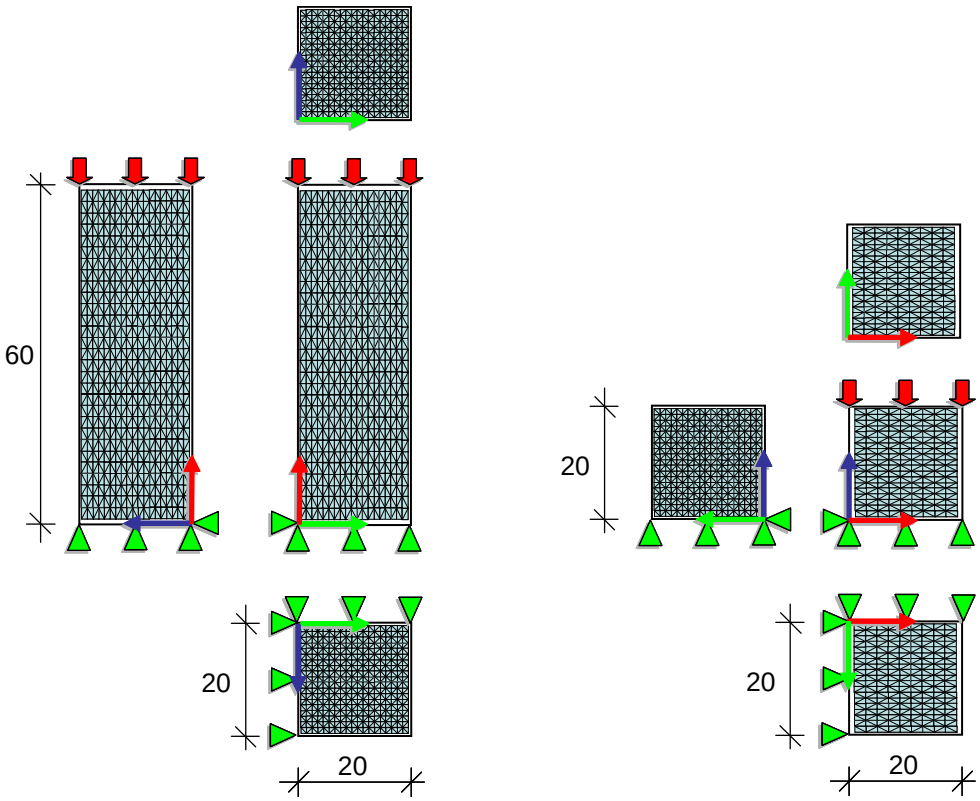

Figure 6.18: *Schematic of compression models (longitudinal and radial/tangential to the grain) (original in colour).*

Figure 6.19: *Tested specimen **C-R/T** (original in colour).*

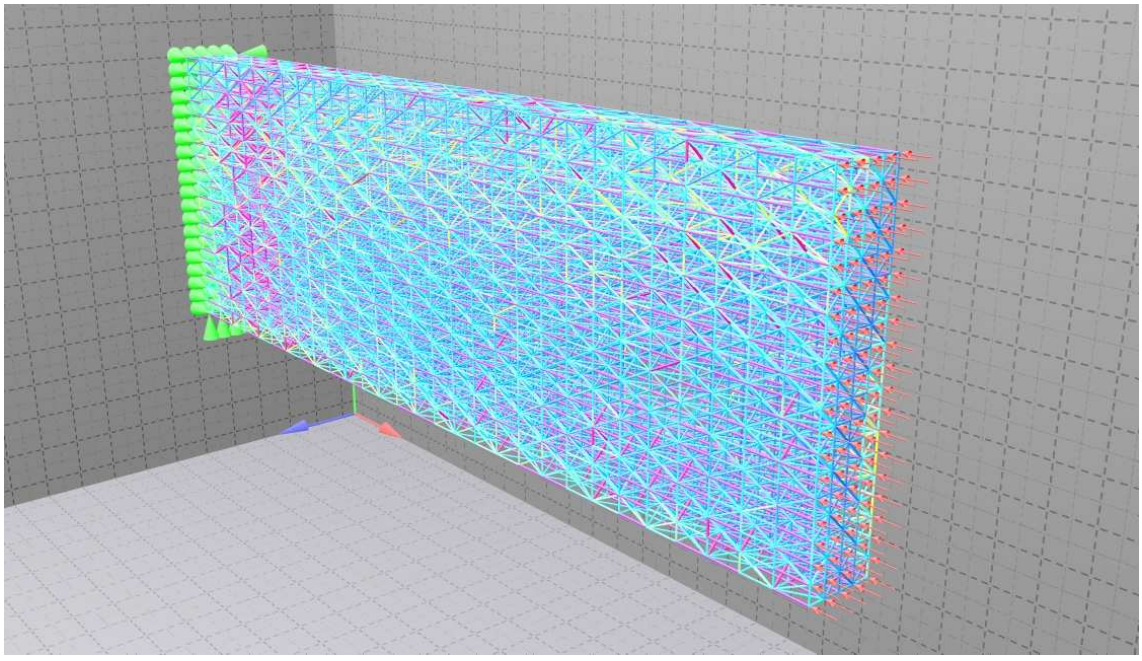

Figure 6.20: *Rendered output of **C-L** series, broken links and strength ratio is depicted on links (original in colour).*

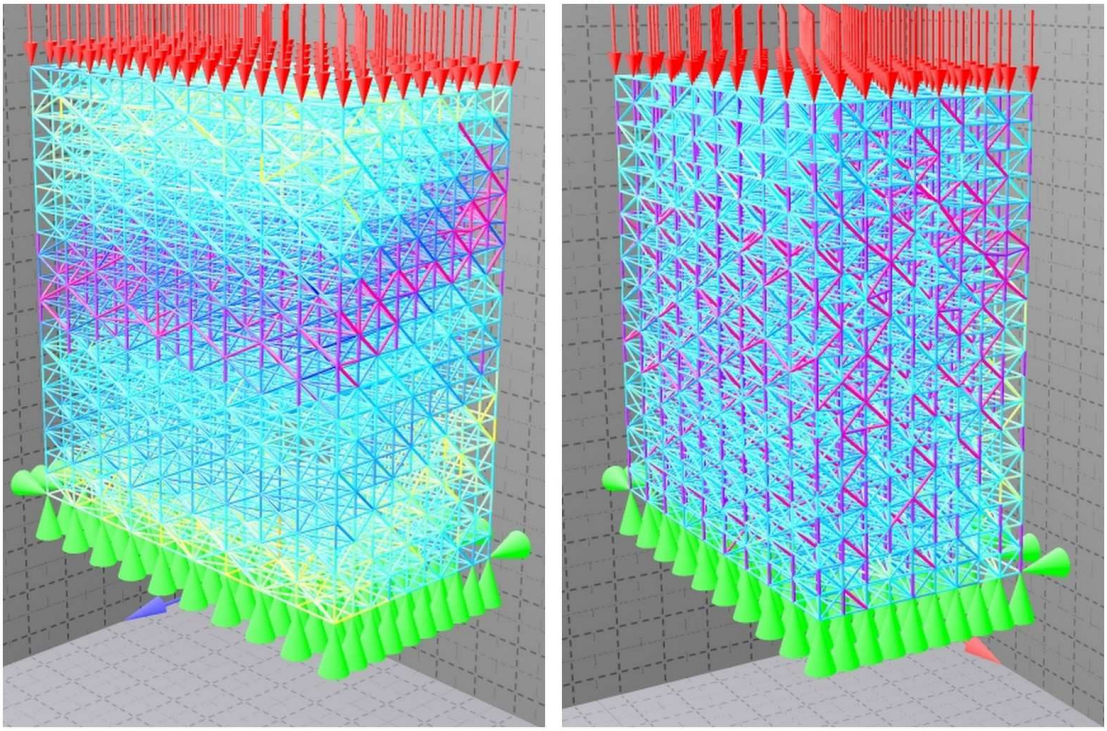

Figure 6.21: *Rendered output of **C-R** and **C-T** series, broken links and strength ratio is depicted on links (original in colour).*

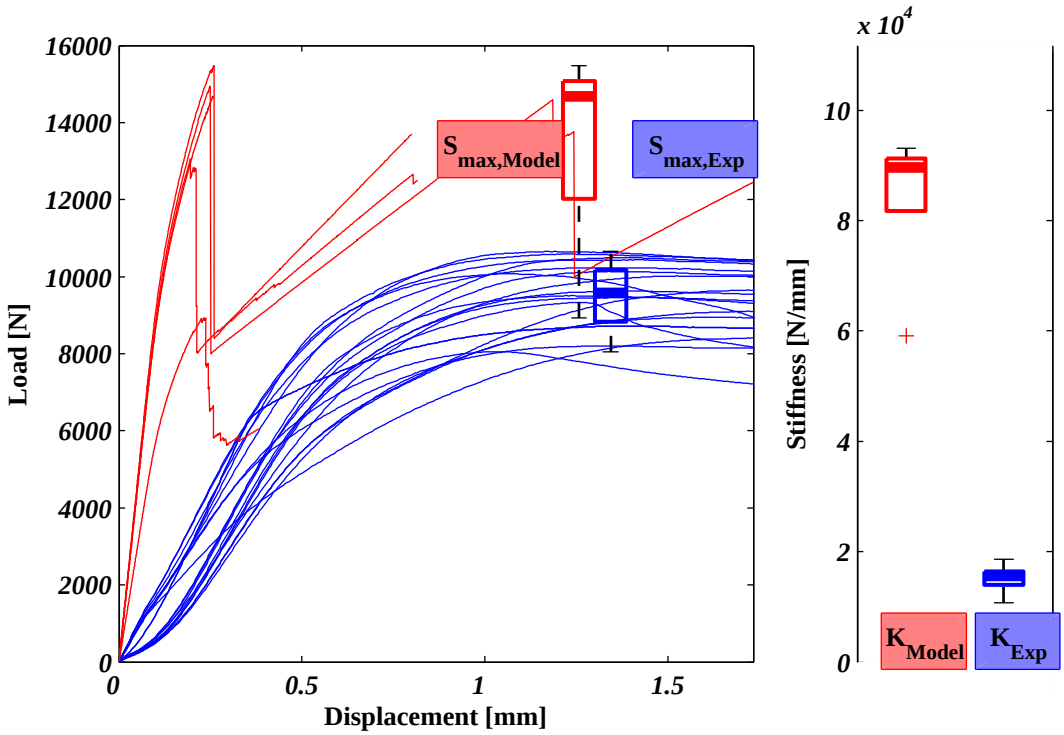

Figure 6.22: *Comparison of load-displacement among test and model for **C-L** series (original in colour).*

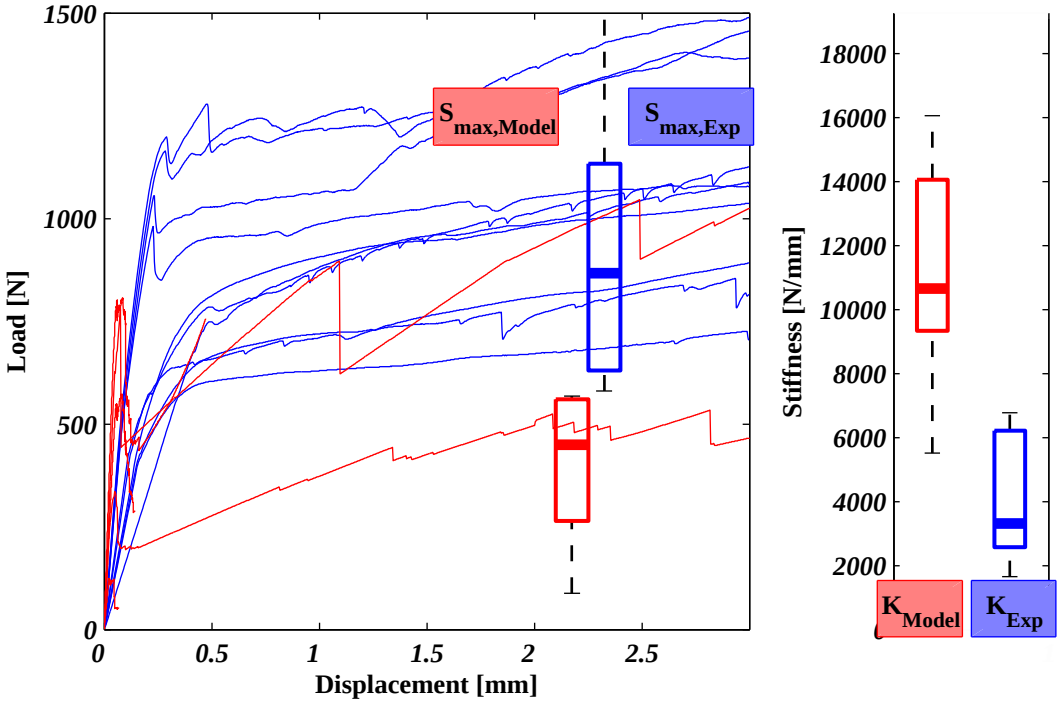

Figure 6.23: *Comparison of load-displacement among test and model for* ***C-R*** *series (original in colour).*

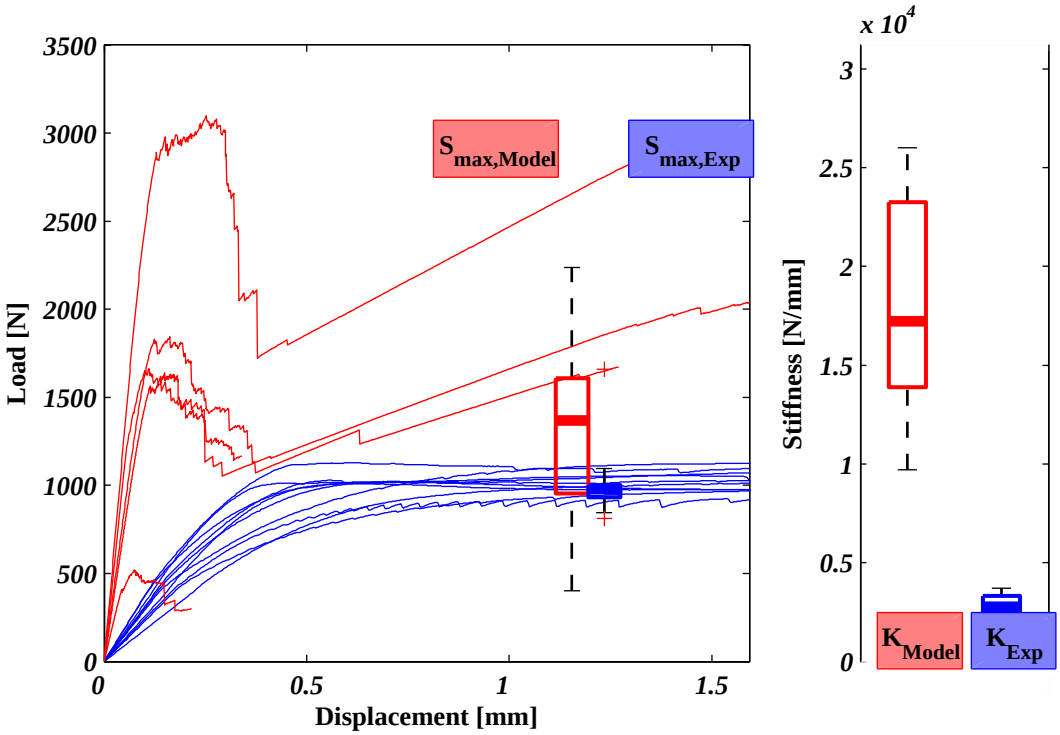

Figure 6.24: *Comparison of load-displacement among test and model for* ***C-T*** *series (original in colour).*

6.5.4 Parallel Tension (T-L)

Tension tests parallel to the grain were conducted with dimensions based on tests by Fournier et al. (2007) but with a slightly different cross section of 4 by 6 mm to match a grid size of 2x2 mm. The sizes can be seen in Fig. 6.26. The specimen was fixed in the testing machine similar to the shear tests. Relative displacement was measured at a distance of 70 mm with the improvised extensometer made of two displacement transducers, as seen in Fig. 6.26.

All test specimens broke in a sudden brittle manner within the 70 mm gauge length. The respective model simulations behaved slightly differently, which will be explained in more detail in chapter 7. Some lattice models still transmitted load after a sudden failure due to some unbroken diagonal elements. However, the LDP curve of the model output was cut off after a sudden drop in load of $> 30\%$.

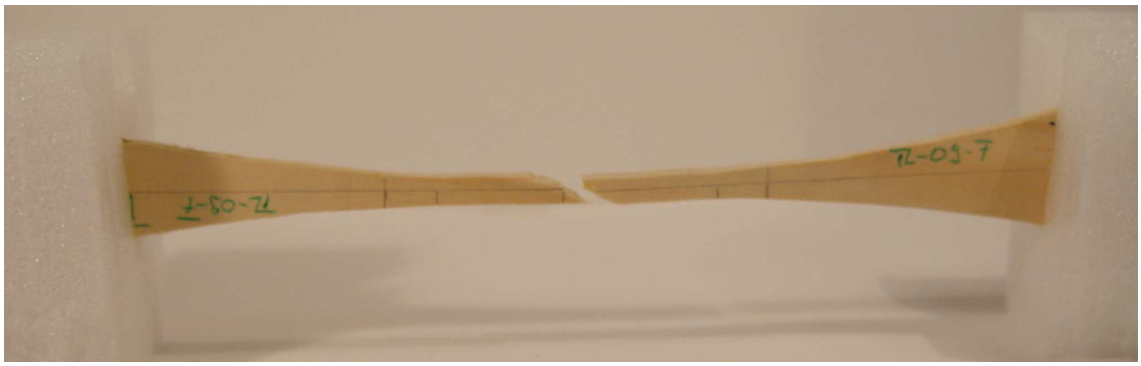

Figure 6.25: *Tested specimen **T-L** (original in colour).*

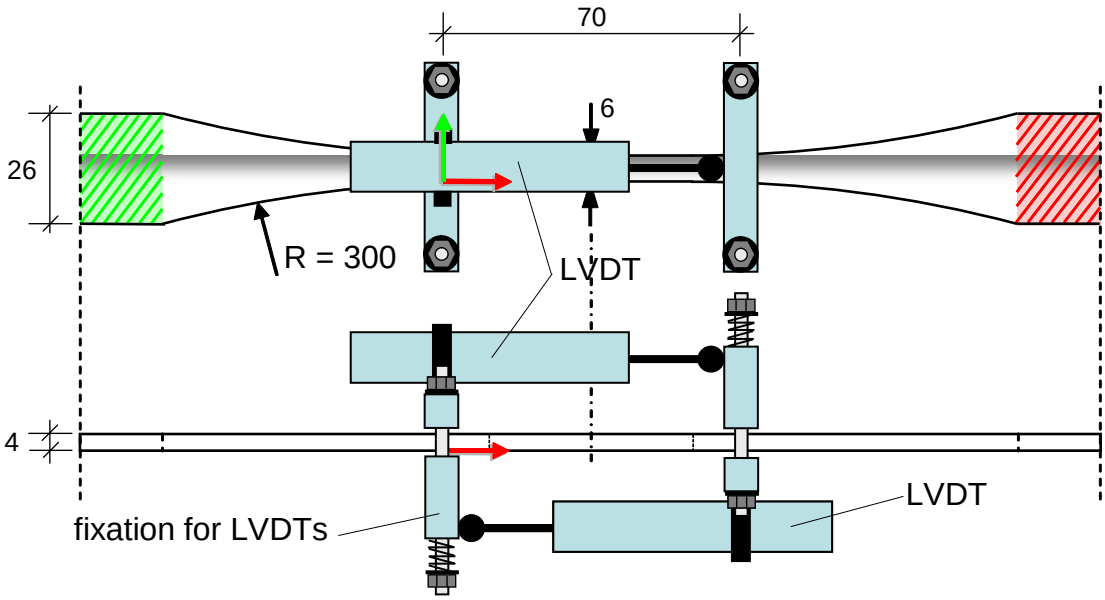

Figure 6.26: *Schematic of tension model, fixation in the test rig (original in colour).*

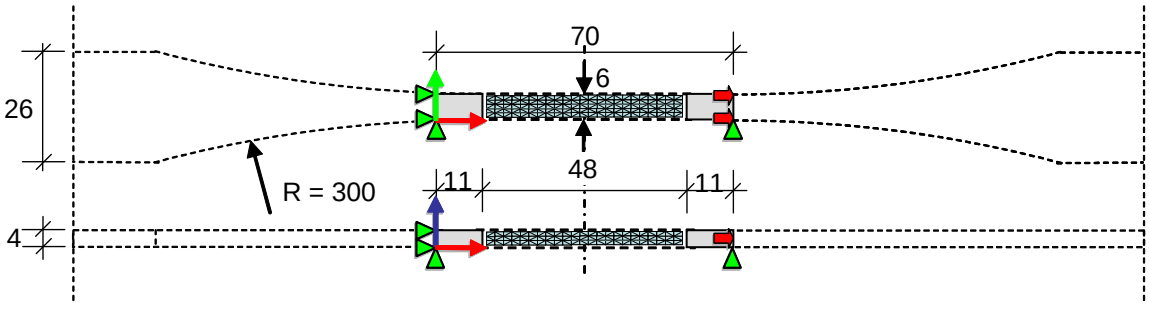

Figure 6.27: *Schematic of tension model (longitudinal) (original in colour).*

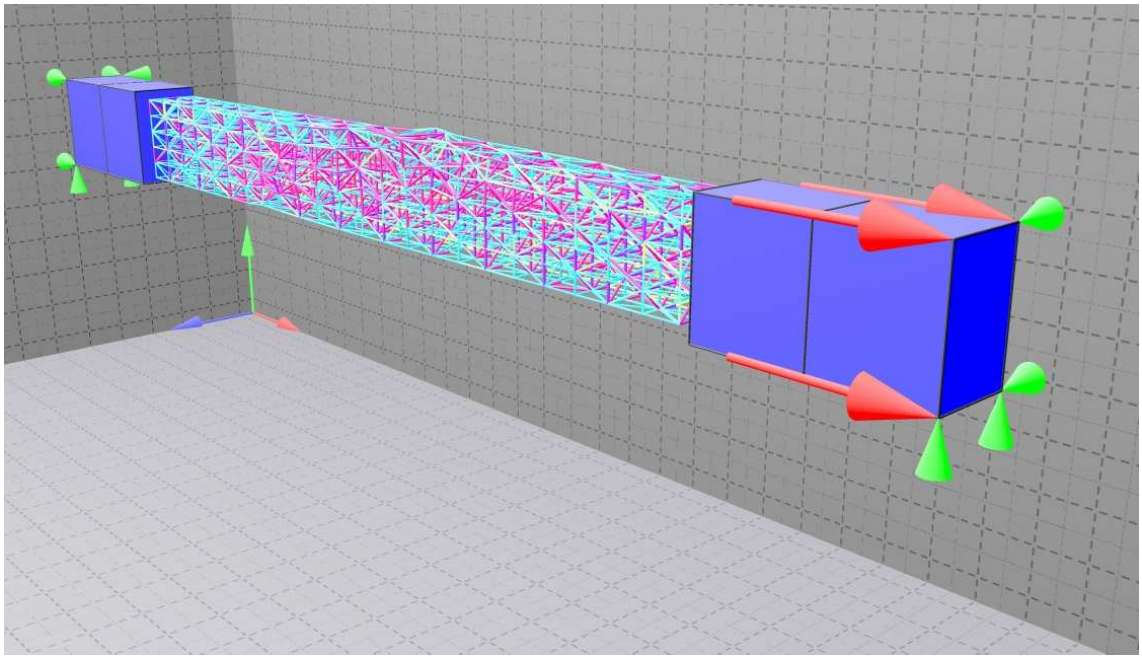

Figure 6.28: *Rendered output of **T-L** series, broken links and strength ratio is depicted on links (original in colour).*

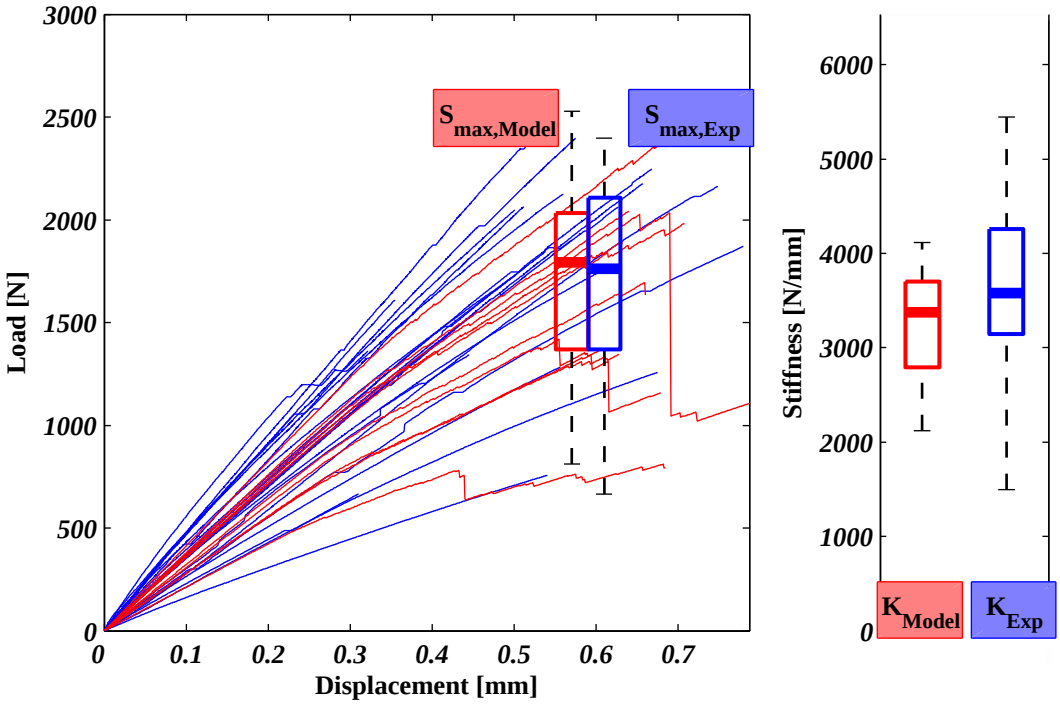

Figure 6.29: *Comparison of load-displacement among test and model for **T-L** series (original in colour).*

6.5.5 Ductile Calibration

In a subsequent step the parameters have been adjusted to exhibit more microductile softening to better fit the model LDPs to the ones obtained from the laboratory test specimens. Problems were encountered with the 3D model with considered micro-ductility. The solution algorithm stopped at maximum load indicating that a singularity point was encountered due to negative stiffness values of softening links. This is discussed further in section 7.2. Therefore, only a 2D model of the **T-R/T** series is presented here with varying micro-ductility parameters. Wood morphology is implemented in the 2D model, which consists of one lattice layer, in a similar way as it was done for the 3D case. The model schematic is the 2D equivalent of Fig. 6.6 with plane stress elements and a plane lattice of unit thickness.

Note: For the 2D model, different elastic stiffness parameters were determined from the given target elastic moduli similar to subsection 6.3. The resulting fit parameter is 0.1662 with resulting elastic moduli E_{xx} =10337 N/mm^2, E_{yy} =696 N/mm^2, G_{zx} =350 N/mm^2, $\nu_{xz} = 0.495$ and $\nu_{yx} = 0.034$.

For illustration purpose, the unmodified LDPs are drawn as green dashed lines in Fig. 6.30. One can observe that with increasing micro-ductility, an increase in strength, variation of maximum load and overall ductility can be seen. Furthermore, the 'snap-back' and jagged character becomes smoothed.

Table 6.8: *Input parameters for the ductile 2D lattice models,* ***T-R/T*** *series.*

parameter	**value**	**unit**
elastic parameters		
elasticity parameters E_j		⇒ see above
$\overline{K}_{①,1}$	2234	[N/mm]
$\overline{K}_{①,2}$	620	[N/mm]
$\overline{K}_{①,4}$	875	[N/mm]
strength and PY parameters		
$\overline{S}_{T,1}$	100	[N]
$\overline{S}_{C,1}$	12	[N]
$\overline{S}_{T,2}$	7	[N]
$\overline{S}_{C,2}$	4	[N]
$\overline{S}_{T,4}$=$\overline{S}_{C,4}$	20	[N]
$\gamma_{T,1}$	1.01	[-]
$\gamma_{C,1}$	0.01	[-]
$\gamma_{T,2}$	**1.5, 2, 3, 5**	[-]
$\gamma_{C,2}$	0.01	[-]
$\gamma_{T,4}$=$\gamma_{C,4}$	**1.5, 2, 3, 5**	[-]
wood morphology		
$c_{v,l}$	0.2	[-]
$\lambda_{T,1..9}$	1	[-]
$\lambda_{C,1..9}$	1	[-]
$\lambda_{K,1..9}$	1	[-]
growth ring parameters		⇒ Table 6.4
wood density profile		⇒ Table 6.5

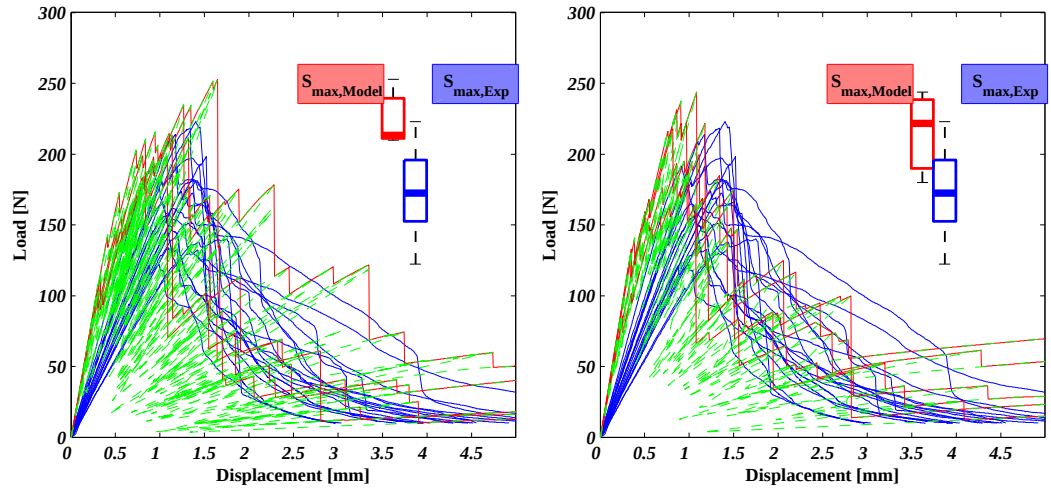

(a) $\gamma_{T,\{2,4\}}$=1.5 (b) $\gamma_{T,\{2,4\}}$=2

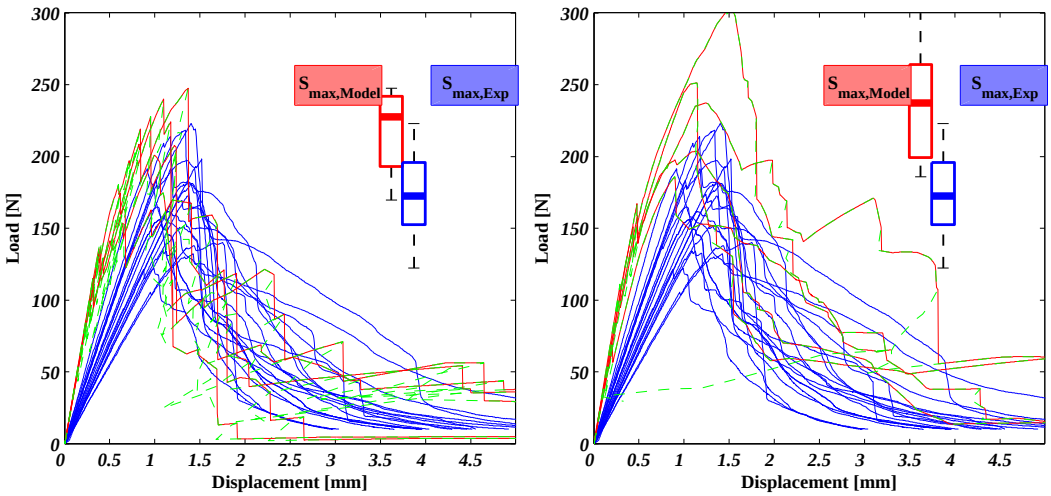

(c) $\gamma_{T,\{2,4\}}$=3 (d) $\gamma_{T,\{2,4\}}$=5

Figure 6.30: *Comparison of load-displacement among test and model for the ductile* ***T-R/T*** *series with* $\gamma_{T,\{2,4\}}$*=1.5, 2, 3 and 5 (original in colour).*

6.6 Joint Model (J-M10)

The timber joint model uses all of the aspects of *LAT3D* described in the previous chapter. These are namely geometric nonlinear beam elements (section 5.9), solid elements (subsection 5.2.2), material nonlinear lattice elements (section 5.4), their combination in a hybrid model (subsection 5.7.1) and elements for bolt-lattice and washer-lattice contact (section 5.8). Problems with the SSC algorithm led to a long time to solve the nonlinear solution for large lattices as used in this model. Furthermore, the algorithm stopped due to wrong load factor decision before the maximum displacement or singularity of the stiffness matrix was actually reached. Therefore, only a limited model output is presented here.

6.6.1 Structure Composition

For the full 3D joint model, only one half is actually modelled, making use of the symmetric arrangement of two timber members. Therefore the displacement, measured from bolt to the timber model edge, is multiplied by two. The symmetry was chosen in order to minimise the computational effort, although in practice the model could consist of two timber members. The bolt (nonlinear beam elements) is fixed at the symmetry line and free to rotate at the point where the loading is applied. The washer, simulated with special contact elements (subsection 5.8.2), is attached to the bolt element's node at the outer surface. The timber part consists of several blocks of solid elements and one lattice block, with 'notches' at the sides that are filled again with solid elements, in order to minimise the number of DoFs. Fig. 6.31 shows the schematic of the overall arrangement of the different elements types and blocks.

It was tried to achieve a brittle failure with a decreased edge distance (loaded edge) of $4d$ instead of $7d$ as required by BS EN 1995-1-1 (2004).

6.6.2 Results

An example of the rendered output of a 3D joint model is given in Fig. 6.32. The plot represents the initial state without any load being applied, thus no contact element is closed.

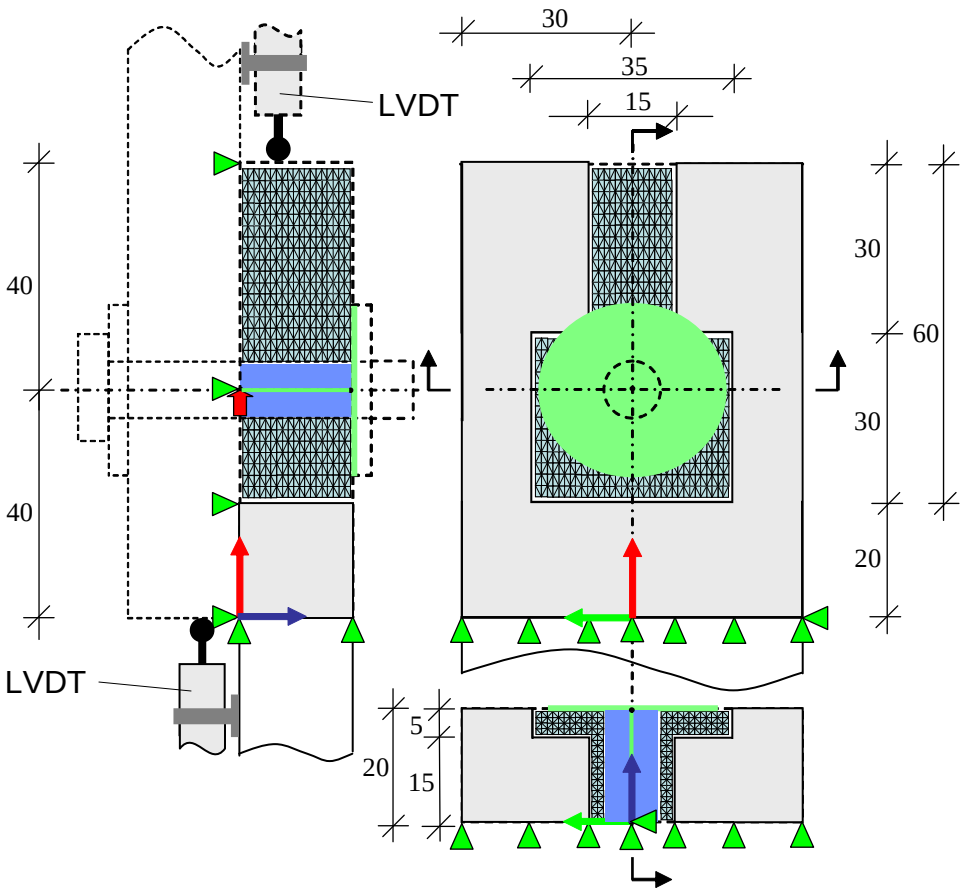

Figure 6.31: *Schematic of 3D joint model. (original in colour)*

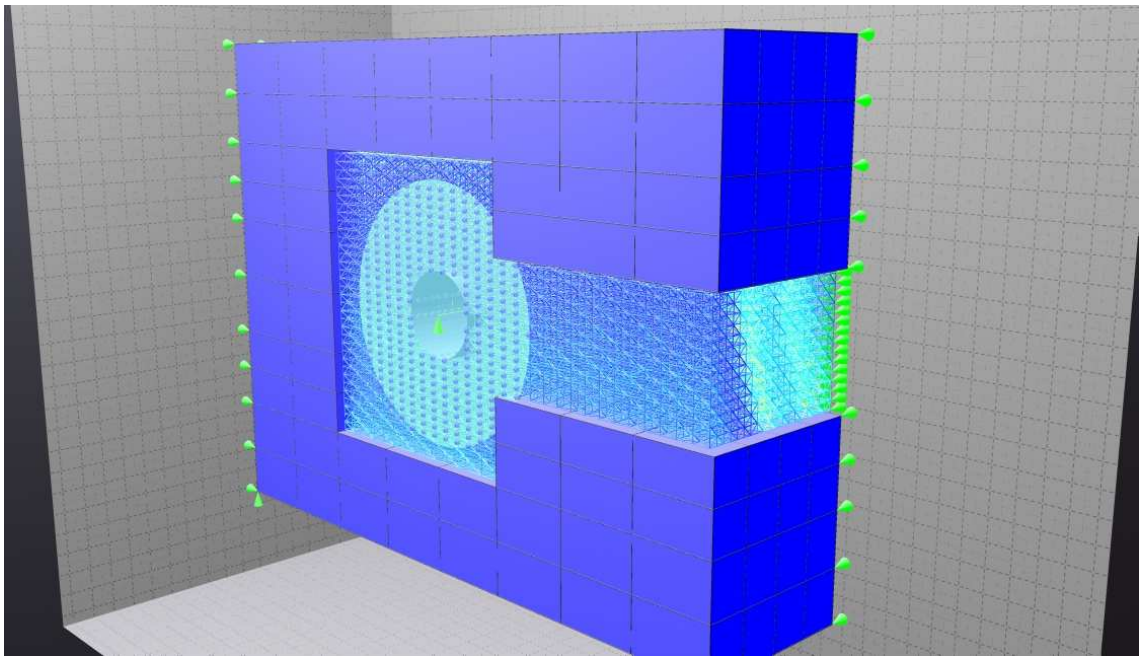

Figure 6.32: *Rendered representation of 3D initial joint model (original in colour).*

Fig. 6.33 shows the deformed state of a joint model with active contact nodes and broken links at the bolt's far side and underneath the washer and Fig. 6.34 shows the broken links as shaded rectangles in the respective plane (purple for compression and pink for tension).

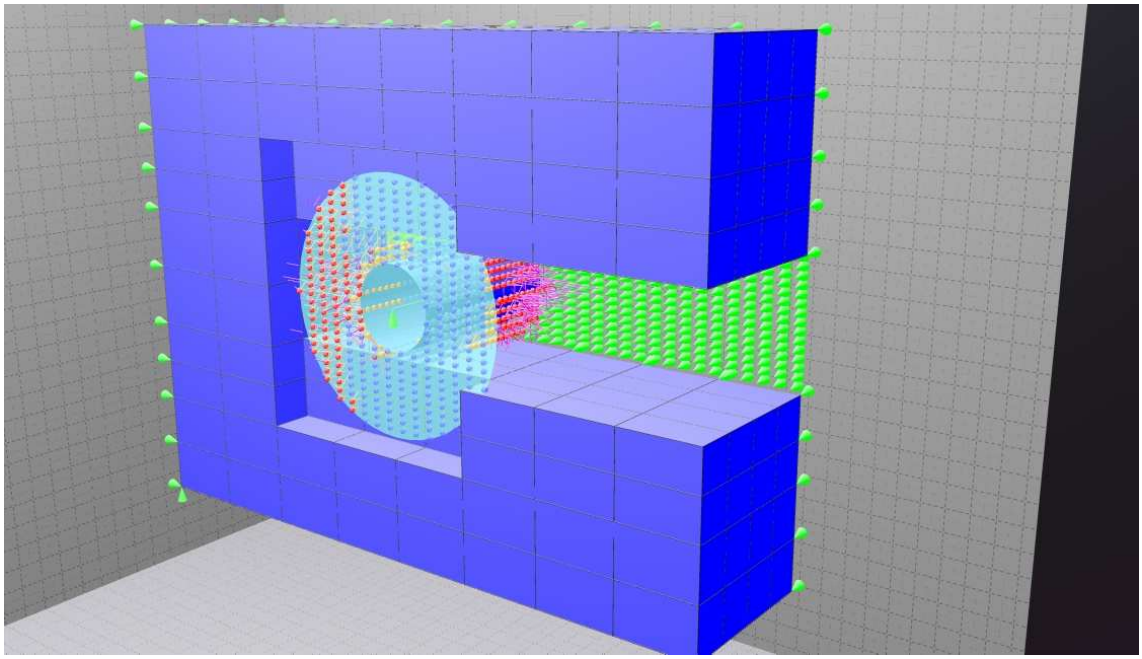

Figure 6.33: *Rendered representation of deformed 3D joint model (original in colour).*

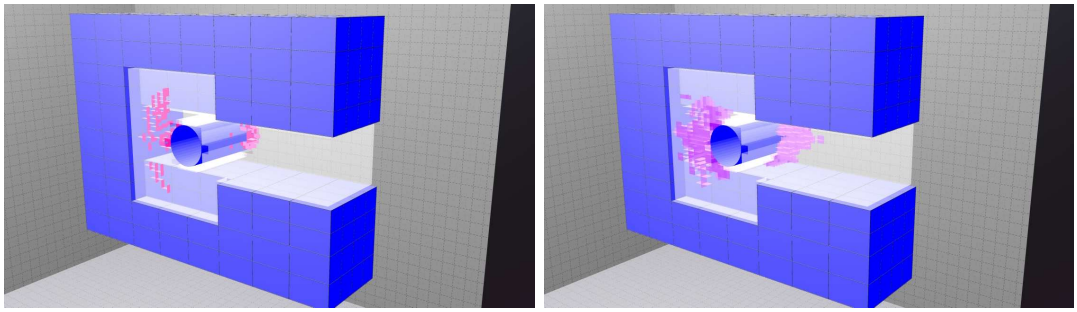

Figure 6.34: *Rendered representation of deformed 3D joint model with broken links highlighted (original in colour).*

The load displacement plots for the **J-M10** series is presented in Fig. 6.35. As one can see the specimens failed at relative large displacements of around 15 mm. The model prediction stopped at a displacement of 0.25 mm. This was due to the problem encountered with the modified SSC algorithm for which the LDP jumped

to a negative displacement value and is discussed further in chapter 7.

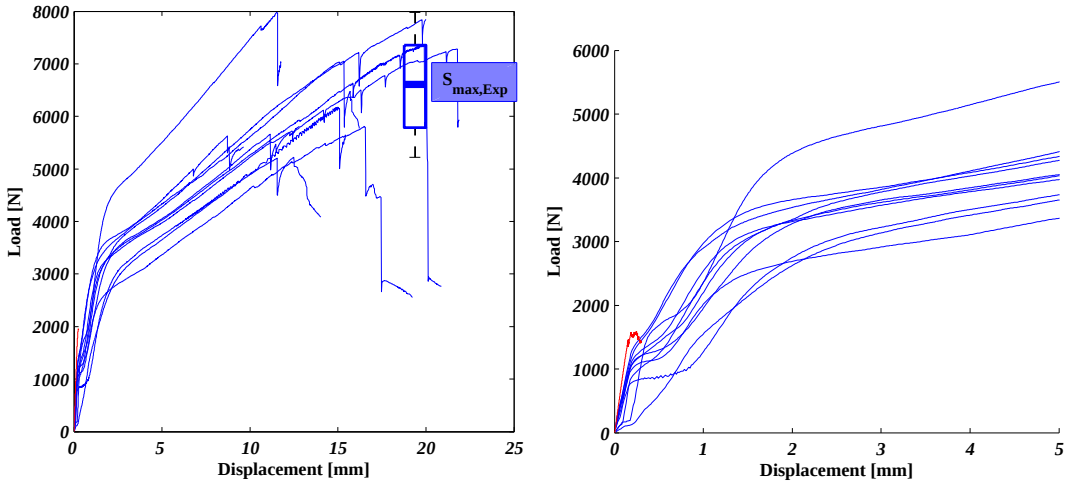

Figure 6.35: *Comparison of load-displacement among test and 3D model ($\gamma_{T,\{2,4\}}$=1) for **J-M10** series (left) and zoomed (right) (original in colour).*

Due to very long calculation times (roughly one week) it was not possible to obtain several solutions for the 3D joint model. Instead the 2D version of the joint model is presented in Fig. 6.36 with the same resulting error in the SSC solution algorithm as in the 3D counterpart but after a larger plastic deformation. Since the 2D model represents one unit thickness, the LDP is multiplied with the width of 20 mm as can be seen in Fig. 6.36. The bolt has a finite length and rotationally constrained at both ends. Thus, only the two dimensional function of the joint is modelled.

Although, thus only a limited comparison between model and test series can be made, the graphs show similar load levels up to the yield point. It was not possible to obtain the bulk joint stiffness from the tests due to the initial friction as a result from the hand tightened nut which lead to a significant nonlinear behaviour in the beginning of the load displacement curve (This frictional effect was minimised in the test series for the 2D elastic-plastic beam model in chapter 4 with graphite powder). However, when only the initial curve of the LDPs are compared the model's stiffness prediction is around three to four times higher (3D model) than measured stiffness from the test series. The neglected effect of a rotating bolt and thus an uneven load distribution along the fastener shank would in fact lead to higher stiffness predictions. In case of the 3D model this difference in stiffness is of a factor of around two.

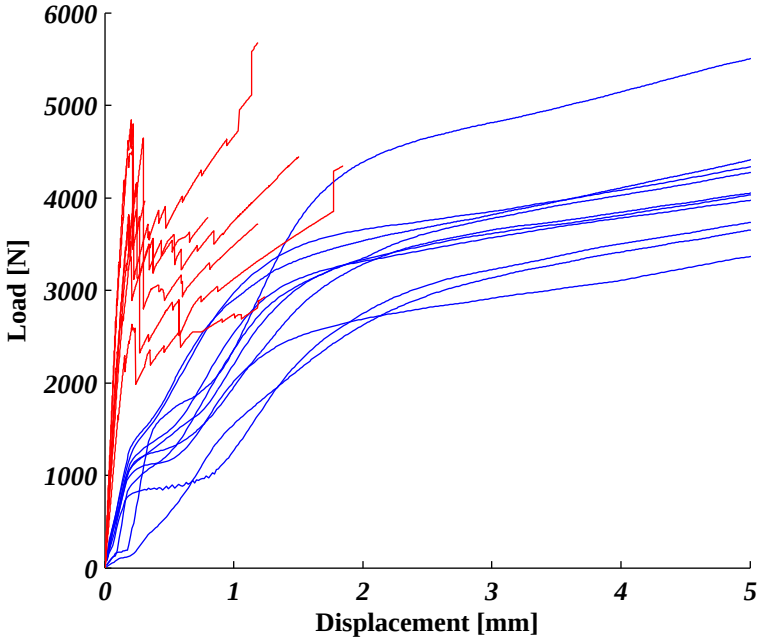

Figure 6.36: *Comparison of modified LDP between test and 2D model ($\gamma_{T,\{2,4\}}$=2) for **J-M10** series (original in colour).*

Fig. 6.37 shows the LDP of one 2D joint model with the erroneous load step encircled.

Fig. 6.38 depicts the deformed 2D joint model with two cracks developing from the bolt contact towards the loaded edge.

Fig. 6.39 shows an example of a failed tested specimen. A crack developing from the bolt-timber interface towards the loaded edge can be seen. All of the specimens in group *A* failed by splitting (cleavage) while 2 specimens in group *F* exhibited row-tear out failure.

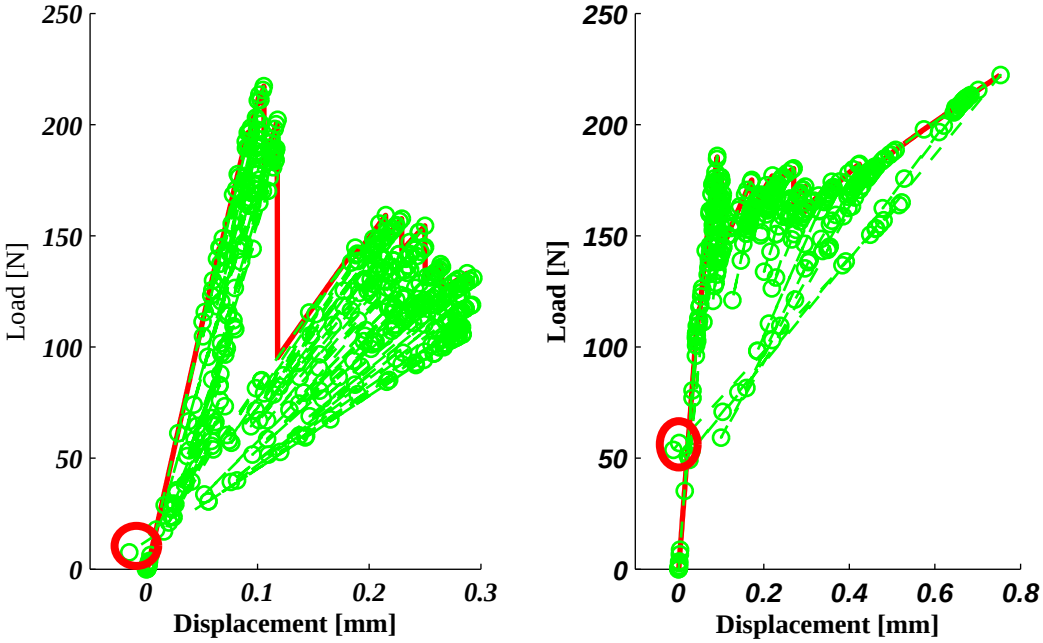

Figure 6.37: *Unmodified LDP of single 2D model (unit thickness), $\gamma_{T,\{2,4\}}$=1 (left) and $\gamma_{T,\{2,4\}}$=2 (right) from **JM10** series, erroneous load step is encircled (original in colour).*

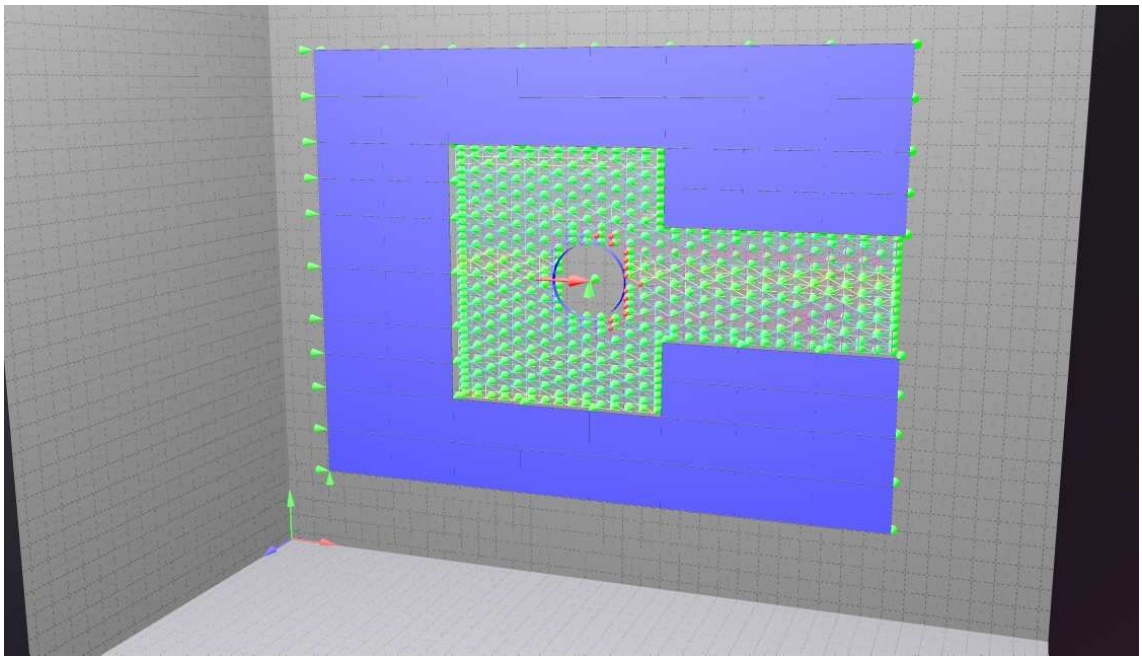

Figure 6.38: *Rendered representation of cracked 2D **J-M10** model, $\gamma_{T,\{2,4\}}$=1 (original in colour).*

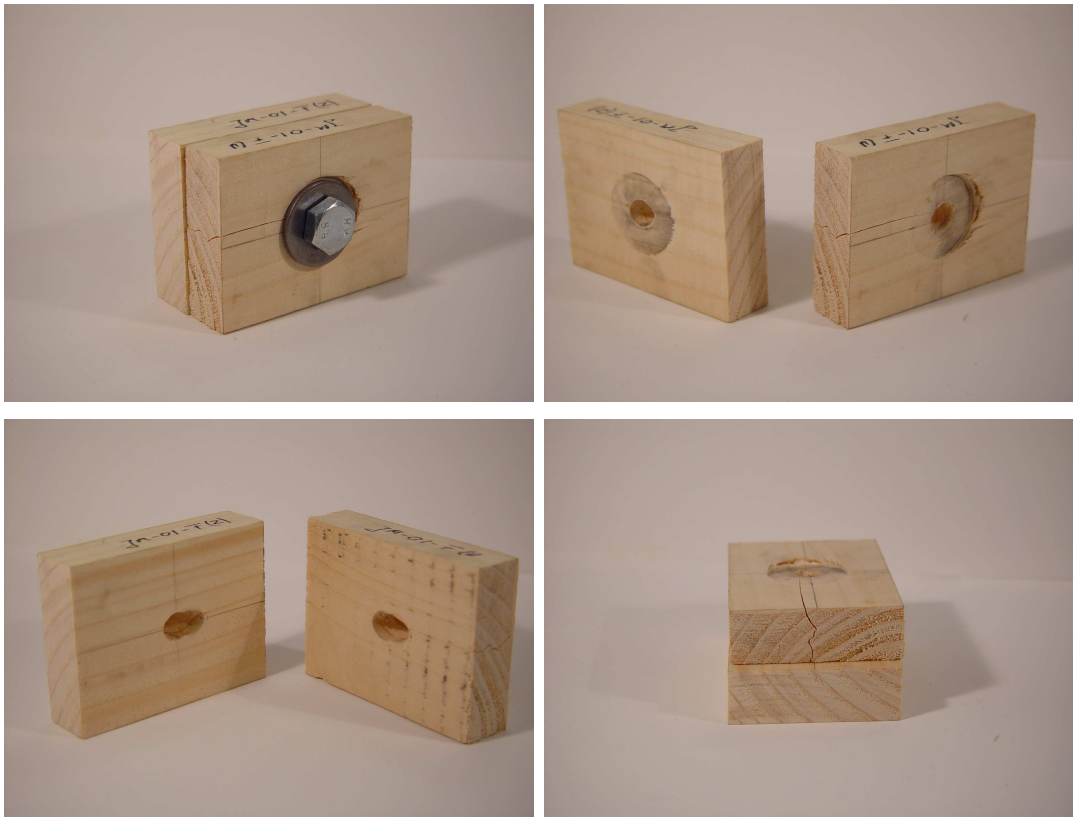

Figure 6.39: *Tested specimen **J-M10**, (original in colour).*

7 Discussion and Conclusions

7.1 General

This chapter presents some discussion and conclusions on the results from the FE model compared to the laboratory tests of the respective test series. An analysis of the lattice model and the general applicability of the modelling technique will be discussed.

In the previous chapters the various modelling approaches leading up to the final lattice model for joints were described. Underlying nonlinear solution techniques such as the SSC algorithm and their extension and implementation in the program *LAT3D* were shown, including the modified MIF algorithm which makes the recalculation of the global stiffness matrix unnecessary. Several other methods to increase the computational speed and means to reduce the required memory space were introduced (such as the use of solid elements in areas of lower stress gradients and a special lattice cell arrangement).

The results of several test series compared to their respective lattice models were presented in the previous chapter. While the match among test and model require further fine-tuning of the model parameters, it can be stated that in principle 3D lattice models are capable of predicting timber behaviour in terms of ultimate load and fracture path, albeit with the requirement for considerable computational effort.

7.2 Computational Issues

The MIF reduces significantly the computational effort. It is unnecessary to solve the global stiffness matrix for each load step. This method can be applied to any solution algorithm that solves a lattice consisting of 1D elements (beams or bars). Furthermore, geometric nonlinearity of beam elements which were used to represent

bolt deformation in the joint model can be implemented and accounted for in the MIF. However, computational time saved with the MIF can only be achieved if a smaller amount of links need to be changed as it is the case for cracking of timber. When a large amount of plastic links accumulate the efficiency of the MIF decreases.

The SSC algorithm works well with brittle link elements. The number of load steps does usually not exceed the number of broken links. This was already demonstrated in Jirasek & Bazant (1995). However, when links with plastic hardening are considered, as it is the case in this dissertation, the algorithm has several problems:

- **Complex stress state**
  Switching from tension to compression or vice versa (see Fig. 5.22 due to complex stress states (diagonals and lateral links with brittle and ductile behaviour, respectively) ⇒ the algorithm takes a wrong decision on the subsequent load factor and either stops or ends at a negative overall displacement.

- **Number of plastic links**
  A large number of plastic links increases the number of load steps (see subsection 5.6.3).

- **Singularity points**
  Close-to-singularity points right after the maximum load is reached might arise due to the negative stiffness values which are introduced for the link's softening branch.

7.2.1 Complex Stress State

Problems occurred with the solution algorithm when plastic hardening is considered. Certain stress situations brought the algorithm to a stop (singular global stiffness matrix) or the load factor lead to a negative loading which would not be permissible as seen in the 2D and 3D joint models. This could be a result of the solution algorithm that bases the decision, of whether a negative or positive load step in an load step is chosen, on the number of links for which their assumed status consistent or inconsistent with their strain increment (appendix section A.1). Based on the fact that plastic links have still a positive stiffness these links are excluded from this counting. However, it might be the case that even a very low stiffness from the plastic links would require a negative load step and therefore the wrong decision is

made.

7.2.2 Number of Plastic Links

Furthermore, the general issue is that when a number of lattice links are in the plastic compressed state($-$⑫) and other links in state ② require a negative load step all plastically compressed links switch back to status $-$⑬. In the next step all the previously compressed links require a different load step to reach again their plastic status $-$⑫ (at maximum compressive strain $\epsilon_{C,max}$) since different stiffness for the links were determined. That would mean that each plastic link needs one load step to get back to its plastic hardening state. It was tried to compensate for this large amount of additional load steps by introducing a threshold load factor λ_{Tresh} in order to collect all these close load factors of these links in one step, as described in subsection 5.6.3. However, with this method used, an error accumulates due to improperly used load factors. Furthermore, still a huge number of links switch back and forth for each single link that breaks, especially in a pure compression case (e.g. test series **C-L**, **C-R** and **C-T**). The number of required load steps when compared to models with purely micro-ductile or brittle links increased dramatically.

7.2.3 Singularity Points

When micro-ductility is considered. Links with a negative stiffness alongside with links having a similar positive stiffness can create a singularity in the global stiffness matrix. This issue and a proposed solution was discussed by Rots & Invernizzi (2004) and is mentioned in subsection 3.3.4. The problem was encountered for the 3D micro-ductile models. Therefore only a representative 2D cleavage model was shown in the previous chapter.

7.3 Problems with General Lattice Structure

As mentioned in subsection 6.3, a lattice cell with diagonal elements (that model shear resistance and lateral strain) can not represent an arbitrary orthotropic stress state. The resulting K parameters are constrained and therefore can not be adjusted freely. Since wood exhibits a distinct orthoptropy, with a strong

longitudinal axis compared to its perpendicular to the grain axes, the lattice is very limited in its application.

Furthermore, the Young's modulus ratios that were used from the USDA (1999) resulted in higher elastic properties than what was measured in the laboratory tests on the actual specimens. However, a lower value could not be achieved with the lattice model either due to the before described reason. Therefore in terms of elastic properties the comparison between test and model delivers quite different results.

The proposed solution is to use angular springs in order to differentiate between shear effects and lateral strain, but was not implemented. It is the author's assumption that these angular springs and consequently additional DoFs, strength and stiffness parameters would make a significant difference in the calibration routine. As mentioned in section 6.3 this would release the constraints, imposed by the used lattice cell structure, to simulate only limited orthotropic elastic behaviour.

Similarly, the model's strength parameters can not be adjusted freely. Diagonal and longitudinal elements are interdependent. This can be observed, for example, in the tension tests **T-L** where a large number of lateral links switch to plastic hardening due to the effect of lateral strain. Therefore, the diagonal links break as well, although it would be expected that these only break when cracking occurred in the lateral direction (which is not observed in the tested specimens).

In the same way, diagonal and lateral links are interdependent. This can be seen for the cleavage and compression model. The latter model would require lower strength parameters to better fit the test data, however, on the contrary, the cleavage model requires higher parameters in order to better match the laboratory data.

Therefore, the different interests to optimise the match among model and experiment for different parameters are in conflict with each other. Angular springs or beam elements would, in this case, also be an advisable solution.

7.3.1 Problem of Different E-Modulus in Compression and Tension Tests

The elastic properties measured in the compression tests did not agree at all with the reported literature values. Bodig & Jayne (1993) report a Young's modulus of 10 GPa (compared to laboratory tests $E_{||}$ =2.4 GPa) in the longitudinal direction and around 1.25 GPa (compared to laboratory tests $E_{\perp}$ =.16 GPa) perpendicular to the grain for Sitka spruce. So far it is not clear where this difference in stiffness originates since the tensile test delivered an expectable Young's modulus (as well documented in the Wood Handbook, USDA (1999)).

Since the elastic parameters for the lattice K_j were determined with the ratios $(\frac{E_j}{E_{xx}})$ obtained from USDA (1999) also, the results in terms of stiffness from the lattice model don't agree well with the experimental test series. This would have not been the case if the test series had delivered LDPs that match better the values taken from the literature.

7.4 Conclusions

Lattice models seem to be a reasonable approach to model fracture behaviour. Examples for timber can be found, as mentioned in the literature review, in Landis et al. (2002), Landis et al. (2003), Davids et al. (2003), Parrod (2002), Parrod et al. (2002), Vasic (2000) and Fournier et al. (2007). However, neither plastic hardening nor microductility for timber under compression was considered in these models. To take into account the effect should enhance the model's capabilities significantly and would enable the models to predict realistically compression in the lateral and longitudinal direction as shown in this thesis.

Taking into account these effects required a more general solution algorithm thus the SSC developed by Jirasek & Bazant (1995) was modified. With this modification, problems arose especially when more complex stress states are considered as e.g. in the joint model series **J-M10**.

Comparisons between experiments and lattice models (modified SSC) show that realistic predictions can be made in terms of the fracture path. Heterogeneity was implemented by creating an artificial growth ring structure. This has a significant

influence on the fracture path which can be observed in the model as well as in tests (e.g cleavage model in Fig. 6.5 and 6.7). The requirement to include the structured heterogeneity of timber was stressed already by Fournier et al. (2007). The implementation as done here in this research with an adjusted mean strength and stiffness parameter according to the link's position in an artificial growth ring structure seems to deliver reasonable predictions. However, it has to be made sure that the grid size is under the observed variation in between one growth ring.

The use of solid elements in parts of low stresses and no plastic or brittle deformation seems a good solution to the problem of the large number of required DoFs otherwise. Although it is not possible for the solid elements to represent any heterogeneous elasticity, this should not affect the bulk elastic behaviour of the entire model.

Problems with the SSC algorithm with included plastic hardening links might need reworking or a different solution method might be used altogether such as the one described in subsection 3.3.4. Combined with the other used techniques to minimise the computational effort the program *LAT3D* could be used efficiently.

8 Outlook

In the following, a brief outlook is given on the future use of the program LAT3D and its suggested improvements.

8.1 Lattice Model

From the results and the limited success of the model to match experimental results, it is obvious that the model needs further adjustment in terms of the calibrated parameters. However, the main reason remains the incapabilities of the used lattice cell structure to represent general orthotropy in terms of elastic and strength properties. A more appropriate lattice structure should be adopted. A solution could be angular springs or beam elements, with additional strength and stiffness parameters, that uncouple the shear behaviour from lateral and longitudinal strain. Still, the actual match between test results and model would have been better if the measured LDPs from the compression tests had resembled better the literature values.

Other possibilities to change the lattice structure include to organise the elements in a hexagonal arrangement as seen in Fig. 8.1. Fewer links per cell are required and therefore the calibration would be more efficient (given that angular springs are also used). The diagonals are aligned in a non-symmetric way to create the hexagonal pattern in the YZ plane (cross-sectional plane). This arrangement, although it has no lateral links, could reflects better the cellular structure of wood in the cross sectional plane. Only one type of elements (diagonals) breaks when cells are separated.

The optimisation method (trial&error) to calibrate the strength parameters could be improved by the use of multi objective techniques (simplex algorithm, genetic algorithm etc.) that mathematically solve the problem to find an optimal fit of

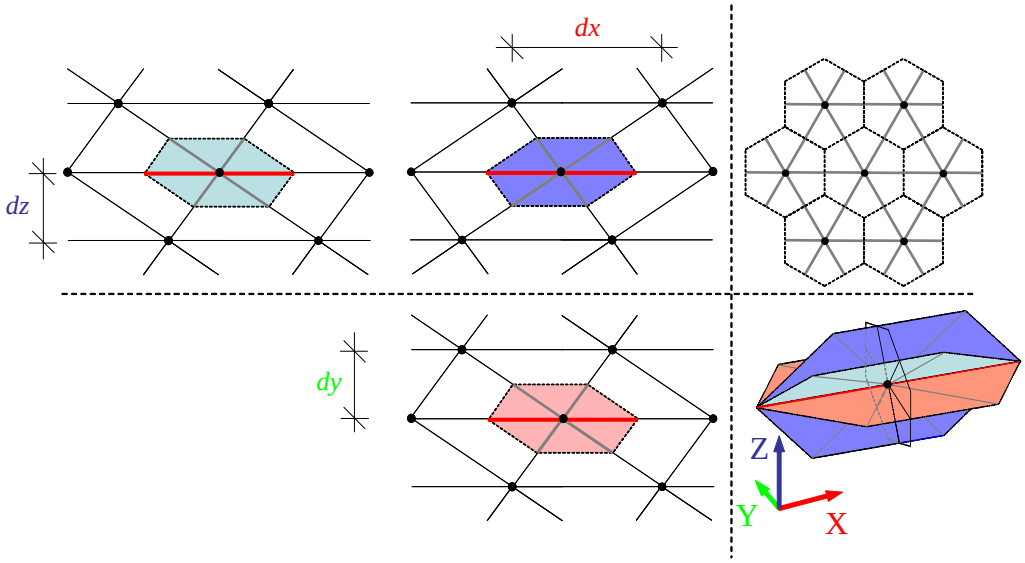

Figure 8.1: *Lattice cell structure for 3D hexagonal arrangement. Note: coordinate planes do not coincide with material planes.*

model results to the experimental data. However, this would require much larger computational capacities.

The program *LAT3D* could serve as a framework in which these extensions can be built into. *MATLAB* is a versatile tool and commonly used in academia and is easy to learn. Therefore, the program *LAT3D* itself can be extended rather simply.

Regarding the problems with the SSC algorithm and the use of plastic hardening links, it will be necessary to improve on the flaws in the method or implement a different solution strategy altogether, as mentioned in the previous chapter.

With these improvements it should be possible to perform extended parameter studies with the *LAT3D* model. It could then serve as a tool for researchers to investigate different joint arrangements than the symmetric single shear joint and other timber structures.

9 References

Aicher, S. & Kloeck, W. (2001). Linear versus quadratic failure criteria for in-plane loaded wood based panels. *Otto-Graf-Journal*, *12*.

Alam, P. & Ansell, M. P. (2003). Failure analysis and finite element modelling of timber-steel-timber composites connected by shot-fired bainitically-hardened nails and subjected to short-term lateral shear. In *ESWM-Stockholm May 25-28*, Stockholm.

Amestoy, P. R., Davis, T. A., & Duff, I. S. (1996). An approximate minimum degree ordering algorithm. *SIAM Journal on Matrix Analysis and Applications*, *17*(4), 886–905.

Anderson, G. T. (2001). Experimental investigation of group action factor for bolted wood connections. Master's thesis, Virginia Polytechnic Institute and State University.

Anderson, T. (1991). *Fracture Mechanics - Fundamentals and Applications*. CRC Pres, Inc.

Arramon, Y. P., Mehrabadi, M. M., Martin, D. W., & Cowin, S. C. (2000). A multidimensional anisotropic strength criterion based on kelvin modes. *International Journal of Solids and Structures*, *37*(21), 2915–2935.

Aune, P. & Patton-Mallory, M. (1986a). Lateral load-bearing capacity of nailed joints based on the yield theory - experimental verification. Technical report, U.S. Department of Agriculture, Forest Service, Forest Products Laboratory.

Aune, P. & Patton-Mallory, M. (1986b). Lateral load-bearing capacity of nailed joints based on the yield theory - theoretical development. Technical report, U.S. Department of Agriculture, Forest Service, Forest Products Laboratory.

Ballerini, M. & Rizzi, M. (2005). A numerical investigation on the splitting strength of beams loaded perpendicular-to-grain by multiple dowel-type connections. In *Working Comission W18 - Timber Structures*, Karlsruhe.

Balma, D. A. (1999). Evaluation of bolted connections in wodd plastic composites. Master of science in civil engineering, Washington State University.

Bazant, Z. & Cedolin, L. (1979). Blunt crack band propagation in finite element analysis. *ASCE Journal Engineering Mechanics Division*, *105*(2), 297–315.

Bazant, Z. P. & Yavari, A. (2005). Is the cause of size effect on structural strength fractal or energetic-statistical? *Engineering Fracture Mechanics*, *72*(1), 1–31.

Berton, S. & Bolander, J. E. (2006). Crack band model of fracture in irregular lattices. *Comput. Methods Appl. Mech. Engrg.*, *195*, 7172–7181.

Blass, H. (1994). Characteristic strength of nailed joints. *Forest Products Journal*, *44*(4), 33–39.

Blass, H. J. & Kraemer, V. (2001). Effective bending capacity of dowel-type fasteners. In *International Council for Research and Innovation in Building and Construction, Working Commission CIB-W18*, (pp. 71–80)., Stuttgart.

Blass, H. J., Schmid, M., Litze, H., & Wagner, B. (2000). Nail plate reinforced joints with dowel-type fasteners. In *World Conference on Timber Engineering*, (pp. S. 8.6.4–1 – 8)., Whistler, Canada. Dep. of Wood Sci., Univ. of British Columbia.

Bleron, F., Bocquet, J., & Duchanois, G. (2001). Contribution to the optimization of timber joints performance - analysis of dowel type fasteners embedment strength. In *RILEM*, Stuttgar.

Bocquet, J. (1997). *Modelisation des Deformations Locales du Bois dans les Assemblages Broches et Boulonnes.* PhD thesis, University Blaise Pascal - Clermont.

Bodig, J. & Jayne, A. (1993). *Mechanics of Wood and Wood Composites,.* Krieger Publishing Company, Malabar, FL, USA.

Bridgeman, P. (1952). *Studies in Large Plastic Flow and Fracture with Special Emphasis on the Effects of Hydrostatic Pressure.* McGraw-Hill, New York.

BS 373 (1957). *Methods of Testing Small Clear Specimens of Timber.* British Standards Institution.

BS 5268-2 (1996). *Structural Use of Timber. Code of Practice for Permissible Stress Design, Materials and Workmanship.* British Standards Institution.

BS 5268-2 (2002). *Structural Use of Timber. Code of Practice for Permissible Stress Design, Materials and Workmanship*. British Standards Institution.

BS 5268:Part 2 (1991). *Structural Use of Timber. Code of Practice for Permissible Stress Design, Materials and Workmanship*. British Standards Institution.

BS EN 13183-1 (2002). *Moisture Content of a Piece of Sawn Timber - Part 1 Determination by Oven Dry Method*. British Standards Institution.

BS EN 1995-1-1 (2004). *Eurocode 5 - Design of Timber Structures - Part 1-1: General - Common Rules and Rules for Buildings*. British Standards Institution.

BS EN 383 (2007). *Timber Strucutres - Test Methods - Determination of Embedding Strength and Foundation Values for Dowel Type Fasteners*. British Standards Institution.

BS EN 408 (1995). *Timber structures. Structural timber and glued laminated timber. Determination of some physical and mechanical properties*. British Standards Institution.

Canadian Wood Council (2008). Tackle climate change, use wood. BC Forstry Climate Change - Working Group, [http://www.bcforestinformation.com/assets/pdf/tackle-climate-change.pdf] (February 2009).

Cazacu, O. & Cristescu, N. D. (1999). A paraboloid failure surface for transversely isotropic materials. *Mechanics of Materials*, *31*, 381–393.

Cazacu, O., Cristescu, N. D., & Shao, J. F. (1999). A new anisotropic failure criterion for transversely isotropic solids. *Mechanics of Cohesive-frictional Materials*, *3*(1), 89–103.

Chen, C., Lee, T., & Jeng, D. (2003). Finite element modeling for the mechanical behavior of dowel-type timber joints. *Computers and Structures*, *81*, 2731–2738.

Cointe, A. & Rouger, F. (2004). Simplification of the neural network model for predicting the load carrying capacity of dowel-type connections. In *International Council for Research and Innovation in Building and Construction, Working Commission CIB-W18, Edinburgh, UK*, Edinburgh, UK.

Cramer, C. (1968). Load distribution in multiple-bolt tension joints. *Journal of the Structural Division ASCE*, *94*(ST5), 1101–1117.

Cusatis, G., Bazant, Z. P., & Luigi, C. (2006). Confinement-shear lattice csl model for fracture propagation in concrete. *Comput. Methods Appl. Mech. Engrg.*, *195*, 7154–7171.

Cuthill, E. & McKee, J. (1969). Reducing the bandwidth of sparse symmetric matrices. In *24th Nat. Conf. ACM*, (pp. 157–172).

Daudeville, L. (1999). Fracture in spruce: Experiment and numerical analysis by linear and non-linear fracture mechanics. *Holz als Roh- und Werkstoff*, *57*(6), 425 – 432.

Daudeville, L., Davenne, L., & Yasumura, M. (1999). Prediction of the load carrying capacity of bolted timber joints. *Wood Science and Technology*, *33*, 15–29.

Daudeville, L. & Yasumura, M. (1996). Failure analysis of timber bolted joints by fracture mechanics. *Materials and Structures*, *29*, 418–425.

Davids, W. G., Landis, E. N., & Vasic, S. (2003). Lattice models for the prediction of load-induced failure and damage in wood. *Society of Wood Science and Technology, Wood and Fibre Science*.

DAZ Production, Inc. (2004). *Bryce4*. DAZ Production, Inc., 1350 E. Draper Parkway, Draper UT, 84020, United States [Computer Program].

DD ENV 1995-1-1 (1994). *Eurocode 5 - Design of Timber Structures - Part 1-1: General - Common Rules and Rules for Buildings*. British Standards Institution.

DIN 1052:2004-08 (2004). *Design of Timber Structures - General Rules and Rules for Buildings*. Germany: DIN.

Dodson, M. A. (2003). The effects of row spacing and bolt spacing in 6-bolt and 4-bolt wood-to-steel connections. Master's thesis, Washington State University.

Dugdale, D. (1960). Yielding of steel sheets containing slits. *Journal of the Mechanics and the Physics of Solids*, *8*, 100–108.

Ehlbeck, J., Goerlacher, R., & Werner, H. (1989). Determination of perpendicular-to-grain tensile stresses in joints with dowel-type fasteners: a draft proposal for design rules. In *International Council for Research and Innovation in Building and Construction, Working Commission CIB-W18, Berlin, GDR*.

Erki, M. (1991). Modelling the load - slip behaviour of timber joints with mechanical fasteners. *Canadian Journal of Civil Engineering*, *18*(4), 607–615.

Forestry Commission (2008). *Forestry Statistics 2008 - UK Grown Timber*. Forestry Commission, Economics and statistics division [http://www.forestry.gov.uk] (January 2009).

Foschi, R. O. (1974). Load-slip characteristic of nails. *Wood Science*, *7*(1), 69–76.

Fournier, C. R., Davids, W. G., Nagy, E., & Landis, E. N. (2007). Morphological lattice models for the simulation of softwood failure and fracture. *Holzforschung*, *61*, 360–366.

Franke, S., Franke, B., Schober, K.-U., & Rautenstrauch, K. (2008). The strength behavior of wood in experiment and simulations. In *World Conference on Timber Engineering WCTE, Miyazaki, Japan*.

Gander, W. & Gautschi, W. (2000). Adaptive quadrature - revisited. *BIT CS technical report:*, *49*(1), 84–101.

Gilbert, J. R., Ng, E. G., & Peyton, B. W. (1994). An efficient algorithm to compute row and column counts for sparse Cholesky factorization. *SIAM Journal on Matrix Analysis and Applications*, *15*(4), 1075–1091.

Gong, M. (1990). A study of wood elasticity. Master's thesis, Nanjing Forestry University, Nanjing, Jiangsu, China.

Gonzalez, C. & Llorca, J. (2007). Virtual fracture testing of composites: A computational micromechanics approach. *Engineering Fracture Mechanics*, *74*, 1126–1138.

Griffith, A. A. (1921). The phenomena of rupture and flow in solids. *Philosophical Transactions of the Royal Society of London*, *221*, 163–197.

Grimsel, M. (1999). *Mechanisches Verhalten von Holz*. PhD thesis, Technischen Universitaet Dresden.

Grosse, M. & Rautenstrauch, K. (2004). Numerical modelling of timber and connection elements used in timber-concrete-composite constructions. In *International Council for Research and Innovation in Building and Construction, Working Commission CIB-W18, Edinburgh, UK*, volume 37-7-15, Edinburgh, UK.

Guan, Z. & Rodd, P. (2000). The role of reinforcing materials in timber connections. In *World Conference on Timber Engineering*, Whistler Resort, British Columbia, Canada.

Harada, M., Hayashi, Y., Hayashi, T., Karube, M., & Ohgama, T. (2005). Effect of moisture content of members on mechanical properties of timber joints. *J Wood Sci*, *51*, 282–285.

Harrington, J. J. (2002). *Hierarchical Modelling of Softwood Hygro-Elastic Properties*. PhD thesis, University of Canterbury.

Hassan, N. & Mohamedien, M. (1997). Rational model for multibolted connections for gfrp members. *Journal of Composites for Construction*, *1*(2), 71–76.

Heine, C. (2001). *Simulated Response of Degrading Hysteretic Joints with Slack Behavior*. PhD thesis, Virginia Polytechnic Institute and State University.

Hillerborg, A., Modeer, M., & Petersson, P. E. (1976). Analysis of crack formation and crack growth in concrete by means of fracture mechanics and finite elments. *Cement and Concrete Research*, *6*, 773–782.

Holmberg, S., Persson, K., & Petersson, H. (1998). Nonlinear mechanical behaviour and analysis of wood and fibre materials. *Computers and Structures*, *72*, 459–480.

Ince, R., Arslan, A., & Karihaloo, B. (2003). Lattice modelling of size effect in concrete strength. *Engineering Fracture Mechanics*, *70*, 2307–2320.

Inglis, C. E. (1913). Stresses in a plate due to the presence of cracks and sharp corners. *Transactions of the Institute of Naval Architects*, *55*, 219–241.

Jennings, A. & McKeown, J. J. (1992). *Matrix Computation* (2nd ed.). John Wiley & Sons.

Jensen, J. L. (2005a). Quasi-non-linear fracture mechanics analysis of splitting failure in momentresisting dowel joints. *Journal of Wood Science*, *51*, 583–588.

Jensen, J. L. (2005b). Quasi-non-linear fracture mechanics analysis of splitting failure in simply supported beams loaded perpendicular to grain by dowel joints. *Journal of Wood Science*, *51*, 577–582.

Jensen, J. L. (2005c). Quasi-non-linear fracture mechanics analysis of the splitting failure of single dowel joints loaded perpendicular to grain. *Journal of Wood Science*, *51*, 559–565.

Jensen, J. L. (2005d). Splitting strength of beams loaded perpendicular to grain by dowel joints. *Journal of Wood Science*, *51*, 480–485.

Jernkvist, L. O. (2000). Fracture of wood under mixed mode loading i. derivation of fracture criteria + ii. experimental investigation. *Engineering Fracture Mechanics*, *68*, 549–563.

Jirasek, M. & Bazant, Z. P. (1995). Macroscopic fracture characteristics of random particle systems. *International Journal of Fracture*, *69*(3), 201–228.

Johansen, K. W. (1949). Theory of timber connections. *Inter. Assoc. of Bridge and Structural Engineering, Bern, Switzerland*, *9*, 249–262.

Jorissen, A. (1998). *Double Shear Timber Connections with Dowel Type Fasteners*. PhD thesis, Delft University Press, Delft, Netherlands.

Kamachi, K. & Ando, N. (2006). New method to estimate the load-slip characteristics of the double-shear bolted timber-to-timber joints. In *Proceedings WCTE*, Oregon, USA.

Kharouf, N., McClure, G., & Smith, I. (1999). Fracture modeling of bolted connections in wood and composites. *J. Mat. in Civ. Engrg.*, *11*(4), 345–352.

Kharouf, N., McClure, G., & Smith, I. (2003). Elasto-plastic modeling of wood bolted connections. *Computers and Structures*, *81*, 747–754.

Khokhar, A., Zhang, H., Ridley-Ellis, D., & Moore, J. (2008). Determining the shear modulus of sitka spruce from torsion tests. In *World Conference on Timber Engineering WCTE, Miyazaki, Japan*.

Landis, E., Fournier, C., & Davids, W. (2003). Modeling scale effects in wood with lattice models. In *ASCE Engineering Mechanics Conference*, Universiy of Washington, Seattle.

Landis, E. N., Vasic, S., & Davids, W. G. (2002). Coupled experiments and simulations of microstructural damage in wood. *Experimental Mechanics*, *42*(4), 389–394.

Lantos, G. (1969). Load distribution in a row of fasteners subjected to lateral load. *Wood Science*, *1*(3), 129–136.

Lilliu, G. & van Mier, J. (2000). Simulation of 3d crack propagation with the lattice model. In *MaterialsWeek*.

Lilliu, G. & van Mier, J. (2003). 3d lattice type fracture model for concrete. *Engineering Fracture Mechanics*, *70*, 927–941.

Lin, C.-J., Tsai, M.-J., Lee, C.-J., Wand, S.-Y., & Lin, L.-D. (2007). Effects of ring characteristics on the compressive strength and dynamic modulus of elasticity of seven softwood species. *Holzforschung*, *61*, 441–418.

Luschnitz (1997). Experimental tests of bolted joints showing enhanced resistance - unpublished.

Mackenzie-Helnwein, P., Eberhardsteiner, J., & Mang, H. A. (2003). A multi-surface plasticity model for clear wood and its application to the finite element analyis of structural details. *Computational Mechanics*, *31*, 204–218.

Mackerle, J. (2005). Finite element analyses in wood research: a bibliography. *Wood Sci Technol*, *39*, 579–600.

McGuire, W., Gallagher, R. H., & Ziemian, R. D. (2000). *Matrix Structural Analysis* (2nd ed.). John Wiley & Sons, Inc.

McLean, J. (2007). *Wood Properties of four Genotypes of Sitka Spruce*. PhD thesis, University of Glasgow Chemistry Department.

Mischler, A., Prion, H., & Lam, F. (2000). Load-carrying behaviour of steel-to-timber dowel connections. In *World Conference on Timber Engineering*, Whistler Resort, British Columbia, Canada.

Mohammad, M. & Quenneville, J. (1999). Behaviour of wood-steel-wood bolted glulam connections. In *International Council for Research and Innovation in Building and Construction, Working Commission CIB-W18, Graz, Austria*.

Mohammad, M. & Quenneville, J. (2001). Bolted wood/steel and wood/steel/wood connections: Verification of a new design approach. *Can. J. Civ. Eng.*, *28*(2), 254–263.

Moses, D. & Prion, H. (2003). A three-dimensional model for bolted connections in wood. *Canadian Journal of Civil Engineering*, *30*(3), 555–567(13).

Moses, D. & Prion, H. (2004). Stress and failure analysis of wood composites: a new model. *Composites: Part B*, *35*, 251–261.

Moss, P. J. (1997). Multiple-bolted joints in wood members - a literature review. Technical report, Department of Agriculture, Forest Service, Forest Products Laboratory.

Nairn, J. A. (2007a). Material point method simulations of transverse fracture in wood with realistic morphologies. *Holzforschung*, *61*, 375–381.

Nairn, J. A. (2007b). A numerical study of the transverse modulus of wood as a function of grain orientation and properties. *Holzforschung*, *61*, 406–413.

Nardin, A., Bostroem, L., & Zaupa, F. (2000). The effect of knots on the fracture of wood. In *World Conference on Timber Engineering*, Whistler Resort, British Columbia, Canada.

Nelder, J. & Mead, R. (1965). A simplex method for function minimisation. *Computer Journal*, *7*, 308–313.

Nishiyama, N. & Ando, N. (2003). Analysis of load-slip characteristics of nailed wood joints: Application of a two-dimensional geometric nonlinear analysis. *Journal of Wood Science*, *49*, 505–512.

Ostoja-Starzewski, M. (2002). Lattice models in micromechanics. *Appl Mech Rev*, *55*(1).

Paris, F. (2001). A study of failure criteria of fibrous composite materials. Technical Report NASA/CR-2001-210661, George Washington University, Joint Institute for the Advancement of Flight Sciences, Langley Research Center.

Park, Y.-I. D. & Spiecker, H. (2005). Variations in the tree-ring structure of norway spruce (picea abies) under contrasting climates. *Dendrochronologia*, *23*(2), 93–104.

Parrod, P. (2002). A lattice model for fibrous materials. Master's thesis, University of Maine.

Parrod, P., Landis, E. N., Davids, W. G., & Vasic, S. (2002). Morphology-based models for wood and wood composites. In *15th ASCE Engineering Mechanics Conference*, Columbia University NY.

Patton-Mallory, M., Smith, F., & Pellicane, P. (1998). Modeling bolted connections in wood: a three-dimensional finite-element approach. *Journal of Testing and Evaluation*, *26*(2), 115–124.

Ping, X. & Huawu, L. (2004). Models of microfibril elastic modulus parallel to the cell axis. *Wood Science Technology*, *38*, 363–374.

Porteous, A. & Kermani, A. (2005). Fully overlapping nailed joints with steel gussets in timber structrures. *Journal of Structural Engineering ASCE*.

Prado, E. & van Mier, J. (2003). Effect of particle structure on mode i fracture process in concrete. *Engineering Fracture Mechanics*, *70*, 1793–1807.

Quenneville, J. & Mohammad, M. (2000). On the failure modes and strength of steel/wood/steel bolted timber connections loaded parallel-to-grain. *Canadian Journal of Civil Engineering*, *27*, 761–773.

Racher, P. & Bocquet, J. (2005). Non-linear analysis of dowelled timber connections: A new approach for embedding modelling. *Electronic Journal of Structural Engineering*, *5*.

Rammer, D. R. & Winistorfer, S. G. (2001). Effect of moisture content on dowel-bearing strength. *Wood and Fiber Science*, *33*(1), 126–139.

Ramskill, T. E. (2002). *Effect of Cracking on Lag Bolt Performance*. PhD thesis, Virginia Polytechnic Institute and State University.

Reichert, T. & Ridley-Ellis, D. (2006). Modelling geometric non-linear behaviour of single shear bolted joints. In *World Conference on Timber Engineering WCTE, Oregon, USA*.

Reichert, T. & Ridley-Ellis, D. (2008). 3d lattice model for post-yield and fracture behaviour of timber. In *World Conference on Timber Engineering WCTE, Miyazaki, Japan*.

Reshke, R., Mohammad, M., & Quenneville, J. (2000). Influence of joint configuration parameters on strength of perpendicular-to-grain bolted timber connections. In *World Conference on Timber Engineering*, Whistler Resort, British Columbia, Canada.

Rots, J. G. & Invernizzi, S. (2004). Regularized sequentially linear saw-tooth softening model. *International Journal for Numerical and Analytical Methods in Geomechanics*, *28*(7-8), 821–856.

Saouma, V. (1997). Lecture notes in fracture mechanics. Department of Civil Environmental and Architectural Engineering, University of Colorado, Boulder, USA.

SAS IP, Inc. (2007). *ANSYS Workbench 11.0*. SAS IP, Inc. [Computer Program].

Sawata, K. & Yasumura, M. (2003). Estimation of yield and ultimate strengths of bolted timber joints by nonlinear analysis and yield theory. *J Wood Sci*, *49*, 383–391.

Schmid, M. (2002). *Anwendung der Bruchmechanik auf Verbindungen mit Holz - Application of Fracture Mechanics to Timber Joints (engl.)*. PhD thesis, University of Karlsruhe.

Schmid, M., Blass, H. J., & Frasson, R. P. M. (2002). Effect of distances, spacing and number of dowels in a row on the load carrying capacity of connections with dowels failing by splitting. In *International Council for Research and Innovation in Building and Construction, Working Commission CIB-W18,*, volume 35-7-5., Kyoto, Japan.

Schmidt, J. & Kaliske, M. (2006). Three-dimensional material modelling of spruce wood using a multi-surface-plasticity model. *Holz als Roh- und Werkstoff*, *64*, 393–402.

Sedighi-Gilani, M. & Navi, P. (2007). Micromechanical approach to wood fracture by three-dimensional mixed lattice-continuum model at fiber level. *Wood Sci Technol*, *41*, 619–634.

Shih, C. & Lee, D. (1978). Further developments in anisotropic plasticity 1978. *ASME J Eng Math Technol*, *100*, 294–302.

Smith, I., Landis, E., & Gong, M. (2003). *Fracture and Fatigue in Wood*. John Wiley & Sons. Ltd.

Smith, I., Snow, M., Asiz, A., & Vasic, S. (2007). Failure mechanics in wood-based materials: A review of discrete, continuum, and hybrid finite-element representations. *Holzforschung*, *61*, 352–359.

Snow, M., Smith, I., & Asiz, A. (2004). Dowel joints in engineered wood products: Assessment of simple fracture mechanics models. In *International Council for Research and Innovation in Building and Construction, Working Commission CIB-W18, Edinburgh, UK*, volume 37-7-14, Edinburgh, UK.

Snow, M. A. (2006). *Fracture Development in Engineered Wood Product Bolted Connections*. PhD thesis, University of New Brunswick.

Tabiei, A. & Wu, J. (2000). Three-dimensional nonlinear orthotropic finite element material model for wood. *Composite Structures*, *50*, 143–149.

The MathWorks, Inc. (2007). *MATLAB 7*. The MathWorks, Inc., 3 Apple Hill Drive, Natick, MA 01760-2098, United States [Computer Program].

Thibaut, B., Gril, J., & Fournier, M. (2001). Mechanics of wood and trees: Some new highlights for an old story. *C. R. Acad. Sci. Paris*, *IIb*, 701–716.

Tsai, S. & Wu, E. (1971). A general theory of strength of anisotropic materials. *Journal of Composite Materials*, *5*, 58–80.

USDA (1999). *Wood Handbook: Wood as an Engineering Material*. Forest Products Laboratory, Forest Service, United States Department of Agriculture.

van der Put, T. (1990). Tension perpendicular to the grain at notches and joints. In *International Council for Research and Innovation in Building and Construction, Working Commission CIB-W18, Lisbon, Portugal*.

Vasic, S. (2000). *Applications of Fracture Mechanics to Wood*. PhD thesis, University of New Brunswick.

Vasic, S. & Smith, I. (2000). Non-linear fracture mechanics analysis of thickness effect in green wood. In *World Conference on Timber Engineering*, Whistler Resort, British Columbia, Canada.

Vasic, S., Smith, I., & Landis, E. N. (2005). Finite element techniques and models for wood fracture mechanics. *Wood Sci Technol*, *39*, 3–17.

Wavefront Technologies (1984). *Obj File Format*. Wavefront Technologies, 530 East Montecito Street, Santa Barbara, CA 93103, United States [Computer Program].

Wilkinson, T. (1986). Load distribution among bolts parallel to load. *Journal of Structural Engineering*, *112*(4), 835–852.

Wilkinson, T. (1993). Bolted connection design values based on european yield model. *ASCE Journal of Structural Engineering*, *119*(7).

Wu, E. (1967). Application of fracture mechanics to anisotropic plates. *Journal of Applied Mechanics*, *34*(4), 967–974.

Zhu, E. C., Guan, Z., Rodd, P., & Pope, D. J. (2005). A constitutive model for osb and its application in finite element analysis. *Holz als Roh und Werkstoff*, *63*, 87–93.

A Appendix

The Appendix contains the following sections:

- examples of the SSC algorithm
- density and moisture measurement of test specimens
- a list of model input file commands, along with their parameters and function
- listings of the model input files, that were used in the result chapter
- a list of written *MATLAB* programs
- WCTE2006 paper
- WCTE2008 paper

A.1 Examples of the SSC Algorithm

Here, 5 examples to illustrate the working of the SSC algorithm in simple one dimensional models shall be presented. These are

- the original example as presented in Jirasek & Bazant (1995)
- a modified version with compressed links instead of tensioned
- a modified version with brittle links (snap-back)
- an example with included plastic deformation
- an example with included plastic deformation and brittle links

The examples are depicted in the respective following figures (Fig. A.1, A.2, A.3, A.4 and A.5). The geometry of the structure is shown at the bottom left. The applied force is marked with a red triangle and the fixed displacement with a green one. The length of the link elements is set to a unit length of 1 mm. Therefore, strain equals absolute displacement for the respective link.

Note: in the output of the deformed structure a magnification factor of 1/10 is applied to the calculated displacements in order to fit the deformation into the figure.

The solution algorithm is summarised in tables for each load step i and, if required for this respective step, with the additional iteration (right aligned).

Note: since no variation in stiffness and strength properties is applied to the lattice elements, the input parameters represent the actual link parameters.

A.1.1 Original Example

The following example demonstrates the original SSC algorithm as presented in Jirasek & Bazant (1995). The structure, as can be seen in Fig. A.1, consists of 4 link elements connecting 3 DoFs and is loaded with a force applied at DoF 3 ($\{F_{ref}\} = \{0, 0, 1\}^T$) and is constrained at DoF 1.

The set input parameters for the 4 link elements are:

parameter	**value**	**unit**
$\overline{K}_{①,l}$	1	[N/mm]
$\gamma_{T,l}$	3	[-]
		for $l = 1..4$
$S_{T,1}$	1	[N]
$S_{T,2}$	2.5	[N]
$S_{T,3}$	1.25	[N]
$S_{T,4}$	2	[N]

thus follows:

$K_{s,T,l}$	-0.5	[N/(mm/mm)]
		for $l = 1..4$
$\epsilon_{p,T,1}$	1	[-]
$\epsilon_{p,T,2}$	2.5	[-]
$\epsilon_{p,T,3}$	1.25	[-]
$\epsilon_{p,T,4}$	2	[-]
$\epsilon_{f,T,1}$	3	[-]
$\epsilon_{f,T,2}$	7.5	[-]
$\epsilon_{f,T,3}$	3.75	[-]
$\epsilon_{f,T,4}$	6	[-]

As an initial value the state of all links is ①. The reference load vector $\{F_{ref}\} = \{0, 0, 1\}^T$ is used to determine with the current global stiffness matrix $[K_i]$ the displacement vector $\{\Delta_{i,ref}\}$. Internally this is achieved with the MIF (subsection 5.6.4). The strain increment $d\epsilon_{i,l}$ for each link l and load step i is extracted from the displacement vector. Since, in this example, the length of the elements is 1 mm and movement occurs only in one dimension, strain is simply the difference in displacement of the respective DoFs. The load factor $\lambda_{i,l}$ for link l is determined according to,

$$\lambda_{i,l} = \frac{\epsilon_{cr,l} - \epsilon_{i-1,l}}{d\epsilon_{i,l}} \tag{A.1}$$

where $\epsilon_{cr,l}$ is the respective critical strain (depends on the present status, Table 5.5) and $d\epsilon_{i,l}$ is the strain increment.

For the actual load step the minimum positive load factor is chosen unless negative factors exist. In the latter case the algorithm looks for links (with status ② and ⑤) for which their strain increment is consistent with their assumed status (i.e.

② with positive $d\epsilon_{i,l}$ and ⑤ with negative $d\epsilon_{i,l}$) and for which this is not the case. If more inconsistent than consistent links are present then the negative load factor ($\lambda_i = min(\lambda^+_{i,l})$) is chosen, otherwise a positive one ($\lambda_i = max(\lambda^-_{i,l})$).

In case of a positive load factor **inconsistent** links are transferred (② to ⑤ and vice versa). This happens in the same way for **consistent** links if a negative load factor is chosen.

With the changed stiffness due to the status ⑤ ('unloading') a new stiffness matrix needs to be solved for a new reference displacement vector $\{\Delta_{i,ref}\}$ and subsequently new strain increments once more in an additional iterative step. The previously described decision on whether a positive or negative load is taken is repeated and with the changed stiffness matrix a final decision on the load factor is made.

The solution algorithm for the example is summarised in the following table.

step $i = 1$

$[K_1]\{\Delta_{1,ref}\} = \{F_{ref}\} \Rightarrow \{\Delta_{1,ref}\} = \{0, 0.5, 1\}^T$

link l	status	$K_{1,l}$	$f_{0,l}$	$\epsilon_{0,l}$	$d\epsilon_{1,l}$	$\epsilon_{cr,l}$	$\lambda_{1,l}$	new status
1	①	**1**	**0**	**0**	**0.5**	**1**	**2**	②
2	①	1	0	0	0.5	2.5	5	①
3	①	1	0	0	0.5	1.25	2.5	①
4	①	1	0	0	0.5	2	4	①

$\Rightarrow \lambda_1 = min\lambda^+_1 = 2$, **chosen link l=1**

$\{F_1\} = \lambda_1\{F_{ref}\} = \{0, 0, 2\}^T$

$\{\Delta_1\} = \lambda_1\{\Delta_{1,ref}\} = \{0, 1, 2\}^T$

step $i = 2$

$[K_2]\{\Delta_{2,ref}\} = \{F_{ref}\} \Rightarrow \{\Delta_{2,ref}\} = \{0, 2, 2.5\}^T$

link l	status	$K_{2,l}$	$f_{1,l}$	$\epsilon_{1,l}$	$d\epsilon_{2,l}$	$\epsilon_{cr,l}$	$\lambda_{2,l}$	new status
1	②	-0.5	1	1	2	3	1	②
2	①	1	1	1	2	2.5	0.75	①
3	**①**	**1**	**1**	**1**	**0.5**	**1.25**	**0.5**	**②**
4	①	1	1	1	0.5	2	2	①

$\Rightarrow \lambda_2 = min\lambda_2^+ = 0.5$, **chosen link l=3**

$\{F_2\} = \{F_1\} + \lambda_2\{F_{ref}\} = \{0, 0, 2.5\}^T$

$\{\Delta_2\} = \{\Delta_1\} + \lambda_2\{\Delta_{2,ref}\} = \{0, 2, 3.25\}^T$

step $i = 3$

$[K_3]\{\Delta_{3,ref}\} = \{F_{ref}\} \Rightarrow \{\Delta_{3,ref}\} = \{0, 2, 4\}^T$

link l	status	$K_{3,l}$	$f_{2,l}$	$\epsilon_{2,l}$	$d\epsilon_{3,l}$	$\epsilon_{cr,l}$	$\lambda_{3,l}$	new status
1	②	-0.5	0.5	2	2	3	0.5	②
2	**①**	**1**	**2**	**2**	**2**	**2.5**	**0.25**	**②**
3	②	-0.5	1.25	1.25	2	3.75	1.25	②
4	①	1	1.25	1.25	2	2	0.375	①

$\Rightarrow \lambda_3 = min\lambda_3^+ = 0.25$, **chosen link l=2**

$\{F_3\} = \{F_2\} + \lambda_3\{F_{ref}\} = \{0, 0, 2.75\}^T$

$\{\Delta_3\} = \{\Delta_2\} + \lambda_3\{\Delta_{3,ref}\} = \{0, 2.5, 4.25\}^T$

step $i = 4$

$[K_4]\{\Delta_{4,ref}\} = \{F_{ref}\} \Rightarrow \{\Delta_{4,ref}\} = \{0, -1, 1\}^T$

link l	status	$K_{4,l}$	$f_{3,l}$	$\epsilon_{3,l}$	$d\epsilon_{4,l}$	$\epsilon_{cr,l}$	$\lambda_{4,l}$	new status
1	②	-0.5	0.25	-1	-1	3	-0.5	②
2	②	-0.5	2.5	2.5	-1	7.5	-5	②
3	②	-0.5	1	1.75	2	3.75	1	⑤
4	①	1	1.75	1.75	2	2	0.125	①

Two links, link l=1 and 2 (negative $d\epsilon_{4,1}$ and $d\epsilon_{4,2}$) are inconsistent with assumed status ② for a positive load step while one link, link 3 (positive $d\epsilon_{4,3}$) is consistent with ②

$\Rightarrow$ neg. load factor $max\lambda_4^-$

link 3 changes to ⑤ with $K_3 = \sigma_3/\epsilon_{4,3} = 0.571$, iteration is required: step $i = 4'$

intermediate step $i = 4'$

$[K_{4'}]\{\Delta_{4',ref}\} = \{F_{ref}\} \Rightarrow \{\Delta_{4',ref}\} = \{0, -1, 1\}^T$

link l	status	$K_{4',l}$	$f_{3,l}$	$\epsilon_{4',l}$	$d\epsilon_{4',l}$	$\epsilon_{cr,l}$	$\lambda_{4',l}$	new status
1	②	**-0.5**	**0.25**	**2.5**	**-1**	**3**	**-0.5**	④
2	②	-0.5	2.5	2.5	-1	7.5	-5	②
3	⑤	0.571	1	1.75	0.636	1.75	+0	⑤
4	①	1	1.75	1.75	0.636	2	0.393	①

Now link l=1,2 and 3 (positive $d\epsilon_{4',1}$, $d\epsilon_{4',2}$ and negative $d\epsilon_{4',3}$) are all inconsistent with assumed status ②, ② and ⑤

$\Rightarrow$ neg. load factor $\lambda_4 = max\lambda_{4'}^- = -0.5$, **chosen link l=1**

link l=3 is transferred from ⑤ to ③

$\{F_4\} = \{F_3\} + \lambda_4\{F_{ref}\} = \{0, 0, 2.25\}^T$

$\{\Delta_4\} = \{\delta_3\} + \lambda_4\{\Delta_{4,ref}\} = \{0, 3, 4.432\}^T$

step $i = 5$

$[K_5]\{\Delta_{5,ref}\} = \{F_{ref}\} \Rightarrow \{\Delta_{5,ref}\} = \{0, -2, -1.364\}^T$

link l	status	$K_{5,l}$	$f_{4,l}$	$\epsilon_{4,l}$	$d\epsilon_{5,l}$	$\epsilon_{cr,l}$	$\lambda_{5,l}$	new status
1	④	0	0	3	-2	3	-	④
2	**②**	**-0.5**	**2.25**	**3**	**-2**	**7.5**	**-2.25**	**④**
3	③	0.571	0.818	1.432	0.636	1.75	0.5	③
4	①	1	1.432	1.432	0.636	2	0.893	①

link l=2 (negative $d\epsilon_{5,2}$) is inconsistent with assumed status ②

$\Rightarrow \lambda_5 = max\lambda_5^- = -2.25$, **chosen link l=2**

$\{F_5\} = \{F_4\} + \lambda_5\{F_{ref}\} = \{0, 0, 0\}^T$

$\{\Delta_5\} = \{\delta_4\} + \lambda_5\{\Delta_{5,ref}\} = \{0, 7.5, 7.5\}^T$

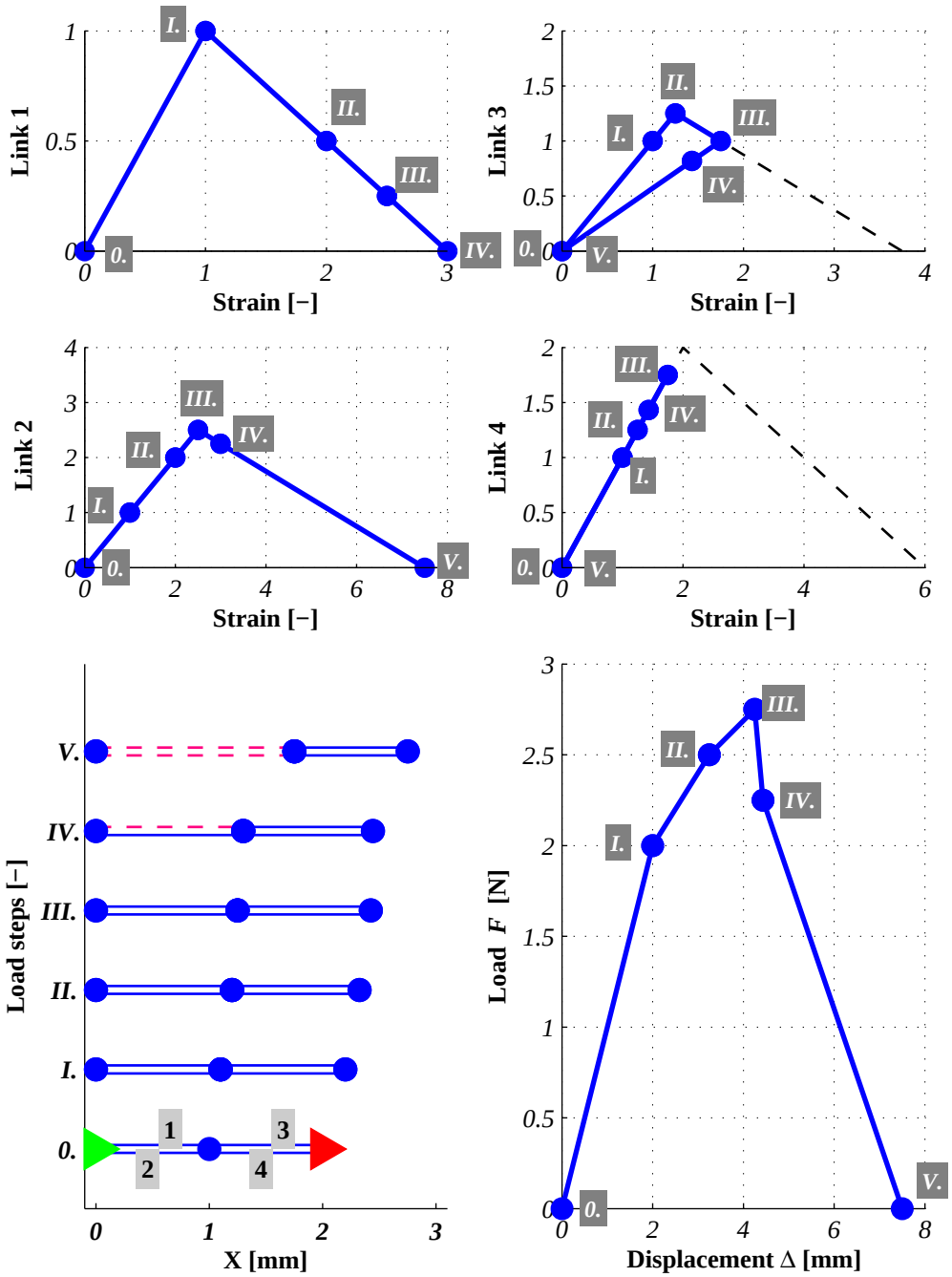

Figure A.1: *Example of SSC algorithm from Jirasek & Bazant (1995), load-strain plots of individual link elements (top) and model LDP with deformed structure plot (below), (original in colour)*

A.1.2 Original Example in Compression

The same arrangement as described in Jirasek & Bazant (1995) can be used in compression. For this, new status definitions are introduced as described in subsection 5.6.2. The additional states are $-①$, $-②$, $-③$ and $-⑤$ with respect to their tensile counterparts. The set parameters are exactly the same as in the previous example. Additionally, the compressive strength parameters are the same as the tensile parameters $S_{C,l} = -S_{T,l}$ and thus follows $\epsilon_{p,C,l} = -\epsilon_{p,T,l}$ and $\epsilon_{f,C,l} = -\epsilon_{f,T,l}$. The structure is constrained at DoF 3 and the applied load vector is $\{F_{ref}\} = \{1, 0, 0\}^T$.

The set input parameters are:

parameter	**value**	**unit**
$K_{①,l}$	1	[N/(mm/mm)]
$\gamma_{T,l}$	3	[-]
		for $l = 1..4$
$S_{\mathbf{C},1}$	1	[N]
$S_{\mathbf{C},2}$	2.5	[N]
$S_{\mathbf{C},3}$	1.25	[N]
$S_{\mathbf{C},4}$	2	[N]
thus follows:		
$K_{s,l}$	-0.5	[N/(mm/mm)]
		for $l = 1..4$
$\epsilon_{p,\mathbf{C},1}$	1	[-]
$\epsilon_{p,\mathbf{C},2}$	2.5	[-]
$\epsilon_{p,\mathbf{C},3}$	1.25	[-]
$\epsilon_{p,\mathbf{C},4}$	2	[-]
$\epsilon_{f,\mathbf{C},1}$	3	[-]
$\epsilon_{f,\mathbf{C},2}$	7.5	[-]
$\epsilon_{f,\mathbf{C},3}$	3.75	[-]
$\epsilon_{f,\mathbf{C},4}$	6	[-]

While the resulting load displacement plot is the same, the individual load-strain curves for the links are a mirrored image of the previous original example (Fig. A.2).

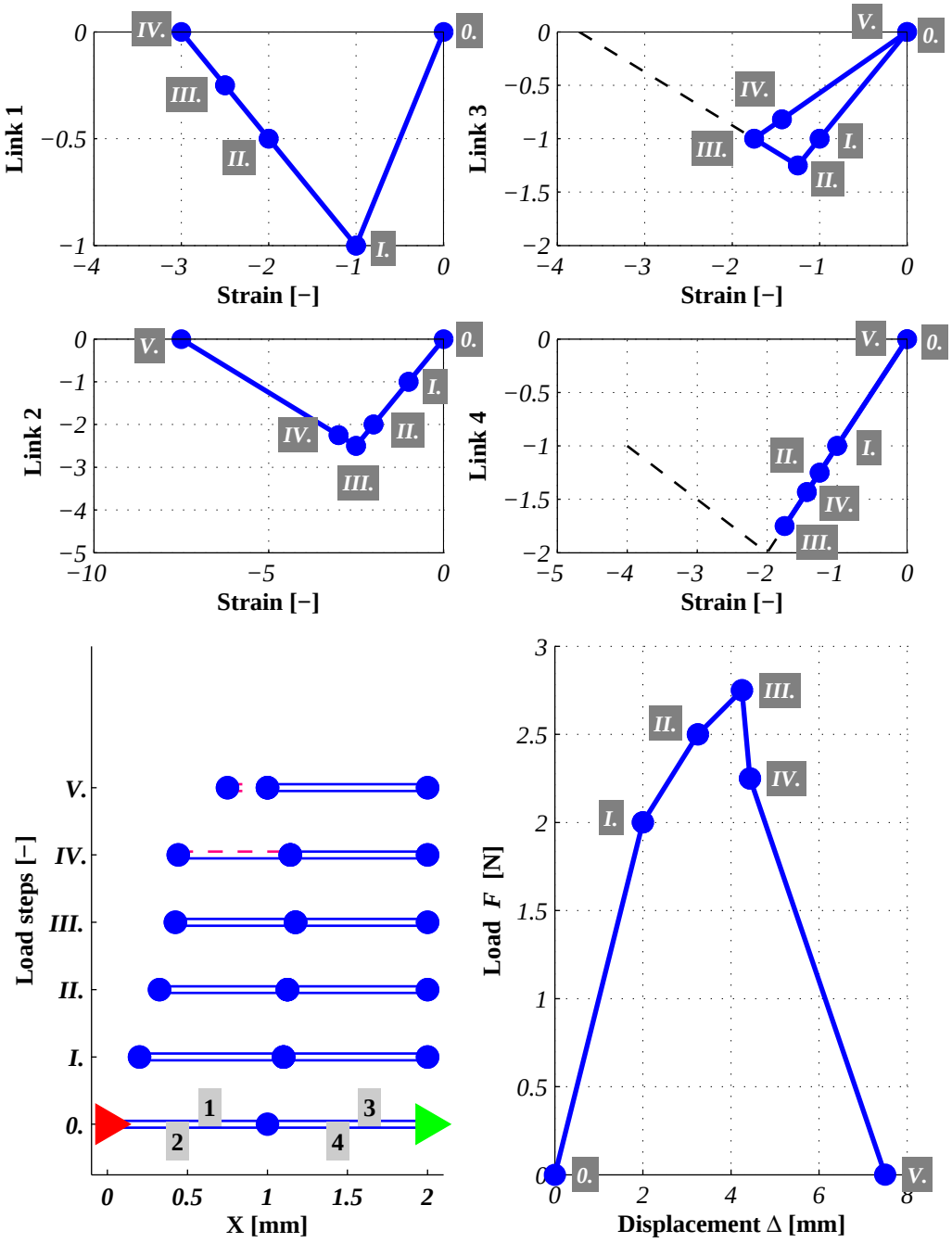

Figure A.2: *Same example of SSC algorithm from Jirasek & Bazant (1995) but in compression, load-strain plots of individual link elements (top) and model LDP with deformed structure plot (below), (original in colour)*

A.1.3 Original Example with Brittle Links (Snap-Back)

When the *brittleness* of individual link elements is set high (i.e. $\gamma_{T,l} \Rightarrow 1$) snap-back behaviour occurs. This is demonstrated in the following example and depicted in Fig. A.3.

The set input parameters are:

parameter	**value**	**unit**
$K_{\textcircled{1},l}$	1	[N/(mm/mm)]
$\gamma_{T,l}$	**1.2**	[-]
		for $l = 1..4$
$S_{T,1}$	1	[N]
$S_{T,2}$	2.5	[N]
$S_{T,3}$	1.25	[N]
$S_{T,4}$	2	[N]

thus follows:

$K_{s,T,l}$	-5	[N/(mm/mm)]
		for $l = 1..4$
$\epsilon_{p,T,1}$	1	[-]
$\epsilon_{p,T,2}$	2.5	[-]
$\epsilon_{p,T,3}$	1.25	[-]
$\epsilon_{p,T,4}$	2	[-]
$\epsilon_{f,T,1}$	1.2	[-]
$\epsilon_{f,T,2}$	3	[-]
$\epsilon_{f,T,3}$	1.5	[-]
$\epsilon_{f,T,4}$	2.4	[-]

The solution algorithm for the example is summarised in the following tables.

step $i = 1$

$[K_1]\{\Delta_{1,ref}\} = \{F_{ref}\} \Rightarrow \{\Delta_{1,ref}\} = \{0, 0.5, 1\}^T$

link l	status	$K_{1,l}$	$f_{0,l}$	$\epsilon_{0,l}$	$d\epsilon_{1,l}$	$\epsilon_{cr,l}$	$\lambda_{1,l}$	new status
1	**①**	**1**	**0**	**0**	**0.5**	**1**	**2**	**②**
2	①	1	0	0	0.5	2.5	5	①
3	①	1	0	0	0.5	1.25	2.5	①
4	①	1	0	0	0.5	2	4	①

$\Rightarrow \lambda_1 = min\lambda_1^+ = 2$, **chosen link l=1**

$\{F_1\} = \lambda_1\{F_{ref}\} = \{0, 0, 2\}^T$

$\{\Delta_1\} = \lambda_1\{\Delta_{1,ref}\} = \{0, 1, 2\}^T$

step $i = 2$

$[K_2]\{\Delta_{2,ref}\} = \{F_{ref}\} \Rightarrow \{\Delta_{2,ref}\} = \{0, -0.25, 0.25\}^T$

link l	status	$K_{2,l}$	$f_{1,l}$	$\epsilon_{1,l}$	$d\epsilon_{2,l}$	$\epsilon_{cr,l}$	$\lambda_{2,l}$	new status
1	**②**	**-5**	**1**	**1**	**-0.25**	**1.2**	**-0.8**	**④**
2	−①	1	1	1	-0.25	-2.5	14	①
3	①	1	1	1	0.5	1.25	0.5	−①
4	①	1	1	1	0.5	2	2	①

Link l=1 (negative $d\epsilon_{2,1}$) is inconsistent with assumed status ②

$\Rightarrow$ neg. load factor $\lambda_2 = max\lambda_2^- = -0.8$, **chosen link l=1**

$\{F_2\} = \{F_1\} + \lambda_2\{F_{ref}\} = \{0, 0, 1.2\}^T$

$\{\Delta_2\} = \{\Delta_1\} + \lambda_2\{\Delta_{2,ref}\} = \{0, 1.2, 1.8\}^T$

step $i = 3$

$[K_3]\{\Delta_{3,ref}\} = \{F_{ref}\} \Rightarrow \{\Delta_{3,ref}\} = \{0, 1, 1.5\}^T$

link l	status	$K_{3,l}$	$f_{2,l}$	$\epsilon_{2,l}$	$d\epsilon_{3,l}$	$\epsilon_{cr,l}$	$\lambda_{3,l}$	new status
1	④	0	0	1.2	1	n.a.	n.a.	④
2	**①**	**1**	**1.2**	**1.2**	**1**	**2.5**	**1.3**	**②**
3	**①**	**1**	**0.6**	**0.6**	**0.5**	**1.25**	**1.3**	**②**
4	①	1	0.6	0.6	0.5	2	2.8	①

$\Rightarrow \lambda_3 = min\lambda_3^+ = 1.3$, **chosen link l=2 and 3**

$\{F_3\} = \{F_2\} + \lambda_3\{F_{ref}\} = \{0, 0, 2.5\}^T$

$\{\Delta_3\} = \{\Delta_2\} + \lambda_3\{\Delta_{3,ref}\} = \{0, 2.5, 3.75\}^T$

step $i = 4$

$[K_4]\{\Delta_{4,ref}\} = \{F_{ref}\} \Rightarrow \{\Delta_{4,ref}\} = \{0, -0.2, -0.45\}^T$

link l	status	$K_{4,l}$	$f_{3,l}$	$\epsilon_{3,l}$	$d\epsilon_{4,l}$	$\epsilon_{cr,l}$	$\lambda_{4,l}$	new status
1	④	0	0	2.5	-0.2	n.a.	n.a.	④
2	②	-5	2.5	2.5	-0.2	3	-2.5	②
3	**②**	**-5**	**1.25**	**1.25**	**-0.25**	**1.5**	**-1**	**④**
4	−①	1	1.25	1.25	-0.25	-2	13	−①

Two links, link l=2 and 3 (negative $d\epsilon_{4,2}$ and $d\epsilon_{4,3}$) are inconsistent with assumed status ② and ②

$\Rightarrow$ neg. load factor $\lambda_4 = max\lambda_4^- = -1$, **chosen link l=3**

$\{F_4\} = \{F_3\} + \lambda_4\{F_{ref}\} = \{0, 0, 1.5\}^T$

$\{\Delta_4\} = \{\Delta_3\} + \lambda_4\{\Delta_{4,ref}\} = \{0, 2.7, 4.2\}^T$

step $i = 5$

$[K_5]\{\Delta_{5,ref}\} = \{F_{ref}\} \Rightarrow \{\Delta_{5,ref}\} = \{0, -0.2, 0.8\}^T$

link l	status	$K_{5,l}$	$f_{4,l}$	$\epsilon_{4,l}$	$d\epsilon_{5,l}$	$\epsilon_{cr,l}$	$\lambda_{5,l}$	new status
1	④	0	0	2.7	-0.2	n.a.	n.a.	④
2	**②**	**-5**	**1.5**	**2.7**	**-0.2**	**3**	**-1.5**	**④**
3	④	0	0	1.5	1	n.a.	n.a.	④
4	①	1	1.5	1.5	1	2	0.5	−①

Link l=2 (negative $d\epsilon_{5,2}$) is inconsistent with assumed status ②

$\Rightarrow$ neg. load factor $\lambda_5 = max\lambda_5^- = -1.5$, **chosen link l=2**

$\{F_5\} = \{F_4\} + \lambda_5\{F_{ref}\} = \{0, 0, 0\}^T$

$\{\Delta_5\} = \{\Delta_4\} + \lambda_5\{\Delta_{5,ref}\} = \{0, 3, 3\}^T$

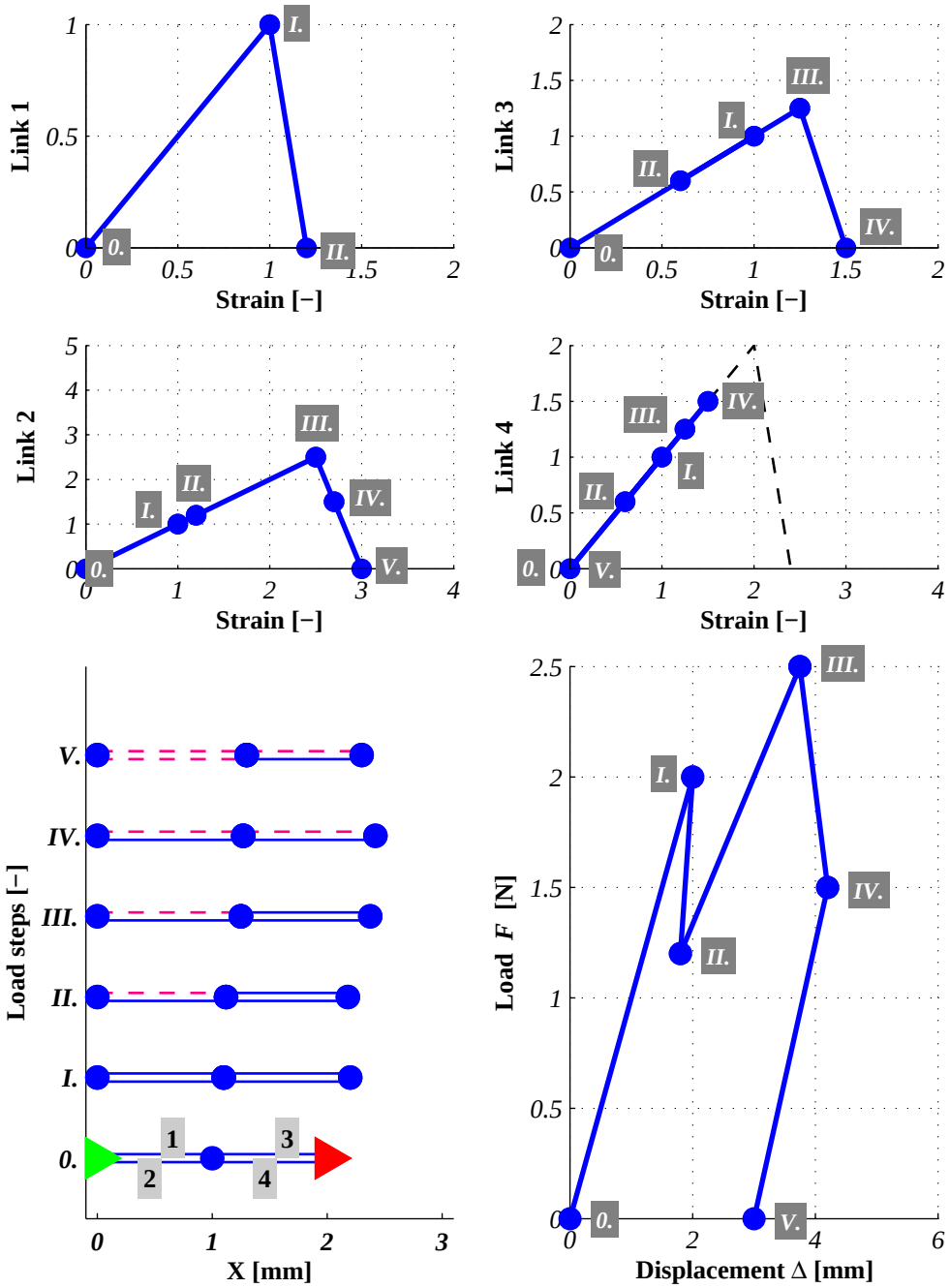

Figure A.3: *Example of SSC algorithm similar to Jirasek & Bazant (1995) but with brittle links ($\gamma_{T,l} = 1.2$), load-strain plots of individual link elements (top) and model LDP with deformed structure plot (below), (original in colour)*

A.1.4 Example with Plastic Compression

When plastic links are considered new links states are introduced ($-$⑫, $-$⑬ and $-$⑮) as pictured in Fig. 5.19.
An example shall demonstrate the behaviour of plastic link elements. The structure consists of 2 link elements with 3 DoFs and is loaded with a force applied at DoF 3 with $\{F_{ref}\} = \{1, 0, 0\}^T$ and is constrained at DoF 3. Since the load does not reach zero the solution algorithm is stopped when the displacement reached a limit of 5 mm. The LDPs for the individual link elements and the resulting LDP for the structure can be seen in Fig. A.4.

The set input parameters are:

parameter	**value**	**unit**
$K_{①,l}$	1	[N/(mm/mm)]
$\gamma_{C,l}$	**0.25**	[-]
		for $l = 1..2$
$S_{C,1}$	-1	[N]
$S_{C,2}$	-0.5	[N]

thus follows:

$K_{s,C,l}$	0.25	[N/(mm/mm)]
		for $l = 1..4$
$\epsilon_{p,C,1}$	-1	[-]
$\epsilon_{p,C,2}$	-0.5	[-]
$\epsilon_{f,C,1}$	$\approx \infty$	[-]
$\epsilon_{f,C,2}$	$\approx \infty$	[-]

The solution algorithm for the example is summarised in the following tables.

step $i = 1$

$[K_1]\{\Delta_{1,ref}\} = \{F_{ref}\} \Rightarrow \{\Delta_{1,ref}\} = \{2, 1, 0\}^T$

link l	status	$K_{1,l}$	$f_{0,l}$	$\epsilon_{0,l}$	$d\epsilon_{1,l}$	$\epsilon_{cr,l}$	$\lambda_{1,l}$	new status
1	$-$①	1	0	0	-1	-1	1	$-$①
2	$-$①	**1**	**0**	*0*	**-1**	**-0.5**	**0.5**	$-$⑫

$\Rightarrow \lambda_1 = min\lambda_1^+ = 0.5$, **chosen link l=2**

$\{F_1\} = \lambda_1\{F_{ref}\} = \{0.5, 0, 0\}^T$

$\{\Delta_1\} = \lambda_1\{\Delta_{1,ref}\} = \{1, 0.5, 0\}^T$

step $i = 2$

$[K_2]\{\Delta_{2,ref}\} = \{F_{ref}\} \Rightarrow \{\Delta_{2,ref}\} = \{5, 4, 0\}^T$

link l	status	$K_{2,l}$	$f_{1,l}$	$\epsilon_{1,l}$	$d\epsilon_{2,l}$	$\epsilon_{cr,l}$	$\lambda_{2,l}$	new status
1	$-$①	**1**	**-0.5**	**-0.5**	**-1**	**-1**	**0.5**	$-$⑫
2	$-$⑫	0.25	-0.5	-0.5	-4	$-\approx\infty$	n.a.	$-$⑫

$\Rightarrow \lambda_2 = min\lambda_2^+ = 0.5$, **chosen link l=1**

$\{F_2\} = \{F_1\} + \lambda_2\{F_{ref}\} = \{1, 0, 0\}^T$

$\{\Delta_2\} = \{\Delta_1\} + \lambda_2\{\Delta_{2,ref}\} = \{3.5, 2.5, 0\}^T$

step $i = 3$

$[K_3]\{\Delta_{3,ref}\} = \{F_{ref}\} \Rightarrow \{\Delta_{3,ref}\} = \{8, 4, 0\}^T$

link l	status	$K_{3,l}$	$f_{2,l}$	$\epsilon_{2,l}$	$d\epsilon_{3,l}$	$\epsilon_{cr,l}$	$\lambda_{3,l}$	new status
1	$-$⑫	0.25	-1	-1	-4	$-\approx\infty$	n.a.	$-$⑫
2	$-$⑫	0.25	-1	-2.5	-4	$-\approx\infty$	n.a.	$-$⑫

$\Rightarrow$ λ_3=0.1875, **load factor is limited by maximum displacement of** 5 mm

$\{F_3\} = \{F_2\} + \lambda_3\{F_{ref}\} = \{1.1875, 0, 0\}^T$

$\{\Delta_3\} = \{\Delta_2\} + \lambda_3\{\Delta_{3,ref}\} = \{5, 3.25, 0\}^T$

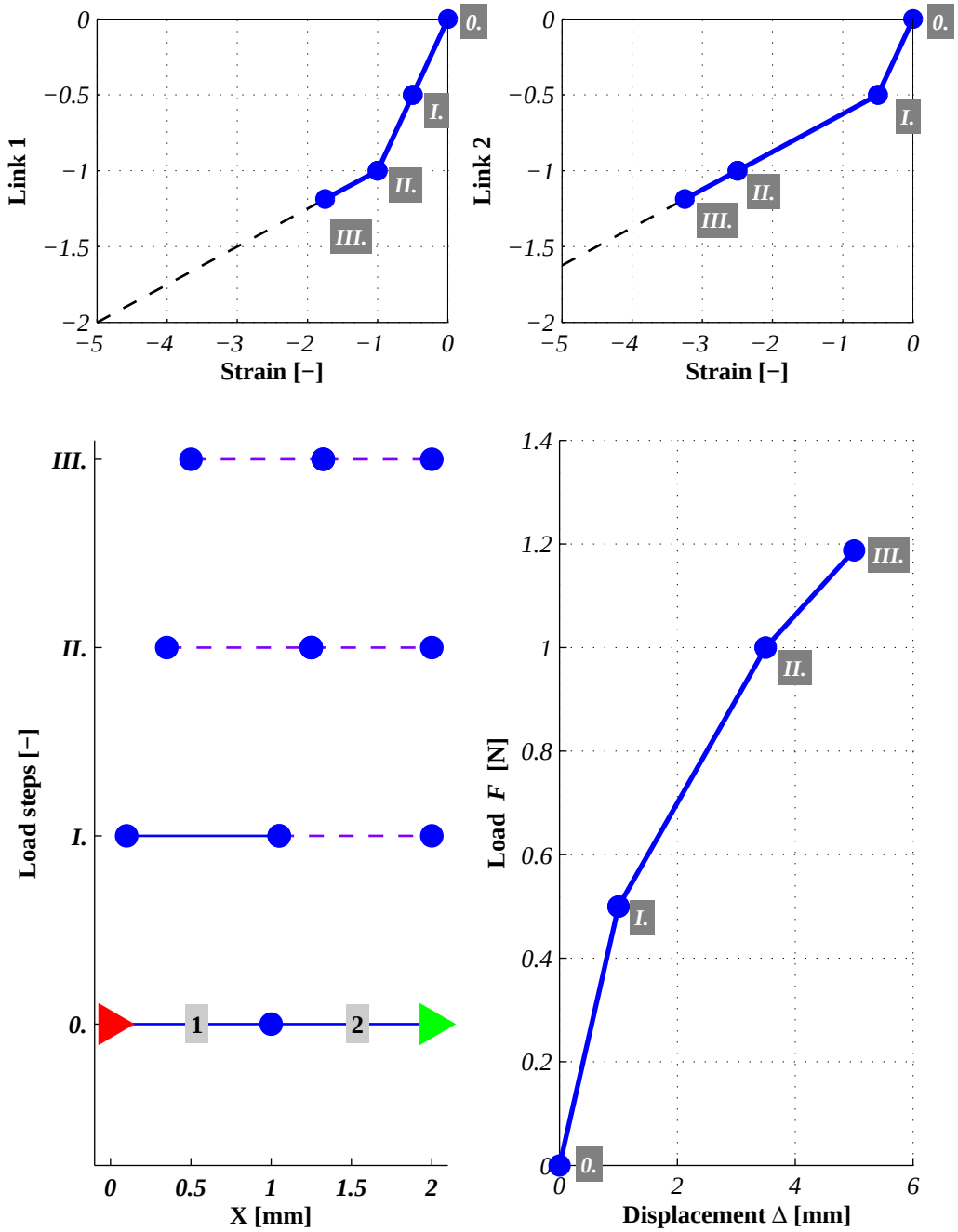

Figure A.4: *Example of SSC algorithm including plastic compression, load-strain plots of individual link elements (top) and model LDP with deformed structure plot (below), (original in colour)*

A.1.5 Example with Plastic Compression and Brittle Links

An example illustrates the case of combined plastic and brittle link elements. 4 link elements and 3 DoFs are used. The structure is loaded with a force applied at DoF 3 with $\{F_{ref}\} = \{1, 0, 0\}^T$ and is constrained at DoF 3. The LDPs for the individual link elements and the resulting LDP for the structure can be seen in Fig. A.5. The links 1 and 3 first start to change to plastic hardening and, with link 2 and 4 consecutively braking, will unload (status $-$⑬) and reload as can be seen in the figure.

The set input parameters are:

parameter	**value**	**unit**
$K_{①,l}$	1	[N/(mm/mm)]
$\gamma_{C,1}$	0.25	[-]
$\gamma_{C,2}$	1.2	[-]
$\gamma_{C,3}$	0.25	[-]
$\gamma_{C,4}$	1.2	[-]
$S_{C,1}$	-0.05	[N]
$S_{C,2}$	-0.4	[N]
$S_{C,3}$	-0.15	[N]
$S_{C,4}$	-0.25	[N]

thus follows:

$K_{s,C,1}$	0.25	[N/(mm/mm)]
$K_{s,C,2}$	-0.5	[N/(mm/mm)]
$K_{s,C,3}$	0.25	[N/(mm/mm)]
$K_{s,C,4}$	-0.5	[N/(mm/mm)]
$\epsilon_{p,C,1}$	-0.05	[-]
$\epsilon_{p,C,2}$	-0.4	[-]
$\epsilon_{p,C,3}$	-0.15	[-]
$\epsilon_{p,C,4}$	-0.25	[-]
$\epsilon_{f,C,1}$	$\approx \infty$	[-]
$\epsilon_{f,C,2}$	-0.48	[-]
$\epsilon_{f,C,3}$	$\approx \infty$	[-]
$\epsilon_{f,C,4}$	-0.3	[-]

The solution algorithm for the example is summarised in the following tables.

step $i = 1$

$[K_1]\{\Delta_{1,ref}\} = \{F_{ref}\} \Rightarrow \{\Delta_{1,ref}\} = \{1, 0.5, 0\}^T$

link l	status	$K_{1,l}$	$f_{0,l}$	$\epsilon_{0,l}$	$d\epsilon_{1,l}$	$\epsilon_{cr,l}$	$\lambda_{1,l}$	new status
1	$-$(1)	**1**	**0**	**0**	**-0.5**	**-0.05**	**0.1**	$-$(12)
2	$-$(1)	1	0	0	-0.5	-0.4	0.8	$-$(1)
3	$-$(1)	1	0	0	-0.5	-0.15	0.3	$-$(1)
4	$-$(1)	1	0	0	-0.5	-0.25	0.5	$-$(1)

$\Rightarrow \lambda_1 = min\lambda_1^+ = 0.1$, **chosen link l=1**

$\{F_1\} = \lambda_1\{F_{ref}\} = \{0.1, 0, 0\}^T$

$\{\Delta_1\} = \lambda_1\{\Delta_{1,ref}\} = \{0.1, 0.05, 0\}^T$

step $i = 2$

$[K_2]\{\Delta_{2,ref}\} = \{F_{ref}\} \Rightarrow \{\Delta_{2,ref}\} = \{1.3, 0.5, 0\}^T$

link l	status	$K_{2,l}$	$f_{1,l}$	$\epsilon_{1,l}$	$d\epsilon_{2,l}$	$\epsilon_{cr,l}$	$\lambda_{2,l}$	new status
1	$-$(12)	0.25	-0.05	-0.05	-0.8	$-\approx\infty$	n.a.	$-$(12)
2	$-$(1)	1	-0.05	-0.05	-0.8	-0.4	0.438	$-$(1)
3	$-$(1)	**1**	**-0.05**	**-0.05**	**-0.5**	**-0.15**	**0.2**	$-$(12)
4	$-$(1)	1	-0.05	-0.05	-0.5	-0.25	0.4	$-$(1)

$\Rightarrow \lambda_2 = min\lambda_2^+ = 0.2$, **chosen link l=3**

$\{F_2\} = \{F_1\} + \lambda_2\{F_{ref}\} = \{0.3, 0, 0\}^T$

$\{\Delta_2\} = \{\Delta_1\} + \lambda_2\{\Delta_{2,ref}\} = \{0.36, 0.15, 0\}^T$

step $i = 3$

$[K_3]\{\Delta_{3,ref}\} = \{F_{ref}\} \Rightarrow \{\Delta_{3,ref}\} = \{1.6, 0.8, 0\}^T$

link l	status	$K_{3,l}$	$f_{2,l}$	$\epsilon_{2,l}$	$d\epsilon_{3,l}$	$\epsilon_{cr,l}$	$\lambda_{3,l}$	new status
1	$-$(12)	0.25	-0.09	-0.21	-0.8	$-\approx\infty$	n.a.	$-$(12)
2	$-$(1)	1	-0.21	-0.21	-0.8	-0.4	0.238	$-$(1)
3	$-$(12)	0.25	-0.15	-0.15	-0.8	$-\approx\infty$	n.a.	$-$(1)
4	$-$(1)	**1**	**-0.15**	**-0.15**	**-0.8**	**-0.25**	**0.125**	$-$(2)

$\Rightarrow \lambda_3 = min\lambda_3^+ = 0.125$, **chosen link l=4**

$\{F_3\} = \{F_2\} + \lambda_3\{F_{ref}\} = \{0.425, 0, 0\}^T$

$\{\Delta_3\} = \{\Delta_2\} + \lambda_3\{\Delta_{3,ref}\} = \{0.56, 0.25, 0\}^T$

step $i = 4$

$[K_4]\{\Delta_{4,ref}\} = \{F_{ref}\} \Rightarrow \{\Delta_{4,ref}\} = \{0.589, -0.211, 0\}^T$

link l	status	$K_{4,l}$	$f_{3,l}$	$\epsilon_{3,l}$	$d\epsilon_{4,l}$	$\epsilon_{cr,l}$	$\lambda_{4,l}$	new status
1	$-$(12)	0.25	-0.115	-0.31	-0.8	$-\approx\infty$	n.a.	$-$(15)
2	$-$(1)	1	-0.31	-0.31	-0.8	-0.4	0.113	$-$(1)
3	$-$(12)	0.25	-0.175	-0.25	0.211	$-\approx\infty$	n.a.	$-$(12)
4	$-$(2)	-5	-0.25	-0.25	0.211	-0.3	-0.238	$-$(2)

Link l=4 (positive $d\epsilon_{4,4}$) is inconsistent with assumed status $-$(2)
$\Rightarrow$ neg. load factor $max\lambda_4^-$

Since link l=1 (negative $d\epsilon_{4,1}$) is consistent with assumed status $-$(12) and a negative load step is chosen the link changes from $-$(12) to $-$(15) with $K_1 = \sigma_1/\epsilon_{4,1} = 0.371$, iteration is required: step $i = 4'$

step $i = 4'$

$[K_{4'}]\{\Delta_{4',ref}\} = \{F_{ref}\} \Rightarrow \{\Delta_{4',ref}\} = (0.519, -0.211, 0)$

link l	status	$K_{4',l}$	$f_{3,l}$	$\epsilon_{3,l}$	$d\epsilon_{4',l}$	$\epsilon_{cr,l}$	$\lambda_{4',l}$	new status
1	$-$(15)	0.371	-0.115	-0.31	-0.729	$-\approx\infty$	n.a.	$-$(13)
2	$-$(1)	1	-0.31	-0.31	-0.729	-0.4	0.123	$-$(1)
3	$-$(12)	0.25	-0.175	-0.25	0.211	$-\approx\infty$	n.a.	$-$(12)
4	$-$(2)	**-5**	**-0.25**	**-0.25**	**0.211**	**-0.3**	**-0.238**	(4)

Link l=4 (positive $d\epsilon_{4',4}$) is still inconsistent with assumed status $-$(2)

$\Rightarrow$ neg. load factor $\lambda_4 = max\lambda_4^- = -0.238$, **chosen link l=4**

Link l=1 is transferred from $-$(15) to $-$(13)

$\{F_4\} = \{F_3\} + \lambda_4\{F_{ref}\} = \{0.188, 0, 0\}^T$
$\{\Delta_4\} = \{\Delta_3\} + \lambda_4\{\Delta_{4,ref}\} = \{0.4368, 0.3, 0\}^T$

step $i = 5$

$[K_5]\{\Delta_{5,ref}\} = \{F_{ref}\} \Rightarrow \{\Delta_{5,ref}\} = \{4.729, 4, 0\}^T$

link l	status	$K_{5,l}$	$f_{4,l}$	$\epsilon_{4,l}$	$d\epsilon_{5,l}$	$\epsilon_{cr,l}$	$\lambda_{5,l}$	new status
1	$-$(13)	**0.371**	**-0.051**	**-0.137**	**-0.729**	**-0.31**	**0.238**	$-$(12)
2	$-$(1)	1	-0.137	-0.137	-0.729	-0.4	0.361	$-$(1)
3	$-$(12)	0.25	-0.188	-0.3	-4	$-\approx\infty$	n.a.	$-$(12)
4	(4)	0	0	-0.3	-4	n.a.	n.a.	(4)

$\Rightarrow \lambda_5 = min\lambda_5^+ = 0.238$, **chosen link l=1**

$\{F_5\} = \{F_4\} + \lambda_5\{F_{ref}\} = \{0.425, 0, 0\}^T$

$\{\Delta_5\} = \{\Delta_4\} + \lambda_5\{\Delta_{5,ref}\} = \{1.56, 1.25, 0\}^T$

step $i = 6$

$[K_6]\{\Delta_{6,ref}\} = \{F_{ref}\} \Rightarrow \{\Delta_{6,ref}\} = \{4.8, 4, 0\}^T$

link l	status	$K_{6,l}$	$f_{5,l}$	$\epsilon_{5,l}$	$d\epsilon_{6,l}$	$\epsilon_{cr,l}$	$\lambda_{6,l}$	new status
1	$-$(12)	0.25	-0.115	-0.31	-0.8	$-\approx\infty$	n.a	$-$(12)
2	$-$(1)	**1**	**-0.31**	**-0.31**	**-0.8**	**-0.4**	**0.113**	$-$(2)
3	$-$(12)	0.25	-0.425	-1.25	-4	$-\approx\infty$	n.a.	$-$(12)
4	(4)	0	0	-1.25	-4	n.a.	n.a.	(4)

$\Rightarrow \lambda_6 = min\lambda_6^+ = 0.113$, **chosen link l=2**

$\{F_6\} = \{F_5\} + \lambda_6\{F_{ref}\} = \{0.538, 0, 0\}^T$

$\{\Delta_6\} = \{\Delta_5\} + \lambda_6\{\Delta_{6,ref}\} = \{2.1, 1.7, 0\}^T$

step $i = 7$

$[K_7]\{\Delta_{7,ref}\} = \{F_{ref}\} \Rightarrow \{\Delta_{7,ref}\} = \{3.79, 4, 0\}^T$

link l	status	$K_{7,l}$	$f_{6,l}$	$\epsilon_{6,l}$	$d\epsilon_{7,l}$	$\epsilon_{cr,l}$	$\lambda_{7,l}$	new status
1	$-$(12)	0.25	-0.138	-0.4	0.211	$-\approx\infty$	n.a	$-$(12)
2	$-$(2)	-5	-0.4	-0.4	0.211	-0.48	-0.38	$-$(2)
3	$-$(12)	0.25	-0.538	-1.7	-4	$-\approx\infty$	n.a.	$-$(15)
4	(4)	0	0	-1.7	-4	n.a.	n.a.	(4)

Link l=2 (positive $d\epsilon_{7,2}$) is inconsistent with assumed status -(2)

$\Rightarrow$ neg. load factor $max\lambda_4^-$

Since link l=3 (negative $d\epsilon_{7,3}$) is consistent with assumed status $-$(12) and a negative load step is chosen the link changes from $-$(12) to $-$(15) with $K_1 = \sigma_1/\epsilon_{4,1} = 0.316$, iteration is required: step $i = 7'$

step $i = 7'$

$[K_{7'}]\{\Delta_{7',ref}\} = \{F_{ref}\} \Rightarrow \{\Delta_{7',ref}\} = \{2.952, 3.163, 0\}^T$

link l	status	$K_{7',l}$	$f_{6,l}$	$\epsilon_{6,l}$	$d\epsilon_{7',l}$	$\epsilon_{cr,l}$	$\lambda_{7',l}$	new status
1	$-$(12)	0.25	-0.138	-0.4	0.211	$-\approx\infty$	n.a	$-$(12)
2	$-$(2)	**-5**	**-0.4**	**-0.4**	**0.211**	**-0.48**	**-0.38**	(4)
3	$-$(15)	0.316	-0.538	-1.7	-3.163	$-\approx\infty$	n.a.	$-$(13)
4	(4)	0	0	-1.7	-3.163	n.a.	n.a.	(4)

Link l=2 (positive $d\epsilon_{7',2}$) is still inconsistent with assumed status $-$(2)

$\Rightarrow$ neg. load factor $\lambda_7 = max\lambda_{7'}^- = -0.48$, **chosen link l=2**

Link l=3 is transferred from $-$(15) to $-$(13)

$\{F_7\} = \{F_6\} + \lambda_7\{F_{ref}\} = \{0.158, 0, 0\}^T$

$\{\Delta_7\} = \{\Delta_6\} + \lambda_7\{\Delta_{7,ref}\} = \{0.978, 0.498, 0\}^T$

step $i = 8$

$[K_8]\{\Delta_{8,ref}\} = \{F_{ref}\} \Rightarrow \{\Delta_{8,ref}\} = \{7.163, 3.163, 0\}^T$

link l	status	$K_{8,l}$	$f_{7,l}$	$\epsilon_{7,l}$	$d\epsilon_{8,l}$	$\epsilon_{cr,l}$	$\lambda_{8,l}$	new status
1	$-$(12)	0.25	-0.138	-0.48	-4	$-\approx\infty$	n.a	$-$(12)
2	(4)	0	0	-0.48	-4	n.a.	n.a	(4)
3	$-$**(13)**	**0.316**	**-0.538**	**-0.498**	**-3.163**	**-1,7**	**0.38**	$-$**(12)**
4	(4)	0	0	-0.498	-3.163	n.a.	n.a.	(4)

$\Rightarrow \lambda_8 = min\lambda_8^+ = 0.113$, **chosen link l=3**

$\{F_8\} = \{F_7\} + \lambda_8\{F_{ref}\} = \{0.538, 0, 0\}^T$

$\{\Delta_8\} = \{\Delta_7\} + \lambda_8\{\Delta_{8,ref}\} = \{3.7, 1.7, 0\}^T$

step $i = 9$

$[K_9]\{\Delta_{9,ref}\} = \{F_{ref}\} \Rightarrow \{\Delta_{9,ref}\} = \{8, 4, 0\}^T$

link l	status	$K_{9,l}$	$f_{8,l}$	$\epsilon_{8,l}$	$d\epsilon_{9,l}$	$\epsilon_{cr,l}$	$\lambda_{9,l}$	new status
1	$-$(12)	0.25	-0.538	-2	-4	$-\approx\infty$	n.a	$-$(12)
2	(4)	0	0	-2	-4	n.a.	n.a	(4)
3	$-$(12)	0.25	-0.538	-1.7	-4	$-\approx\infty$	0.38	$-$(12)
4	(4)	0	0	-1.7	-4	n.a.	n.a.	(4)

$\Rightarrow \lambda_9$=0.163 **load factor is limited by maximum displacement of 5mm**

$\{F_9\} = \{F_8\} + \lambda_9\{F_{ref}\} = \{0.7, 0, 0\}^T$

$\{\Delta_9\} = \{\Delta_8\} + \lambda_9\{\Delta_{9,ref}\} = \{5, 2.35, 0\}^T$

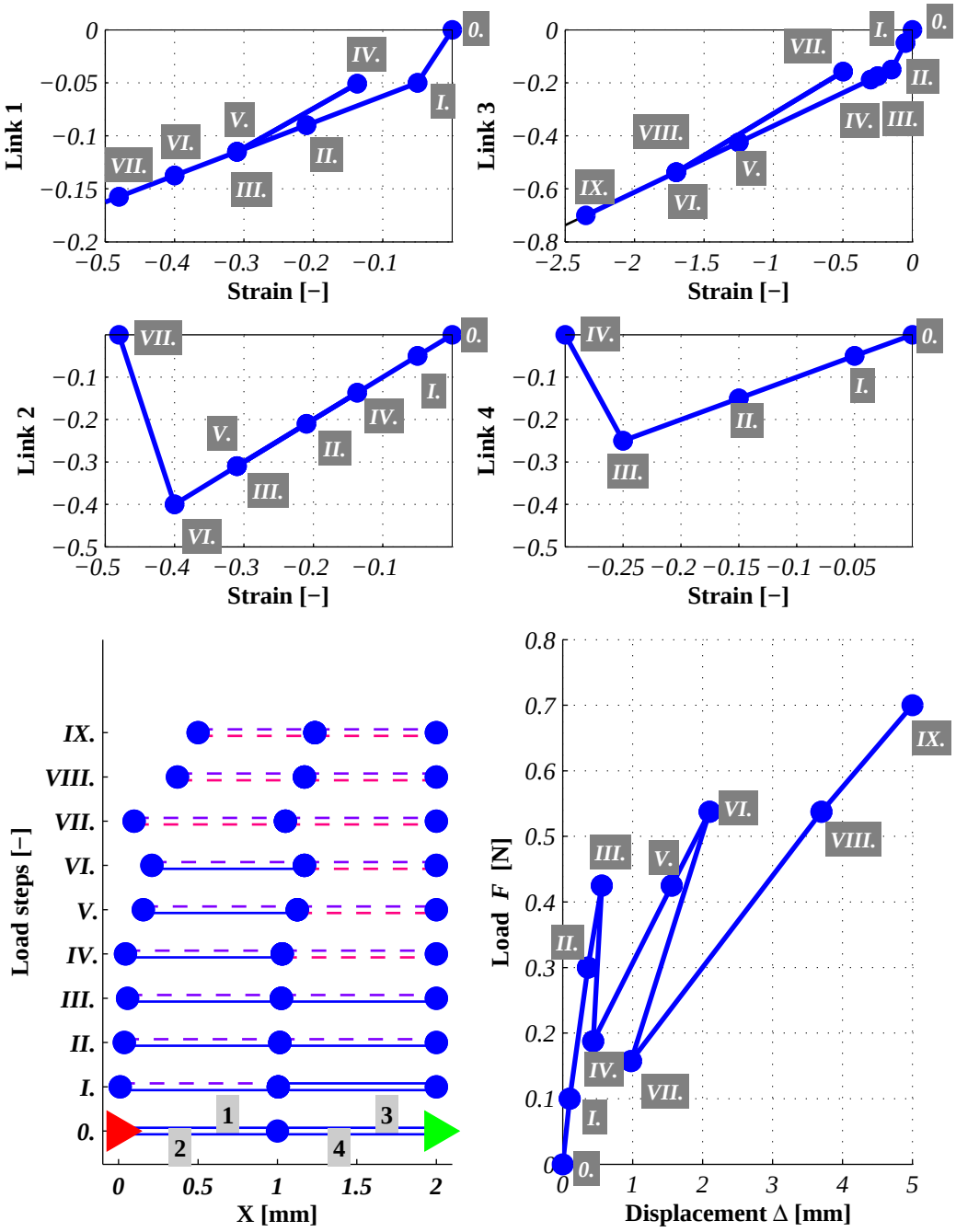

Figure A.5: *Example of SSC algorithm including plastic compression and brittle links, load-strain plots of individual link elements (top) and model LDP with deformed structure plot (below), (original in colour)*

A.2 Density and Moisture Measurements of Tested Specimens

Density and moisture content measurements are listed in Table A.1.

Table A.1: *Density and moisture content of tested samples.*

specimen	density ρ [kg/m^3]	moisture content MC [%]
T-R/T-01-A	331	14.2
T-R/T-02-A	297	14.5
T-R/T-03-A	401	14.0
T-R/T-04-A	292	14.5
T-R/T-05-A	425	14.2
T-R/T-06-A	405	14.2
T-R/T-09-A	297	14.6
T-R/T-10-A	397	14.2
T-R/T-11-A	377	14.1
T-R/T-12-A	411	13.7
T-R/T-13-A	291	14.2
T-R/T-02-F	366	15.1
T-R/T-03-F	339	15.0
T-R/T-04-F	327	14.8
T-R/T-05-F	339	14.6
T-R/T-06-F	357	14.8
T-R/T-07-F	324	15.0
T-R/T-08-F	335	14.8
T-R/T-09-F	335	14.9
T-R/T-10-F	329	14.9
T-R/T-11-F	337	14.9
T-R/T-12-F	349	14.9
C-L-01-A	298	15.5
C-L-02-A	285	15.5
C-L-03-A	310	15.3

specimen	**density ρ [kg/m^3]**	**moisture content MC [%]**
C-L-04-A	292	15.1
C-L-05-A	311	14.9
C-L-06-A	291	15.1
C-L-07-A	303	15.0
C-L-08-A	299	14.7
C-L-09-A	297	15.2
C-L-10-A	324	15.1
C-L-12-A	309	13.1
C-L-01-F	303	15.4
C-L-02-F	312	15.4
C-L-04-F	326	15.6
C-L-05-F	317	15.2
C-L-06-F	284	15.4
C-L-07-F	311	15.5
C-L-08-F	318	15.4
C-L-09-F	343	15.6
C-L-10-F	299	15.5
C-L-11-F	296	15.4
C-R-01-A	308	14.8
C-R-02-A	327	14.3
C-R-03-A	326	14.5
C-R-04-A	312	14.5
C-R-05-A	316	13.9
C-T-06-A	318	14.3
C-T-07-A	306	14.4
C-T-08-A	313	14.3
C-T-09-A	321	14.2
C-T-10-A	315	13.8
C-R-01-F	299	14.1
C-R-02-F	314	13.9

specimen	density ρ [kg/m^3]	moisture content MC [%]
C-R-03-F	299	14.1
C-R-04-F	298	14.4
C-R-05-F	289	14.2
C-T-06-F	292	13.8
C-T-07-F	296	14.1
C-T-08-F	294	14.0
C-T-09-F	330	14.3
C-T-10-F	317	14.0
S-RL/TL-21-A	350	12.9
S-RL/TL-22-A	343	12.7
S-RL/TL-23-A	331	13.0
S-RL/TL-24-A	376	13.3
S-RL/TL-25-A	343	13.1
S-RL/TL-26-A	434	12.3
S-RL/TL-27-A	334	11.7
S-RL/TL-28-A	336	12.6
S-RL/TL-29-A	443	12.7
S-RL/TL-30-A	424	12.3
S-RL/TL-01-1-F	315	13.7
S-RL/TL-02-1-F	326	14.2
S-RL/TL-03-1-F	310	13.7
S-RL/TL-04-1-F	356	14.8
S-RL/TL-05-1-F	316	14.5
S-RL/TL-06-1-F	321	14.3
S-RL/TL-07-1-F	342	13.9
S-RL/TL-08-1-F	343	13.5
S-RL/TL-09-1-F	314	13.9
S-RL/TL-10-1-F	340	14.1
T-L-01-A	408	12.6
T-L-02-A	433	14.0

specimen	density ρ [kg/m^3]	moisture content MC [%]
T-L-03-A	367	12.6
T-L-04-A	368	13.4
T-L-05-A	411	14.0
T-L-06-A	435	13.2
T-L-07-A	371	13.6
T-L-08-A	381	13.5
T-L-09-A	396	13.7
T-L-10-A	390	13.5
T-L-11-A	405	13.3
T-L-12-A	381	13.7
T-L-01-F	356	13.8
T-L-02-F	380	13.7
T-L-03-F	266	13.6
T-L-04-F	368	13.7
T-L-05-F	386	13.9
T-L-06-F	390	13.9
T-L-07-F	358	13.9
T-L-08-F	292	13.8
T-L-09-F	303	14.0
T-L-10-F	373	14.2
T-L-11-F	288	13.5
T-L-12-F	340	14.4
J-M10-01-A(1)	338	12.8
J-M10-01-A(2)	342	12.8
J-M10-02-A(1)	350	13.4
J-M10-02-A(2)	364	13.1
J-M10-03-A(1)	328	12.6
J-M10-03-A(2)	346	13.2
J-M10-04-A(1)	352	13.2
J-M10-04-A(2)	331	12.5
J-M10-05-A(1)	331	12.5

specimen	**density ρ [kg/m^3]**	**moisture content MC [%]**
J-M10-05-A(2)	346	12.5
J-M10-01-F(1)	302	12.4
J-M10-01-F(2)	295	12.5
J-M10-02-F(1)		
J-M10-02-F(2)	388	12.6
J-M10-03-F(1)	314	12.0
J-M10-03-F(2)	315	12.0
J-M10-04-F(1)	295	12.3
J-M10-04-F(2)	300	12.4
J-M10-05-F(1)	264	12.2
J-M10-05-F(2)	273	11.4

A.3 Model Input File Commands

The following table lists the names of the commands and parameters that are used in the model input file and their function.

Table A.2: *List of model input file commands.*

command	parameters	function
$PARAMETERS		general input parameters
MaxLoadSteps	*value*	set maximum load steps
MaxCount	*value*	set number of model runs
MaxLoad	*value*	set maximum load
MaxDisp	*value*	set maximum displacement
LoadThreshold	*value*	set threshold value which determines when zero load is reached
MATnonlinear	*true/false*	include material nonlinearity
GEOnonlinear	*true/false*	include geometric nonlinearity (beams)
CONnonlinear	*true/false*	include contact nonlinearity
NonlinearSteps	*value*	set number of intermediate steps in geometric nonlinear analysis
RenewKfrequency	*value*	number of broken links when global stiffness matrix will be renewed (refer to subsection 5.6.5)
LDL	*true/false*	determines whether MATLAB cholesky decomposition or special LDL decomposition is used
SSCThreshold	*value*	threshold value for the SSC algorithm (grouping link changes, refer to subsection 5.6.3)

command	parameters	function
SmoothContact	*true/false*	enables smooth contact
TKfix	*value*	additional small stiffness overlayed on lattice model
l(*index*)	*value*	cell lengths
E(*index*)	*value*	solid elements E-moduli
ny((*index*$_1$),(*index*$_2$))	*value*	Poisson coefficients
K(*index*)	*value*	lattice mean stiffness parameter, direction j=*index* $\overline{K}_{①,j}$
St(*index*)	*value*	lattice mean tensile strength parameter, direction j=*index* $\overline{S}_{T,j}$
Sc(*index*)	*value*	lattice mean compressive strength parameter, direction j=*index* $\overline{S}_{C,j}$
Yft(*index*)	*value*	lattice tensile PY parameter, direction j=*index* $\gamma_{T,j}$
Yfc(*index*)	*value*	lattice compressive PY parameter, direction j=*index* $\gamma_{C,j}$
COV(*index*)	*value*	coefficient of variation for stiffness and strength parameters, direction j=*index* $c_{v,j}$
$WOODSTRUCT		wood structure parameters
Enable	*true/false*	enable wood structure
Frame	*sx, ex, sy, ey, sz, ez*	reference frame around lattice to where rings are created
AlphaMean	*value*	parameter α

command	parameters	function
AlphaCOV	*value*	parameter c_v of α
R_PithMean	*value*	parameter r_{pith}
R_PithCOV	*value*	parameter c_v of r_{pith}
R_ShiftMean	*value*	parameter $\overline{r}_{shift}$
R_ShiftCOV	*value*	parameter c_v of $\overline{r}_{shift}$
DR_CentreMean	*value*	parameter Δr_{centre}
DR_CentreCOV	*value*	parameter c_v of Δr_{centre}
DR_DiffMean	*value*	parameter Δr_{diff}
DR_DiffCOV	*value*	parameter c_v of Δr_{diff}
DR_VarMean	*value*	parameter Δr_{var}
DR_VarCOV	*value*	parameter c_v of Δr_{diff}
NormMinMean	*value*	parameter $\overline{\rho}_{min}$
NormMinCOV	*value*	parameter c_v of $\overline{\rho}_{min}$
NormDiffMean	*value*	parameter $\overline{\rho}_{diff}$
NormDiffCOV	*value*	parameter c_v of $\overline{\rho}_{diff}$
NormExpMean	*value*	parameter $\overline{\rho}_{exp}$
NormExpCOV	*value*	parameter c_v of $\overline{\rho}_{exp}$
WoodStructLinksT	$\lambda_{T,1}$, $\lambda_{T,2}$, $\lambda_{T,3}$ ...	adjustment parameter, subsection 5.5.3
WoodStructLinksC	$\lambda_{C,1}$, $\lambda_{C,2}$, $\lambda_{C,3}$ ...	adjustment parameter, subsection 5.5.3
WoodStructLinksK	$\lambda_{K,1}$, $\lambda_{K,2}$, $\lambda_{K,3}$ ...	adjustment parameter, subsection 5.5.3

command	parameters	function
$MODEL		model geometry parameters
BlockCreate	*BlocNo, sx, ex, sy, ey, sz, ez,* $noel_x$, $noel_y$, $noel_z$, *BlocType,* {*WoodStructNo*}	creates lattice or solid blocks of *BlocType*
BlockConnect	*BlocNo(Master), BlocNo(Slave), FaceNo(Master), FaceNo(Slave)*	connects lattice/solid and solid blocks
BoltCreate	*BoltBlocNo, x, y, z, radius, length, div*	creates bolt elements, coordinates define the centre of bolt, bolt is in Z-direction
HoleSurfaceCreate	*BlocNo, x, y, radius, surfacewidth, UserSurfaceNo*	creates cylindrical hole in latticeand extracts surface nodes into an extra user surface *UserSurfaceNo*
HoleBoltConnect	*BlocNo, UserSurfaceNo, BoltBlocNo*	connects bolt with created extra surface nodes
WasherSurfaceCreate	*BlocNo, x, y, z, FaceNo, radius, UserSurfaceNo*	extracts surface node numbers into extra user surface *UserSurfaceNo*
WasherBoltConnect	*BlocNo, UserSurfaceNo, BoltBlocNo, StartEnd, radius*	connects bolt with washer surface at one of the ends
NotchSurfaceCreate	*BlocNo, sc1, ec1, sc2, ec2, face,* $UserSurface_1$, $UserSurfaceNo_2$, ...	creates notch in lattice
SurfaceCreate	*BlocNo, FaceNo, sx, ex, sy, ey, sz, ez, UserSurfaceNo*	extracts surface node numbers into user surface *UserSurfaceNo*

command	parameters	function
$BC		boundary conditions and load
BC_GetDispHigh	*BlocNo, face, dof*	node where model displacement is determined (BC_GetDispHigh-BC_GetDisplow)
BC_GetDispLow	*BlocNo, face, dof*	node where model displacement is determined
BC_Zero_Block	*BlocNo, dx, dy, dz*	sets respective DoFs (*dx,dy,dz*) of a block to zero
BC_Zero_Face	*BlocNo, FaceNo, dx, dy, dz*	sets respective DoFs (*dx,dy,dz*) of a surface to zero
BC_Zero_Corner	*BlocNo, CornerNo, dx, dy, dz*	sets respective DoFs (*dx,dy,dz*) of a corner a surface to zero
BC_Zero_Edge	*BlocNo, EdgeNo, dx, dy, dz*	sets respective DoFs (*dx,dy,dz*) of an edge a surface to zero
F_Add_Face_EQL	*BlocNo, FaceNo, dx, dy, dz, ForceVal, ForceNo*	adds load to a surface (equally distributed)
F_Add_Face_UDL	*BlocNo, FaceNo, dx, dy, dz, StressVal, ForceNo*	adds a uniform distributed load to surface
BC_Zero_Block_Rot	*BlocNo, dx, dy, dz*	sets respective rotational DoFs (*drx,dry,drz*) of a block to zero
BC_Zero_Face_Rot	*BlocNo, FaceNo, dx, dy, dz*	sets respective rotational DoFs (*drx,dry,drz*) of a surface to zero
BC_Zero_Corner_Rot	*BlocNo, CornerNo, dx, dy, dz*	sets respective rotational DoFs (*drx,dry,drz*) of a corner a surface to zero

command	parameters	function
BC_Zero_Edge_Rot	*BlocNo, EdgeNo, dx, dy, dz*	sets respective rotational DoFs (*drx,dry,drz*) of an edge a surface to zero
Const_Face_Dof	*BlocNo, FaceNo, dx, dy, dz*	constrains DoFs of one surface
$OUTPUT		output parameters for postprocessor *PLOT3D*
FigPlot	*true/false*	determines whether *MATLAB* figure is plotted
PlotSteps	*value*	frequency of *MATLAB* figure plots
SaveSteps	*value*	frequency of model save files
NewMaxDisp	*true/false*	determines whether new maximum displacement must first be reached before new figure is plotted
ShowNodes	*true/false*	determines whether nodes are shown
ShowSurfaceLines	*true/false*	determines whether surface lines are shown
ShowAllLines	*true/false*	determines whether rest of lattice lines are shown
ShowNormalForceStrain	*value*	1...force plot, 2...strain plot, 3...strength plot
Scale	*value*	scale factor
ShowBCs	*true/false*	show boundary conditions
ShowBCsZ	*true/false*	show boundary conditions in Z
ShowLines	s_1, s_2, s_3, s_4, s_5, s_6, s_7, s_8, s_9	determines whether normal links in respective directions are plotted
ShowBrokenLines	s_1, s_2, s_3, s_4, s_5, s_6, s_7, s_8, s_9	determines whether broken links in respective directions are plotted

command	parameters	function
ShowCompLines	s_1, s_2, s_3, s_4, s_5, s_6, s_7, s_8, s_9	determines whether compressed links in respective directions are plotted
ScaleBCs	*value*	scale factor of BC symbols
ScaleForce	*value*	scale factor of loading symbols
CircleDiv	*value*	ratio of the linear representation of a circle
OBJFrameGridSize	*value*	size of the grid [mm]
OutSave	*true/false*	determines whether model output files are saved
OBJLineWidth	*value*	width of lines in OBJ output
OBJLineDiv	*value*	ratio of the linear representation of a cyinder in OBJ output
OBJFrame	*sx, ex, sy, ey, sz, ez*	size of the box plotted around model in OBJ output
PlotCount	*value*	number of figure plot
PlotCountAVGStart	*value*	model start number for average plot
PlotCountAVGEnd	*value*	model end number for average plot
PlotStep	*value*	plot step of one model
PlotType	*value*	type of plot: 1... *MATLAB* figure, 2... OBJ plot, 3... LDP plot 4... LDP average plot
PlotOBJs	*value*	type of OBJ layer to plot
OBJPath	*string*	pathname of OBJ plot figure, layer OBJ
OBJFile	*string*	filename of OBJ plot figure, layer OBJ

command	parameters	function
OBJBCpath	*string*	pathname of OBJ plot figure, layer BC
OBJBCfile	*string*	filename of OBJ plot figure, layer BC
OBJLATpath	*string*	pathname of OBJ plot figure, layer LAT
OBJLATfile	*string*	filename of OBJ plot figure, layer LAT
OBJLATBROKEpath	*string*	pathname of OBJ plot figure, layer LATBROKE
OBJLATBROKEfile	*string*	filename of OBJ plot figure, layer LATBROKE
OBJSOLIDpath	*string*	pathname of OBJ plot figure, layer SOLID
OBJSOLIDfile	*string*	filename of OBJ plot figure, layer SOLID
OBJVISpath	*string*	pathname of OBJ plot figure, layer VIS
OBJVISfile	*string*	filename of OBJ plot figure, layer VIS
OBJBOXpath	*string*	pathname of OBJ plot figure, layer BOX
OBJBOXfile	*string*	filename of OBJ plot figure, layer BOX
OBJMATpath	*string*	pathname of OBJ plot figure, layer MAT
OBJMATfile	*string*	filename of OBJ plot figure, layer MAT
OUTPath	*string*	pathname of OUT file
OUTFile	*string*	filename of OUT file
LDPPlot	*true/false*	LDP plot on/off
LDPSave	*true/false*	LDP saved in file on/off
LDPPath	*string*	pathname of LDP file
LDPFile	*string*	filename of LDP file

command	parameters	function
		PWD for pathname can be used to obtain the **P**resent **W**orking **D**irectory
$COLOUR		element colour definition
VIS_Nontransparent	*value*	minimum number of tensile links which need to be broken before shaded surface is plotted in VIS file
VIS_Nontransparent_c	*value*	minimum number of compressive links which need to be broken before shaded surface is plotted in VIS file
Bolt	*r,g,b,o*	sets colour (*r,g,b*) and opacity for bolt elements
Surface	*r,g,b,o*	sets colour (*r,g,b*) and opacity for a general surface
LinkBroken	*r,g,b,o*	sets colour (*r,g,b*) and opacity for broken link elements
LinkComp	*r,g,b,o*	sets colour (*r,g,b*) and opacity for compressed link elements
BC	*r,g,b,o*	sets colour (*r,g,b*) and opacity for boundary conditions
Load	*r,g,b,o*	sets colour (*r,g,b*) and opacity for loading arrows
SolidElem	*r,g,b,o*	sets colour (*r,g,b*) and opacity for solid elements
PlaneElem	*r,g,b,o*	sets colour (*r,g,b*) and opacity for plane elements
LatSurface	*r,g,b,o*	sets colour (*r,g,b*) and opacity for lattice surface elements
OBJframe	*r,g,b,o*	sets colour (*r,g,b*) and opacity for OBJ frame box
OBJframetr	*r,g,b,o*	sets colour (*r,g,b*) and opacity for OBJ frame box grid lines

command	parameters	function
Celltransp1_c	r,g,b,o	sets colour (r,g,b) and opacity for shaded surface that is plotted in VIS file when one link is in compression etc.
Celltransp1_t	r,g,b,o	sets colour (r,g,b) and opacity for shaded surface that is plotted in VIS file when one link is broken etc.
Master	r,g,b,o	sets colour (r,g,b) and opacity for master contact elements
ContactActive	r,g,b,o	sets colour (r,g,b) and opacity for active contact node
ContactInActive	r,g,b,o	sets colour (r,g,b) and opacity for inactive contact node

A.4 Model Input Files of Test Series

Listing A.1: *Model input file T-R.*

```
$PARAMETERS
MaxLoadSteps = 10000
MaxCount = 10
MaxLoad = 10000
MaxDisp = 5
LoadThreshold = 0.01
MATnonlinear = true
LDL = false
RENEW_K_freq = 100
SSCThreshold = 0.1

Beam = false
TKfix = true
l(1) = 2
l(2) = 1
l(3) = 1

ElasticityMode=3
E(1) = 9608
E(2) = 681
E(4) = 557
E(8) = 325

ny(1,3) = 0.4862
ny(1,2) = 0.4862
ny(3,2) = 0.3719
ny(2,3) = 0.3719
ny(2,1) = 0.0345
ny(3,1) = 0.0345

EngStrain = 1

COV(1) = 0.2
COV(2)  = 0.2
COV(4)  = 0.2
COV(8)  = 0.2


K(1) = 1423.5
```

```
K(2) = 357.3
K(4) = 1392.2
K(8) = 1297.9

COV(1) = 0.2
COV(2)  = 0.2
COV(4)  = 0.2
COV(8)  = 0.2

K(1) = 1423.5
K(2) = 357.3
K(4) = 1392.2
K(8) = 1297.9

St(1) = 100
Yft(1) = 1.01
Sc(1) = 12
Yfc(1) = 0.01

St(2) = 7
Yft(2) = 1.01
Sc(2) = 4
Yfc(2) = 0.01

St(4) = 20
Yft(4) = 1.01
Sc(4) = 20
Yfc(4) = 1.01

St(8) = 7
Yft(8) = 1.01
Sc(8) = 7
Yfc(8) = 1.01
$END

$WOODSTRUCT
Enable = true
Frame =  −5, 75, −35, 35, −5, 25, 1

AlphaMean = 3.865
AlphaCOV = 0.083
R_PithMean = 39.507
R_PithCOV = 0.215
R_ShiftMean = 0.408
```

```
R_ShiftCOV = 0.719
DR_CentreMean = 5.884
DR_CentreCOV = 0.277
DR_DiffMean = -0.072
DR_DiffCOV =  -3.803
DR_VarMean = -0.007
DR_VarCOV = -283.014

NormMinMean = 0.717
NormMinCOV = 0.146
NormDiffMean = 0.982
NormDiffCOV = 0.211
NormExpMean = 1.958
NormExpCOV = 1.014

WoodStructLinksT = 2  ,1.5,1.5,1.5,1.5,1.5,1.5,1.5,1.5
WoodStructLinksC = 1.5,1  ,1  ,1.5,1.5,1.5,1.5,1.5,1.5
WoodStructLinksK = 2  ,2  ,2  ,2  ,2  ,2  ,2  ,2  ,2
$END


$MODEL_GEOMETRY
%solid elements
BlockCreate     3,  0, 32, 6.5,  11, 0, 20, 4, 1, 4, 1
BlockCreate     2,  0, 32, -11,-6.5, 0, 20, 4, 1, 4, 1

BlockCreate     5,  0, 48,  11,  30, 0, 20, 6, 2, 4, 1
BlockCreate     4,  0, 48, -30, -11, 0, 20, 6, 2, 4, 1

BlockCreate     7, 32, 48,   2,  11, 0, 20, 2, 2, 4, 1
BlockCreate     6, 32, 48, -11,  -2, 0, 20, 2, 2, 4, 1

BlockCreate     9, 48, 70,   2,  30, 0, 20, 2, 3, 4, 1
BlockCreate     8, 48, 70, -30,  -2, 0, 20, 2, 3, 4, 1

BlockConnect        3,1,3,4
BlockConnect        2,1,4,3

BlockConnect        7,1,1,2
BlockConnect        6,1,1,2

BlockConnect        5,3,3,4
BlockConnect        4,2,4,3

```

```
128 BlockConnect        5,7,3,4
129 BlockConnect        4,6,4,3
130
131 BlockConnect        9,5,1,2
132 BlockConnect        9,7,1,2
133
134 BlockConnect        8,4,1,2
135 BlockConnect        8,6,1,2
136
137 NotchSurfaceCreate  1, 12, 16,  5, 8,   0,   21,  7,  0,  8, 9, 0,0
138
139 BlockCreate     1, 1,  31, -6, 6, 0.5, 19.5, 15, 12, 19, 4, 1
140
141 SurfaceCreate       1,2, 20, 36, 0, 6, 0, 20, 20
142 $END
143
144
145 $BC
146 BC_GetDispHigh  9,2,2
147 BC_GetDispLow   8,2,2
148
149 BC_zero_corner  8,1,1,1,1
150 BC_zero_face    8,1,0,1,0
151 BC_zero_edge    8,4,1,1,0
152
153 BC_zero_edge    9,2,1,0,0
154
155 F_add_face_udl  9,1,0,1,0,1,1
156 Const_face_dof  9,1,0,1,0
157 $END
158
159
160 $OUTPUT
161 [...]
162 $END
163
164
165 $COLOUR
166 [...]
167 $END
```

Listing A.2: *Model input file T-L.*

```
$PARAMETERS
MaxLoadSteps = 15000
MaxCount = 5
MaxLoad = 15000
MaxDisp = 1
LoadThreshold = 0.01
MATnonlinear = true
LDL = false
RENEW_K_freq = 100
SSCThreshold = 0.1

Beam = false
TKfix = true
l(1) = 2
l(2) = 1
l(3) = 1

%elastic parameters for solid block
ElasticityMode=3
E(1) = 9608
E(2) = 681
E(4) = 557
E(8) = 325

ny(1,3) = 0.4862
ny(1,2) = 0.4862
ny(3,2) = 0.3719
ny(2,3) = 0.3719
ny(2,1) = 0.0345
ny(3,1) = 0.0345

EngStrain = 1

K(1) = 1423.5
K(2) = 357.3
K(4) = 1392.2
K(8) = 1297.9

COV(1) = 0.2
COV(2)  = 0.2
COV(4)  = 0.2
COV(8)  = 0.2

St(1) = 100
```

```
Yft(1) = 1.01
Sc(1) = 12
Yfc(1) = 0.01

St(2) = 7
Yft(2) = 1.01
Sc(2) = 4
Yfc(2) = 0.01

St(4) = 20
Yft(4) = 1.01
Sc(4) = 20
Yfc(4) = 1.01

St(8) = 7
Yft(8) = 1.01
Sc(8) = 7
Yfc(8) = 1.01
$END


$WOODSTRUCT
Enable = true
Frame =  -5, 75, -15, 21, -5, 9, 1

%WoodStruct parameters taken from SLO - (TL pix were too small)
AlphaMean = 1.815
AlphaCOV = 0.349
R_PithMean = 33.168
R_PithCOV = 0.246
R_ShiftMean = 0.609
R_ShiftCOV = 0.493
DR_CentreMean = 6.313
DR_CentreCOV = 0.192
DR_DiffMean = -0.031
DR_DiffCOV =  -5.031
DR_VarMean = -0.119
DR_VarCOV = -7.641

NormMinMean = 0.717
NormMinCOV = 0.146
NormDiffMean = 0.982
NormDiffCOV = 0.211
NormExpMean = 1.958
```

```
89  NormExpCOV = 1.014
90
91  WoodStructLinksT = 2  ,1.5,1.5,1.5,1.5,1.5,1.5,1.5,1.5
92  WoodStructLinksC = 1.5,1  ,1  ,1.5,1.5,1.5,1.5,1.5,1.5
93  WoodStructLinksK = 2  ,2  ,2  ,2  ,2  ,2  ,2  ,2  ,2  ,2
94  $END
95
96
97  $MODEL_GEOMETRY
98  %solid elements
99  BlockCreate     2, 0 , 11, 0, 6, 0, 4, 2, 1, 1, 1
100 BlockCreate     3, 59, 70, 0, 6, 0, 4, 2, 1, 1, 1
101
102 BlockConnect        2,1,2,1
103 BlockConnect        3,1,1,2
104
105 BlockCreate     1, 12, 58, 0.5, 5.5, 0.5, 3.5, 23, 5, 3, 4, 1
106 $END
107
108
109 $BC
110 BC_GetDispHigh  3,2,1
111 BC_GetDispLow   2,1,1
112
113 BC_zero_corner  2,1,1,1,1
114 BC_zero_face    2,1,1,0,0
115 BC_zero_edge    2,4,1,1,0
116
117 BC_zero_edge    2,1,1,0,1
118
119 BC_zero_edge    3,8,0,1,0
120 BC_zero_edge    3,5,0,0,1
121
122 F_add_face_udl  3,2,1,0,0,1,1
123 Const_face_dof  3,2,1,0,0
124 $END
125
126
127 $OUTPUT
128 [...]
129 $END
130
131
132 $COLOUR
```

```
[...]
$END
```

Listing A.3: *Model input file S-LR/LT.*

```
$PARAMETERS
MaxLoadSteps = 10000
MaxCount = 10
MaxLoad = 10000
MaxDisp = 1
LoadThreshold = 0.01
MATnonlinear = true
RENEW_K_freq = 100
SSCThreshold = 0.1
LDL = false
Beam = false
TKfix = true
l(1) = 2
l(2) = 1
l(3) = 1

ElasticityMode=3
E(1) = 9608
E(2) = 681
E(4) = 557
E(8) = 325

ny(1,3) = 0.4862
ny(1,2) = 0.4862
ny(3,2) = 0.3719
ny(2,3) = 0.3719
ny(2,1) = 0.0345
ny(3,1) = 0.0345

EngStrain = 1

COV(1) = 0.2
COV(2)  = 0.2
COV(4)  = 0.2
COV(8)  = 0.2

K(1) = 1423.5
K(2) = 357.3
```

```
K(4) = 1392.2
K(8) = 1297.9

St(1) = 100
Yft(1) = 1.01
Sc(1) = 12
Yfc(1) = 0.01

St(2) = 7
Yft(2) = 1.01
Sc(2) = 4
Yfc(2) = 0.01

St(4) = 20
Yft(4) = 1.01
Sc(4) = 20
Yfc(4) = 1.01

St(8) = 7
Yft(8) = 1.01
Sc(8) = 7
Yfc(8) = 1.01
$END


$WOODSTRUCT
Enable = true
Frame =  -5, 53, -5, 27, -5, 11, 1

AlphaMean = 1.815
AlphaCOV = 0.349
R_PithMean = 33.168
R_PithCOV = 0.246
R_ShiftMean = 0.609
R_ShiftCOV = 0.493
DR_CentreMean = 6.313
DR_CentreCOV = 0.192
DR_DiffMean = -0.031
DR_DiffCOV =  -5.031
DR_VarMean = -0.119
DR_VarCOV = -7.641

NormMinMean = 0.717
NormMinCOV = 0.146
```

```
NormDiffMean = 0.982
NormDiffCOV = 0.211
NormExpMean = 1.958
NormExpCOV = 1.014

WoodStructLinksT = 2  ,1.5,1.5,1.5,1.5,1.5,1.5,1.5,1.5
WoodStructLinksC = 1.5,1  ,1  ,1.5,1.5,1.5,1.5,1.5,1.5
WoodStructLinksK = 2  ,2  ,2  ,2  ,2  ,2  ,2  ,2  ,2
$END


$MODEL_GEOMETRY
%solid elements
BlockCreate     8, 0 ,  4,    0,   22, 0, 6, 1, 1, 2, 1
BlockCreate     9, 44, 48,    0,   22, 0, 6, 1, 1, 2, 1

BlockCreate     3, 14, 37,   17,   22, 0, 6, 5, 2, 2, 1
BlockCreate     2, 11, 34,    0,    5, 0, 6, 5, 2, 2, 1

BlockCreate     6, 4 , 11, 12.5,   22, 0, 6, 2, 3, 2, 1
BlockCreate     4, 4 , 11,    0, 12.5, 0, 6, 2, 5, 2, 1

BlockCreate     5, 37, 44,  9.5,   22, 0, 6, 2, 5, 2, 1
BlockCreate     7, 37, 44,    0,  9.5, 0, 6, 2, 3, 2, 1

BlockConnect        4,1,2,1
BlockConnect        5,1,1,2

BlockConnect        3,1,3,4
BlockConnect        2,1,4,3

BlockConnect        4,2,2,1
BlockConnect        5,3,1,2

BlockConnect        6,4,3,4
BlockConnect        7,5,4,3

BlockConnect        8,6,2,1
BlockConnect        8,4,2,1

BlockConnect        9,5,1,2
BlockConnect        9,7,1,2

NOTCHSURFACECREATE  1,  0,  1, 4, 12, 0, 6, 0, 7, 8,  0, 0, 0
```

```
127 NOTCHSURFACECREATE  1, 12, 13, 0,  8, 0, 6, 9, 0, 0, 10, 0, 0
128
129 BlockCreate     1, 12, 36, 5.5, 16.5, 0.5, 5.5, 12, 11, 5, 4, 1
130 $END
131
132
133 $BC
134 BC_GetDispHigh  9,2,1
135 BC_GetDispLow   8,1,1
136
137 BC_zero_corner  8,1,1,1,1
138 BC_zero_face    8,1,1,0,0
139 BC_zero_edge    8,1,1,0,1
140 BC_zero_edge    8,4,1,1,0
141
142 BC_zero_edge    9,5,0,0,1
143 BC_zero_edge    9,8,0,1,0
144
145 F_add_face_udl  9,2,1,0,0,1,1
146 Const_face_dof  9,2,1,0,0
147 F_add_face_udl  9,2,1,0,0,1,2
148 Const_face_dof  9,2,1,0,0
149 $END
150
151
152 $OUTPUT
153 [...]
154 $END
155
156 $COLOUR
157 [...]
158 $END
```

Listing A.4: *Model input file C-L.*

```
1 $PARAMETERS
2 MaxLoadSteps = 15000
3 MaxCount = 5
4 MaxLoad = 10000
5 MaxDisp = 5
6 LoadThreshold = 0.01
7 SSCThreshold = 1
8 MATnonlinear = true
```

```
RENEW_K_freq = 100

LDL = false
Beam = false
TKfix = true
l(1) = 2
l(2) = 1
l(3) = 1

ElasticityMode=3
E(1) = 9608
E(2) = 681
E(4) = 557
E(8) = 325

ny(1,3) = 0.4862
ny(1,2) = 0.4862
ny(3,2) = 0.3719
ny(2,3) = 0.3719
ny(2,1) = 0.0345
ny(3,1) = 0.0345

EngStrain = 1

COV(1) = 0.2
COV(2)  = 0.2
COV(4)  = 0.2
COV(8)  = 0.2

K(1) = 1423.5
K(2) = 357.3
K(4) = 1392.2
K(8) = 1297.9

St(1) = 100
Yft(1) = 1.01
Sc(1) = 12
Yfc(1) = 0.01

St(2) = 7
Yft(2) = 1.01
Sc(2) = 4
Yfc(2) = 0.01

```

```
St(4) = 20
Yft(4) = 1.01
Sc(4) = 20
Yfc(4) = 1.01

St(8) = 7
Yft(8) = 1.01
Sc(8) = 7
Yfc(8) = 1.01
$END


$WOODSTRUCT
Enable = true
Frame =  -5, 65, -5, 25, -5, 25, 1

AlphaMean = 2.885
AlphaCOV = 0.71
R_PithMean = 50.990
R_PithCOV = 0.280
R_ShiftMean = 0.421
R_ShiftCOV = 0.699
DR_CentreMean = 5.170
DR_CentreCOV = 0.245
DR_DiffMean = -0.096
DR_DiffCOV =  -1.975
DR_VarMean = 0.204
DR_VarCOV = 6.242

NormMinMean = 0.717
NormMinCOV = 0.146
NormDiffMean = 0.982
NormDiffCOV = 0.211
NormExpMean = 1.958
NormExpCOV = 1.014

WoodStructLinksT = 2  ,1.5,1.5,1.5,1.5,1.5,1.5,1.5,1.5
WoodStructLinksC = 1.5,1  ,1  ,1.5,1.5,1.5,1.5,1.5,1.5
WoodStructLinksK = 2  ,2  ,2  ,2  ,2  ,2  ,2  ,2  ,2
$END


$MODEL_GEOMETRY
BlockCreate 1, 1, 59, 0.5, 19.5, 0.5, 4.5, 29, 19, 4, 4, 1
```

```
$END


$BC
BC_GetDispHigh  1,2,1
BC_GetDispLow   1,1,1

BC_zero_corner  1,1,1,1,1
BC_zero_face    1,1,1,0,0
BC_zero_edge    1,4,1,1,0

BC_zero_edge    1,1,1,0,1

F_add_face_udl  1,2,1,0,0,-1,1
Const_face_dof  1,2,1,0,0
$END


$OUTPUT
[...]
$END


$COLOUR
[...]
$END
```

Listing A.5: *Model input file C-R.*

```
$PARAMETERS
MaxLoadSteps = 15000
MaxCount = 5
MaxLoad = 10000
MaxDisp = 3
RENEW_K_freq = 100
LoadThreshold = 0.01
SSCThreshold = 1

MATnonlinear = true
LDL = false
Beam = false
TKfix = true
l(1) = 2
```

```
15 l(2) = 1
16 l(3) = 1
17
18 ElasticityMode=3
19 E(1) = 9608
20 E(2) = 681
21 E(4) = 557
22 E(8) = 325
23
24 ny(1,3) = 0.4862
25 ny(1,2) = 0.4862
26 ny(3,2) = 0.3719
27 ny(2,3) = 0.3719
28 ny(2,1) = 0.0345
29 ny(3,1) = 0.0345
30
31 EngStrain = 1
32
33 COV(1) = 0.2
34 COV(2)  = 0.2
35 COV(4)  = 0.2
36 COV(8)  = 0.2
37
38 K(1) = 1423.5
39 K(2) = 357.3
40 K(4) = 1392.2
41 K(8) = 1297.9
42
43 St(1) = 100
44 Yft(1) = 1.01
45 Sc(1) = 12
46 Yfc(1) = 0.01
47
48 St(2) = 7
49 Yft(2) = 1.01
50 Sc(2) = 4
51 Yfc(2) = 0.01
52
53 St(4) = 20
54 Yft(4) = 1.01
55 Sc(4) = 20
56 Yfc(4) = 1.01
57
58 St(8) = 7
```

```
59 Yft(8) = 1.01
60 Sc(8) = 7
61 Yfc(8) = 1.01
62 $END
63
64
65 $WOODSTRUCT
66 Enable = true
67 Frame =  −5, 25, −5, 25, −5, 25, 1
68
69 AlphaMean = 7.788
70 AlphaCOV = 0.048
71 R_PithMean = 54.761
72 R_PithCOV = 0.23
73 R_ShiftMean = 0.528
74 R_ShiftCOV = 0.621
75 DR_CentreMean = 5.247
76 DR_CentreCOV = 0.206
77 DR_DiffMean = −0.120
78 DR_DiffCOV =  −1.224
79 DR_VarMean = 0.319
80 DR_VarCOV = 2.354
81
82 NormMinMean = 0.717
83 NormMinCOV = 0.146
84 NormDiffMean = 0.982
85 NormDiffCOV = 0.211
86 NormExpMean = 1.958
87 NormExpCOV = 1.014
88
89 WoodStructLinksT = 2  ,1.5,1.5,1.5,1.5,1.5,1.5,1.5,1.5
90 WoodStructLinksC = 1.5,1  ,1  ,1.5,1.5,1.5,1.5,1.5,1.5
91 WoodStructLinksK = 2  ,2  ,2  ,2  ,2  ,2  ,2  ,2  ,2  ,2
92 $END
93
94
95 $MODEL_GEOMETRY
96 BlockCreate 1, 1, 19, 0.5, 19.5, 0.5, 9.5, 9, 19, 9, 4, 1
97 $END
98
99
100 $BC
101 BC_GetDispHigh  1,4,2
102 BC_GetDispLow   1,3,2
```

```
103
104 BC_zero_corner  1,1,1,1,1
105 BC_zero_face    1,3,0,1,0
106 BC_zero_edge    1,4,1,1,0
107
108 BC_zero_edge    1,9,0,1,1
109
110 F_add_face_udl  1,4,0,1,0,-1,1
111 Const_face_dof  1,4,0,1,0
112 $END
113
114
115 $OUTPUT
116 [...]
117 $END
118
119
120 $COLOUR
121 [...]
122 $END
```

Listing A.6: *Model input file C-T.*

```
1  $PARAMETERS
2  MaxLoadSteps = 15000
3  MaxCount = 5
4  MaxLoad = 10000
5  MaxDisp = 3
6  LoadThreshold = 0.01
7  SSCThreshold = 1
8
9  MATnonlinear = true
10 LDL = false
11 RENEW_K_freq = 100
12 Beam = false
13 TKfix = true
14 l(1) = 2
15 l(2) = 1
16 l(3) = 1
17
18 ElasticityMode=3
19 E(1) = 9608
20 E(2) = 681
```

```
E(4) = 557
E(8) = 325

ny(1,3) = 0.4862
ny(1,2) = 0.4862
ny(3,2) = 0.3719
ny(2,3) = 0.3719
ny(2,1) = 0.0345
ny(3,1) = 0.0345

EngStrain = 1

COV(1) = 0.2
COV(2)  = 0.2
COV(4)  = 0.2
COV(8)  = 0.2

K(1) = 1423.5
K(2) = 357.3
K(4) = 1392.2
K(8) = 1297.9

St(1) = 100
Yft(1) = 1.01
Sc(1) = 12
Yfc(1) = 0.01

St(2) = 7
Yft(2) = 1.01
Sc(2) = 4
Yfc(2) = 0.01

St(4) = 20
Yft(4) = 1.01
Sc(4) = 20
Yfc(4) = 1.01

St(8) = 7
Yft(8) = 1.01
Sc(8) = 7
Yfc(8) = 1.01
$END


```

```
$WOODSTRUCT
Enable = true
Frame =  −5, 25, −5, 25, −5, 25, 1

AlphaMean = 3.131
AlphaCOV = 0.142
R_PithMean = 49.493
R_PithCOV = 0.173
R_ShiftMean = 0.503
R_ShiftCOV = 0.562
DR_CentreMean = 5.125
DR_CentreCOV = 0.231
DR_DiffMean = −0.049
DR_DiffCOV =  −2.796
DR_VarMean = 0.229
DR_VarCOV = 2.412

NormMinMean = 0.717
NormMinCOV = 0.146
NormDiffMean = 0.982
NormDiffCOV = 0.211
NormExpMean = 1.958
NormExpCOV = 1.014

WoodStructLinksT = 2  ,1.5,1.5,1.5,1.5,1.5,1.5,1.5,1.5
WoodStructLinksC = 1.5,1  ,1  ,1.5,1.5,1.5,1.5,1.5,1.5
WoodStructLinksK = 2  ,2  ,2  ,2  ,2  ,2  ,2  ,2  ,2
$END


$MODEL_GEOMETRY
BlockCreate 1, 1, 19, 0.5, 19.5, 0.5, 9.5, 9, 19, 9, 4, 1
$END


$BC
BC_GetDispHigh  1,4,2
BC_GetDispLow   1,3,2

BC_zero_corner  1,1,1,1,1
BC_zero_face    1,3,0,1,0
BC_zero_edge    1,4,1,1,0

BC_zero_edge    1,9,0,1,1
```

```
109
110 F_add_face_udl  1,4,0,1,0,-1,1
111 Const_face_dof  1,4,0,1,0
112 $END
113
114
115 $OUTPUT
116 [...]
117 $END
118
119
120 $COLOUR
121 [...]
122 $END
```

Listing A.7: *Model input file J-M10.*

```
1  $PARAMETERS
2  MaxLoadSteps = 20000
3  MaxCount = 1
4  MaxLoad = 10000
5  MaxDisp = 20
6  LoadThreshold = 0.01
7  MATnonlinear = true
8  CONnonlinear = true
9  GEOnonlinear = true
10 NonlinearSteps = 2
11
12 RENEW_K_freq = 100
13 LDL = false
14 SSCThreshold = 1
15
16 SmoothContact = true
17 Beam = false
18 TKfix = true
19 l(1) = 2
20 l(2) = 1
21 l(3) = 1
22
23 ElasticityMode=3
24 E(1) = 9608
25 E(2) = 681
26 E(4) = 557
```

```
E(8) = 325

ny(1,3) = 0.4862
ny(1,2) = 0.4862
ny(3,2) = 0.3719
ny(2,3) = 0.3719
ny(2,1) = 0.0345
ny(3,1) = 0.0345

EngStrain = 1

COV(1) = 0.2
COV(2)  = 0.2
COV(4)  = 0.2
COV(8)  = 0.2

K(1) = 1423.5
K(2) = 357.3
K(4) = 1392.2
K(8) = 1297.9

St(1) = 100
Yft(1) = 1.01
Sc(1) = 12
Yfc(1) = 0.01

St(2) = 7
Yft(2) = 1.01
Sc(2) = 4
Yfc(2) = 0.01

St(4) = 20
Yft(4) = 1.01
Sc(4) = 20
Yfc(4) = 1.01

St(8) = 7
Yft(8) = 1.01
Sc(8) = 7
Yfc(8) = 1.01
$END


$WOODSTRUCT
```

```
Enable = true
Frame =  −5, 85, −35, 35, −5, 25, 1

AlphaMean = 2.907
AlphaCOV = 0.316
R_PithMean = 48.809
R_PithCOV = 0.308
R_ShiftMean = 0.540
R_ShiftCOV = 0.560
DR_CentreMean = 5.881
DR_CentreCOV = 0.211
DR_DiffMean = −0.138
DR_DiffCOV =  −1.599
DR_VarMean = 0.361
DR_VarCOV = 7.402

NormMinMean = 0.717
NormMinCOV = 0.146
NormDiffMean = 0.982
NormDiffCOV = 0.211
NormExpMean = 1.958
NormExpCOV = 1.014

WoodStructLinksT = 2  ,1.5,1.5,1.5,1.5,1.5,1.5,1.5,1.5
WoodStructLinksC = 1.5,1  ,1  ,1.5,1.5,1.5,1.5,1.5,1.5
WoodStructLinksK = 2  ,2  ,2  ,2  ,2  ,2  ,2  ,2  ,2  ,2
$END


$MODEL_GEOMETRY
%solid elements
BlockCreate      2, 50, 80,  7.5, 17.5, 0, 20, 3, 2, 4, 1
BlockCreate      3, 50, 80,−17.5, −7.5, 0, 20, 3, 2, 4, 1

BlockCreate      4,  0, 80, 17.5,   30, 0, 20, 8, 2, 4, 1
BlockCreate      5,  0, 80,  −30,−17.5, 0, 20, 8, 2, 4, 1

BlockCreate      6, 20, 50,  7.5, 17.5, 0, 15, 3, 2, 3, 1
BlockCreate      7, 20, 50,−17.5, −7.5, 0, 15, 3, 2, 3, 1

BlockCreate      8,  0, 20,  7.5, 17.5, 0, 20, 2, 2, 4, 1
BlockCreate      9,  0, 20,−17.5, −7.5, 0, 20, 2, 2, 4, 1

BlockCreate     10,  0, 20, −7.5,  7.5, 0, 20, 2, 2, 4, 1
```

```
115
116 %connect LATTICE with SOLIDS
117 %in Y
118 BlockConnect        2,1,3,11
119 BlockConnect        3,1,4,13
120
121 BlockConnect        4,1,3,4
122 BlockConnect        5,1,4,3
123
124 BlockConnect        6,1,3,14
125 BlockConnect        7,1,4,16
126
127 %in Z
128 BlockConnect        6,1,6,15
129 BlockConnect        7,1,6,17
130
131 %in X
132 BlockConnect        2,1,1,10
133 BlockConnect        3,1,1,12
134
135 BlockConnect        8,1,2,1
136 BlockConnect        9,1,2,1
137 BlockConnect        10,1,2,1
138
139 %connect SOLIDS
140 %in Y
141 BlockConnect        2,4,4,3
142 BlockConnect        3,5,3,4
143
144 BlockConnect        8,4,4,3
145 BlockConnect        9,5,3,4
146
147 BlockConnect        10,8,4,3
148 BlockConnect        10,9,3,4
149
150 %in X
151 BlockConnect        2,6,1,2
152 BlockConnect        6,8,1,2
153
154 BlockConnect        3,7,1,2
155 BlockConnect        7,9,1,2
156
157 HoleSurfaceCreate   1, 40, 0, 5, 2, 20
158
```

```
159 NotchSurfaceCreate  1, 15, 30, 25, 36, 0, 20, 10, 0, 11,  0, 0, 0
160 NotchSurfaceCreate  1, 15, 30, -1, 10, 0, 20, 12, 0,  0, 13, 0, 0
161
162 NotchSurfaceCreate  1, -1, 15, 25, 36, 0, 15,  0, 0, 14,  0, 0,15
163 NotchSurfaceCreate  1, -1, 15, -1, 10, 0, 15,  0, 0,  0, 16, 0,17
164
165 BlockCreate     1, 21, 79,-17, 17, 0.5, 19.5,29, 34, 19, 4, 1
166 BoltCreate      20, 40, 0, 9.55, 4.99, 20.001, 5
167
168 HoleBoltConnect     20, 20
169
170 WasherSurfaceCreate 1, 40, 0, 0, 6, 15, 40
171 WasherBoltConnect   1, 40, 20, 2, 15
172 $END
173
174
175 $BC
176 BC_GetDispHigh  20,5,1
177 BC_GetDispLow   10,1,1
178
179 %origin fully fixed
180 BC_zero_corner  5,1,1,1,1
181
182 %two edges
183 BC_zero_edge    5,4,1,1,0
184
185 BC_zero_edge    5,1,1,0,1
186 BC_zero_edge    4,1,1,0,1
187 BC_zero_edge    8,1,1,0,1
188 BC_zero_edge    9,1,1,0,1
189 BC_zero_edge    10,1,1,0,1
190
191 %in X base of specimen
192 BC_zero_face    4,1,1,0,0
193 BC_zero_face    5,1,1,0,0
194 BC_zero_face    8,1,1,0,0
195 BC_zero_face    9,1,1,0,0
196 BC_zero_face    10,1,1,0,0
197
198 %full surface in Z (one side of specimen)
199 BC_zero_face    1,5,0,0,1
200 BC_zero_face    2,5,0,0,1
201 BC_zero_face    3,5,0,0,1
202 BC_zero_face    4,5,0,0,1
```

```
BC_zero_face    5,5,0,0,1
BC_zero_face    6,5,0,0,1
BC_zero_face    7,5,0,0,1
BC_zero_face    8,5,0,0,1
BC_zero_face    9,5,0,0,1
BC_zero_face    10,5,0,0,1

%BOLT
BC_zero_face_rot    20,5,1,0,1
BC_zero_face_rot    20,6,1,0,1

BC_zero_face    20,5,0,1,1
BC_zero_face    20,6,0,1,0

F_add_face_udl  20,5,1,0,0,1,1
$END


$OUTPUT
[...]
$END


$COLOUR
[...]
$END
```

A.5 MATLAB Files

The following table lists all used MATLAB files and their function. These can also be found on the attached CD.

Table A.3: *List of* MATLAB *files.*

file name	function
LAT3D.m	main routine
PLOT3D.m	output plots
GrowthRingDetection.m	draws circles on scanned images of cross sections
Optimise_Elastic_Parameters.m	determines elastic stiffness parameters K from E-moduli
WoodStruct_Determination.m	obtains density values from data file (lab tests)
subfunctions	
BBarcreate_coord.m	creates strain-displacement vector of bar element
BBeam3D.m	creates strain-displacement vector of 3D beam element
BC_apply.m	applies boundary conditions
Block_Create.m	defines blocks of elements
Bolt_Contact_Create.m	defines contact elements between bolt and lattice
Bolt_Create.m	defines bolt beam elements
Calc_Load_Disp.m	determines current load and displacement from displacement vector
Check_Max_Disp_Load.m	defines bolt beam elements
CheckStrain.m	checks for incorrect strain
Check_Max_Disp_Load.m	checks if maximum load or disp. is reached

file name	function
chessboard.m	creates checked matrix
chessboard_wide.m	creates checked matrix (wide)
Circle.m	creates linear approximation of a circle (PLOT3D.m)
Circle_Matrix.m	creates matrix with circle shape (Block_Create.m)
circularc.m	creates an arc-circle
Connect_Create.m	connects two blocks (lattice/solid)
Fadd.m	routine to add a force to global force vector
Figs2EPS.m	routine to create an '.eps' file from a MATLAB figure
Initialise_Output_Colour.m	reads in the colour parameters from model file
Initialise_Parameters.m	reads in the normal parameters from model file
Interpol.m	interpolation function
Intersect_circle2line.m	determines intersection of a line and a circle (GrowthRingDetection.m)
Intersect_line2line.m	determines intersection of two lines (GrowthRingDetection.m)
kBarcreate_angle.m	creates local stiffness matrix of a 3D bar element according to angles
kBarcreate_connect.m	creates local stiffness matrix of a 3D bar element, used in connecting blocks
kBarcreate_contact.m	creates local stiffness matrix of a 3D bar element, used in contact

file name	function
kBarcreate_coord.m	creates local stiffness matrix of a 3D bar element according to coordinates
kBeam3D.m	creates local stiffness matrix of a 3D beam element in X
KLinkChange.m	routine to change link status and stiffness
kPlane4lin.m	creates local stiffness matrix of a 2D planer element
kSolid8lin.m	creates local stiffness matrix of a 3D solid element
Lattice_Main.m	main routine
Lat_Hole_Surface_Create.m	creates hole in lattice and determines surface nodes
Lat_MeanDiffGet.m	determines mean strength value based on the position of link
Lat_Notch_Create.m	creates notch in lattice and determines surface nodes
Lat_Washer_Surface_Create.m	determines surface nodes under washer
LDPlot.m	creates load displacement plots
LDPlot_Mean.m	creates averaged load displacement plots
LDP_Info_TXT.m	extracts LDP from text files (lab tests)
Link_Show.m	shows link status strain and force
Link_Temp_create.m	creates link element templates (Block_Create.m)
LoadDispmodif.m	modifies LDP (no 'snap-back')
LOGNRD_get.m	creates random log-normal distributed values
lognrndO.m	function used by LOGNRD_get.m
MIFM_Algorithm.m	MIF function

file name	function
Model_OBJ_Create.m	creates '.obj' output file
Model_Plot.m	plots model in MATLAB figure
Model_Save.m	saves '.out' output file
NBeam3D.m	shape function of 3D beam element
newcol.m	adds a new colour definiton
NRD_get.m	creates random normal distributed values
NRD_get_neg.m	creates random normal distributed values (incl. neg. values)
OBJPlot_Arrow.m	'.obj' plot, arrows
OBJPlot_Cylinder.m	'.obj' plot, cylinder
OBJPlot_Polygon.m	'.obj' plot, polygon
OBJPlot_Polygon_Text.m	'.obj' plot, polygon (including texture)
OBJPlot_Sphere.m	'.obj' plot, sphere
Plot_Arrow.m	plots in MATLAB figure, arrow
Plot_Circle.m	plots in MATLAB figure, circle
Plot_Circle_Fill.m	plots in MATLAB figure, filled circle
Plot_Cylinder.m	plots in MATLAB figure, cylinder
PRead.m	reads from model input file, line
Preprocessor.m	preprocessor routine
ReadInBlock.m	reads from model input file, block

file name	function
ReNew_K.m	renews global stiffness matrix
Ring_3P.m	creates a 3-point circle
Rot_Matrix.m	creates a rotation matrix
Rot_Matrix_Angle.m	creates a rotation matrix, angles
ROT_Matrix_Coord.m	creates a rotation matrix, coordinates
SSC_Algorithm.m	SSC algorithm
Surface_Create.m	determines surface nodes
Time_Disp.m	displays current time
TKadd.m	adds local stiffness matrix to global one
TKadd_MPC.m	adds multi-point constraints from global stiffness matrix
TKadd_MPC_Val.m	adds multi-point constraints from global stiffness matrix, value
TKsub.m	subtracts local stiffness matrix from global one
TKsub_MPC.m	subtracts multi-point constraints from global stiffness matrix
TK_Create.m	creates global stiffness matrix
Update.m	updates all element and nodal information
Washer_Contact_Create.m	defines contact elments between washer and lattice
WoodStruct_NormGet.m	determine rho value according to the position of a link element

file name	function
Wood_Struct_Create.m	creates wood strucutre
Write_Colour_Table.m	write colour info in '.mat' file

A.6 Paper, WCTE 2006

Modelling Geometric Non-Linear Behaviour of Single Shear Bolted Joints

Thomas Reichert
Research Student
Napier University (School of the Built Environment)
Edinburgh, UK

Dan Ridley-Ellis
Senior Research Engineer
Napier University (Centre for Timber Engineering)
Edinburgh, UK

1. Summary

Findings are presented of the first stage of an investigation of second-order effects that influence the resistance and stiffness of single shear bolted joints. These effects develop as a result of joint deformation and the rotation of all, or part, of the bolt. A two-dimensional finite element model incorporating these effects is introduced and predicted behaviour compared to laboratory test results of pre-tensioned M16 single shear joints. The model is shown to accurately predict the load-slip curve, giving better predictions of resistance than the present Eurocode design equations indicating potentially underutilised strength reserve. Furthermore, the model allows the individual components of the second order effects to be quantified separately.

2. Introduction

Second order effects in bolted timber connections, namely the 'rope effect' (axial force in the fastener), rotational constraint (due to washer, head and nut) and friction between adjoining timber surfaces, represent a significant load resistance reserve over and above that calculated by Johansen theory. Some of these effects have now been incorporated into Eurocode 5 (EN 1995-1-1) design equations, but there may still remain better ways to utilise this strength reserve for design. Furthermore, their influence on joint slip behaviour has not yet been rigorously researched.

A two-dimensional finite element model has been used to study these effects and the predictions compared to laboratory test results using properties obtained from fastener embedment and washer embedment tests. The investigation represents the preliminary work of a wider study: the model and the findings will serve in the development of a complete three-dimensional model of timber joints with multiple bolts that is able to account for these second order non-linear effects and their interaction with fracture as the limiting factor of joint resistance. Such a model will be useful, when validated and calibrated against laboratory data, to research joint behaviour in more detail without the need for extensive testing programmes.

To take into account these effects, a geometric non-linear analysis (large deformation, contact and material non-linearity) has to be performed. With this the equilibrium forces and moments are calculated for the deformed system. Plasticity in the bolt is also modelled, but shall not be further considered in this paper. Similar models have been presented by Nishiyama and Ando (2003) and Sawata and Yasumura (2003). A geometric nonlinear analysis considering the rope effect and rotational constraint in dowel type joints was also performed by Erki (1991).

3. The Beam and Spring Model

The commercial package ANSYS was used to create the two dimensional model, which is capable of performing geometric as well as material non linear analysis. The general configuration is shown in Fig 1. The bold lines show the fastener, nut and washer and shaded areas represent the two

adjoining timber members, which are actually modelled with timber embedment springs (shown by the saw-tooth lines). The components are:

a) Fastener
The fastener is represented by regular beam elements with circular cross section, which allow for elastic-plastic bending, axial tension, stress stiffening effects and large deformation analysis. The tension yield strength is determined by tension tests of bolts, but for the results presented here the elastic limits were not exceeded and an elastic modulus of 210 kN/mm^2 has been assumed.

b) Washer, head and nut
The washer, head and nut are modelled with infinitely stiff beam elements which ensure no flexure occurs. This behaviour is assumed for simplicity of model formulation. Although slight bending was observed in tests, it is not expected that this will have significant influence on overall joint behaviour. The washer is linked with the bolt shaft in the global Y-direction, allowing it to rotate independently to the head and nut. Therefore the rotational constraint of the fastener results from the moment that is applied through the nut to the washer.

c) Timber embedment for fastener
The timber embedment for the fastener has been modelled with two pairs of elastic-perfectly plastic springs arranged below and above the fastener. Properties are calculated from the results of embedment test data, from which the embedment strength and initial foundation modulus are taken. One of the pairs represents timber deformation in the global Y-direction and the other in the global X-direction. Contact elements have been used to model the interaction between the deformed fastener and the timber-embedment spring nodes (filled circles in *fig 1*). Therefore it is possible to take into account both an oversized bolt hole and a slack washer.

d) Timber embedment for washer
The same applies for the embedment underneath the washers. The behaviour of the springs is described by bi-linear load-slip curves according to the compressed area that they are representing underneath the washer. To guarantee that each washer embedment spring moves with the washer, they are coupled with the global vertical displacement of the washer.

The Newton-Raphson method was used to perform the non-linear analysis and the whole model is displacement controlled. A fixed displacement is assigned to the springs' end nodes on the right hand side timber to simulate the overall joint displacement (hollow circles). For each time step, load is calculated from the summation of forces in the vertical springs on the right hand side timber.

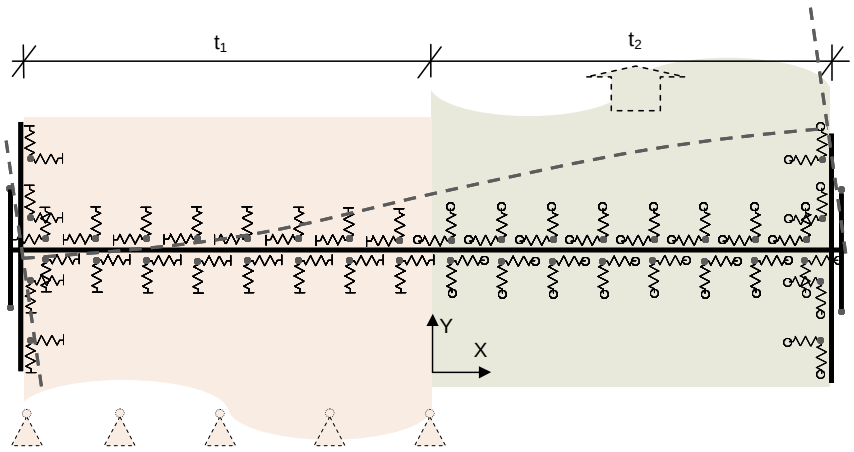

Fig 1 Schematic of model configuration

The model is set with the following parameters: bolt diameter (d), timber thicknesses (t_1 , t_2), bolt hole oversize, washer inner and outer diameter, possibility of slack washer, bolt preload, together with material parameters obtained from:

a) Fastener embedment tests according to BS EN 383:1993 (embedment strength and foundation modulus – values w_{02} and w_{04} are used)

b) Washer embedment tests (embedment yield strength, foundation modulus and post-yield hardening gradient)

Model outputs are obtained in accordance with EN26891:1991 (initial joint stiffness determined from the modified initial slip) and EN 26891:1991 (resistance at a displacement of 15 mm).

4. Laboratory Tests

For the laboratory tests presented in this paper, M16 (d = 15.6 mm) joints were manufactured with an edge-distance of 55 mm (>3d) and an end distance of 128 mm (>7d) to prevent splitting of the specimens. Eccentricity of the applied load was minimized by using notched steel plates joining the timbers to the test machine. It was attempted to minimise friction between the timbers by the use of graphite powder on the sliding surfaces. The timber used was C16 Sitka Spruce.

An inserted strain gauge was used to measure the axial force in the centre of the bolt, having been previously calibrated against know direct tension loads. Testing the bolt under in bending load confirmed that the gauge measurement was negligibly sensitive to flexure of the bolt. For these tests, the faster was preloaded by tightening the bolt to 250 N. During the tests, the global rotation of the bolt was calculated from the measurement of two displacement transducers arranged vertically under a rigid lever fixed to the bolt's end.

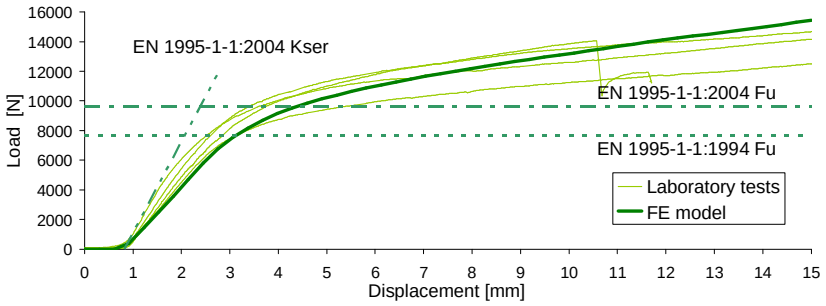

Fig 2 Laboratory measurements and finite element model prediction (load-slip)

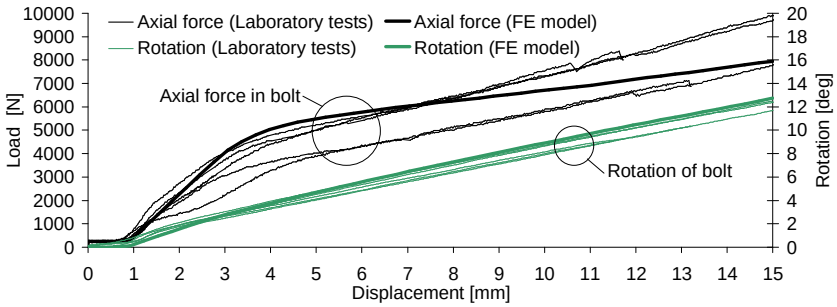

Fig 3 Laboratory measurements and finite element model predictions (bolt load and rotation)

Fig 2 shows the load-slip relationship for five replicate tests in comparison to mean values from Eurocode 5 prediction. Measurements of bolt axial force and bolt rotation are shown in *fig 3*. To compensate for variation in exact bolt hole oversize and starting position the test series curves have been shifted to the same value of initial slip.

The results confirm that the improvement made in the published Eurocode 5 to take into account the 'rope effect' compared to the 1994 draft results in better prediction of the joint resistance. However, the resistance still appears very conservative. This stems from the fact that the strength reserve is not only caused by the 'rope effect' but also by the increasing effective embedment length of the fastener, which results from the rotational constraint.

5. Discussion and Conclusion

The graphs also show the predictions of the finite model for comparison. In this case, the model does not include calculation of friction between the timbers. The effect of rotational constraint is included which results in a good prediction of the actual load-slip behaviour and joint resistance. In accounting for bolt strength reserve the present code does not consider any influence from unequal timber thicknesses. The strength reserve might be even more pronounced for the unsymmetrical case. Better equations might be found to take into account the rotational constraint in the calculation of the load carrying capacity of bolted joints.

In terms of the joint stiffness, in this case, the Eurocode overestimated the real stiffness while the model underestimated it. This could stem from the neglected friction in the model, as the measures used to remove friction from the laboratory tests might not have been successful.

The rotation of the bolt is predicted accurately by the model, with a slightly steeper gradient in the pre-yield range than afterwards. Agreement between the prediction and measurement of axial force in the bolt was less good, with the model predicting a lower gradient in the post-yield range than observed in the tests.

The project is supported by the School of the Built Environment, Napier University. Sponsorship from Finnforest UK permitted participation in the World Conference on Timber Engineering. More information about the project is available at http://cte.napier.ac.uk.

6. References

[1] EN 1995-1-1:2004. *Design of timber structures. General. Common rules and rules for buildings*. European Committee for Standardization, Brussels, Belgium.

[2] Nishiyama N. and Ando N. 2003. Analysis of load-slip characteristics of nailed wood joints: Application of a Two-Dimensional Geometric Nonlinear Analysis. *Journal of Wood Science* Vol. 49, pp. 505-512.

[3] Sawata K. and Yasumura M. 2003. Estimation of yield and ultimate strengths of bolted timber joints by nonlinear analysis and yield theory. *Journal of Wood Science* Vol. 49, pp. 383–391.

[4] Erki M. A. 1991. Modelling the Load - Slip behaviour of timber joints with mechanical fasteners. *Canadian Journal of Civil Engineering* Vol. 18, No. 4, pp. 607-616.

[5] EN 383:1993. *Timber Structures – Test Methods – Determination of Embedding Strength and Foundation Values for Dowel Type Fasteners.* European Committee for Standardization, Brussels, Belgium.

[6] EN 26891:1991. *Timber Structures – Joints made with Mechanical Fasteners – General Principles for the Determination of Strength and Deformation Characteristics*. European Committee for Standardization, Brussels, Belgium.

A.7 Paper, WCTE 2008

3D Lattice Model for Post-Yield and Fracture Behaviour of Timber

Thomas REICHERT
Research Student
Centre for Timber Engineering, Napier University
Edinburgh, UK

Dr Daniel RIDLEY-ELLIS
Principal Research Fellow
Centre for Timber Engineering, Napier University
Edinburgh, UK

Summary

The paper describes the development of a bespoke Finite Element program to model timber with a three dimensional lattice of single spring elements. These springs mimic meso-scale timber behaviour, namely the crushing and separation of fibre bunches by following a tri-linear load-displacement curve. Strength and stiffness parameters for longitudinal, lateral and diagonal elements are randomised for heterogeneity. To save computing time, two specialised algorithms have been implemented to perform a nonlinear analysis faster than an iterative Newton-Raphson algorithm. The algorithms have been adopted and extended to suit a 3D lattice model for timber. Furthermore lattice elements have only been used in areas where plasticity and fracture is expected, with transverse isotropic continuum elements elsewhere. The general calibration procedure of this hybrid model to tested timber specimens of Sitka spruce (*Picea sitchensis*) is described.

1. Concept Lattice Model

Lattice models have been used widely for concrete, but have only recently been applied to timber, e.g. [1][2][3]. A clear advantage of modelling timber with a lattice is the possibility to predict brittle failure without prior knowledge of the failure location and therefore with no need for re-meshing the Finite Element (FE) model.

The basic unit cell in a lattice has to be constructed to be periodically repeating in space (Fig. 1). In this lattice, each cell consists of six different types of elements. Longitudinally orientated springs transfer load in the X direction (grain direction) and lateral springs in the Y and Z direction. Diagonal springs resist shear in the XY, XZ and YZ plane, as well as providing additional X, Y and Z components. This can be simplified by the assumption of transverse isotropy, to four independent elements by equating the Y and the Z direction. Thus, elements in the XY plane are the same as

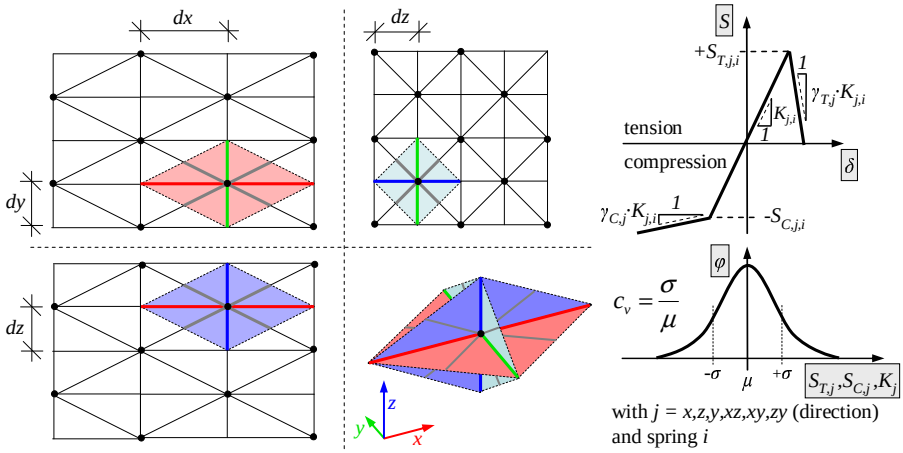

Fig. 1 Lattice structure with longitudinal (red), lateral (green/blue) and diagonal (grey) "half" springs in one unit cell (left), load-displacement curve for spring i (top, right) and a definition of c_v with mean and standard deviation (bottom, right)

their respective elements in the XZ plane. A complete nomenclature can be found at the end of this paper.

In order to create a lattice with as few nodes as possible, they have been arranged in a diagonal checked pattern. Thus, instead of constructing nodes at each potential junction of springs only every second one is used. Each element follows a tri-linear load-displacement curve with limit strength and yield strength values respectively under tension and compression, followed by a softening or fracture line.

Material heterogeneity can be implemented by assigning randomised strength ($S_{C,j}$ and $S_{T,j}$) and stiffness (K_j) properties to springs based on a mean value for each spring type j (x, y/z, xy/xz and yz) and a coefficient of variation (c_v). This coefficient is assumed to be 0.2 since it has only minor influence on the bulk model behaviour [2]. The growth rings can be taken into account as structured variation of properties in the lattice. This is implemented by mapping generated growth rings on the lattice and changing the mean strength and stiffness properties of lattice members according to their assumed position within these rings (section 1.2).

1.1 Nonlinear Solution

Former lattice models for timber, e.g. [1][2][3], adopted a simple technique to solve for the nonlinear solution: After assembling the global stiffness matrix, this system of equations is solved for a fixed displacement step. The resulting stress for each element is computed and checked if it exceeds its predefined maximum strength. Elements are removed accordingly and the process is repeated until no element fails. Then the next displacement is assigned. This algorithm is repeated until the final displacement step assigned or the system becomes singular. However, with this technique any accumulated elastic work stored in the lattice before breaking occurs is neglected. Since the model described in this paper will be used to perform contact and geometric nonlinear analysis in the future, the solution algorithm required a more general approach, as for example the Newton-Raphson algorithm.

To further save computation time, a specialised technique [4] has been adopted. Jirásek and Bažant call it the "Method of Inelastic Forces" (MIF) and the "Step Size Control" (SSC) algorithm. The latter allows for faster computation by following the solution path through single linear steps from one element changing its stiffness to the next element changing. Thus, no additional iteration is necessary. Further, the MIF treats any change that would occur in the matrix due to a change in the element's stiffness, as an added inelastic force that represents the difference between the system with changed stiffness and the elastic one. Thus, only the force vector has to be modified and it is not necessary to solve the global stiffness matrix again. The interested reader is referred to a more detailed description of this algorithm in the original paper [4]. For this research, the SSC method has been modified to allow for a tri-linear load-displacement definition of the spring elements as depicted in Fig. 1.

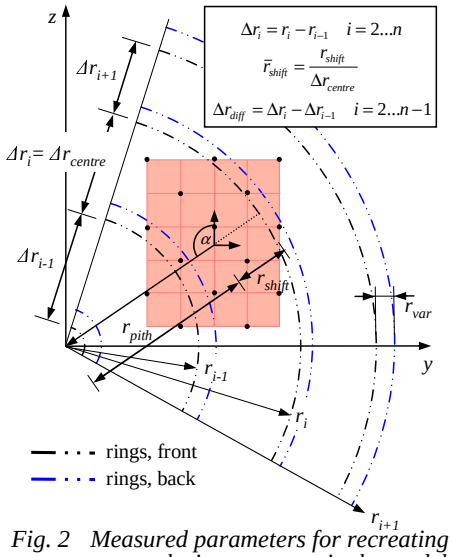

Fig. 2 Measured parameters for recreating a growth ring structure in the model

1.2 Structured Heterogeneity

Heterogeneity, on the level of the growth ring structure, is mapped on a lattice of the cell size of 2 x 1 x 1 mm (*dx* x *dy* x *dz*). This size results from a balance between acceptable computational effort for larger lattices and represented detail of the growth ring structure. The mean ring width measured from test specimens has been 5.47 mm, with a c_v of 24.8%. Specimens with ring width less than 2 mm were discarded. This ensures that one growth ring encompasses at least two lattice cells.

Several measurements were taken from the tested specimens. The cross section of each one (front and back) was scanned with an ordinary flatbed

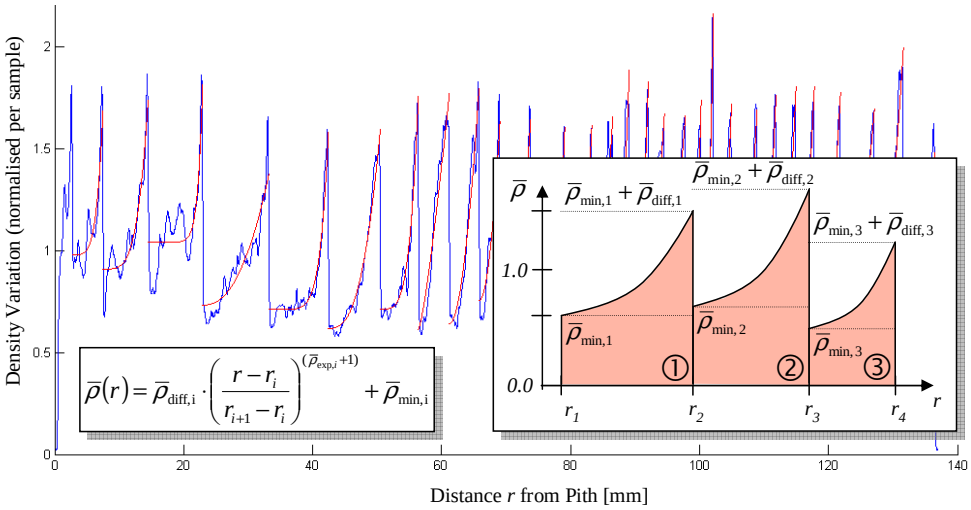

Fig. 3 Density profile with fitted curve of power functions in each growth ring

scanner. A programme was written that enables the user to draw 3-point circles onto the latewood of each growth ring in these images. By averaging the centre points of each circle, the assumed position of the pith can be determined. With this information the following parameters can be obtained from one specimen (Fig. 2): α, r_{pith}, $\bar{r}_{shift}$, *mean* Δr_{diff} and *mean* r_{var}.

Mean values are calculated along with their coefficients of variation from the specimens of one test series. This serves then as input parameters to create a random ring structure for the lattice model, based on the characteristics of tested specimens.

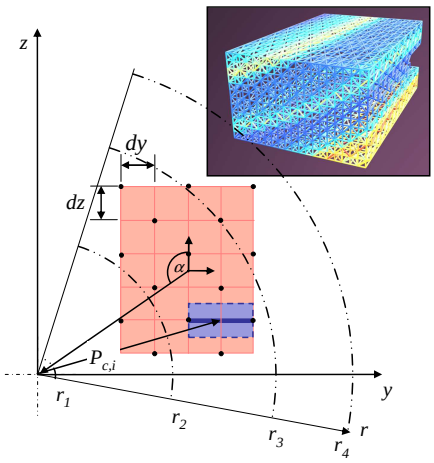

Fig. 4 Density profile mapped on lattice

1.3 Mapping the Density Profile

In order to map the ring structure on the lattice, the simplest assumption would be to correlate stiffness and strength variation directly with density variation within a growth ring. Therefore, density measurements from Sitka spruce samples were taken and have been normalised. The experimental work was done by the chemistry department in the University of Glasgow, which used an Itrax density scanner [7]. Fig. 3 shows a density profile for one radial strip, plotted from pith to bark (blue line). Each peak represents the end of one growth ring. A good approximation of these lines is a fitted power function curve (red line) that encompasses one growth ring from one peak to the next one. The equation for these approximated curves is given in the left box of Fig. 4. The right box depicts the resulting curve for this equation for three rings. From several of these radial specimens mean values of $\bar{\rho}_{min,i}$, $\bar{\rho}_{diff,i}$, $\bar{\rho}_{exp,i}$ and their c_v can be calculated, serving as further input parameters to generate a density profile for the model.

Each individual *full* spring encompasses an area of the cross section of $dy \cdot dz$ for longitudinal and diagonal springs and $2 \cdot dy \cdot dz$ for lateral springs, as shown in Fig. 4. The average normalised density of this area from a randomly generated profile is calculated. Finally, the mean strength and stiffness parameters for this particular spring are simply adjusted by multiplying this value with the original mean parameters.

2. Methodology

As shown in the load-displacement curve definition of one spring *i* in Fig. 1, three types of mean parameters have to be adjusted: firstly, the mean stiffness values *K* that can be directly (with limitations) derived from E-moduli, secondly, the mean strength parameters S_C and S_T for each spring type that will be determined by trial and error, and thirdly, the parameters γ_T and γ_C that define the softening curve.

All tested specimens came from one timber species, Sitka spruce (*Picea sitchensis*).

Given that the timber behaves transverse isotropic on the small scale that it is modelled, it can be assumed that parameters in the Y and Z direction are the same. Thus, in summary, there are four independent mean elastic parameters (K_x, $K_y = K_z$, K_{yz}, $K_{xz} = K_{xy}$, K_{yz}), six independent mean strength parameters ($S_{C,x}$, $S_{T,x}$, $S_{C,y} = S_{C,z}$, $S_{T,y} = S_{T,z}$, $S_{CT,xy} = S_{CT,xz}$, $S_{CT,yz}$) and two softening stiffness parameters in compression ($\gamma_{C,x}$ and $\gamma_{C,y} = \gamma_{C,z}$). The remaining represent a very steep softening curve, thus ($\gamma_{T,x} = \gamma_{T,y} = \gamma_{T,z} = \gamma_{CT,xy} = \gamma_{CT,xz} = \gamma_{CT,yz} \approx -\infty$).

While the stiffness parameters can be obtained from given *E*-moduli, the strength parameters are adjusted by means of comparisons between tested small clear specimens under various loading conditions and their respective FE models. Fig. 5 demonstrates the methodology of the calibration.

2.1 Elastic Parameters

The *K* values for a lattice can not be adjusted entirely freely to represent full anisotropic or simply transverse isotropic behaviour. The geometry imposes certain limitations. These could be overcome by introducing angular springs that act in between the existing springs in one unit cell. With this, it would be possible to adjust, for example, the elastic stiffness K_x and K_z independently from the shear modulus G_{xz}.

However, this has not been done for this research as it adds considerably to the computational problem. In this model (without angular springs), calculating the possible elastic parameters from the independent spring stiffness of a lattice cell can be performed according to [5] and shall be presented here briefly. This can be achieved by equating strain energy stored in a unit lattice cell and energy stored in the respective continuum of the same volume.

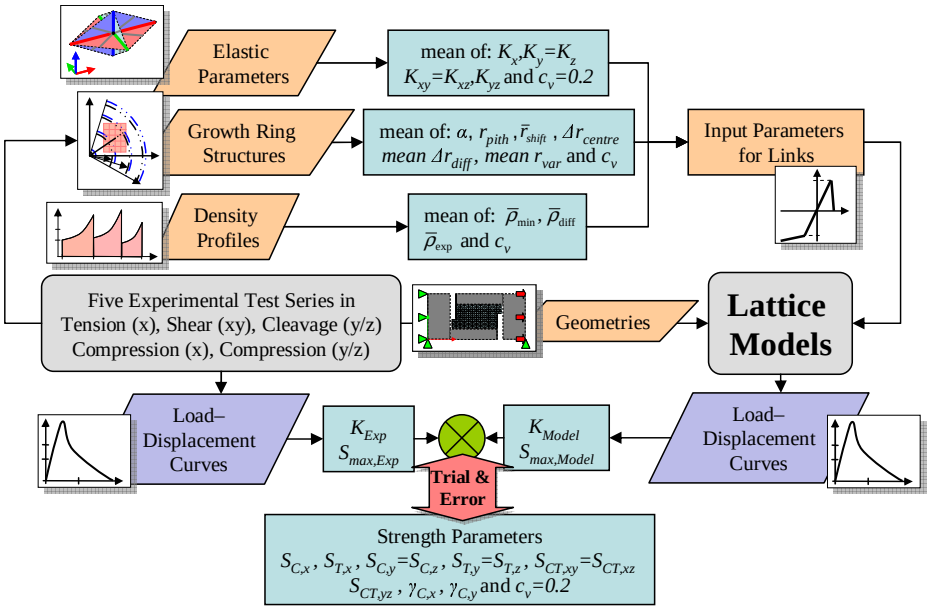

Fig. 5 Flowchart for the calibration process

$$U_{cell} = U_{continuum} \tag{1}$$

The strain energy can further be written as:

$$U_{cell} = \sum_b \frac{1}{2} E_b = \frac{1}{2} \sum_b^{N_b} (F \cdot u)^{(b)} \quad U_{continuum} = \frac{1}{2} \int_V \sigma \cdot \varepsilon dV \tag{2}$$

The former can be arranged as:

$$U_{cell} = \frac{1}{2} \sum_b^{N_b} (Ku \cdot u)^{(b)} \quad U_{continuum} = \frac{1}{2} \varepsilon \cdot C \cdot \varepsilon \tag{3}$$

A subsequent step involves equating both strain energies and connecting displacement *u* with strain ε, thus deriving the stiffness tensor *C*. At the final stage *C* can be written as:

$$C_{ijkm} = \frac{1}{V} \sum_b^{N_b} l^{(b)^2} \cdot K^{(b)} \cdot n_i^{(b)} n_j^{(b)} n_k^{(b)} n_m^{(b)} \qquad i, j, k, m = 1..3 \tag{4}$$

V represents the volume of the unit cell repeating in space (*V=2·dx·dy·dz*). The resulting stiffness tensor C_{ijkm} of the size 3x3x3x3 can be transferred due to symmetry to the more widely used Voigt Notation with C_{ij} of the size 6x6. From this, the *E*-moduli and Poisson coefficients can be directly obtained by calculating the inverse C^{-1}. Thus, it is possible to calculate the elastic constants from assumed spring stiffness. However, as mentioned before, due to the geometry of the lattice only limited elastic moduli can be obtained with certain *K*s. Therefore, a program was written that optimises the *K* values to find relatively close *E*-moduli and Poisson coefficient predictions.

As input values, the *E*-modulus in the longitudinal direction was measured from tension test data (E_x = 9792 N/mm²). The remaining *E*-moduli and Poisson ratios were then determined with ratios taken from the Wood Handbook [6]. Since it is assumed that the material behaves transverse isotropic on the small scale of the lattice cells, several elastic parameters are the same. For these instances the mean value is taken as shown in Table 1.

The best fit was achieved by optimising a target function, which is the sum of squared, normalised differences between the calculated elastic parameter and the target parameter (E-modulus, shear-modulus and Poisson ratio). The optimisation routine resulted in the following parameters.

Table 1 Determination of elastic parameters

Elastic Continuum Parameters	Target [N/mm²], [-]	Result [N/mm²], [-]
E_x	9792	9608
$E_y = E_z$	592	681
$G_{xy} = G_{xz}$	612	557
G_{yz}	*not fitted to*	325
$v_{xy} = v_{xz}$	0.43	0.4862
$v_{yz} = v_{zy}$	0.34	0.3719
$v_{yx} = v_{zx}$	*not fitted to*	0.0345
fit Φ_K		0.0635

Lattice Stiffness Parameters	Result [N/mm]
K_x	1423.5
$K_y = K_z$	357.3
$K_{xy} = K_{xz}$	1392.2
K_{yz}	1297.9

Using these resulting *K* values for the lattice and resulting *E, G, v* for solid elements, which adjoin the latter, they will both behave in the same way as far as bulk elastic properties are concerned

2.2 Strength Parameters

Five different calibration tests have been undertaken to obtain load-displacement data for simple stress states: a tensile, shear and cleavage test along with compression tests in the longitudinal and lateral direction. These results serve as an input to calibrate the lattice's strength parameters.

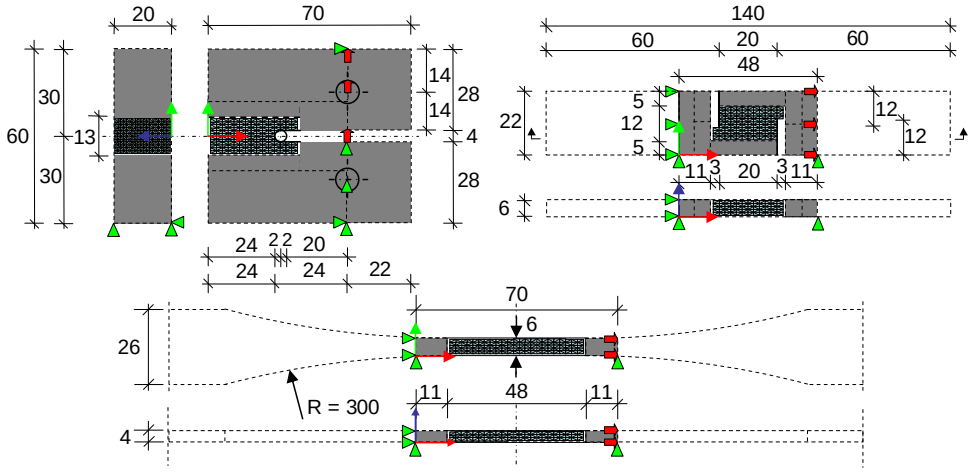

Fig. 6 Model depiction of three test arrangements (from the top left): cleavage (y/z), shear (xy) and tension (x). Note that only part of the specimen is modelled with a lattice, for the remainder transverse isotropic elastic solid elements are used (grey area)

The first three of these types of tests shall be presented here. A depiction of the respective test specimens and FE models is shown in Fig. 6. The red arrows and green triangles represent the applied forces and boundary conditions respectively.

2.3 Program Output

As one of the postprocessor's features, the FE program generates output files in form of 3D surfaces. Individual layers of geometric data of the deformed model as e.g. the lattice elements, solid elements and boundary conditions can be exported. These surfaces can be visualised with a rendering program (e.g. Bryce). To picture the fracture path the FE program generates surfaces (two for each plane in the *xy*, *xz* and *yz*-direction due to the shifted cell arrangement) with different shades of red according to the amount of broken links that this surface encompasses, see Fig. 7.

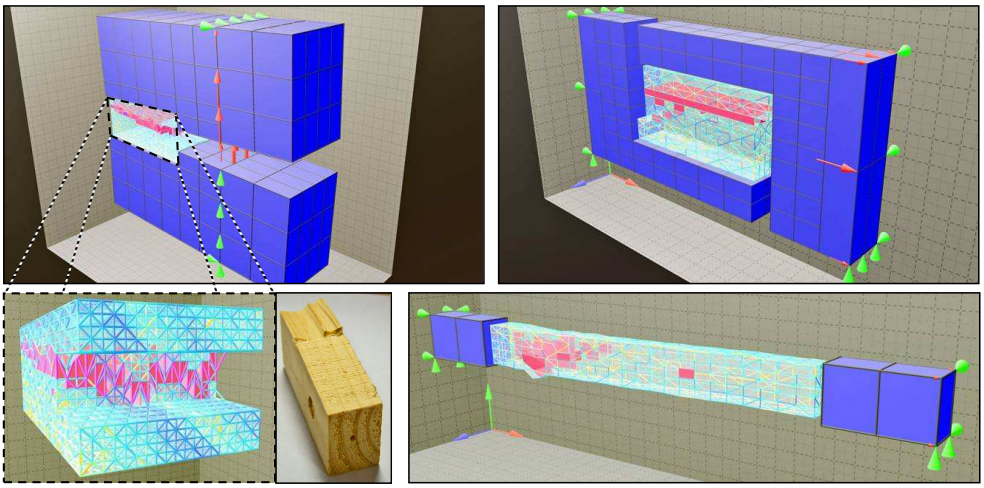

Fig. 7 Model depiction of a cleavage, shear and tension test, lattice colour represents variation in elastic and strength properties, influence of growth ring structure on fracture path for model and tests pictured (bottom, left)

3. Preliminary Results

After a preliminary adjustment of the strength parameters $S_{T,x}$, $S_{T,y/z}$, $S_{CT,xy/xz}$, load-displacement graphs can be obtained. They are plotted in Fig. 8, along with a box plot of the stiffness and maximum load of the model and experimental tests. Similar maximum loads are observed among model and experimental results for all three loading conditions and can be fine-tuned further.

However, predicted and measured stiffness, due to the inherent limitation of the lattice cells to fully model the ratios of elastic properties, show less agreement. Furthermore, post peak behaviour in the experimental shear tests was more pronounced than the model's prediction, which after a short plastic deformation shows brittle fracture. This probably stems from the wide meshed lattice that is used for these relative small shear specimens. Since the model allows adjustment of the softening curve of a spring ($\gamma_{T,j}$), this could serve to be another parameter to adjust for bulk post peak behaviour. However, cleavage models, using a denser mesh, showed better agreement in this regard.

Variation in the system's properties was in all cases predicted to be smaller than observed ones. As an initial assumption for these models, the density was mapped directly without any factor on the lattice's properties. Better model predictions might be obtained by applying a factor to the density variation for specific spring types.

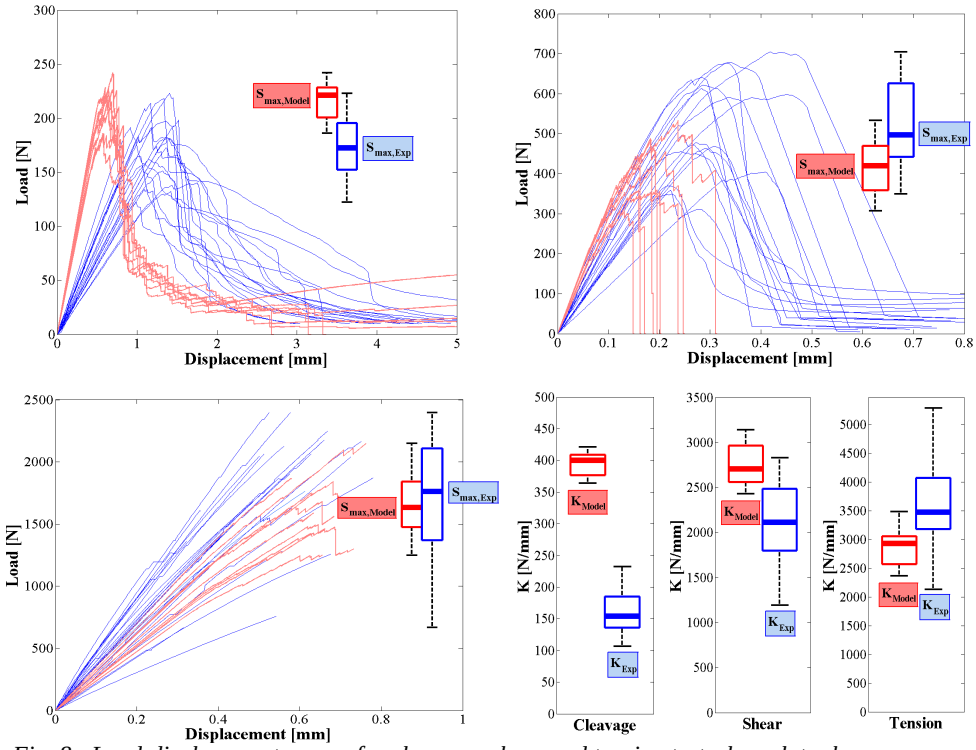

Fig. 8 Load-displacement curves for cleavage, shear and tension tests, box plots show variation in K and S_{max} for model (red) and experiments (blue)

4. Discussion, Conclusions and Acknowledgements

Lattice models seem to be a reasonable approach to model fracture behaviour. Comparisons between experiments and lattice models show that realistic predictions can be made in terms of stiffness, maximum load and fracture path. Heterogeneity was implemented by creating an artificial growth ring structure. This has a significant influence on the fracture path which can be observed in the model as well as in tests (see cleavage model in Fig. 7).

However, since it was important to minimise the computational effort various techniques and approximations were applied. For example, one major drawback is that the lattice does not perfectly represent transverse isotropy (i.e. can not be adjusted freely to any given set of elastic properties). The only solution, to use angular springs, leads to even more strength parameters that need to be determined and to more computation time.

The authors acknowledge the experimental work for measuring density samples taken place in the Agricultural & Analytical Chemistry Department at the University of Glasgow. Furthermore, they want to express their gratitude for the financial support from the Royal Academy of Engineering, Edinburgh, which enabled the participation in the WCTE conference.

5. References

[1] Davids, W. G., Landis, E. N., Vasic, S., "Lattice Models for the Prediction of Load-Induced Failure and Damage in Wood", *Wood Fibre Science*, Vol. 35 PT1, 2003, p.120.

[2] Fournier, C.R., Davids, W.G., Nagy, E., Landis, E.N., "Morphological Lattice Models for the Simulation of Softwood Failure and Fracture", *7th WCCM*, Los Angeles, USA, 2006.

[3] Vasic, S., Smith, I., Landis, E., "Finite Element Techniques and Models for Wood Fracture Mechanics", *Wood Science and Technology*, Vol. 39, 2005, pp. 3-17.

[4] Jirásek, M. and Bažant, Z., "Macroscopic Fracture Characteristics of Random particle Systems", *International Journal of Fracture*, Vol. 69, 1995, pp. 201-228.

[5] Ostoja-Starzewski, M., "Lattice Models in Micromechanics", *Applied Mechanics Reviews*, Vol. 55, No 1, 2002.

[6] Green, D.W., Winandy, J.E. and Kretschmann, D.E.,"Wood Handbook—Wood as an Engineering Material", Chapter 4, *General Technical Report FPL–GTR–113*, Madison, WI: U.S. Department of Agriculture, Forest Service, Forest Products Laboratory, 1999, p. 463.

[7] McLean, J.P., "Wood Properties of four Genotypes of Sitka Spruce", *PhD Thesis*, University of Glasgow, Chemistry Department, 2007.

Nomenclature

α	angle between Y-axis and vector from lattice centre to pith	[rad]
σ, ε, C	stress, strain and elasticity tensor	[N/mm², -, N/mm²]
$\bar{\rho}(r)$	normalised density at radial distance r	[-]
$\bar{\rho}_{diff,i}$	difference between max normalised density and min for ring i	[-]
$\bar{\rho}_{exp,i}$	exponent parameter in approximated, normalised density function for ring i	[-]
$\bar{\rho}_{min,i}$	minimum parameter in approximated, normalised density function for ring i	[-]
v_{xy}	Poisson ratio (load applied in X and displacement in Y)	[-]
$\gamma_{C,x,i}$	parameters defining compression softening curve for spring i in X	[-]
φ	probability density	[-]
σ, μ, c_v	mean value, standard deviation, coefficient of variation (σ/μ)	[N, N/mm,-]
dx	lattice spacing in X	[mm]
E_x, G_{xy}	E-modulus in X, shear modulus in XY-plane	[N/mm², N/mm²]
F	force in one spring	[N]
i,j,k,m	arbitrary variables	[-]
K_{Test},K_{model}	overall stiffness for test and model	[N/mm, N/mm]
K_x	mean stiffness parameter in X	[N/mm]
$K_x{}^i$	stiffness parameter in X for spring i	[N/mm]
$l^{(b)}$	length of vector $n^{(b)}$	[mm]
$n^{(b)}$	normalised vector of spring (b) in unit cell	[-]
N_b	number of half springs in one unit cell (18)	[-]
$P_{c,i}$	vector from pith to spring i	[-]
r, r_i, Δr_i	radial distance from pith, radius of ring i, ring width of ring i	[mm, mm, mm]
$\Delta r_{diff,i}$	difference between ring width of ring i and ring i-1	[mm]
r_{pith}	distance from lattice centre to pith	[mm]
$\bar{r}_{shift}$	parameter defining position of specimen in centre growth ring	[-]
r_{var}	difference between radius of ring i, front and backside	[mm]
$S_{C,x,i}$	individual strength parameter for tension in X for spring i	[N]
$S_{T,x}$	mean strength parameter for compression in X	[N]
$S_{max,test/model}$	maximum load for tests and model	[N]
u	displacement in one spring	[mm]
U	strain energy	[N/mm²]
V	volume of lattice unit cell	[mm³]